Topological optimization of complex heterogeneous materials

Daicong Da

UNIVERSITÉ PARIS-EST

UNIVERSITÉ PARIS-EST

ÉCOLE DOCTORALE SCIENCE INGÉNIERIE ET ENVIRONNEMENT

A thesis submitted for the degree of *Doctor of Philosophy*

Specialty: *Advanced Mechanics*

by

Daicong DA

Subject of thesis:

Topological optimization of complex heterogeneous materials

Thesis defensed on Nov. 27 2018 in front of the jury composed of:

Piotr BREITKOPF	Ingénieur de Recherche HDR Université de Technologie de Compiègne	Reviewer
Qi XIA	Professor Huazhong University of Science and Technology	Reviewer
Chao JIANG	Professor Hunan University	Examiner
Julien YVONNET	Professor (Advisor) Université Paris-Est Marne-la-Vallée	Examiner
Guangyao LI	Professor (Co-advisor) Hunan University	Examiner

Abstract

Mechanical and physical properties of complex heterogeneous materials are determined on one hand by the composition of their constituents, but can on the other hand be drastically modified by their microstructural geometrical shape. Topology optimization aims at defining the optimal structural or material geometry with regards to specific objectives under mechanical constraints like equilibrium and boundary conditions. Recently, the development of 3D printing techniques and other additive manufacturing processes have made possible to manufacture directly the designed materials from a numerical file, opening routes for totally new designs. The main objectives of this thesis are to develop modeling and numerical tools to design new materials using topology optimization. More specifically, the following aspects are investigated. First, topology optimization in mono-scale structures is developed. We primarily present a new evolutionary topology optimization method for design of continuum structures with smoothed boundary representation and high robustness. In addition, we propose two topology optimization frameworks in design of material microstructures for extreme effective elastic modulus or negative Poisson's ratio. Next, multiscale topology optimization of heterogeneous materials is investigated. We firstly present a concurrent topological design framework of 2D and 3D macroscopic structures and the underlying three or more phases material microstructures. Then, multiscale topology optimization procedures are conducted not only for heterogeneous materials but also for mesoscopic structures in the context of non-separated scales. A filter-based nonlocal homogenization framework is adopted to take into account strain gradient. Finally, we investigate the use of topology optimization in the context of fracture resistance of heterogeneous structures and materials. We propose a first attempt for the extension of the phase-field method to viscoelastic materials. In addition, phase-field methods for fracture able to take into account initiation, propagation and interactions of complex both matrix and interfacial micro cracks networks are adopted to optimally design the microstructures to improve the fracture resistance.

Résumé

Les propriétés effectives mécaniques et physiques des matériaux hétérogènes dépendent d'une part de leurs constituants, mais peuvent également être fortement modifiées par leur répartition géométrique à l'échelle de la microstructure. L'optimisation topologique a pour but de définir la répartition optimale de matière dans une structure en vue de maximiser un ou plusieurs objectifs tels que les propriétés mécaniques sous des contraintes telles que la masse de matière. Récemment, les développements rapides de l'impression 3D ou d'autres techniques de fabrication additive ont rendu possible la fabrication de matériaux avec des microstructures "à la demande", ouvrant de nouvelles perspectives inédites pour la conception de matériaux. Dans ce contexte, les objectifs de cette thèse sont de développer des outils de modélisation et de simulation numériques pour concevoir des matériaux et des structures hétérogènes ayant des propriétés optimisées basés sur l'optimisation topologique. Plus précisément, nous nous intéressons aux points suivants.

Premièrement, nous proposons des contributions à l'optimisation topologique à une seule échelle. Nous présentons tout d'abord une nouvelle méthode d'optimisation topologique avec évolution pour la conception de structures continues par description lisse de bords. Nous introduisons également deux techniques d'homogénéisation topologique pour la conception de microstructures possédant des propriétés effectives extrêmes et des « meta propriétés » (coefficient de Poisson négatif). Dans une seconde partie, des techniques multi échelle basées sur l'optimisation topologique sont développées. Nous proposons d'une part une approche concourante de structures hétérogènes dont les microstructures peuvent posséder plus de deux matériaux. Nous développons ensuite une approche d'optimisation topologique dans un cadre d'homogénéisation pour des échelles faiblement séparées, induisant des effets de gradient.

Enfin dans une troisième partie, nous développons l'optimisation topologique pour maximiser la résistance à la fracture de structures ou de matériaux hétérogènes. La méthode de champs de phase pour la fracture est combinée à la méthode BESO pour concevoir des microstructures permettant d'augmenter fortement la résistance à la rupture. La technique prend en compte l'initiation, la propagation et la rupture complète de la structure.

Publications related to the thesis

1. Liang Xia, Daicong Da, Julien Yvonnet. Topology optimization for maximizing the fracture resistance of quasi-brittle composites. *Computer Methods in Applied Mechanics and Engineering*, 332:234–254, 2018

2. Daicong Da, Julien Yvonnet, Liang Xia, Guangyao Li. Topology optimization of particle-matrix composites for optimal fracture resistance taking into account interfacial damage. *International Journal for Numerical Methods in Engineering*, 1–23, 2018

3. Daicong Da, Julien Yvonnet, Liang Xia, Minh Vuong Le, Guangyao Li. Topology optimization of periodic lattice structures taking into account strain gradient. *Computers and Structures*, 210:28–40, 2018

4. Daicong Da, Xiangyang Cui, Kai Long, Guangyao Li. Concurrent topological design of composite structures and the underlying multi-phase materials. *Computers and Structures*, 179:1–14, 2017

5. Daicong Da, Xiangyang Cui, Kai Long, Guanxin Huang, Guangyao Li. Design of material microstructures for maximum effective elastic modulus and macrostructures. *Engineering Computations*, 35(2):622–640, 2018

6. Daicong Da, Jiahui Chen, Xiangyang Cui, Guangyao Li. Design of materials using hybrid cellular automata. *Structural and Multidisciplinary Optimization*, 56(1):131–137, 2017

7. Daicong Da, Liang Xia, Guangyao Li, Xiaodong Huang. Evolutionary topology optimization of continuum structures with smooth boundary representation. *Structural and Multidisciplinary Optimization*, 57(6):2143–2159, 2018

8. Daicong Da, Julien Yvonnet, Liang Xia, Guangyao Li. Size effect analysis in topology optimization for periodic structures using the classical homogenization. (Submitted), -:-, 2018

9. Daicong Da, Julien Yvonnet, Liang Xia, Guangyao Li. Topology optimization of mesoscopic structures with fixed periodic microstructures. (Submitted), -:-, 2018

10. Daicong Da, Julien Yvonnet, Benoit Bary, Thomas Helfer, Olivier Fandeur, Qi-Chang He. Phase-field for crack propagation in linear viscoelastic materials. (In preparation), -:-, 2018

11. Daicong Da, Julien Yvonnet, Liang Xia, Guangyao Li. Topology optimization for maximizing the fracture resistance of periodic composites. (In preparation), -:-, 2018

Acknowledgements

First of all, I would like to extend my sincere appreciation to my supervisor, Professor Julien Yvonnet, for his guidance during my PhD study in France. I have been very fortunate to have studied with him in the past few years. I am grateful for his help and the endless discussions between us, not only about academic research, but also about positive attitudes towards life. The journey we went to China together will be the best memories to be treasured. I would like to take this opportunity to wish him and his family health and happiness. My deep and sincere gratitude goes also to my supervisor in China, Professor Guangyao Li, who has granted me great freedom in academic research and has always been supportive and rigorous. I am very grateful for he has supported me to pursue my PhD study abroad, which have significantly broadened my horizons and enriched my experience.

Special thanks goes to Professor Liang Xia for his encouragement as a researcher and for his concern as a brother. Special thanks goes also to Professors Xiangyang Cui, Kai Long and Xiaodong Huang for their discussion and rigorous attitude in our collaboration, which will continue to encourage me to pursue a higher level of research.

I am also very grateful to all the professors who participated in my doctoral defense. Finally, I would like to thank my relatives and all my intimate friends for their company and support during my PhD study.

Contents

Abstract ii

Résumé iii

Publications related to the thesis iv

Acknowledgements vi

1 Introduction 1
- 1.1 Background and motivations . . . 1
- 1.2 Literature review . . . 3
  - 1.2.1 Topology optimization methods . . . 3
  - 1.2.2 Material design and multiscale optimization . . . 5
  - 1.2.3 Fracture resistance design . . . 8
- 1.3 Outline of the thesis . . . 9

I Topology optimization of mono-scale structures 12

2 Evolutionary topology optimization of continuum structures with smooth boundary representation 13
- 2.1 ETO method framework . . . 14
  - 2.1.1 Design and FEA models . . . 14
  - 2.1.2 Problem statements and sensitivity analysis . . . 15
    - 2.1.2.1 Problem statements . . . 15
    - 2.1.2.2 Sensitivity analysis . . . 17
  - 2.1.3 Nodal sensitivity numbers and level set function . . . 18
  - 2.1.4 Update of structural topology . . . 20
  - 2.1.5 Convergence criterion . . . 22
- 2.2 ETO procedure . . . 22
- 2.3 Numerical examples . . . 23
  - 2.3.1 Minimum compliance for a cantilever beam . . . 23
  - 2.3.2 Minimum compliance for a MBB beam . . . 26
  - 2.3.3 Minimum compliance for a roller-supported half-wheel . . . 27

2.3.4 2D Design for structural natural frequency . . . 32
2.3.5 3D Design for structural compliance . . . 32
2.3.6 3D Design for structural natural frequency . . . 34
2.4 Concluding remarks . . . 35

3 Design of materials for maximum effective elastic modulus and negative Poisson's ratio 38
3.1 Design of materials using the BESO . . . 39
3.1.1 Principle of the strain energy-based method and sensitivity analysis 39
3.1.2 Topological design optimization model and numerical implementation . . . 40
3.1.3 Numerical examples . . . 42
3.1.3.1 2D example for maximizing the shear modulus . . . 42
3.1.3.2 2D example for maximizing the bulk modulus . . . 43
3.1.3.3 3D example for maximizing the shear modulus . . . 46
3.1.3.4 3D example for maximizing the bulk modulus. . . . 46
3.2 Design of materials using the hybrid cellular automata . . . 47
3.2.1 Optimization model . . . 48
3.2.2 Updating rule and convergence criterion . . . 50
3.2.3 Numerical examples . . . 50
3.3 Concluding remarks . . . 52

II Multiscale topology optimization 55

4 Concurrent topological design of structures and multi-phase materials 56
4.1 Concurrent optimization design formulation . . . 57
4.2 Material interpolation scheme and sensitivity analysis . . . 59
4.2.1 Material interpolation scheme . . . 59
4.2.2 Sensitivity analysis . . . 60
4.3 BESO method and numerical implementation . . . 62
4.3.1 Sensitivity numbers . . . 62
4.3.2 Variables updating . . . 63
4.3.3 Numerical implementation . . . 64
4.4 Concurrent optimization for structural stiffness . . . 65
4.4.1 Design of a 2D cantilever beam . . . 65
4.4.2 Design of a 2D MBB beam . . . 68
4.4.3 Design of a 3D cantilever beam . . . 71
4.4.4 Design of a 3D MBB beam . . . 72
4.5 Concluding remarks . . . 74

5 Multiscale topology optimization in the context of non-separated scales 76
5.1 Size effect analysis in topology optimization for periodic structures using the classical homogenization . . . 77
5.1.1 The classical homogenization method . . . 77
5.1.1.1 Localization problem . . . 77
5.1.1.2 Definition and computation of the effective material properties . . . 79
5.1.1.3 Numerical implementation for the local problem with PER . . . 81
5.1.2 Topology optimization model and procedure . . . 82
5.1.2.1 Optimization model and sensitivity number . . . 82
5.1.2.2 Finite element meshes and relocalization scheme . . . 83
5.1.2.3 Optimization procedure . . . 84
5.1.3 Numerical examples . . . 85
5.1.3.1 Doubly-clamped elastic domain . . . 86
5.1.3.2 L-shaped structure . . . 87
5.1.3.3 MBB beam . . . 89
5.2 Topology optimization of periodic structures taking into account strain gradient . . . 93
5.2.1 Nonlocal filter-based homogenization for non-separated scales . 94
5.2.1.1 Definition of local and mesoscopic fields through the filter 94
5.2.1.2 Microscopic unit cell calculations . . . 97
5.2.1.3 Mesoscopic structure calculations . . . 101
5.2.2 Topology optimization procedure . . . 103
5.2.2.1 Model definition and sensitivity numbers . . . 103
5.2.2.2 Overall optimization procedure . . . 104
5.2.3 Validation of the nonlocal homogenization approach . . . 104
5.2.4 Numerical examples . . . 106
5.2.4.1 Cantilever beam with a concentrated load . . . 107
5.2.4.2 Four-point bending lattice structure . . . 112
5.3 Topology optimization of structures with fixed periodic microstructures 113
5.3.1 Optimization model and procedure . . . 115
5.3.2 Numerical examples . . . 117
5.3.2.1 A double-clamped beam . . . 117
5.3.2.2 A cantilever beam . . . 120
5.4 Concluding remarks . . . 120

III Phase field modeling and fracture resistance design **123**

6 Phase field for crack propagation in linear viscoelastic materials **124**
6.1 Extension of the phase field method to viscoelasticity 124
6.1.1 Variational principle 125
6.1.2 Mechanical problem 126
6.1.3 Phase field problem 126
6.2 Generalized Maxwell viscoelastic model 128
6.3 Overall algorithm 129
6.4 Numerical examples 129
6.4.1 A homogeneous 2D plate 129
6.4.2 A heterogeneous 2D composite plate 130
6.4.3 A heterogeneous 3D composite plate 130
6.5 Concluding remarks 135

7 Topology optimization for maximizing the fracture resistance **136**
7.1 Topology optimization for optimal fracture resistance of quasi-brittle composites 138
7.1.1 Phase field modeling of crack propagation 138
7.1.1.1 Phase field approximation of cracks 138
7.1.1.2 Thermodynamics of the phase field crack evolution . . 139
7.1.1.3 Weak forms of displacement and phase field problems . 141
7.1.1.4 Finite element discretization 142
7.1.2 Topology optimization model for fracture resistance 143
7.1.2.1 Model definitions 144
7.1.2.2 Sensitivity analysis 145
7.1.2.3 Extended BESO method 148
7.1.3 Numerical examples 150
7.1.3.1 Design of a 2D reinforced plate with one pre-existing crack notch 151
7.1.3.2 Design of a 2D reinforced plate with two pre-existing crack notches 154
7.1.3.3 Design of a 2D reinforced plate with multiple pre-existing cracks 156
7.1.3.4 Design of a 3D reinforced plate with a single pre-existing crack notch surface 158
7.2 Topology optimization for optimal fracture resistance taking into account interfacial damage 159
7.2.1 Phase field modeling of bulk crack and cohesive interfaces 161

7.2.1.1 Regularized representation of discontinuous field 161
7.2.1.2 Energy functional 162
7.2.1.3 Displacement and phase field problems 164
7.2.1.4 Finite element discretization and numerical implementation 166
7.2.2 Topology optimization method 168
7.2.2.1 Model definitions 169
7.2.2.2 Sensitivity analysis 170
7.2.3 Numerical examples 172
7.2.3.1 Design of a plate with one initial crack under traction . 172
7.2.3.2 Design of a plate without initial cracks for traction loads 175
7.2.3.3 Design of a square plate without initial cracks in tensile loading 178
7.2.3.4 Design of a plate with a single initial crack under three-point bending 178
7.2.3.5 Design of a plate containing multiple inclusions 181
7.3 Topology optimization for maximizing the fracture resistance of periodic composites 182
7.3.1 Topology optimization model 183
7.3.2 Numerical examples 184
7.3.2.1 Design of a periodic composite under three-point bending 185
7.3.2.2 Design of a periodic composite under non-symmetric three-point bending 188
7.4 Concluding remarks 193

8 Conclusion and perspectives **195**

A The ETO Matlab code **198**

Bibliography **202**

Dedicated to my loving parents and my fiancée CC

Chapter 1

Introduction

In this first Chapter, the background and motivations of the thesis are presented in Section 1.1. Literature review on related subjects, including topology optimization methods, material design and multiscale optimization, fracture resistance design are given in Section 1.2. Outline of the thesis is presented lastly in Section 1.3.

1.1 Background and motivations

Topological optimization has been an active research topic in the last decades and has become a subject of major importance with the growing development of additive manufacturing processes, which allow fabricating workpieces like lattice structures with arbitrary geometrical details. In that context, topology optimization [15, 3] aims to define the optimal structural or material geometry with regards to specific objectives (e.g. maximal stiffness, minimal mass, or maximizing other physical/mechanical properties), under mechanical constraints like equilibrium and boundary conditions. The key merit of topology optimization over conventional size and shape optimization is that the former can provide more design freedom, consequently leading to the creation of novel and highly efficient designs. By the topology optimization technique, designers can make the best use of limited materials and guide the concept design of various practical structures, especially in automotive and aerospace engineering.

In the recent years, there is an increasing use of high-performance heterogeneous materials such as fibrous composite, concrete materials, 3D printed materials etc. Mechanical and physical properties of complex heterogeneous materials are determined on one hand by the composition of their constituents, but can on the other hand be drastically modified, at a constant volume fraction of heterogeneities, by their geometrical shape and by the presence of interfaces. Topological optimization of microstructures can help designing materials with higher effective properties while maintaining the volume fraction of constituents, or to obtain new properties which are not naturally available (metamaterials). Recently, the development of 3D printing techniques or additive manufacturing processes have made possible to manufacture directly the

designed materials from a numerical file, opening routes for totally new designs, as is shown in Fig. 1.1. It is no exaggeration to say that "additive manufacturing" and "topology optimization" are the best couple for each other. To this end, systematic and comprehensive research on topological design of complex heterogeneous materials is of great significance for academic research and engineering applications.

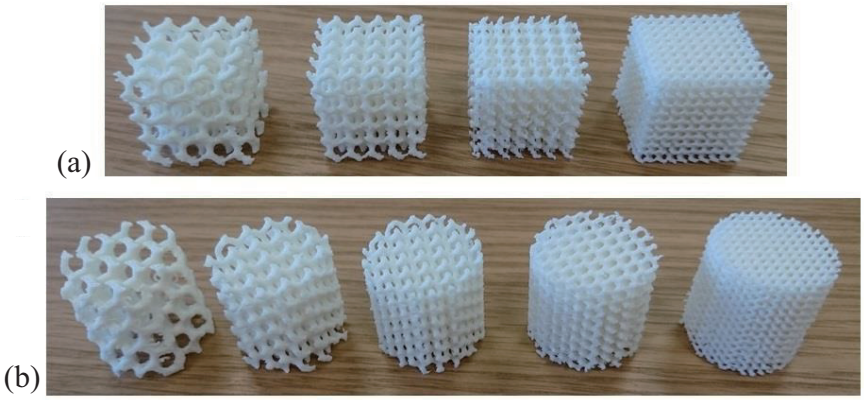

FIGURE 1.1: 3D printed lattice materials: (a) cubic and (b) cylindrical configurations [115].

However, in topology optimization applied to material modeling, the assumption of scale separation is often assumed. This assumption states that the characteristic length of the microstructural details are much smaller than the dimensions of the structure, or that the characteristic wavelength of the applied load is much larger than that of the local fluctuation of mechanical fields [58]. In additive manufacturing of architectured materials like lattice structures, the manufacturing process might induce limitations on the size of local details, which can lead to a violation of scale separation when the characteristic size of the periodic unit cell within the lattice is not much smaller than that of the structure. In such case, classical homogenization methods may lead to inaccurate description of the effective behavior as non local effects, or strain-gradient effects, may occur within the structure. On the other hand, using a fully detailed description of the lattice structure in an optimization framework could be computationally very costly. One objective of this thesis work is to develop multiscale topology optimization procedures not only for heterogeneous materials but also for mesoscopic structures in the context of non-separated scales.

On the other hand, fatigue or failure characteristics of engineering structures are another subject of great concern, as shown in Fig. 1.2. Microcracking is known as significant factor affecting the mechanical properties and the long term behavior of engineering facilities. The accurate modelling of these phenomena including their coupled effects have then to receive a special attention. In addition, topology optimization design of composite materials accounting for fracture resistance is a rather challenging

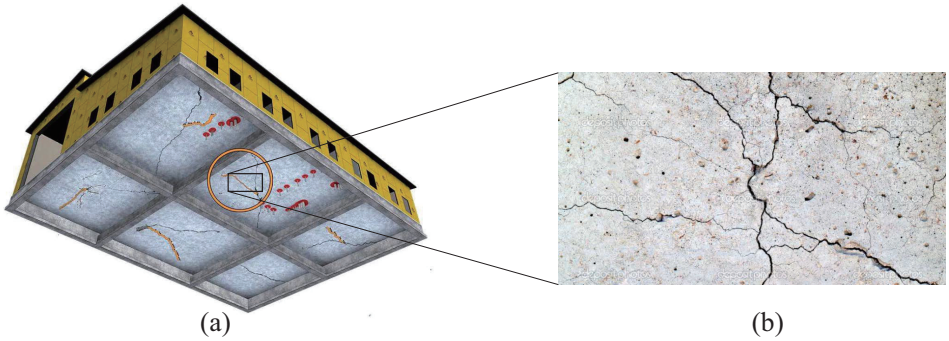

(a) (b)

FIGURE 1.2: Damage phenomena in engineering: (a) macroscopic structure; (b) cracks [122].

task. It is desired to improve the fracture resistance of heterogeneous materials in terms of the required mechanical work, through an optimal placement of the inclusion phase, taking into account the cracks nucleation, propagation and interaction. However, this research remains relatively unexplored so far with the following reasons. Firstly, there is lack of robust numerical methods for fracture propagation in presence of complex heterogeneous media until recently, especially when interface effects are presented. Secondly, these numerical simulation models should be formulated in a context compatible with topological optimization scheme. For these reasons, there has been very limited research in the literature on topology optimization for maximizing the fracture resistance of heterogeneous materials before the recent works from the author and his collaborators [173, 46].

1.2 Literature review

In the following, Section 1.2.1 provides a brief literature review on the developments of topology optimization methods. Section 1.2.2 reviews material microstructure design and extension to multiscale topological optimization with or without scale separation. Section 1.2.3 presents the newly proposed fracture resistance design framework, by combing the phase field method to take into account the heterogeneities and their interfaces in the material.

1.2.1 Topology optimization methods

Over the past decades, topology optimization has undergone a tremendous development since the seminal paper by [15]. The key merit of topology optimization over conventional size and shape optimization is that the former can provide more design freedom, consequently leading to the creation of novel and highly efficient designs. So far, various topology optimization methods have been proposed, e.g., density-based

methods [14, 191, 17], evolutionary procedures [179, 180], level-set method (LSM) [138, 164, 5], hybrid cellular automaton [154] and phase field method [24]. All of these methods are based on finite element analysis (FEA) where the design domain is discretized into a number of finite elements. With such a setting, the optimization procedure is then to determine which points of the design domain should be full of material (solid elements) and the others void (or soft elements), as shown in Fig. 1.3. According to the update algorithm, these methods can be categorized in general into two groups: density variation and shape/boundary variation. So far, topology optimization technique has already become an effective tool for both academic researches and engineering applications. A general review of various methods and their applications has been presented by [49]. Regarding their strengths, weaknesses, similarities and dissimilarities, a critical review and comparison on different approaches is also given by [146].

Level-set method (LSM) is a typical shape/boundary variation approach which maintains the capability of topological change. It describes the structural topology implicitly by the iso-contours of a level-set function. By LSM, a fixed rectilinear spatial grid and a finite element mesh of a given design domain are constructed separately, which allows the separation of the topological description from the physical model. With the merits of the flexibility in handling complex topological changes and the smoothness of boundary representation, LSM has been successfully applied to an increasing variety of design problems, involving e.g., multi-phase materials [163], shell structures [128], geometric nonlinearities [102], stress minimization [4] and contact problem [117]. The reader is referred to the comprehensive review in [51] for more theoretical details of different LSMs for structural topology optimization.

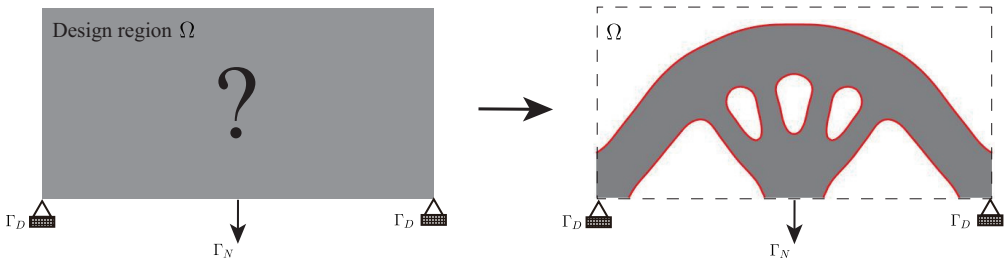

FIGURE 1.3: Illustration for structure topology optimization.

Density-based methods are the most commonly used topology optimization approaches, such as the popular solid with isotropic material with penalization (SIMP) method. The SIMP method uses continuous design variables for topology optimization, which can be interpreted as material pseudo densities [14, 191, 113]. The physical justification of SIMP was provided by [16]. A popular 99-line topology optimization Matlab code using the SIMP method was developed in [141] for education purposes.

As a successor of the 99-line code, a more efficient 88-line Matlab code was also provided by Andreassen et al. [12] with high computational efficiency and alternative filter implements. More details including theory, numerical methods and applications on the SIMP method can be found in [17].

As another important branch of topology optimization, evolutionary structural optimization (ESO) [179, 180, 151] and its later version bidirectional ESO (BESO) [76] have shown promising performance when applying to a wide range of structural design problems. ESO-type methods use a simple heuristic scheme to evolve the structural topology towards an optimum by gradual removing redundant or inefficient materials. The BESO method allows not only material removal, but also material addition, showing efficient and reliable performance in various design problems [78, 77, 74, 168, 169, 171, 79, 161, 41]. The early development of ESO-type methods was summarized by Xie and Steven [180]. The development of the BESO method and its various applications up to year 2010 can been founded in [77].A comprehensive review on the BESO method for advanced design of structures and materials was recently presented by Xia et al. [175].

As an extension to the original BESO method, the author and his collaborators have proposed a new evolutionary topology optimizatio (ETO) method [44] to design continuum structures, by introducing a sensitivity-based level-set function (LSF). The proposed ETO method identifies the topology far beyond elements, and it does not involve the removal/addition of elements during the optimization process, resulting in a smoothed boundary representation and high robustness. The smooth structural topology has been extended to the robust topology optimization of continuum structures under loading and material uncertainties in [105]. Inspired by the ETO method, the material removal scheme of the evolutionary-type methods has been combined with LSM to nucleate holes in the structure for optimization design of heat conduction [176].

Recently, a new computational framework for structural topology optimization based on the concept of moving morphable components is proposed [65]. The basic idea of this method is to use a set of deformable components as the basic building block of optimization structures, so as to tailor the structure topology through deformation, merge and overlap operations between components. Therefore, the design variables of the method are reduced during the topology optimization process, and the topological geometries of the structure can be presented explicitly [189, 67, 188].

1.2.2 Material design and multiscale optimization

Initially restricted to optimizing the geometry of structures, the topology optimization techniques have been extended to optimizing the topology of the phase within materials, e.g. in periodic microstructures, to design high performance materials [144, 148,

142, 183, 63, 62, 162, 11, 35, 79] or materials with properties not found in nature (negative Poisson's ratio, zero compressibility, negative bulk modulus, etc. (see [166, 38, 43, 126]) or complex multiphysics problems [119, 118]. These techniques are based on optimizing the homogenized properties of the representative volume element, and using numerical solving methods like finite elements to compute the homogenized properties [107, 72, 73, 10], given one geometry of the phases and their microscopic properties, as is shown in Fig. 1.4. A review of topological optimization of microstructures in the linear context can be found in e.g. [30].

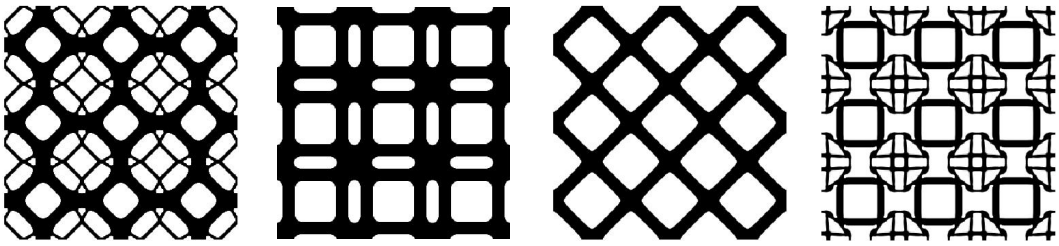

(a) (b) (c) (d)

FIGURE 1.4: Material topologies with extreme elastic modulus and negative Poisson's ratio: (a) and (b) show the geometries with maximum bulk modulus, (c) shows the geometry with maximum shear modulus, (d) shows the geometry with negative Poisson's ratio [43]

Rather than pure material design, material microstructures have also been tailored for a fixed [80] structure to maximize macroscopic performance under specific boundary conditions, e.g. structural stiffness [42]. In order to fully release the design freedom within multiscale optimization, Rodrigues et al. [135] first described a hierarchical computational procedure for optimization of material distribution as well as the local material properties of mechanical elements, which has later been extended to 3D in [40] and to account for hyperelasticity. Via this design strategy, simultaneous structure and materials design has been studied extensively, such as for composite laminate orientations [139, 140, 39], closed liquid cell materials [104], or multi-objective functions, e.g. maximum stiffness and minimum resistance to heat dissipation in [90], or minimum thermal expansion of the surfaces in [50]. Extensions to nonlinear materials [169], multiple phase materials [41] and optimization considering uncertainties [68, 182] have been proposed recently.

In the context of non-separated scales, the effectiveness of the classical homogenization-based multiscale topology optimization framework for periodic lattice structures has been firstly investigated in [45]. The characteristic dimensions of the periodic unit cells in the lattice are comparable with the dimensions of the whole structure such that the two scales can clearly not be separated. The dimensions of the unit cell range from large to small as compared with the dimensions of the whole structure to highlight the

size effect. By assuming the material microstructures are infinitely small, the inverse homogenization designs for macroscopic structural performance were compared with the mono-scale topology optimization framework in [181, 192].

On the other hand, several computational homogenization methods modeling complex heterogeneous media when scales are not separated are available (e.g. gradient models in [130, 89], nonlocal elsticity theories in [53] and domain decomposition methods in [94]). Among which, the filter-based nonlocal homogenization technique developed in [185, 186, 152] has been adopted in [47] to develop a topology optimization procedure for heterogeneous lattice materials in the context of non-separated scales, taking into account the strain gradient effects. The technique generalizes the homogenization theory by replacing spatial averaging operators by linear low-pass filters, and the major advantage is that it can take into account an arbitrary level of strain gradient without higher order elements, in a classical finite element framework.

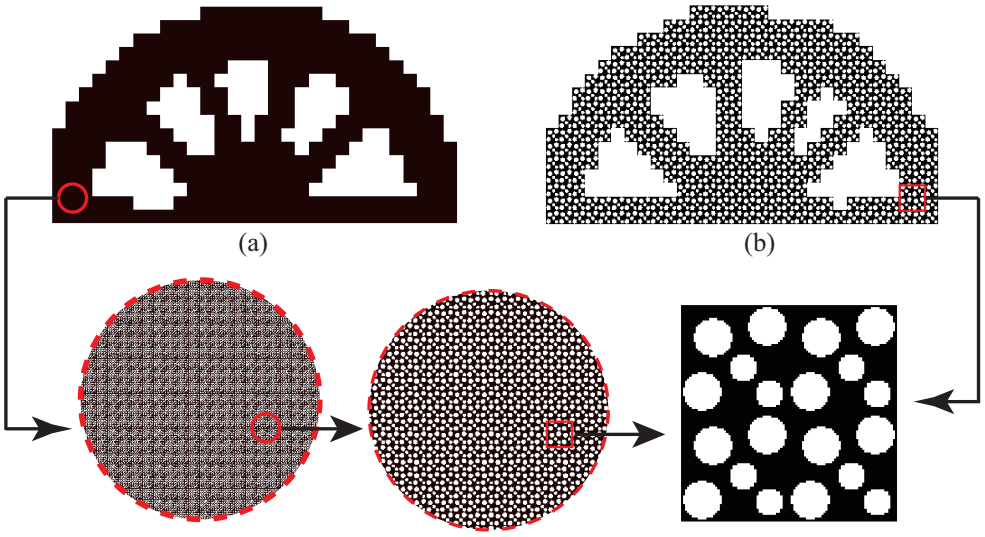

FIGURE 1.5: Illustration of the two-scale optimized structure composed of the patterned microstructure periodically: (a) with scale separation; (b) non-separated scales.

In the case of giving fixed/optimized microscopic periodic cells, multiscale topological design of mesoscopic structures without scale separation has been firstly proposed in [48]. The idea is to use a computational homogenization method which takes into account the strain gradient effects combined with a topological optimization scheme of mesoscopic structures, allowing the topological optimization problem to be performed on a coarse mesh, instead of using the fully detailed description of the structure for computational saving, as shown in Fig. 1.5. In addition, other studies, e.g. [187, 2] have also been devoted to topology optimization of structures in the context of non-separated scales.

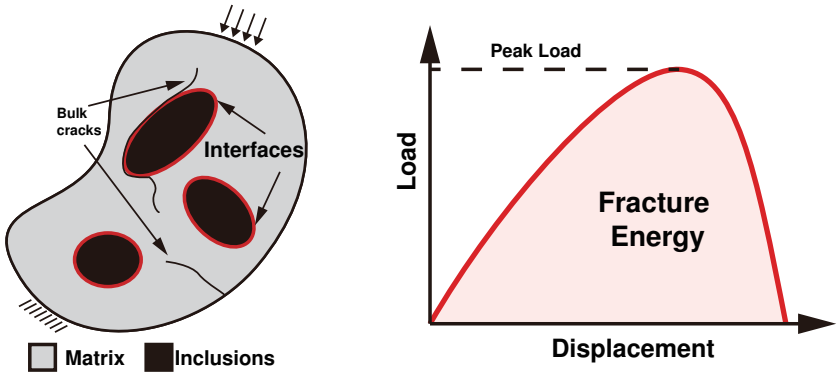

(a) (b)

FIGURE 1.6: (a) structure containing both bulk cracks and interface cracks, possibly occurring at the interfaces, (b) mechanical response of the damageable structure [46].

1.2.3 Fracture resistance design

Optimization design of composite materials accounting for fracture resistance remains relatively unexplored so far, mainly due to the lack of robust numerical methods for simulation of fracture propagation in presence of complex heterogeneous media and interfaces, until recently. In addition, these numerical simulation models should be formulated in a context compatible with topological optimization (e.g. finite elements). In [61], Gu et al. used a modified greedy optimization algorithm for composites made up of soft and stiff building blocks to improve material toughness. San and Waisman [136] explored the optimal location of carbon black particle to maximize the rupture resistance of polymer composites by a genetic algorithm. In a recent work by the author and his collaborators [173], topology optimization for maximizing the fracture resistance of quasi-brittle composites has been introduced by combining the phase field method and a gradient-based BESO algorithm. However, in the mentioned work, the crack propagation resistance was only evaluated on the basis of phase distribution. In most heterogeneous quasi-brittle materials (e.g. ceramic matrix composites, cementitious materials), the interfacial damage plays a central role in the nucleation and propagation of microcracks [158, 95, 125, 120]. Therefore, we further extended the design framework developed in [173] for defining through topological optimization the optimal phase distribution in a quasi-brittle composite with respect to fracture resistance, taking into account crack nucleation both in the matrix and in the interfaces, as described in Fig. 1.6. To the author's best knowledge, such study is investigated in this thesis for the first time.

Simulating interfacial damage and its interaction with matrix crack for complex heterogeneous materials is a highly challenging issue for meshing algorithms. Many numerical methods such as eXtended Finite Element Method (XFEM) [114, 149], Thick

Level-set method (TLS) [18, 33], and Phase Field Method (PFM) [54, 108, 91], among the most recent popular techniques, have been introduced to investigate this topic.

Based on the pioneer works of Marigo and Francfort [54], the phase field method makes use of a variational principle framework for brittle fracture [25, 26, 26] and of a regularized description of the discontinuities related to the crack front [116, 6]. The method has been adapted to a convenient algorithmic setting by Miehe et al. in [111]. The main advantages of the method are: (a) the crack paths are mesh-independent; (b) initiation and propagation of multiple, complex cracks patterns can be easily handled; (c) the method is convergent with respect to the mesh size and not sensitive to the mesh regularity; (d) it is stable due to its inherent gradient-based formulation. In this thesis, we use the extension of the phase field to interfacial damage as proposed in [123] to take into account both bulk brittle fracture and interfacial damage.

While there do exist numerous researches on topology optimization including material interface behavior (see e.g. [160, 96, 99, 13]), and with the enforcement of stress constraints [52, 69, 177, 27, 101, 32, 31], local buckling constraint [150] or damage constraints [34, 8, 7, 83, 82, 85], topology optimization for maximizing the fracture resistance, taking into account interactions between interfacial damage and bulk brittle fracture for complete fracturing process is to our best knowledge explored for the first time herein.

1.3 Outline of the thesis

The aim of this thesis is to study the topological design of complex heterogeneous materials comprehensively and systematically, including material design, simultaneous multi-phase materials and structure design, multiscale optimization without scale separation, phase field modeling and fracture resistance design, and newly proposed topology optimization method. This thesis is organized as follows.

In contrast to conventional zigzag BESO designs and removal/addition of elements, we develop a new topology optimizaton approach named ETO method in Chapter 2 to design continuum structures with smoothed boundary representation. The proposed ETO method determines implicitly the smooth structural topology by a level-set function (LSF) constructed by nodal sensitivity numbers. The analysis of the design model is replaced by the FEA model with various elemental volume fractions, which are determined by the auxiliary LSF. The introduction of sensitivity LSF results in intermediate volume elements along the solid-void interface of the FEA model, thus contributing to the better convergence of the optimized topology for the design model. The content of this Chapter has been published in [7].

In Chapter 3 we develop primarily a material design framework for inverse homogenization of material microstructures. Strain energy homogenization method is

adopted to account the effective material properties of the complex heterogeneous materials. The discrete BESO method is first adopted to inversely tailor the material microstructures to achieve maximum effective elastic modulus. In addition, we firstly introduce the implicit optimization method namely hybrid cellular automaton (HCA) to material design. The values of elastic modulus of cellular automaton (CA) cells are used as the design variables which are updated upon a local rule until stasfying the optimum equilibrium. The numerical design framework is extended to obtain new properties which are not naturally available, e.g. negative Poisson's ratio. The content of this Chapter is the part of published papers [5] and [6].

With the objective to further release design freedom within the inverse homogenization framework presented in Chapter 3, we develop a so-called concurrent topology optimization of structures and the underlying multi-phase material microstructures in Chapter 4. This framework allows one to determine not only the best material layout at the micro scale, but also the optimal use of the designed material at the macro scale offering more design freedom on the two scales. We design the underlying three or more phases material microstructures for both the solid and compliant composite phases of the macroscale structures. Furthermore, we carry out the concurrent topology optimization for both 2D and 3D materials and structures, which makes this work distinguished from existing literatures on the related subjects. The generated interfaces between different consitutive materials/composites are clear and distinctive which facilitates the manufacturing requirements. The content of this Chapter has been published in [4].

We have so far adopted the assumption of scale separation between microscopic materials and macroscopic structures. From Chapter 5, we focuse on multiscale topology optimization in the context of non-separated scales. In this model, we primarily present a topology optimization for periodic structures based on the classical homogenization. The dimensions of the unit cell range from large to small as compared with the dimensions of the whole structure to highlight the size effect. Within the similar established multiscale topology optimization framework without scale separation, we employ a filter-based nonlocal homogenization method to take into account the effects of strain gradient, allowing the topological optimization problem to be performed on a coarse mesh, instead of using the fully detailed description of the structure for computational saving. In addition, the multiscale optimization model has been implemented to design the geometry of mesoscopic structures with specific microscopic unit cells. The microscopic RVE itself is defined as the design variable, and a stiffness interpolation is introduced to derive the sensitivities in a clear manner. The second section of this Chapter has been published in [3]. The rest has been given in papers [8] and [9].

Phase field modeling is extended in Chapter 6 and coupled to a linear viscoelastic

behavior to mimic the creep of the heterogeneous materials. An energy-based formulation is developed to express the equations governing viscoelastic mechanical and phase field problems. A classical generalized Maxwell model is adopted for modelling this viscoelastic behavior. Both 2D and 3D heterogeneous materials subjected to loading with various durations are analyzed with regard to different crack patterns. The content of this Chapter has been given in [10].

In Chapter 7, we propose a topology optimization framework for optimizing the fracture resistance of quasi-brittle composites through a redistribution of the inclusion phases. A phase field method for fracture able to take into account initiation, propagation and interactions of complex microcracks networks is adopted. This formulation avoids the burden of remeshing problems during crack propagation and is well adapted to topology optimization purpose. An efficient design sensitivity analysis is performed by using the adjoint method, and the optimization problem is solved by an extended BESO method. The sensitivity formulation accounts for the whole fracturing process involving cracks nucleation, propagation and interaction, either from the interfaces and then through the solid phases, or the opposite. The spatial distribution of material phases is optimally designed using the extended BESO method to improve the fractural resistance. We demonstrate through numerical examples that the fracture resistance of the composite can be significantly increased at constant volume fraction of inclusions by the topology optimization process. The first two sections of this Chapter have been published in [1] and [2]. The last section is the part of the paper in preparation [11].

In Chapter 8, we conclude the thesis and give perspectives on future research.

Inspired by the work [141, 77, 12, 189, 172], we attach in Appendix A our Matlab codes regarding topological design of continuum structures using the ETO method for compliance minimization, which have been primarily provided in [7].

Note that the order of Chapters in this thesis is presented in a progressive and systematic way: from linear to nonlinear problems, from scale separation to non-separated scales, and from stiffness design to fracture resistance optimization.

Part I

Topology optimization of mono-scale structures

Chapter 2

Evolutionary topology optimization of continuum structures with smooth boundary representation

In this chapter, we develop an extended bi-directional evolutionary structural optimization (BESO) method for topology optimization of continuum structures with smoothed boundary representation. In contrast to conventional zigzag BESO designs and removal/addition of elements, the newly proposed evolutionary topology optimization (ETO) method, determines implicitly the smooth structural topology by a level-set function (LSF) constructed by nodal sensitivity numbers. The projection relationship between the design model and the finite element analysis (FEA) model is established. The analysis of the design model is replaced by the FEA model with various elemental volume fractions, which are determined by the auxiliary LSF. The introduction of sensitivity LSF results in intermediate volume elements along the solid-void interface of the FEA model, thus contributing to the better convergence of the optimized topology for the design model. The effectiveness and robustness of the proposed method are verified by a series of 2D and 3D topology optimization design problems including compliance minimization and natural frequency maximization. We show that the developed ETO method is capable of generating a clear and smooth boundary representation; meanwhile the resultant designs are less dependent on the initial guess design and the finite element mesh resolution.

The remainder of this chapter is organized as follows: Section 2.1 presents the proposed ETO design framework with the relationship between the FEA and the design models as well as the construction of sensitivity LSF. Several typical topology optimization problems including compliance minimization and natural frequency maximization are formulated. Section 2.2 gives numerical implementations of the developed ETO procedure. Section 2.3 presents a series of numerical validations of the ETO method. Section 2.4 draws the conclusion. A Matlab code using the ETO method for compliance minimization design is provided in Appendix A.

2.1 ETO method framework

2.1.1 Design and FEA models

The conventional BESO method optimizes a structure by gradually removing and adding finite elements upon their sensitivity numbers. That is to say that the element itself is treated as a design variable and the structural topology is typically described via element-wise constant, i.e. element pseudo density. This implementation results in designs with zigzag boundaries, especially when a coarse FE mesh is used. In this work, we propose an extended BESO method, namely evolutionary topology optimization (ETO), aiming at obtaining optimized structures with smooth boundary. Since topology optimization requires to update the structural shape iteratively, FEA of a smooth structure can be ideally performed by using the remeshing technique after each design iteration but computationally highly expensive. The simpler and efficient Area-fraction (or volume-fraction in three dimensional cases) weighted Fixed Grid (AFG) method, which has been widely used by spline and level-set based optimization methods [138, 57, 56, 165, 97, 100, 84], is adopted in the present work.

In the proposed ETO method, we separate the design model from the FEA model and establish the project relationship between two models as shown in Figure 2.1. The design model represents the smooth structural topology, which will be determined by the constructed LSF in the later section. When the design model projects onto the background mesh with the fixed grid, the volume fraction of each element, V_e^f, can be easily calculated and three categories of elements are generated: void elements with $V_e^f = 0$; solid elements with $V_e^f = 1$ and boundary elements with $0 < V_e^f < 1$. FEA will be conducted on the fixed-grid model and material properties of elements will be defined with

$$\rho_e(V_e^f) = (1 - V_e^f)\rho_{min} + V_e^f \rho_0 \tag{2.1}$$

$$E_e(V_e^f) = (1 - V_e^f)E_{min} + V_e^f E_0 \tag{2.2}$$

where ρ^m and E are the density and Young's modulus. The subscripts 0 and min denote the solid and void materials, respectively. ρ_{min} and E_{min} are small values in order to avoid the singularity of mass and stiffness matrices. Thus, the analysis of the design model can be replaced by the fixed-grid FEA model using the ersatz material approach [164, 5] so as to avoid re-meshing after each iteration.

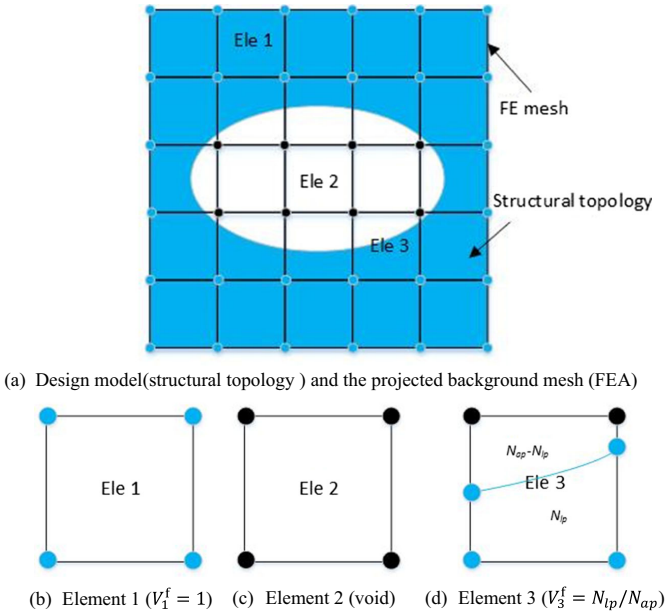

(a) Design model(structural topology) and the projected background mesh (FEA)

(b) Element 1 ($V_1^f = 1$) (c) Element 2 (void) (d) Element 3 ($V_3^f = N_{lp}/N_{ap}$)

FIGURE 2.1: Design model (structural topology) and the projected background mesh (FEA) result three categories of elements.

2.1.2 Problem statements and sensitivity analysis

2.1.2.1 Problem statements

A typical topology optimization problem of structural compliance minimization (i.e., stiffness maximization) subject to a volume constraint based on the design model, is firstly considered here as:

$$\text{Find} : \{\boldsymbol{\rho}\} \tag{2.3}$$

$$\text{Minimize} : C(\boldsymbol{\rho}) \tag{2.4}$$

$$\text{Subject to} : V(\boldsymbol{\rho}) = \int_D \boldsymbol{\rho}\, dx = V^* \tag{2.5}$$

$$: \boldsymbol{\rho}(x) = 0 \; or \; 1, \forall x \in D \tag{2.6}$$

where C is the structural compliance and D is the design domain. V and V^* are the structural volume and its constraint value. $\boldsymbol{\rho}(x)$ denotes the binary function at an arbitrary point within the design domain. $\boldsymbol{\rho}(x) = 1$ means that the point is full of solid and $\boldsymbol{\rho}(x) = 0$ means void.

According to the relationship between the design model and the FEA model as shown in Figure 2.1, the structural volume of the design model, V, can be expressed by

$$V = \sum_{e=1}^{N} V_e^f V_e \;\text{ and }\; 0 \leq V_e^f \leq 1 \tag{2.7}$$

where V_e denotes the volume of the e-th element volume and N is the total element number in the FEA model. It is assumed that an element in the FEA model corresponds to a number of grid points (40×40 in 2D cases in this paper) in the design model. The element would be a solid element, $V_e^f = 1$, when all corresponding grid points, x_o, in the design model are solid, or a void element $V_e^f = 0$ when all points are void. Otherwise, the element would be a boundary element, $0 < V_e^f < 1$, which contains both solid and void grid points in the design model. Thus, the mechanical properties of elements in the FEA model with regard to different volume fractions are calculated according to Equations (2.1)-(2.2). The compliance of the design model should be equal to that of the FEA model, which can be expressed by

$$C = \boldsymbol{F}^T \boldsymbol{U} \tag{2.8}$$

where $\boldsymbol{F}$ and $\boldsymbol{U}$ are the applied load and displacement vectors, respectively. The equilibrium equation of the FEA model is

$$\boldsymbol{F} = \boldsymbol{K}\boldsymbol{U} \tag{2.9}$$

where $\boldsymbol{K}$ is the global stiffness matrix.

Frequency optimization is of great importance in many engineering field, e.g., aerospace and automotive industries. The dynamic behavior of a structure can be represented by the following general eigenvalue problem:

$$(\boldsymbol{K} - \omega_j^2 \boldsymbol{M})\boldsymbol{u}^{(j)} = 0 \tag{2.10}$$

where $\boldsymbol{M}$ is the global mass matrix, ω_j is the $j-$th natural frequency and $\boldsymbol{u}^{(j)}$ is the eigenvector corresponding to ω_j. ω_j and $\boldsymbol{u}^{(j)}$ are related to ech other by the following Rayleigh quotient:

$$\omega_j^2 = \frac{(\boldsymbol{u}^{(j)})^T \boldsymbol{K} \boldsymbol{u}^{(j)}}{(\boldsymbol{u}^{(j)})^T \boldsymbol{M} \boldsymbol{u}^{(j)}} \tag{2.11}$$

The topology optimization for maximizing a natural frequency can be mathematically defined based on the design model as

$$\text{Find} : \{\boldsymbol{\rho}\} \tag{2.12}$$

$$\text{Maximize} : \omega_j(\boldsymbol{\rho}) \tag{2.13}$$

$$\text{Subject to} : V(\boldsymbol{\rho}) = V = \int_D \boldsymbol{\rho}\, dx = V^* \tag{2.14}$$

$$: \boldsymbol{\rho}(x) = 0 \; or \; 1, \forall x \in D \tag{2.15}$$

where ω_j of the design model is equal to that of the FEA model calculated from (2.11).

2.1.2.2 Sensitivity analysis

Ideally, sensitivity analysis should be conducted based on the design model against the design variable, $\boldsymbol{\rho}(x)$ at an arbitrary point. However, the design model is not involved in the analysis and therefore sensitivity analysis is conducted based on the FEA model instead. Although elemental volume fractions V_e^f are used in the FEA model for analyzing the design model, they cannot be used as design variables for topology optimization. The reason is that V_e^f can not be freely varied within the design domain and the intermediate volume fraction, $0 < V_e^f < 1$ is only allowed on the boundary of the structural topology. In other words, any design with intermediate elements other than at boundary should be excluded from the solution domain. Therefore, an artificial variable for the element of the FEA model, x_e, is introduced and the well-known SIMP model [14, 191, 17] is used for the material interpolation scheme as

$$E(x_e) = x_e^P E_0 \tag{2.16}$$

where P is the penalty factor. $P > 1$ is the necessary condition to make sure the existence of $0/1$ solution [17] and $P = 3$ is used in this section. Here, the material interpolation scheme in (2.16) is used to compute the sensitivity field for topology optimization of the design model. $x_e = 1$ means that the e-th element is solid and $x_e = x_{min}$ means that the e-th element is void. Different from the SIMP method [17], intermediate elements have no explicit value of x_e and are just viewed as the combination of solid ($x_e = 1$)with V_e^f and void $(x_e = x_{min})$ with $(1 - V_e^f)$. The material properties of those intermediate elements can be calculated according to Equations (2.1)-(2.2).

With the above material interpolation scheme, the sensitivity of structural compliance on the design variable, x_e, can be derived through the adjoint method [17], as

$$\frac{\partial C}{\partial x_e} = -P x_e^{P-1} \boldsymbol{u}_e^T \boldsymbol{k}_e^0 \boldsymbol{u}_e \tag{2.17}$$

where $\boldsymbol{u}_e$ is the nodal displacement vector of the e-th element and $\boldsymbol{k}_e^0$ denotes the stiffness matrix of the solid element. The sensitivity number for compliance minimization is defined as its sensitivity multiplied with a constant, -1/P, as [77]

$$\alpha_e = -\frac{1}{P}\frac{\partial C}{\partial x_e} = x_e^{P-1} \boldsymbol{u}_e^T \boldsymbol{k}_e^0 \boldsymbol{u}_e \tag{2.18}$$

When the e-th element is solid or void, the sensitivity number of the e-th element can be explicitly written as

$$\alpha_e = \begin{cases} \boldsymbol{u}_e^T \boldsymbol{k}_e^0 \boldsymbol{u}_e \,, & \text{when } \; x_e = 1 \\ x_{min}^{P-1} \boldsymbol{u}_e^T \boldsymbol{k}_e^0 \boldsymbol{u}_e \,, & \text{when } \; x_e = x_{min} \end{cases} \tag{2.19}$$

Since elements in the FEA model can be viewed as solid with V_e^f and void with $(1 - V_e^f)$, the sensitivity number for the e-th element can be approximately estimated with

$$\alpha_e = [x_{min}^{P-1}(1 - V_e^f) + V_e^f]\boldsymbol{u}_e^T \boldsymbol{k}_e^0 \boldsymbol{u}_e \tag{2.20}$$

As for frequency optimization, a material interpolation scheme for density is also required

$$\rho(x_e) = x_e \rho_0 \tag{2.21}$$

Compared with the extensive research on stiffness optimization, topology optimization for natural frequency is more challenging due to the possible localized modes [77, 129]. To avoid artificial localized modes, we can keep the ratio between mass and stiffness constants of void elements to be equal that of solid elements as [77], i.e. $\rho_{min}/E_{min} = \rho_0/E_0$. Using the adjoint method, the element sensitivity of natural frequency on the design variable, x_e, defined as [77]

$$\frac{\partial \omega_j}{\partial x_e} = \frac{1}{2\omega_j} \boldsymbol{u}_i^{(j)T} [\frac{1 - x_{min}}{1 - x_{min}^P} P x_e^{P-1} \boldsymbol{k}_e^0 - \omega_j^2 \boldsymbol{m}_e^0] \boldsymbol{u}_e^{(j)} \tag{2.22}$$

where $\boldsymbol{m}_e^0$ is the mass matrix of the solid element and therefore the sensitivity numbers for solid and void elements are expressed explicitly as

$$\alpha_e = \frac{1}{P}\frac{\partial \omega_j}{\partial x_e} = \begin{cases} \frac{1}{2\omega_j} \boldsymbol{u}_i^{(j)T} [\frac{1-x_{min}}{1-x_{min}^P} \boldsymbol{k}_e^0 - \frac{\omega_j^2}{P} \boldsymbol{m}_e^0] \boldsymbol{u}_e^{(j)} , & \text{when } x_e = 1 \\ \frac{1}{2\omega_j} \boldsymbol{u}_i^{(j)T} [\frac{1-x_{min}}{1-x_{min}^P} x_{min}^{P-1} \boldsymbol{k}_e^0 - \frac{\omega_j^2}{P} \boldsymbol{m}_e^0] \boldsymbol{u}_e^{(j)} , & \text{when } x_e = x_{min} \end{cases} \tag{2.23}$$

Thus, the sensitivity number for the e-th element with volume fraction V_e^f is

$$\alpha_e = \frac{1}{2\omega_j} \boldsymbol{u}_i^{(j)T} \{\frac{1 - x_{min}}{1 - x_{min}^P} [V_e^f + x_{min^{P-1}}(1 - V_e^f)] \boldsymbol{k}_e^0 - \omega_j^2 \boldsymbol{m}_e^0\} \boldsymbol{u}_e^{(j)} \tag{2.24}$$

2.1.3 Nodal sensitivity numbers and level set function

In order to determine the smooth topology of the design model, we propose to construct the level-set function based on the nodal sensitivity numbers of the FEA model. It is well known that the topology optimization problem defined in Equations (2.3)-(2.6) has no 0/1 solution. The reason is that the introduction of more holes, without changing the structural volume, will generally increase the efficiency of a given structure [17]. In the limit of this process, one fails to obtain a 0/1 solution unless a specified size constraint is specified. However, it is extremely challenging to impose an exact size constraint in the topology optimization algorithm [64]. A most convenient and popular way is to use the heuristic filter [147], which works as a low-pass filter that eliminates structural components below a certain length-scale in the optimal design based on an

image processing technique. Here, we adopt the filter scheme, which transfers sensitivity numbers from elements to nodes as

$$\hat{\alpha_j} = \frac{\sum_{e=1}^{M} w_{ej}\alpha_e}{\sum_{e=1}^{M} w_{ej}} \tag{2.25}$$

where $\hat{\alpha_j}$ denotes the sensitivity number at the j-th node. w_{ej} is a linear weight factor with

$$w_{ej} = max(0, r_{min} - r(e, j)) \tag{2.26}$$

where r_{min} is the prescribed filter radius and $r(e, j)$ denotes the distance between element e and node j. To further improve the convergence of the objective function, the nodal sensitivity is further modified with its sensitivity history as we did for conventional element sensitivity number in (3.14) [76]

$$(\tilde{\alpha_j})_l = \frac{(\hat{\alpha_j})_l + (\hat{\alpha_j})_{l-1}}{2} \tag{2.27}$$

where the subscript l denotes the current iteration number. Thus, the updated sensitivity number includes sensitivity information of the previous iteration.

In the following, we develop the LSF for the design model. Different from the traditional LSF governed by the Hamilton-Jacobi equation [138, 56, 164, 5, 165, 97, 100, 84], the current LSF is constructed based on the nodal sensitivity numbers. According to the projection relationship as shown in Figure 2.1, the LSF value of the design model is equal to the nodal sensitivity number of the FEA model, $\phi_j = \tilde{\alpha_j}$. For an arbitrary point, $o(\xi_o, \eta_o)$, within, e.g., rectangular element e, the LSF value can be linearly expressed by

$$\phi(o) = \sum_{j=1}^{4} N_j(o)\phi_e^j \tag{2.28}$$

where ϕ_e^j denotes the LSF value at the j-th node of element e. ξ_o and η_o are non-dimensional coordinates of point o in the natural coordinate system as shown in Figure 2.2. $N_j(o)$ denotes the standard interpolation function. In the 2D case, it is expressed as

$$N_j(\xi_o, \eta_o) = \frac{1}{4}[(1 + \xi_o\xi_j) + (1 + \eta_o\eta_j)] \tag{2.29}$$

where ξ_j and η_j are local coordinates of the j-th node. The construction of the sensitivity-based LSF can be similarly extended for 3D cases.

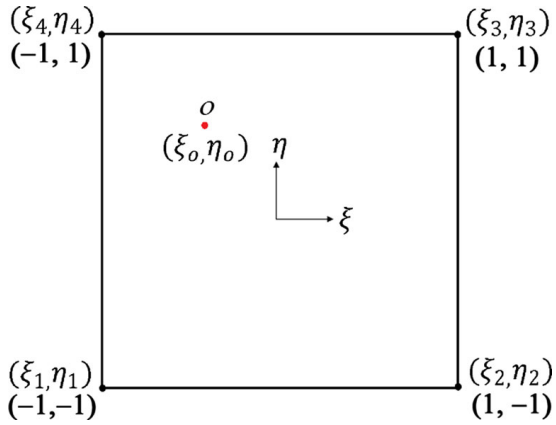

FIGURE 2.2: An arbitrary point, $o(\xi_o, \eta_o)$, within an rectangular element under the natural coordinate system.

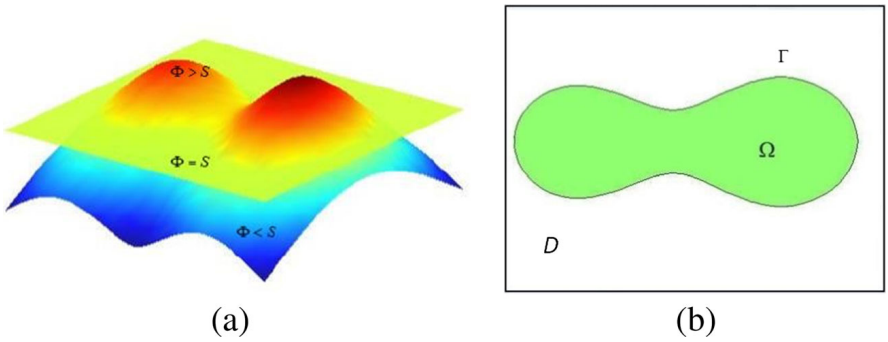

FIGURE 2.3: Illustration of LSF, level set value and the corresponding structural topology for a 2D case: (a) LSF and level-set value; (b) solid region, Ω, void regions, $D \setminus \Omega$ and structural boundary, Γ.

2.1.4 Update of structural topology

With the constructed nodal sensitivity-based LSF $\phi(o)$, the LSM defines the design domain (D) of the design model as solid regions (Ω), void regions ($D \setminus \Omega$) and boundaries (Γ) by setting the level-set value as shown in Figure 2.3.

$$\begin{cases} \phi(o) > S & \Leftrightarrow o \in \Omega \\ \phi(o) = S & \Leftrightarrow o \in \Gamma \\ \phi(o) < S & \Leftrightarrow o \in D \setminus \Omega \end{cases} \tag{2.30}$$

where S is the level-set value which is calculated iteratively by using the bi-section method so as to satisfy the target material volume at each iteration. Different from the topology derived by the normal velocity of the boundary in the traditional LSM [57, 138, 56, 164, 165, 97, 100, 84], the update of topology in the proposed method

is realized by setting the level-set value in each iteration. To calculate the level-set value, the target volume of the design model for the current iteration V_l, needs to be determined first. Since the constraint volume V^* could be larger, smaller or equal to the volume of the initial guess design, the target volume in each iteration will be changed correspondingly so as to finally satisfy the volume constraint, V^*. Given the volume of the last iteration, V_{l-1}, the target volume of the current iteration, V_l, can be calculated according to

$$V_l = \begin{cases} max(V_{l-1}(1-ER), V^*) \,, & \text{if } V_{l-1} \geq V^* \\ min(V_{l-1}(1+ER), V^*) \,, & \text{if } V_{l-1} < V^* \end{cases} \tag{2.31}$$

where ER is an evolution rate, e.g. 2% in this work. Thus, the volume of the design model gradually evolves to its constraint value, V^*, in the framework of the evolutionary optimization procedure.

Since the fixed-grid mesh is used in the FEA model, it has three different types of elements, i.e., solid, void and boundary elements when the smooth topology of the design model projects back to the FEA model. Therefore, it is needed to calculate the volume fraction of each element for the FEA model as

$$V_e^f = \begin{cases} 1 \,, & \text{when } min(\phi_e^j) > S \\ 0 \,, & \text{when } max(\phi_e^j) \leq S \\ N_{lp}/N_{ap}, & \text{otherwise} \end{cases} \tag{2.32}$$

where ϕ_e^j $(j = 1, 2, \dots)$ denotes the LSF values at nodes of element e. For a boundary element, $0 < V_e^f < 1$, the element can be assumed to be divided into fine grid (40×40 in this work) with the total N_{ap} points. N_{lp} denotes the total number of points whose LSF value is larger than the level-set value, S. Thus, the volume of the design model, V, can be calculated by the elemental volume fractions of the FEA model according to (2.7). The level-set value, S, can be numerically determined by using the bisection method. In each iteration, the upper and lower bounds of the level-set values, S_{upper} and S_{lower}, are initially assigned with the maximum and minimum sensitivity numbers, respectively. The level-set value, S, is then set as

$$S = \frac{S_{upper} + S_{lower}}{2} \tag{2.33}$$

Given the level-set value S, the volume of the design model V can be calculated as described above. By comparing the values of V and V_l, the upper or lower bound is

updated by

$$\begin{cases} S_{upper} = S & \text{if } V < V_l \\ S_{lower} = S & \text{if } V > V_l \end{cases} \tag{2.34}$$

The level-set value S, and its bounds S_{upper} and S_{lower} are updated until S_{upper} and S_{lower} are close enough (e.g. $S_{upper} - S_{lower} < 10^{-15}$). When the convergence is reached, the structural volume V, reaches the target volume of the design model for the current iteration, V_l.

2.1.5 Convergence criterion

The optimization procedure iteratively conducts FEA and the update of topology until the volume constraint (V^*) is reached and the following convergence criterion is satisfied

$$\frac{|\sum_{q=1}^{Q}\left(obj_{iter-q+1} - obj_{iter-Q-q+1}\right)|}{\sum_{q=1}^{Q} obj_{iter-q+1}} \leq \tau. \tag{2.35}$$

In (2.35), obj denotes the objective function, e.g. structural compliance C or natural frequency ω_j, l is the current iteration number, Q is the integral number and set to be 5 in this work, and τ is a specified small value. The convergence criterion defined in (2.35) means that the value of the objective function almost stabilizes. In the traditional element-based BESO method, $\tau = 0.1\%$ is normally used. Since the proposed ETO method identifies the topology far beyond elements, a more strict convergence criterion $\tau = 0.01\%$ is used in this work.

2.2 ETO procedure

The optimization iteration of the proposed ETO method is briefly summarized as following:

1. Discretize the design domain using FE mesh for given boundary and loading conditions. Assign the initial property values of elements to construct initial design.
2. Perform fixed-grid FEA and calculate elemental sensitivity numbers.
3. Convert the elemental sensitivity numbers into nodal sensitivity numbers by the filter and average with their history information.
4. Determine the target volume for the next iteration and construct LSF.
5. Calculate elemental volume fraction of the FEA model and update the topology of the design model by the level-set value, S.

6. Go back to Step 2 until the volume constraint and the convergence criterion solution are satisfied.

7. Output results.

The above ETO procedure is similar to that of the BESO method but it does not involve the removal/addition of elements, which is the most important feature of the BESO method. That is why we term it with a new name, ETO rather than BESO.

2.3 Numerical examples

2.3.1 Minimum compliance for a cantilever beam

The first example considers the stiffness maximization design of a cantilever beam under a concentrated loading as shown in Figure 2.4. The design domain has length 60 mm, height 40 mm and thickness 1 mm, where the force is applied downward at the center of the free end with the magnitude of 1 N. The material has Young's modulus of 1 MPa and Poisson's ratio of 0.3. It is assumed that the available material can only cover 50% volume of the design domain. In order to demonstrate the advantage of the presented ETO method, a coarse mesh of size 30×20 is used to subdivide the design structure. The ETO parameters are ER = 2% and r_{min} = 2. The final topology is shown inFigure 2.5(a) with the structural compliance 31.35 mm^2/N. The above problem using the same meshes is solved using the ESO-type method given in [77] with same design parameters. The final topology is shown in Figure 2.5(b) which is similar to the above ETO topology in Figure 2.5(a) but has serrated boundaries. The compliance is 32.59 mm^2/N which is higher than that of the ETO method. The above problem is also solved by the continuous density-based SIMP method with penalty factor P = 3, filter radius r_{min} = 1.5 and sensitivity filtering. The final topology is shown in Figure 2.5(c) which is similar with above two results except there exist "grey" elements which denote intermediate density material. The compliance is 36.77 mm^2/N which is also higher than 31.35 mm^2/N of the ETO topology. This may be attributed to the overestimated strain energy of the intermediate density elements in the SIMP topology.

Figure 2.6 shows the evolution histories of the structural compliance and the volume fraction. The compliance increases as the material volume fraction gradually decreases. After the volume reaches the objective volume, the compliance is convergent to an almost constant value. The evolution history of structural topology is shown Figure 2.7. As can be observed, there is barely topology change but boundary moving after about 30 iterations, and the structure finally converges to Figure 2.7(f) after another 18 iterations.

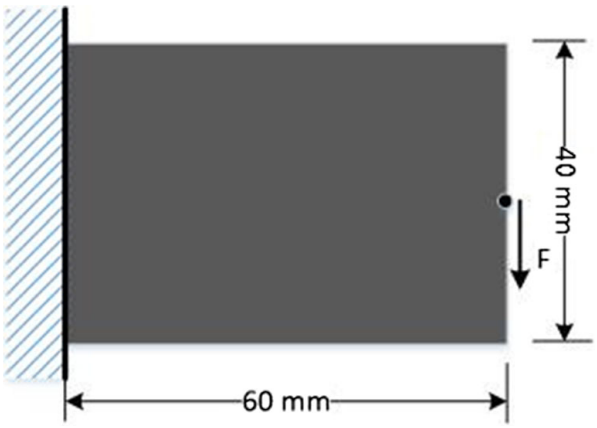

FIGURE 2.4: Dimensions of the design domain and boundary and loading conditions of a cantilever beam.

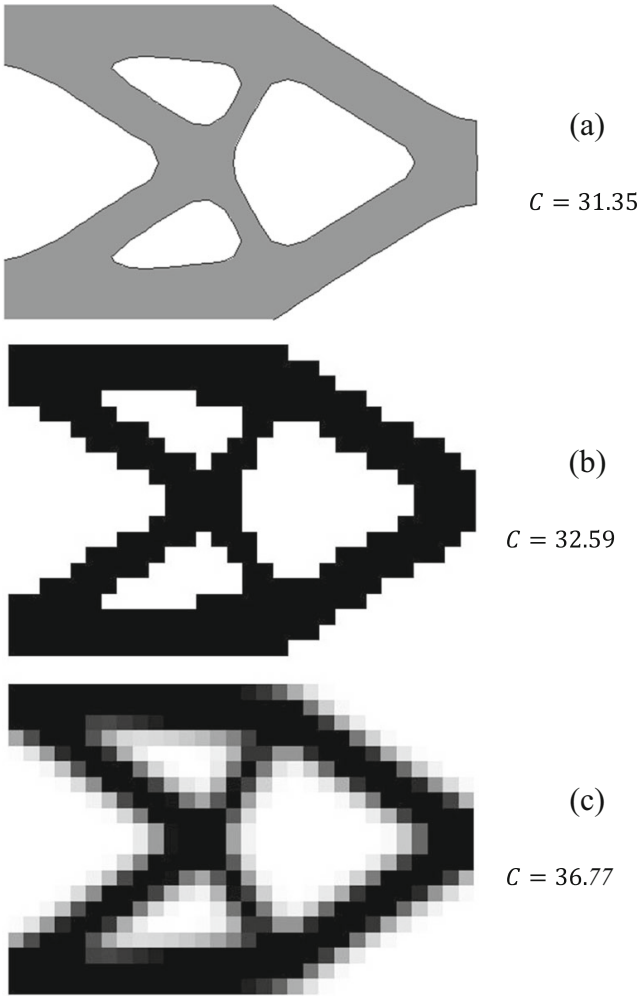

FIGURE 2.5: Final topologies and structural compliance of the cantilever beam using different methods with same coarse mesh.

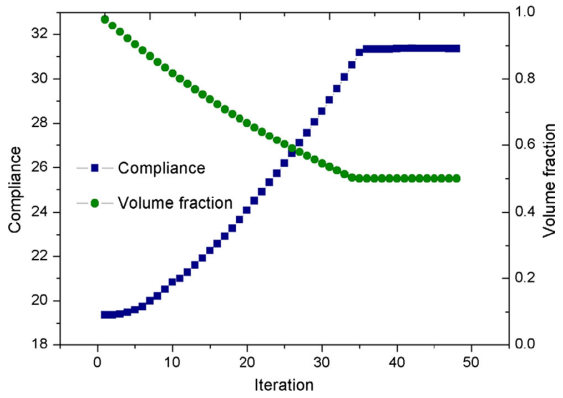

FIGURE 2.6: Evolutionary histories of the compliance and the volume fraction for the cantilever beam.

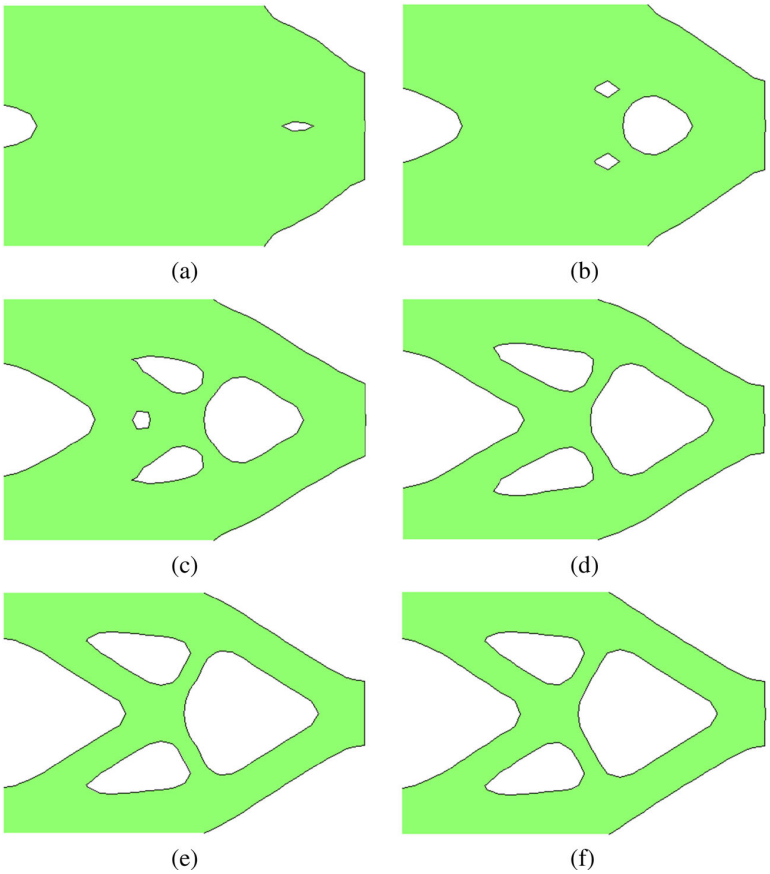

FIGURE 2.7: Evolution of the topology: (a) iteration 5, (b) iteration 10, (c) iteration 20, (d) iteration 30, (e) iteration 40, and (f) final topology.

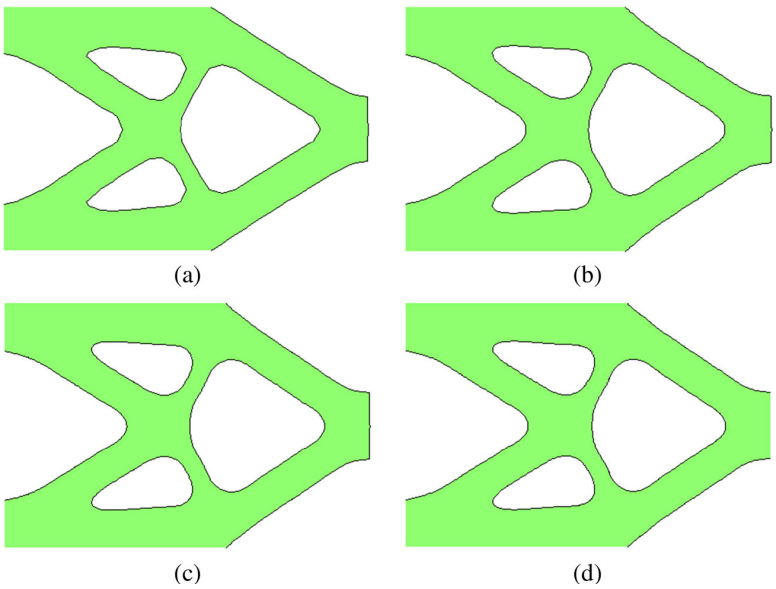

FIGURE 2.8: Mesh-independent solutions of the cantilever: (a) 30×20, (b) 90×60, (c) 150×100, (d) 210×140.

To further verify the developed ETO method, it is necessary to numerically investigate the effect of the mesh refinement of the considered structure. Here, different refined meshes 90×60, 150×100 and 210×140 are assigned for the cantilever beam. Boundary elements are assigned with 40×40 level set grids in all cases. The resulting topologies are displayed in Figure 2.8(b)–(d), respectively. There is no visible difference as compared to Figure 2.7(f), which indicates that the mesh refinement of the structure has negligible effect on designs.

2.3.2 Minimum compliance for a MBB beam

In the second example, we consider the design problem for the Messerschmitt-Bölkow-Blohm (MBB) beam sketched in Figure 2.9. The simple supported beam is loaded at its up center by $F = -1$ N. The symmetric right half with the dimensions 100×40 mm^2 is discretized into 50×20, 100×40 and 200×80 four-node quadrilateral element meshes, with the filter radii set to 3, 6, and 12, respectively. Suppose only 50% of the design domain volume material is available for constructing the final structure and the material Young's modulus is set to $E = 1$ MPa and the Poisson's ratio is set to $\nu = 0.3$. ER is also set to 2%. Initially, the design domain is full of the material. The optimal topologies are shown in Figure 2.10, in which all meshes converge to the same optimal topology in terms of number of internal structural members, which further validates that the proposed method is capable of providing mesh-independent designs. The evolution histories of the compliance and the volume fraction of the MBB design using coarse

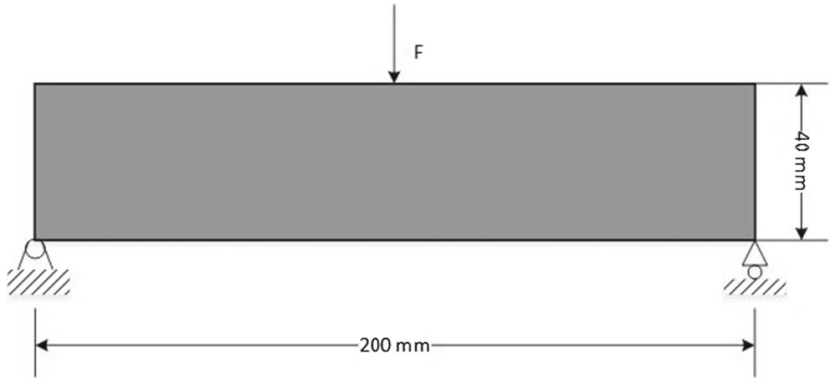

FIGURE 2.9: Dimensions of the design domain and boundary and loading conditions of a MBB beam.

mesh are given in Figure 2.11. It is noted that apparent bumps in the compliance are caused due to significant topology variations. Thereafter, the compliance is recovered and ensures that the topology develops in the correct direction. The evolution history of topology is shown in Figure 2.12.

2.3.3 Minimum compliance for a roller-supported half-wheel

The above examples show that the ETO method is able to find the optimal topology from the full material design. In this section, we conduct ETO starting from initial guess designs whose volumes are close or equal to the objective volume. The obvious advantage of this procedure is that only a portion of elements in the design domain is involved in the analysis and therefore the computation time can be saved especially for finely discretized models. In order to clarify this procedure, we solve the roller-supported half-wheel design using full material design and two initial guess designs as shown in Figure 2.13. The structure is loaded at its bottom center by $F = -1$ N. Material Young's modulus and Poisson's ratio are set to E = 1 MPa and $\nu = 0.3$, respectively. ETO optimization parameters are set to ER = 0.02, and r_{min} = 3. Final topologies obtained from different initial designs are presented in Figure 2.14, which indicates that their topologies and structural compliances are very close to each other. These calculations show that the present ETO method leads to a convergent design solution even for largely different initial guess designs. Figure 2.15 shows the evolution histories of the compliances and the volume fraction when ETO is starting from two initial guess designs. It can be seen that the objective function decreases with the redistribution of the 50% of the material. The optimization algorithm is convergent after 60 and 101 design iterations for initial guesses 1 and 2, respectively.

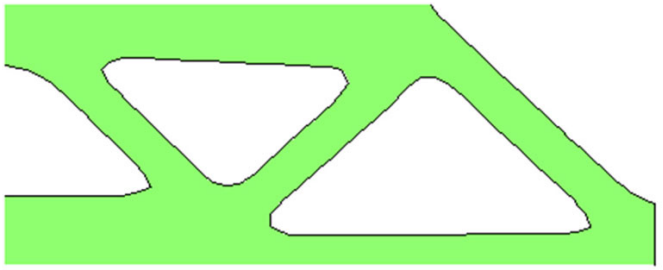

(a) Coarse mesh

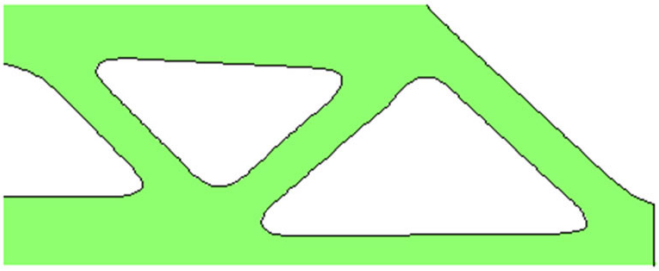

(b) Regular mesh

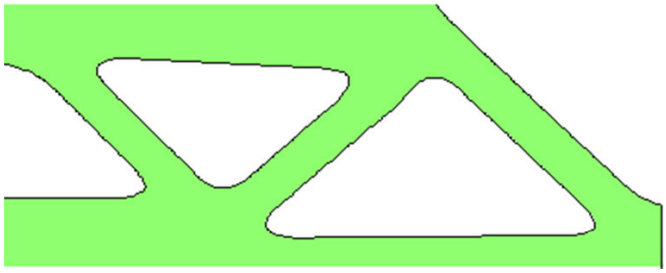

(c) Fine mesh

FIGURE 2.10: Mesh-independent solutions of the MBB beam: (a) 50×20; (b) 100×40; (c) 200×80.

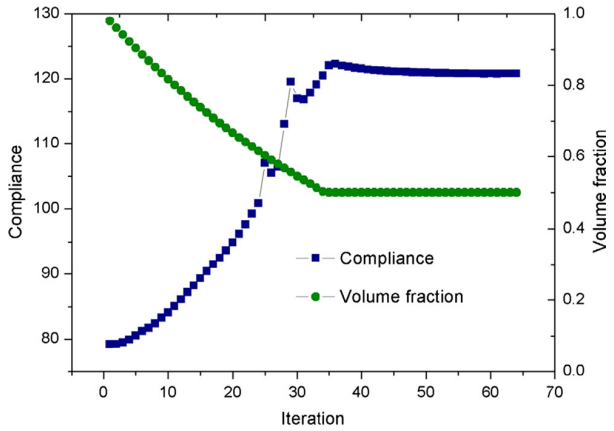

FIGURE 2.11: Evolutionary histories of the compliance and the volume fraction of the MBB beam.

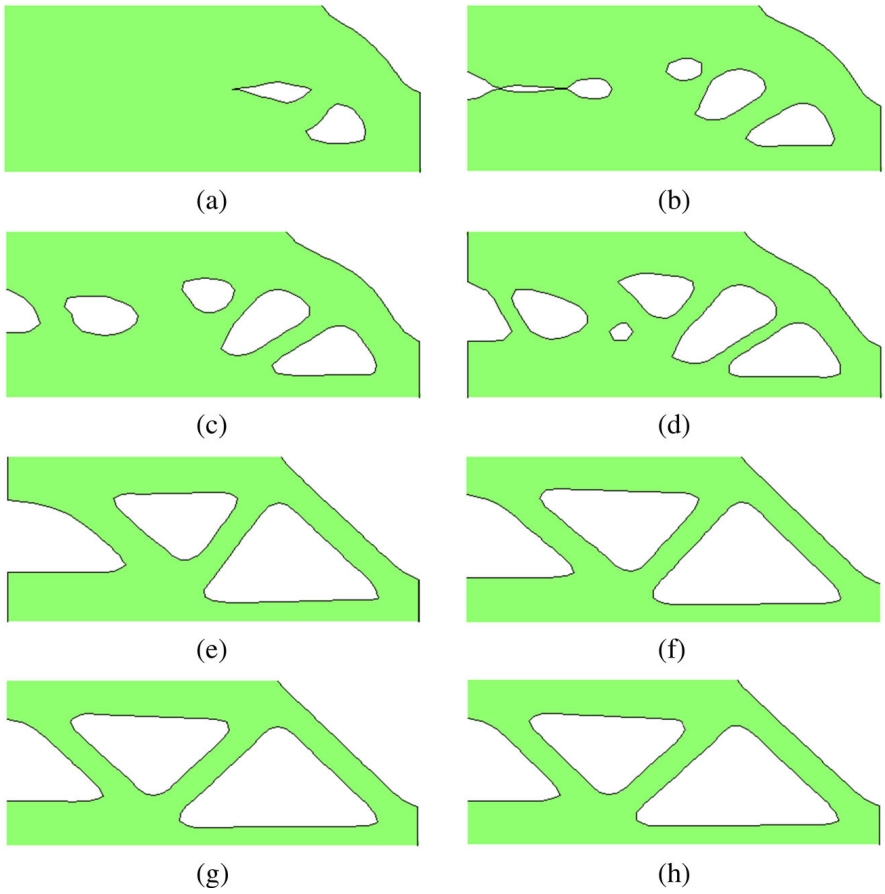

FIGURE 2.12: Evolution of topology: (a) iteration 5, (b) iteration 10, (c) iteration 15, (d) iteration 20, (e) iteration 30, (f) iteration 40, (g) iteration 50, (h) final topology.

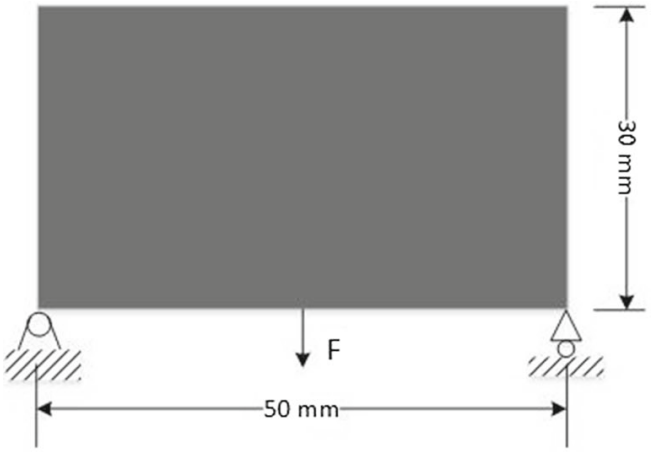

(a) Full material design

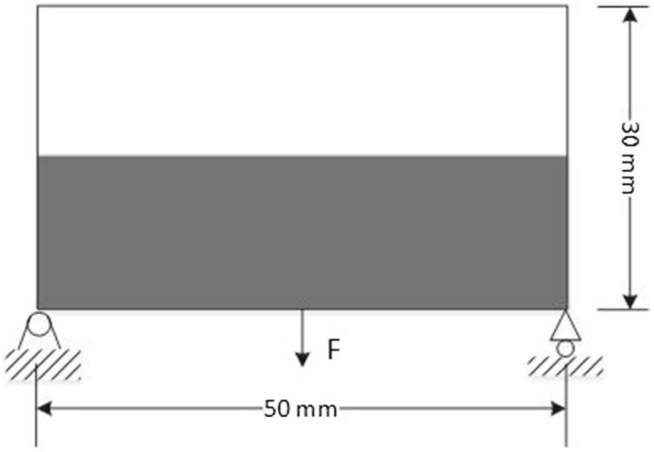

(b) Initial guess design 1

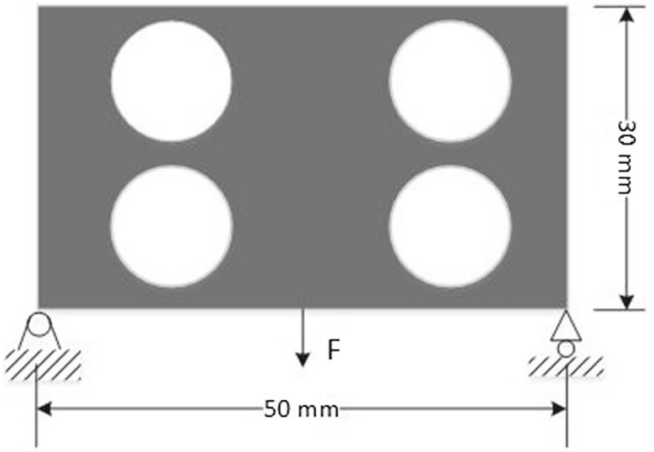

(c) Initial guess design 2

FIGURE 2.13: Dimensions of the design domain and boundary conditions of a roller-supported half-wheel with different initial guess designs.

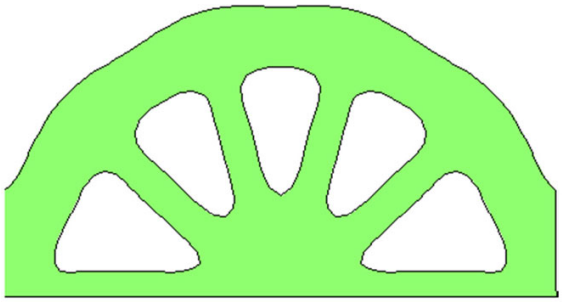

(a) Final topology from full material design: $C = 11.33$

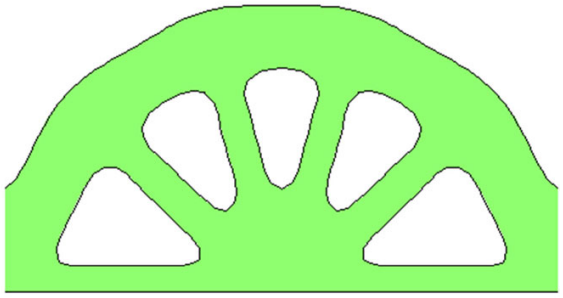

(b) Final topology from initial guess design 1: $C = 11.35$

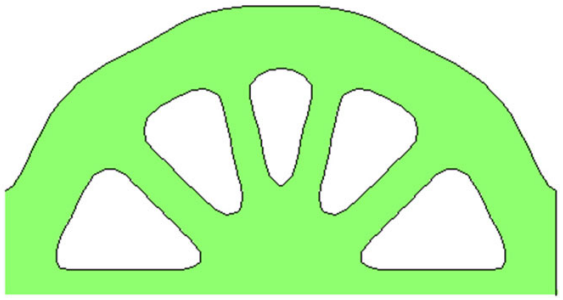

(c) Final topology from initial guess design 2: $C = 11.34$

FIGURE 2.14: Final topologies from three different initial designs.

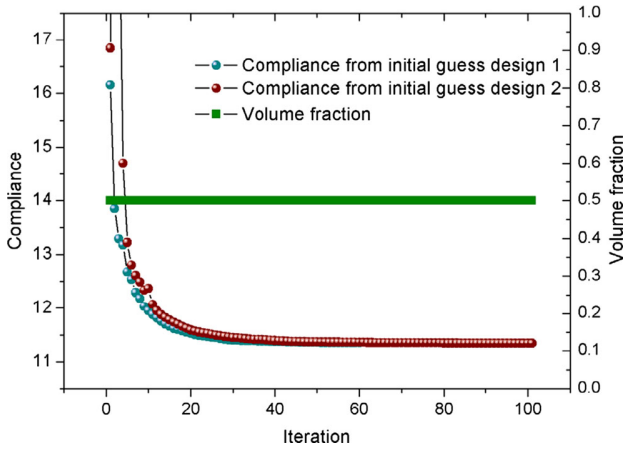

FIGURE 2.15: Evolutionary histories of the compliances and the volume fraction when ETO starts from two initial guess designs.

2.3.4 2D Design for structural natural frequency

We seek the topological design that maximizes the fundamental frequency subject to a volume fraction constraint of 50% of a clamped beam in this example. Design dimensions of the beam are 140×20 mm. The beam is clamped on both sides as shown in Figure 2.16 (a). Young's modulus E = 1 MPa, Poisson's ratio $\nu = 0.3$ and mass density $\rho_m = 10^{-9}$ kg/mm^3 are assumed. A concentrated nonstructural mass $M = 1 \times 10^{-3}$ kg is placed at the center. The rectangular design is divided into 140×20 four node plane stress elements. The ETO parameters are set to ER = 0.02, and r_{min} = 2. The optimal design obtained using the ETO method is shown in Figure 2.16 (b). The optimization converges after 61 design iterations and the fundamental frequency of the resultant topology is ω = 21.75 rad/s. Figure 2.17 shows the evolution histories of the fundamental frequency as well as the volume fraction. It is seen that the volume fraction reaches its constraint value 50% after about 35 design iterations and the first natural frequency converges to a constant value after another 26 design iterations. This is because we set a very strict stop criterion to ensure the structural topological convergence.

2.3.5 3D Design for structural compliance

The present ETO method can be straightforwardly extended to the 3D case. Figure 2.18 (a) shows support and loading conditions of a 3D cantilever beam with $F = -1$ N. Young's modulus $E = 1$ MPa, and Poisson's ration ν = 0.3 are assumed. The objective volume is only 50% of the design domain. The cubic design is divided into $60 \times 20 \times 4$ eight node brick elements. ETO parameters are ER = 0.02, and r_{min} = 3. The final topology which satisfies the volume constraint and the convergence criterion is illustrated in Figure 2.18 (b) with smooth boundaries. The objective function converges to 23.25

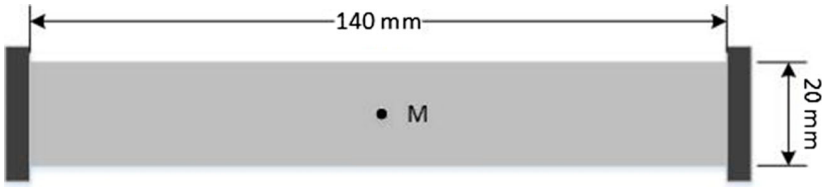

(a) design domain and boundary conditions of frequency optimization

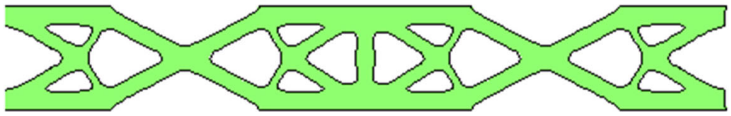

(b) solution

FIGURE 2.16: ETO design of a clamped beam with a concentrated mass.

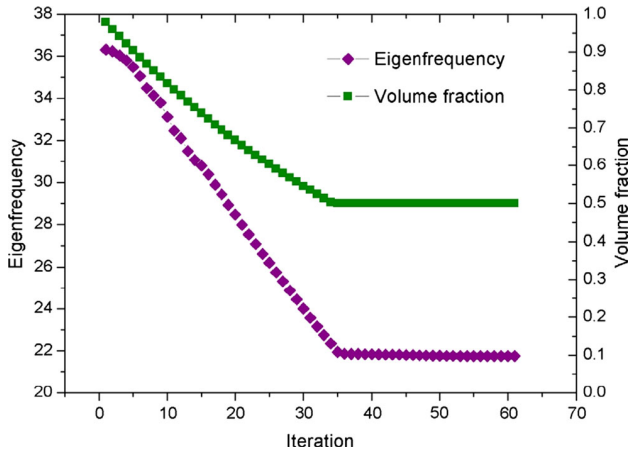

FIGURE 2.17: Evolutionary histories of the first natural frequency and the volume fraction.

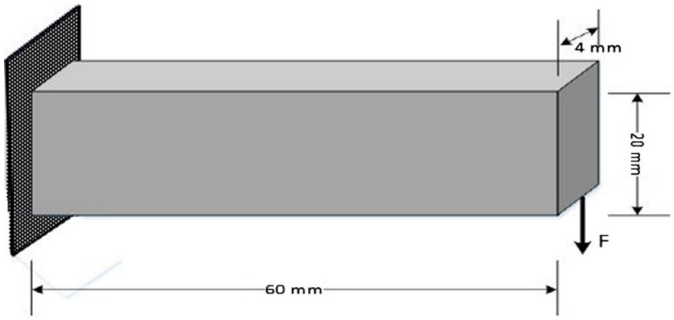

(a) design domain and boundary conditions of a cantilever beam

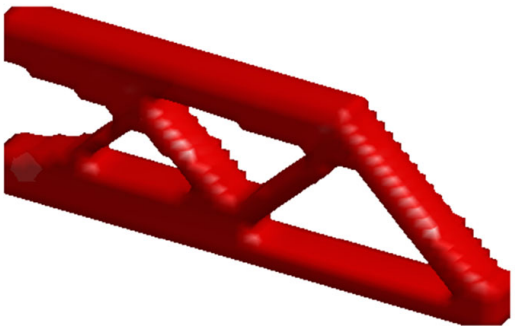

(b) Solution

FIGURE 2.18: ETO design of a 3D cantilever beam with a concentrated force.

mm^2/N after only 63 iterations to satisfy the strict convergence criterion $\tau = 0.01\%$. Figure 2.19 shows the evolution histories of the compliance and volume fraction.

2.3.6 3D Design for structural natural frequency

It should be noted that the most time-consuming part of the optimization process is for solving the equilibrium equations in the FEA. Thus the computational efficiency is of critical importance for large optimization problems, especially for 3D structures. To further demonstrate the efficiency of the present ETO method, we consider a 3D structural frequency design starting from an initial guess design. The 3D design dimensions of the beam are $60 \times 10 \times 10$. The beam is clamped on both sides as shown in Figure 2.20 (a). A concentrated nonstructural mass $M = 1 \times 10^{-3}$ kg is attached to the center of the bottom surface. Young's modulus E = 1 MPa, Poisson's ration $\nu = 0.3$ and mass density $\rho_m = 10^{-9}$ kg/mm^3 are assumed. The objective volume is 30% of the design domain and the initial guess design with 3000 elements which is less than twice the volume constraint as shown in Figure 2.20 (b). The ETO parameters are ER = 0.02, and r_{min} = 1.5. The topology is developed by gradually relocating solid elements following the ETO procedure outlined in Section 2.2 until the objective volume is reached.

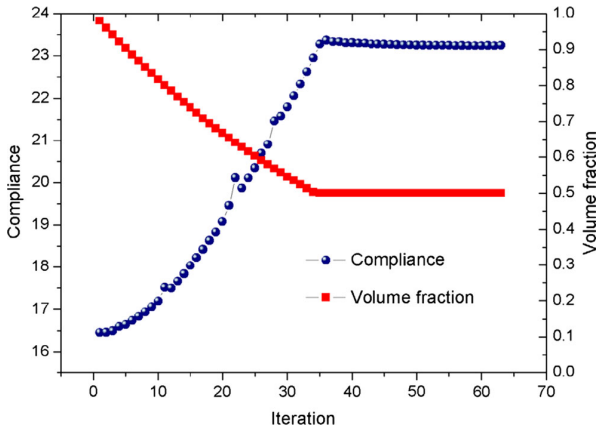

FIGURE 2.19: Evolutionary histories of the compliance and the volume fraction of the 3D cantilever beam.

The optimal designs from the initial guess design is given in Figure 2.20 (c). The total iteration numbers and the final fundamental frequency is 95 and 312.58 rad/s, respectively. Figure 2.21 shows the evolution histories of the fundamental frequency and the volume fraction when ETO starting the initial guess design. In this case, the total volume of the model decreases step by step until the objective volume is reached. Then the volume is unchanged and the natural frequency increases gradually until the convergence criterion is satisfied. Therefore, the proposed method may start from guess designs that are much small than the full design domain. This is of important for optimizing 3D structures where the FEA takes up a large portion of the computational time of optimization.

2.4 Concluding remarks

In this section, we have presented an evolutionary topology optimization (ETO) method for topology optimization of continuum structures. A nodal sensitivity-based level-set function (LSF) is introduced to represent the structural topology implicitly with smooth boundary representation. The structural topology is iteratively tailored by updating the constructed LSF and the level-set value, which are also used for the calculation of elemental volume fractions at each design iteration. The new approach is demonstrated on compliance minimization problems and natural frequency maximization problems of 2D and 3D continuum structures. In contrast to conventional density-based topology optimization methods, the newly proposed ETO method achieves optimized topologies with smooth boundary representation, even when a coarse mesh is employed for FEA. The introduction of LSF and the level-set value results in the fine resolution of

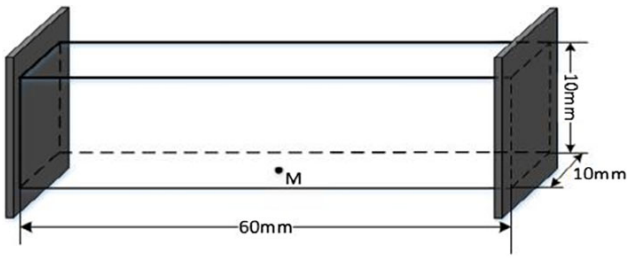

(a) design domain and boundary conditions of frequency optimization

(b) initial gauss design

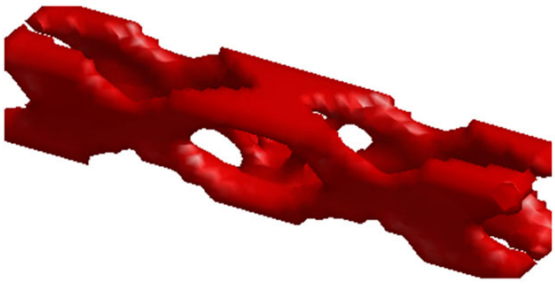

(c) solution

FIGURE 2.20: ETO design of a 3D beam with a concentrated mass.

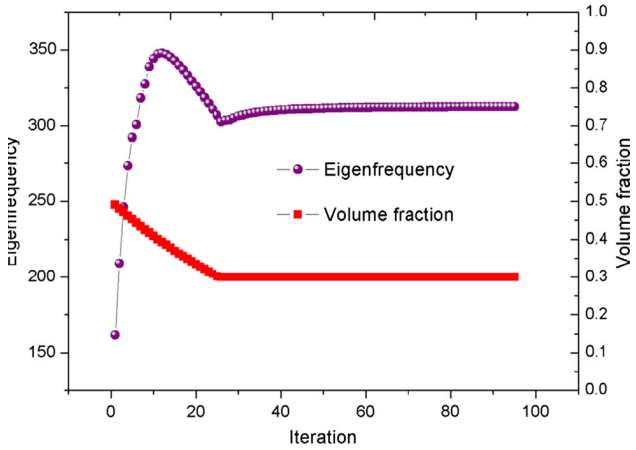

FIGURE 2.21: Evolutionary histories of the first natural frequency and the volume fraction when ETO starts from the initial guess design.

topology far beyond elements, thus contributing to the stable convergence of the solution. Numerical examples show that the developed ETO method is capable of generating convergent and mesh-independent solutions with smooth boundary representation, meanwhile the resultant designs are less dependent on the initial guess topology.

Chapter 3

Design of materials for maximum effective elastic modulus and negative Poisson's ratio

Material design as a quite old research topic is one of the important branches of the topology optimization applications. A seminal paper could be traced back to [144], where the topology of material microstructures is tailored to achieve the prescribed constitutive parameters, called an inverse homogenization scheme. In the past few dacades, this research topic has been very active since it offers great design flexibility to achieve high performance materials or materials with properties not found in the nature. Several reviews on design of material microstructures have been recently presented in [30, 127, 172]. In pure material design, the previous research works [142, 74, 170] have indicated that many optimization factors such as used algorithms and parameters have influence on the optimal solution. In other words, there are multiple local minima for the topological design of materials for extreme properties. Therefore, it is important to attempt different or more concise algorithms to find much wider possible solutions to material design. This Chapter is an attempt to use the strain energy method to predict the effective material properties, combined with the implicit or explicit optimization algorithms to tailor material microstructures so as to find the optimal topology with the selected objective functions. The adoption of the strain energy-based approach instead of the asymptotic homogenization method significantly simplifies the numerical implementation.

In the following, in Section 3.1 we first introduce the principle of the stain energy-based method to predict the effective material properties, followed by the formulation of topological design model with the sensitivity analysis as well as the numerical implementation. The discrete bi-directional evolutionary structural optimization (BESO) algorithm is adopted to the inverse design of porous materials. Finally, several 2D and 3D numerical examples are given to illustrate the optimal topology with the extreme effective elastic moduli.

In Section 3.2, a new approach for the topological design of materials with selected desired properties is presented. The method is based on hybrid cellular automaton (HCA), which is an implicit optimization technique that uses local rules to update design variables iteratively until meeting the prescribed optimality conditions. By means of an energy-based homogenization approach, the effective properties of the considered material are calculated in terms of element mutual energies. By this method, no sensitivity information is required to find the optimal topology for the considered design objectives: maximum bulk or shear modulus, and negative Poisson's ratio. The proposed method is validated by a series of numerical examples.

3.1 Design of materials using the BESO

This section is an attempt to employ the strain energy method and the BESO method to tailor material microstructures so as to find the maximum effective elastic modulus. Even though the BESO method has been employed in [74] for material design, the adoption of the strain energy-based method further simplifies the numerical implementation. A number of interesting and valid material microstructures are obtained to find much wider possible solutions to material design.

3.1.1 Principle of the strain energy-based method and sensitivity analysis

When a porous material is composed of periodic unit cells, its effective elasticity properties of this porous material can be calculated by the strain energy-based method. In this method, a unit test strain ε_{ij}^0 is prescribed on the boundaries of an associated Representative Volume Element (RVE) to the unit cell, and it satisfies the average strain theorem for elastic bodies [70, 190]: $\bar{\varepsilon}_{ij} = \varepsilon_{ij}^0$, where ε_{ij}^0 are constant strains. The average strain-stress relationship is obtained as:

$$\bar{\sigma}_{ij} = \bar{C}_{ijkl}^H \bar{\varepsilon}_{ij} \tag{3.1}$$

where $\bar{C}_{ijkl}^H$ is the effective elastic modulus. The strain energies stored in the RVE can be written as:

$$E_s = \frac{1}{2} \bar{C}_{ijkl}^H \bar{\varepsilon}_{ij} \bar{\varepsilon}_{kl} V \tag{3.2}$$

where V denotes the volume of the RVE. For 2D orthotropic materials, the effective elastic matrix is given by

$$\bar{\mathbf{C}}^H = \begin{bmatrix} \bar{C}_{1111}^H & \bar{C}_{1122}^H & 0 \\ & \bar{C}_{2222}^H & 0 \\ sym & & \bar{C}_{1212}^H \end{bmatrix} \tag{3.3}$$

Four constant strains $\bar{\varepsilon}^1 = (1\ 0\ 0)^T$, $\bar{\varepsilon}^2 = (0\ 1\ 0)^T$, $\bar{\varepsilon}^3 = (0\ 0\ 1)^T$, and $\bar{\varepsilon}^4 = (1\ 1\ 0)^T$ are used to calculate four components of the effective elastic matrix. In the first test, suppose the average strain of the RVE is $\bar{\varepsilon}^1 = (1\ 0\ 0)^T$, the average stress is then $\bar{\sigma}^1 = (\bar{C}^H_{1111}\ \bar{C}^H_{1122}\ 0)^T$ correspondingly. Therefore, the parameter $\bar{C}^H_{1111}$ can be calculated as: $\bar{C}^H_{1111} = 2E^1_s$, where E^1_s denotes the strain energy of the first test [190]. It is seen that the remaining components of the $\bar{\mathbf{C}}^H$ can be obtained through other three different test strain fields. The extension of computation of the effective elastic modulus to 3D is straightforward.

Material interpolation scheme with penalization introduced in [16] is adopted here to derive the sensitivities of the effective properties with respect to the design variable:

$$\mathbf{K}_e = \mathbf{K}_0(\rho_e)^P \tag{3.4}$$

where $\mathbf{K}_0$ indicates the stiffness matrix of solid element. $\mathbf{K}_e$ and ρ_e are the stiffness matrix and the relative density of an arbitrary element e, respectively. P is the penalty exponent. The finite element equilibrium equation of the RVE is

$$\mathbf{KU} = \mathbf{F} \tag{3.5}$$

where $\mathbf{U}$ and $\mathbf{F}$ are the displacement vector and force vector respectively. $\mathbf{K}$ is the global stiffness matrix which is assembled by $\mathbf{K}_e$. Thus, the sensitivity of the strain energy with respect to the design variable ρ_e can be expressed as:

$$\frac{\partial E_s}{\partial \rho_e} = \frac{1}{2}\mathbf{U}^T\frac{\partial \mathbf{K}}{\partial \rho_e}\mathbf{U} = \frac{1}{2}P(\mathbf{U}_e)^T(\rho_e)^{P-1}\mathbf{K}_0\mathbf{U}_e = P\frac{(E_s)_e}{\rho_e} \tag{3.6}$$

It is observed from Equation (3.6) that the sensitivity of the strain energy or effective elastic modulus with respect to design variable only depends on the element relative density and the strain energy. Therefore, the used strain energy-based method is relatively concise and extremely convenient for programming. In addition, it is straightforward to incorporate it with topological design of porous materials or composites for extreme material properties.

3.1.2 Topological design optimization model and numerical implementation

It is well known that effective properties of composite materials are highly dependent on microscopic structural architecture/topology. To obtain heterogeneous materials with extreme properties, the goal, put simply, is to find an optimal material layout

within the given domain (i.e. RVE in material design) for specified boundary conditions and constraints. Therefore, the topology optimization problem of porous materials for extreme elastic modulus can be mathematically written as:

$$\text{Find} : \{\rho_e\} \tag{3.7}$$

$$\text{Maximize} : f = \omega_{ijkl}\bar{C}^H_{ijkl} \tag{3.8}$$

$$\text{Subject to} : \mathbf{KU} = \mathbf{F} \tag{3.9}$$

$$: V_{req} = \sum_{e=1}^{N} V_e\rho_e \tag{3.10}$$

$$: \rho_e = \rho_{min} \text{ or} 1 \tag{3.11}$$

where V_{req} denotes the target volume of solid material and V_e denotes the volume of the e-th element in the RVE. Binary design variable ρ_e is the relative density of the e-th element, where $\rho_e = 1$ indicates that the element is filled with solid material and $\rho_e = \rho_{min}$ means a void element. ω_{ijkl} is the weight factor and different objectives can be defined when ω_{ijkl} takes different values. For example, in 2D cases, the maximization of the material bulk modulus K corresponds to the objective function $f = \frac{1}{4}(\bar{C}^H_{1111} + 2\bar{C}^H_{1122} + \bar{C}^H_{2222})$ and the maximization of the material shear modulus G corresponds to $f = \bar{C}^H_{1212}$. Using the Equation (3.6), the sensitivity information of the selected objective function with respect to design variables can be calculated correspondingly.

In this work, the BESO algorithm is used to inversely optimize the topology of the material RVE. To avoid the common issue as checkerboard pattern in topology optimization, the above formulated sensitivity numbers are firstly smoothed by means of a filtering scheme [23, 28, 141]

$$\alpha_e = \frac{\sum_{j=1}^{N_e} w_{ej}\alpha_j}{\sum_{j=1}^{N_e} w_{ej}}, \tag{3.12}$$

where w_{ej} is a linear weight factor defined as:

$$w_{ej} = \max(0, r_{\min} - \Delta(e, j)), \tag{3.13}$$

determined according to the prescribed filter radius $r_{\min}$ and the element center-to-center distance $\Delta(e, j)$ between elements e and j. Due to the discrete nature of design variables (solid ($\rho_e = 1$) or void phase ($\rho_e = \rho_{min}$)) in the BESO method, the current sensitivity numbers are further smoothed along history evolution to avoid spurious oscillations [76] as:

$$\alpha_e^{(iter)} = \frac{(\alpha_e^{(iter)} + \alpha_e^{(iter-1)})}{2}, \tag{3.14}$$

where $iter$ is the current iteration number, thus, the updated sensitivity number includes all sensitivity information in the previous iterations.

With the modified sensitivity information, the considered structure can be tailored together with the target material volume at the current iteration $V_{(iter)}$. The target material volume can be set as

$$V_{(iter)} = \max\left\{V_{\text{req}}, (1 - c_{\text{er}})V_{(iter-1)}\right\}, \tag{3.15}$$

where c_{er} is an evolutionary volume ratio which can be set by designer to determine the amount of material to be removed from the previous design iteration. Once the volume constraint of the solid material V_{req} is reached, the volume is kept constant at the prescribed value.

The optimization procedure iteratively conducts the finite element analysis (FEA) to determinate the sensitivity numbers and the update of topology in the RVE and the following convergence criterion is satisfied [76]:

$$\frac{\left|\sum_{q=1}^{Q}\left(f_{iter-q+1} - f_{iter-Q-q+1}\right)\right|}{\sum_{q=1}^{Q} f_{iter-q+1}} \leq \tau. \tag{3.16}$$

In the above, Q is s an integer and τ is a specified small tolerance value.

3.1.3 Numerical examples

In this section, several 2D and 3D numerical examples of porous material design for maximizing effective bulk or shear modulus are presented. It is assumed that the solid material is isotropic with Young's modulus $E = 1$ MPa and Poisson's ratio $\nu = 0.3$ in both 2D and 3D examples. The RVE is discretized into 100×100 four-node quadrilateral (Q4) elements for 2D examples and $26 \times 26 \times 26$ brick elements (C3D8 in ABAQUS®) for 3D examples.

3.1.3.1 2D example for maximizing the shear modulus

The objective of this example is to maximize the shear modulus of 2D porous materials. Three different initial designs of the RVE as shown in Figure 3.1 are considered. Initial design A is full solid material except four center elements, initial design B is full solid material except for four corner elements, and initial design C with eight elements at mid-sides of RVE for soft phase. Final volume fractions of solid material are set to 0.5 in all three cases.

Figure 3.2 shows three final topologies of material RVE and their corresponding effective elasticity matrices obtained from different initial designs. It is seen that soft phases are separated by the surrounding solid materials to maximize the effective shear

modulus. The effective shear moduli for these three microstructures are 0.1394 MPa, 0.1392 MPa and 0.1394 MPa. They are very close to each other even though their topological configurations seem totally different. In fact, topologies shown in Figures 3.2 (a) and (b) are identical if the RVE extends towards horizontal and vertical directions periodically. In other words, the RVE shown in Figure 3.2 (b) obtained from initial design B is the same as the structure inside the orange square box in Figure 3.2 (a) (middle). Furthermore, the resulting RVE obtained from initial design C is similar with the structure inside the green square box in Figure 3.2 (a). The results are consistent with the knowledge in inverse homogenization design [144] that different topologies of the RVE can possess the same effective elasticity property, and the initial design of the RVE affects the final result.

Figure 3.3 plots the iteration process of shear modulus and volume fraction of solid phases within the RVE starting with three different initial guesses.It can be noted that the evolution histories of the shear modulus starting from initial designs A, B and C are very similar. The total iteration counts are respectively 44, 45 and 46 which indicates that the proposed topology optimization method has good stability and high computational efficiency.

FIGURE 3.1: (a) Initial design A; (b) initial design B; (c) initial design C.

3.1.3.2 2D example for maximizing the bulk modulus

In this section, the optimization objective is selected as the bulk modulus of a 2D porous materials, and the initial design A shown in Figure 3.1 is used. Figure 3.4 shows the final microstructures and the corresponding effective elasticity matrixes when volume constrains of solid materials are set to be 60%, 50%, 40% and 30%. The fan-like topologies are generated with the reduction of volume fraction of solid material. The total iteration counts are 40, 49, 58 and 70, and the bulk moduli are 0.2396 MPa, 0.1796 MPa, 0.1304 MPa, and 0.0891 MPa, respectively. The Hashin–Shtrikman (HS) bounds [71] can be used to predict the maximum and minimum effective elastic modulus that a composite material could achieve. As for the porous materials, the void phase properties

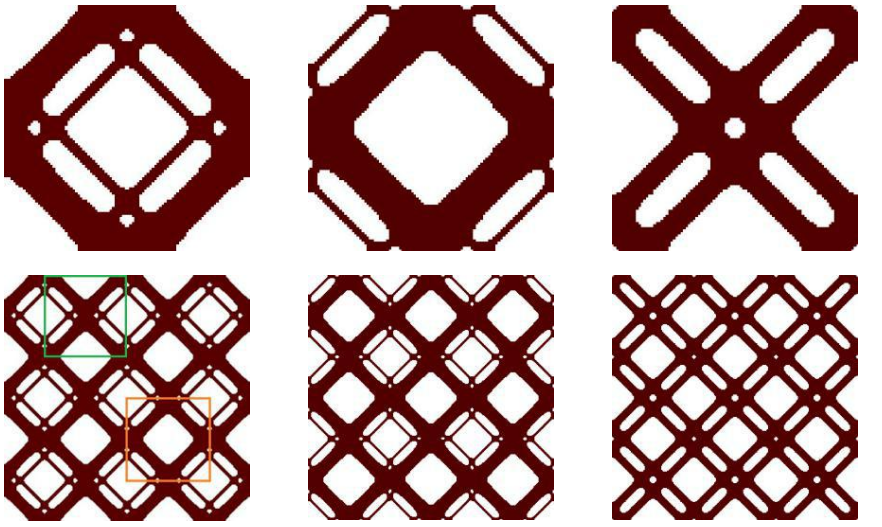

FIGURE 3.2: Optimized topologies of RVE and the effective elasticity matrix: columns (a), (b) and (c) compare the results when the optimization procedure starts from initial designs A, B, and C respectively.

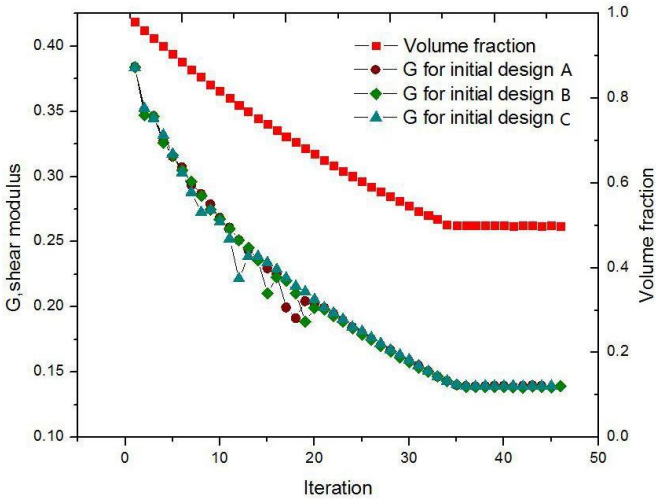

FIGURE 3.3: Iterative process of shear modulus and volume fraction of solid material for maximizing shear modulus.

are equal to zero and the upper bound of bulk modulus can be expressed as [153]:

$$K^* \leq \frac{V_f K^S G^S}{(1-V_f)K^S + G^S} \tag{3.17}$$

where K^S and G^S are the bulk and shear modulus of solid materials respectively. K^* is the bulk modulus of the considered porous material and V_f is the volume fraction of solid phases in the porous material. Figure 3.5 draws the curve of the HS upper bound as the volume fraction of solid phase which shows a good agreement with the present solutions.

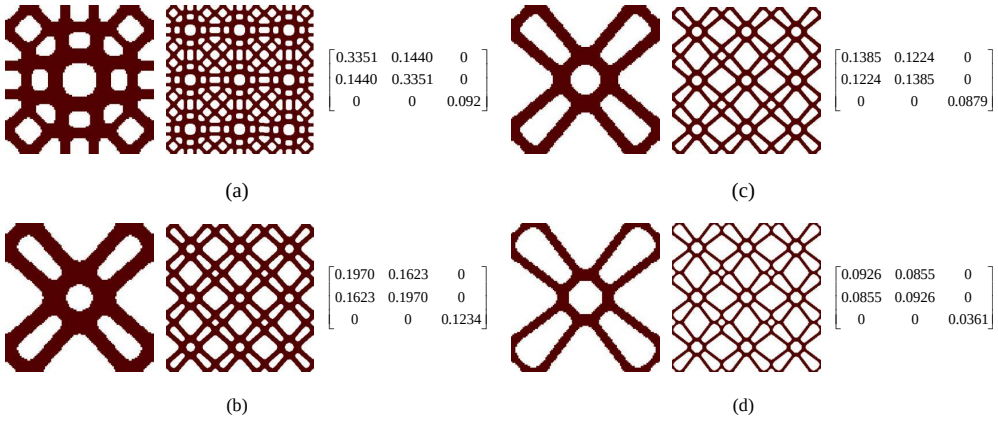

FIGURE 3.4: Optimized topologies of RVE and the effective elasticity matrix for maximum bulk modulus: (a) 60%, $K^* = 0.2396$; (b) 50%, $K^* = 0.1796$; (c) 40%, $K^* = 0.1304$; and (d) 30%, $K^* = 0.0891$.

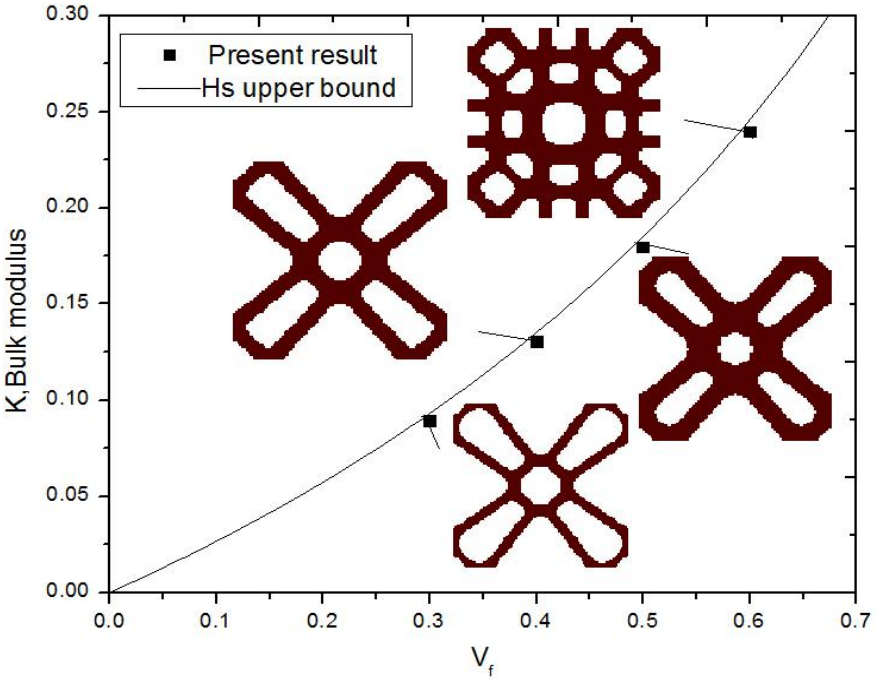

FIGURE 3.5: Comparison between the present solutions and HS bounds.

3.1.3.3 3D example for maximizing the shear modulus

In the following example, the optimization objective is to maximize the effective shear modulus of 3D porous materials. The optimization procedure starts from an initial design which is fully composed of solid material except for eight center elements of the representative cubic cell. Figure 3.6 shows the final RVE, $2 \times 2 \times 2$ RVEs and effective elasticity matrices when the volume constraints are set to be 35%, 25% and 15%, respectively. As can be observed, cross sections of obtained 3D microstructures are similar with the 2D microstructures. The corresponding effective shear moduli are 0.0664 MPa, 0.0387 MPa and 0.0164 MPa and the total number of iterations are 41, 51 and 54, respectively. It is worthwhile noting that the iteration numbers are all less than 55 even though the volume constraint is as low as 15 %.

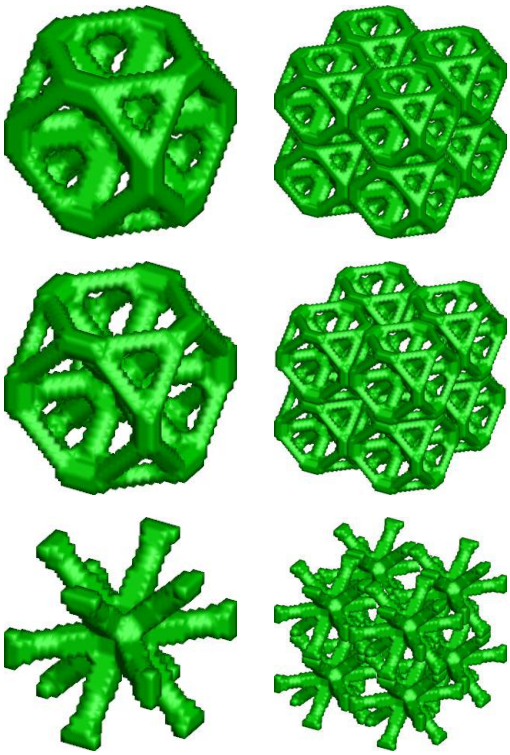

$$\begin{bmatrix} 0.1468 & 0.0711 & 0.0711 & 0 & 0 & 0 \\ 0.0711 & 0.1468 & 0.0711 & 0 & 0 & 0 \\ 0.0711 & 0.0711 & 0.1468 & 0 & 0 & 0 \\ 0 & 0 & 0 & 0.0664 & 0 & 0 \\ 0 & 0 & 0 & 0 & 0.0664 & 0 \\ 0 & 0 & 0 & 0 & 0 & 0.0664 \end{bmatrix} \text{(a)}$$

$$\begin{bmatrix} 0.0854 & 0.0426 & 0.0426 & 0 & 0 & 0 \\ 0.0426 & 0.0426 & 0.0854 & 0 & 0 & 0 \\ 0.0426 & 0.0426 & 0.0854 & 0 & 0 & 0 \\ 0 & 0 & 0 & 0.0387 & 0 & 0 \\ 0 & 0 & 0 & 0 & 0.0387 & 0 \\ 0 & 0 & 0 & 0 & 0 & 0.0387 \end{bmatrix} \text{(b)}$$

$$\begin{bmatrix} 0.0388 & 0.0183 & 0.0183 & 0 & 0 & 0 \\ 0.0183 & 0.0388 & 0.0183 & 0 & 0 & 0 \\ 0.0183 & 0.0183 & 0.0388 & 0 & 0 & 0 \\ 0 & 0 & 0 & 0.0164 & 0 & 0 \\ 0 & 0 & 0 & 0 & 0.0164 & 0 \\ 0 & 0 & 0 & 0 & 0 & 0.0164 \end{bmatrix} \text{(c)}$$

FIGURE 3.6: Optimized topologies of RVE and the effective elasticity matrix for maximum 3D shear modulus: (a) 35%, (b) 25%, and (c) 15%.

3.1.3.4 3D example for maximizing the bulk modulus.

Topological design of 3D porous materials for the bulk modulus is considered here. The optimization process starts from the initial design where eight elements at the corner of cubic unit cell are assigned as void element. The volume fractions of solid materials are set to be 55%, 35% and 15% of the whole design domain. The final microstructural

topologies of the RVE and their $2 \times 2 \times 2$ RVEs and effective elasticity matrixes are shown in Figure 3.7. The total number of iterations are 42, 40 and 66, and the final bulk moduli are 0.2551 MPa, 0.1192 MPa and 0.0265 MPa. As in the previous examples, the microstructural topologies keep consistency with the decrease of the volume fraction of solid material.

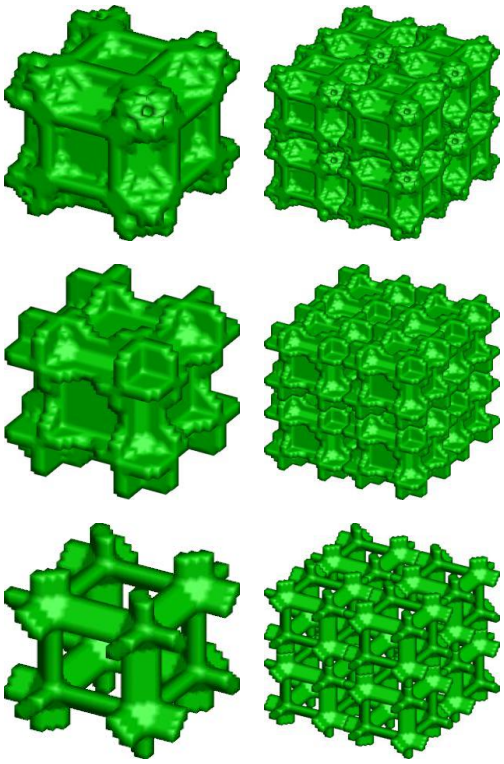

$$\begin{bmatrix} 0.4710 & 0.1472 & 0.1472 & 0 & 0 & 0 \\ 0.1472 & 0.4710 & 0.1472 & 0 & 0 & 0 \\ 0.1472 & 0.1472 & 0.4710 & 0 & 0 & 0 \\ 0 & 0 & 0 & 0.1211 & 0 & 0 \\ 0 & 0 & 0 & 0 & 0.1211 & 0 \\ 0 & 0 & 0 & 0 & 0 & 0.1211 \end{bmatrix} \quad \text{(a)}$$

$$\begin{bmatrix} 0.2333 & 0.0623 & 0.0623 & 0 & 0 & 0 \\ 0.0623 & 0.2333 & 0.0623 & 0 & 0 & 0 \\ 0.0623 & 0.0623 & 0.2333 & 0 & 0 & 0 \\ 0 & 0 & 0 & 0.0529 & 0 & 0 \\ 0 & 0 & 0 & 0 & 0.0529 & 0 \\ 0 & 0 & 0 & 0 & 0 & 0.0529 \end{bmatrix} \quad \text{(b)}$$

$$\begin{bmatrix} 0.0669 & 0.0063 & 0.0063 & 0 & 0 & 0 \\ 0.0063 & 0.0669 & 0.0063 & 0 & 0 & 0 \\ 0.0063 & 0.0063 & 0.0669 & 0 & 0 & 0 \\ 0 & 0 & 0 & 0.0030 & 0 & 0 \\ 0 & 0 & 0 & 0 & 0.0030 & 0 \\ 0 & 0 & 0 & 0 & 0 & 0.0030 \end{bmatrix} \quad \text{(c)}$$

FIGURE 3.7: Optimized topologies of RVE and the effective elasticity matrix for maximum 3D bulk modulus: (a) 55%, $K^* = 0.2551$; (b) 35%, $K^* = 0.1192$; and (c) 15%, $K^* = 0.0265$.

3.2 Design of materials using the hybrid cellular automata

The hybrid cellular automata (HCA) method is a biologically-inspired technique which is actually not explicitly an optimization approach [155]. One of the first application of cellular automata (CAs) to structural design was presented by [81], and the basic idea of this method is that the overall behavior of a particular cell is governed by its neighbors. The physical quantities at all lattices are then updated simultaneously based on the local rules such that the material or structural topologies can be tailored to achieve the selected objectives [87]. During the past decade, structural optimization using the HCA has undergone a remarkable development [1, 139, 140, 20], and it has been demonstrated that the HCA is an efficient and robust method in solving topology

optimization problems [156, 132]. The merits of the HCA include effectiveness, gradient free and easy implementation with other numerical analysis methods [21]. This section aims to extend the HCA to the design of periodic microstructures of porous materials with extreme elastic properties and negative Poisson's ratio.

3.2.1 Optimization model

The idea of the CA requires decomposition of the considered design domain (RUC herein) into a set of cells which is also the basic idea of the finite element (FE) method. The CA cells and the FE meshes are coincident in this work. The values of elastic moduli of cells or elements are used as the design variables which are updated upon a local rule until convergence is met. Similar to topology optimization of homogeneous structures, the modulus at a cell/element e is defined using the modified solid isotropic material with penalization (SIMP) approach:

$$E(\rho_e) = E_{min} + \rho_e^P (E_0 - E_{min}), \tag{3.18}$$

where E_0 is the Young's modulus of solid cell and E_{min} is the Young's modulus of void cell which is a very small value to avoid the singularity of the stiffness matrix. P is the penalization exponent which is artificially introduced to make sure the material distribution converges to a black and white design. ρ_e takes values between 0 and 1, and these limits denote the void cells and solid cells, respectively.

The optimization model using the HCA for extreme material properties can be formulated as follows:

$$\text{Find} : \{\rho_e\} \tag{3.19}$$

$$\text{Maximize} : f = \omega_{ijkl} \bar{C}^H_{ijkl} \tag{3.20}$$

$$\text{Subject to} : \mathbf{KU} = \mathbf{F} \tag{3.21}$$

$$: S_e = \bar{E}_e - E^*_e = 0 \tag{3.22}$$

$$: 0 < \rho_e \leq 1 \tag{3.23}$$

The objective f is a function of the homogenized material constitutive components as formluated in Section 3.1.2. In Equation (3.22), E^*_e is the local strain energy target and $\bar{E}_e$ is an average element strain energy value. This value is calculated as the average within a fixed proximity of each element in the design domain [157] as

$$\bar{E}_e = \frac{E_e + \sum_{j=1}^{N_{ca}} E_j}{N_{ca} + 1}, \tag{3.24}$$

where E_j corresponds to the strain energy of a neighboring element and N_{ca} is the number of neighbors defined in the CA neighborhood. von Neumann neighborhood is employed in this work as illustrated in Figure 3.8, and N_{ca} equals to 4. The E_e is defined as the element strain energy and also viewed as the element contribution to the objective function. For instance, when the objective function is chosen as bulk modulus K, the E_e denotes the element strain energy which corresponds to the bulk modulus. While it comes to maximizing material shear modulus G, E_e denotes the element contribution to the shear modulus. Therefore, using the energy-based homogenization approach, the global homogenized material properties formulated in Equation (3.20) is governed by discrete elements that interact with their neighbors. The use of average element strain energy instead of an actual value is analogous to the filter technique in classic topology optimization to avoid numerical instabilities such as checkerboard phenomenon and mesh dependency. Equation (3.22) achieves the zero-error condition between the average value of the strain energies and their optimum value, indicating that elements which are not void are saturated. When the Equation (3.22) is not satisfied, a local rule of HCA algorithm formulated in following sub-section updates the density design variable ρ_e to make this condition true.

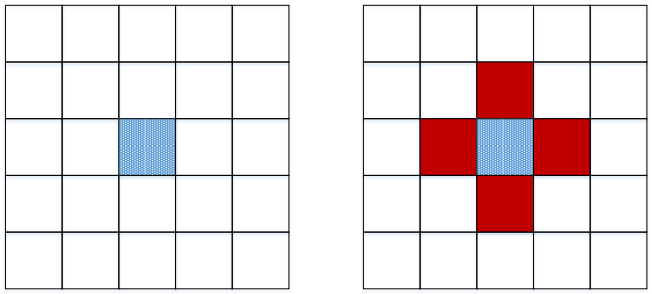

(a) (b)

FIGURE 3.8: Two CA neighborhood layouts; (a) Empty $N_{ca} = 0$; (b) von Neumann $N_{ca} = 4$.

Under the assumption of periodic boundary conditions (PER), the global displacement field of the design domain (RVE) is evaluated by solving the equilibrium problem subjected to the uniform strain fields (three unit test strains for 2D cases, and six unit strains for 3D cases). The PER in the FE model is directly imposed by constraining the nodal displacements on two opposite faces of the RUC, as in [178]. More details about the numerical implementation of the energy-based homogenization using the PER condition to account for material constituent parameters can be found in [170].

As can be seen in the optimization model, the HCA method drives the internal strain energy density of solid cells/elements in design domain to a saturated state. Then, the topology optimization problem considered here can be solved as finding the

optimal layout of solid materials so that the extreme effective properties of material are satisfied. Note that the volume constraint of solid materials is implicitly presented in optimization model, and a post-processing step given in [146] can be employed to adjust the final volume fraction.

3.2.2 Updating rule and convergence criterion

In this work, a local rule in the HCA approach is adopted to update the density design variables ρ_e iteratively, and the material which is composed of final relative density distribution processes the extreme material property. The updating rule of the element relative density is

$$\begin{cases} \rho_e^{(iter+1)} = \bar{\rho_e}^{(iter)} + \Delta\rho_e^{(iter)} \\ \Delta\rho_e^{(iter)} = c_P \times S_e^{(iter)} \\ \bar{\rho_e}^{(iter)} = \frac{\rho_e^{(iter)} + \sum_{j=1}^{N_{ca}} \rho_j^{(iter)}}{N_{ca}+1} \end{cases} \tag{3.25}$$

where $iter$ is the iteration number; $\bar{\rho_e}$ denotes the effective value of the density design variable which is averaged with neighborhood elements in the same way as it is done for the element strain energy in Equation 3.24. $\Delta\rho_e$ presents the local control strategy which is the proportion control in the HCA approach. It can be seen that the local rule 3.25 controls the material distribution in the design domain according to the feedback signal S_e in Equation (3.22). c_P is a constant named as the proportional gain. Other updating control rules such as integral and derivative control methods can be found in [93].

Typically, the convergence criteria for topology optimization using the HCA algorithm are based on the change in density design variable. Since the structural volume of the current design is determined by density design variable, the iterative optimization process converges when no further change in volume is possible [156]. This state can be expressed by

$$\frac{|\Delta V^{iter}| + |\Delta V^{iter-1}|}{2 \times V_0} \leq \tau, \quad \text{where} \quad \Delta V^{iter} = V^{iter} - V^{(iter-1)} \tag{3.26}$$

where V_0 and V^{iter} are the structural volumes of the initial design and of the $iter$-th iteration step, respectively. τ is a specified small tolerance value.

3.2.3 Numerical examples

As mentioned before, there is no unique solution for topological design of materials with extreme properties, and the used algorithms and parameters have influence on

the final results. An RVE with dimensions 100×100 mm is discretized into 100×100 4-node quadrilateral plane stress elements. Following [9, 74], four elements and a circular region (radius equals to $\frac{100}{6}$) with void phase at the center of the RVE are named initial design 1 and 2, respectively. Young's modulus and Poisson's ratio of the solid phase are set to $E = 1$ MPa and $\nu = 0.3$, respectively.

In order to design the material with the maximum bulk modulus, two initial designs of the RVE are employed, and the penalization exponent P is set to 5. The iterative optimization processes converge with the volume fractions of the solid materials 0.493 and 0.575 starting from initial designs 1 and 2, respectively. As for the result starting from initial design 1, we used a post-processing step given in [146] to satisfy the volume fraction constraint 0.5. The final RVEs, corresponding to periodic microstructures and their constitutive matrices obtained from two different initial designs are shown in Figure 3.9, and the total iteration numbers are 156 and 152, respectively. The bulk moduli from initial designs 1 and 2 are, respectively, 0.180 MPa and 0.224 MPa. To verify the developed method, the above problem is solved using the same parameters using the SIMP method [170] with density filtering and filter radius $r_{min} = 2$. When the volume fractions of solid materials are set to 0.5 and 0.575, the resulted bulk moduli are 0.164 MPa and 0.210 MPa, respectively, which are both lower than that of the proposed method. The corresponding Hashin-Strickman (HS) upper bounds [71] are 0.185 and 0.229 show a very good agreement with the present solutions.

For optimal microstructures with maximum shear modulus, the initial design 1 is employed. Two different penalization exponents 5 and 3 are considered. The iterative processes converge with the volume fractions 0.391 and 0.406, respectively. Figure 3.10 shows the final microstructures and corresponding effective elasticity matrices indicating both solutions with clearly identifiable topology layouts. The total iteration numbers are 37 and 50 and the shear moduli are 0.099 and 0.107, respectively.

In order to design the material with negative Poisson's ratio (NPR), we follow the relaxed function of NPR proposed in [170] as

$$f = \bar{C}^H_{1122} - \beta^{iter}(\bar{C}^H_{1111} + \bar{C}^H_{2222}) \tag{3.27}$$

where β is a fixed parameter defined as 0.8 and the exponent $iter$ is the iteration step. Apart from the β^{iter}, the three remainder items in above objective function are all homogenized material constitutive parameters. Therefore, the same strategy is employed to design materials with negative Poisson's ratio as for bulk or shear modulus. The penalization exponent is set to 3 here, and the convergence tolerance changes from 1% to 0.1%. The numerical procedure starting from initial design 2 converges to Figure 3.11 after 57 iterations, and the final volume fraction and Poisson's ratio are 0.388 and -0.590, respectively. The iteration histories of the objective function and of the volume

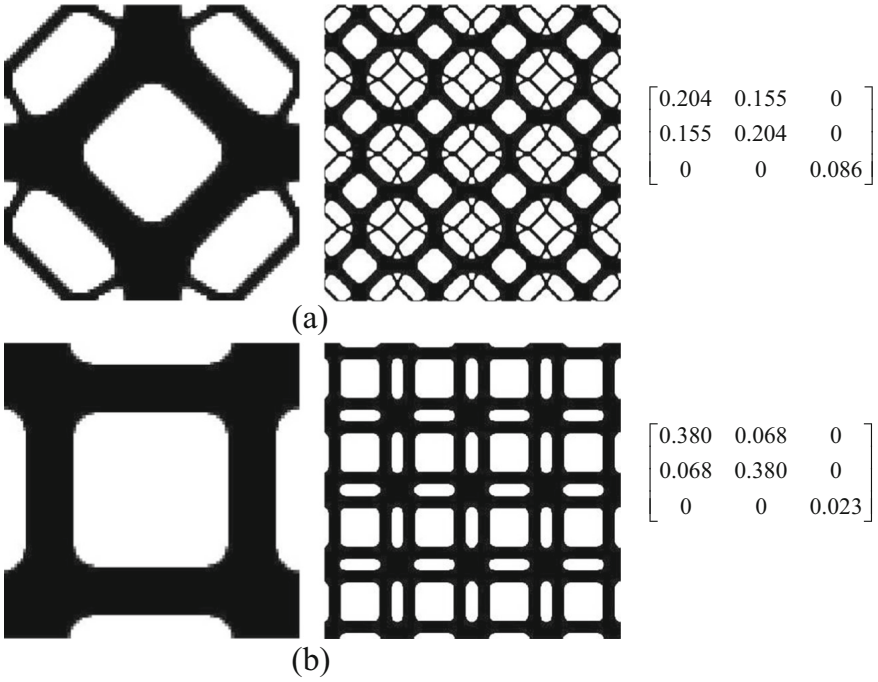

FIGURE 3.9: Optimized RVE topologies (left), corresponding periodic microstructures (middle), and effective constitutive matrix (right) of materials with maximum bulk modulus starting form two initial designs: (a) initial design 1; (b) initial design 2.

fraction are illustrated in Figure 3.12.

3.3 Concluding remarks

In this Chapter, we have proposed two topology optimization frameworks for the design of material microstructures for extreme effective elastic modulus or negative Poisson's ratio. Several 2D and 3D numerical examples have been presented to demonstrate their effectiveness of the proposed topological design framewoks. A series of interesting material microstructures have been obtained to give some solutions for material design with high-performance or "exotic" material properties. Compared with the existed theoretical bounds for bulk moduli of porous materials, the resulting materials satisfy the maximum bulk modulus with different topologies and different volume fractions of solid phases. In addition, the generated structural topologies with desired material properties are described clearly. Furthermore, a series of optimization parameters which could affect the final results have been fully studied, e.g. initial guess designs of the RVE, volume fractions of solid phase, value of penalization factor, etc. In the following Chapter, the optimization model will be extended to consider structural performance at macro scale rather than material properties, by tailoring also the

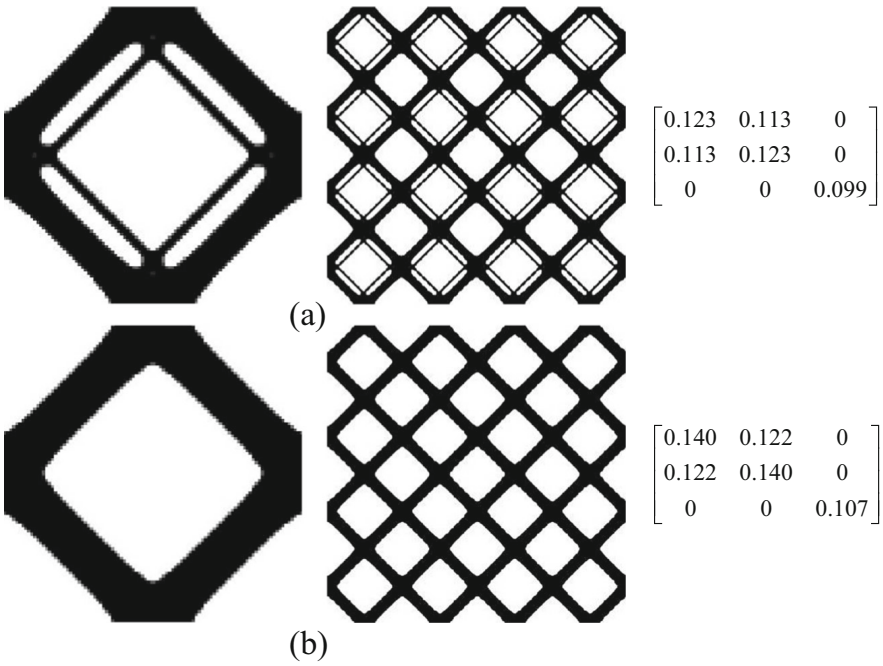

$$\begin{bmatrix} 0.123 & 0.113 & 0 \\ 0.113 & 0.123 & 0 \\ 0 & 0 & 0.099 \end{bmatrix}$$

$$\begin{bmatrix} 0.140 & 0.122 & 0 \\ 0.122 & 0.140 & 0 \\ 0 & 0 & 0.107 \end{bmatrix}$$

FIGURE 3.10: Optimized RVE topologies (left), corresponding periodic microstructures (middle), and effective constitutive matrix (right) of materials with maximum shear modulus with two different penalization factors P: (a) $P = 5$; (b) $P = 3$.

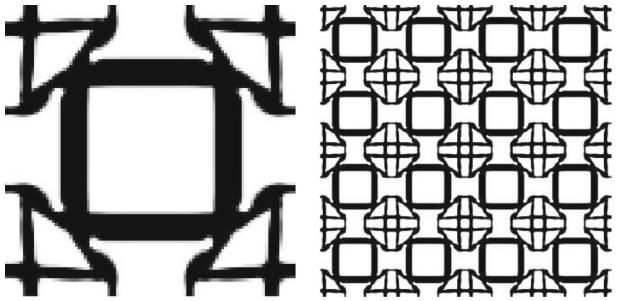

$$\begin{bmatrix} 0.089 & -0.053 & 0 \\ -0.053 & 0.089 & 0 \\ 0 & 0 & 0.004 \end{bmatrix}$$

FIGURE 3.11: Materials with negative Poisson's ratio: RVE topology (left), corresponding periodic microstructure (middle), and effective constitutive matrix (right).

architecture/topology of the material RVE.

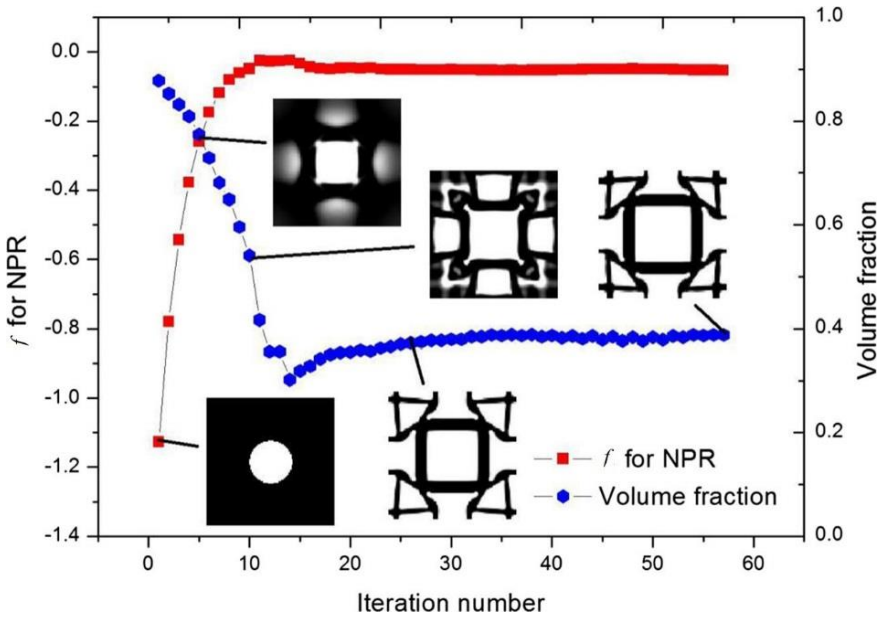

FIGURE 3.12: Iteration histories of the objective function, volume fraction, and intermediate microstructural topologies for the negative Poisson's ratio (NPR).

Part II

Multiscale topology optimization

Chapter 4

Concurrent topological design of structures and multi-phase materials

Following the topological design model employed for pure material design in Chapter 3, a concurrent topology optimization framework of macroscopic structure and the underlying material microstructures is extended in this Chapter. Concurrent topology optimization allows one to determine not only the best material layout at the micro scale, but also the optimal use of the designed material at the macro scale offering more design freedom on the two scales, and is called here multiscale topological design. A hierarchical topology optimization scheme of structure and element-based tailoring porous material has been firstly proposed in [135]. This hierarchical framework has been extended to 3D elastic structures in [40]. In order to address the geometrical and physical nonlinearities at material scale, the concurrent design of material and structure within FE^2 nonlinear multiscale analysis framework has been developed in [169].

These works assumed that the materials/composites used in macrostructural construction are varied pointwisely, thus requiring large amount of computational efforts. The most commonly used strategy is designing a uniform material microstructure or RVE at the microscopic scale for a concurrently changed macrostructure. Via this strategy, concurrent optimization design has already been extended to tailoring structure and the underlying porous material simultaneously for macroscopic structural performance, e.g. stiffness [90] or fundamental frequencies [193]. However, there are only a few works on the concurrent topological design of composite structures and their multi-phase materials. In comparison with porous materials, composites consisting of two or more phase materials are more attractive and advantageous from the perspective of engineering application. A review of recent advances on mechanics of multifunctional multi-phase composite materials and structures can be found in [60].

Based on the classical topology optimization with single isotropic material, Bendsøe and Sigmund [16] proposed a multi-phase material mixture model within the SIMP scheme. Such a model has been extended to various topology optimization problems,

e.g. material design [59] or multiphysic problems [143, 19]. Recently, different types of topology optimization methods were employed to design multi-phase material and structures like level set-based methods [163, 103, 167, 66] and the BESO method [75, 182, 134]. This Chapter is based on the earlier work [75] on multiple material design of mono-scale structures, where the constituent phases are divided into several groups by the BESO method to perform the topology optimization. The key contribution of this Chapter is to integrate the BESO method, homogenization and multi-phase material interpolation scheme to carry out multiscale topology optimization of materials and structures. Comparing with only two phase materials employed at microscopic scale in [182], we design the underlying three or more phases material microstructures for both the solid and compliant composite phases of the macroscale structure. The effective elastic constitutive parameters of multi-phase composites are evaluated by the numerical homogenization analysis. In addition, we have carried out the concurrent topology optimization for both 2D and 3D materials and structures to demonstrate the advantages of the proposed framework.

The remainder of this Chapter is organized as follows: concurrent topology optimization model of composite macrostructure and its multi-phase materials is drawn in Section 4.1. Section 4.2 formulates the multi-phase material interpolation scheme and gives the sensitivity analysis on both macro and micro design variables. The BESO method and numerical implementation procedure are introduced in Section 4.3. Section 4.4 presents several 2D and 3D numerical examples and discussions. Finally, conclusion part is given in Section 4.5.

4.1 Concurrent optimization design formulation

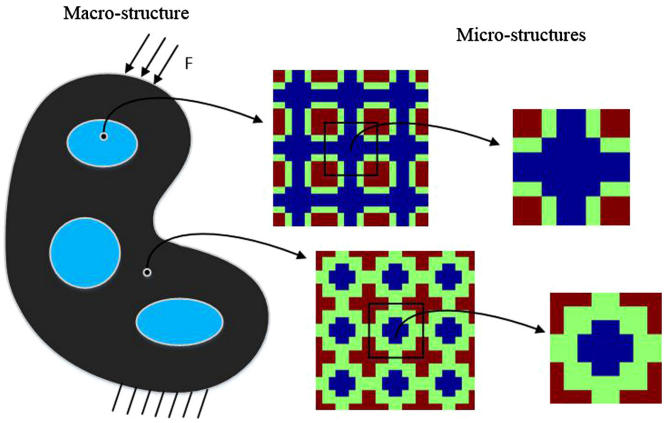

FIGURE 4.1: An arbitrary macrostructure composed of periodic microstructures.

In this Chapter, the concurrent topology optimization problem considers a macrostructure composed of multi-phase materials with periodic microstructures as illustrated in Figure 4.1. The macrostructure is composed of two periodic composites which both have three or more phase constitutive materials. Each multi-material composite serves as a phase in the macrostructure. Then, there are in total three finite element (FE) models which include one macro model for the macrostructure and two micro models for the material RVEs correspondingly. The RVE of the periodic multi-phase composite serves as the design domain in each micro model. The optimization objective is to minimize the structural compliance (or maximize the structural stiffness) by finding the optimal macrostructural topology and the optimal designs of the multi-phase composites used in macrostructural construction. Similar to the classical mono-scale topology optimization, the volume constraints are employed in macro or micro model, defining the target volume of each composite phase or constitutive material, respectively. It is assumed that each composite phase consists of n kinds of base materials with equal Poisson's ratio while Young's moduli are sorted descending, i.e. $E_1^1 > E_2^1 \cdots > E_n^1$ and $E_1^2 > E_2^2 \cdots > E_n^2$, where the superscript indicates the number of micro model and the subscript is the number of base materials in each micro model. Such a concurrent topological design problem of macrostrcture and the underlying multi-phase microstructures for compliance minimization can be formulated as follows:

$$\text{Find} : \{\rho_m^{mac}, \rho_{ij}^{mic,1}, \rho_{ij}^{mic,2}\} \tag{4.1}$$

$$\text{Minimize} : f = \mathbf{F}^T\mathbf{U} \tag{4.2}$$

$$\text{Subject to} : \mathbf{K}\mathbf{U} = \mathbf{F} \tag{4.3}$$

$$: V_1^{mac} = \sum_{m=1}^{M} V_m x_m^{mac} \tag{4.4}$$

$$: \sum_{i=1}^{N} V_i \rho_{ij}^{mic,1} - V_{j*}^{mic,1} - \sum_{i=1}^{j-1} V_{i*}^{mic} = 0, \quad (j = 1, 2, ..., n) \tag{4.5}$$

$$: \sum_{i=1}^{N} V_i \rho_{ij}^{mic,2} - V_{j*}^{mic,2} - \sum_{i=1}^{j-1} V_{i*}^{mic} = 0, \quad (j = 1, 2, ..., n) \tag{4.6}$$

$$: \rho_m^{mac} = \rho_{min} \text{ or } 1; \quad \rho_{ij}^{mic,1} = \rho_{min} \text{ or } 1; \quad \rho_{ij}^{mic,2} = \rho_{min} \text{ or } 1 \tag{4.7}$$

where $\mathbf{U}$ and $\mathbf{F}$ are the displacement and external force vectors, respectively. M and N are the total numbers of finite elements in macro and micro FE models, respectively. The design variables in (4.1) consist of three subsets: macro design variable ρ_m^{mac} represents the layout of two composites in the macrostructure; micro design variables $\rho_{ij}^{mic,1}$ and $\rho_{ij}^{mic,2}$ represent the distribution of employed base materials in micro models 1 and

2, respectively. Note that the micro design variable $\rho_{ij}^{mic,1}$ represents the microstructure for macro elements $\rho_m^{mac} = 1$, and $\rho_{ij}^{mic,2}$ for macro elements $\rho_m^{mac} = \rho_{min}$. ρ_{min} is a predetermined small value. Without special indication, the design variables $\rho_{ij}^{mic,1}$ and $\rho_{ij}^{mic,2}$ will be consistently denoted as ρ_{ij}^{mic} in the following for simplicity. Therefore, ρ_{ij}^{mic} indicates the relative density of the i-th element for the j-th base material in micro models which can be expressed by

$$\rho_{ij}^{mic} = \begin{cases} 1, & \text{for } E \geq E_j \\ \rho_{min}, & \text{for } E < E_{j+1} \end{cases} \tag{4.8}$$

where E is the Young's modulus of the i-th element. $\rho_{ij}^{mic} = 1$ is adopted when the element is filled with the base material j or the base materials with larger Young's modulus than j, and ρ_{ij}^{mic} is equal to ρ_{min} otherwise. Therefore, the term $\sum_{i=1}^{N} V_i \rho_{ij}^{mic,1}$ in Equation (4.5) represents total volumes of the j-th base material and stiffer base materials $(1, \ldots, j-1)$ in the first micro model. The prescribed volume of j-th base material is denoted as $V_{j*}^{mic,1}$ which can be defined by designers. Similarly, $\sum_{i=1}^{N} V_i \rho_{ij}^{mic,2}$ and $V_{j*}^{mic,2}$ are the corresponding terms in the second micro model. V_i denotes the volume of the i-th element in the micro models, and V_m denotes the element volume in the macro model. V_1^{mac} in (4.4) is the prescribed volume of the first phase ($\rho_m^{mac} = 1$) in the macro model.

4.2 Material interpolation scheme and sensitivity analysis

4.2.1 Material interpolation scheme

Material interpolation scheme is an essential part to perform the sensitivity analysis in topology optimization framework. In this section, the modified SIMP model introduced in [14, 191, 145] is employed. For topological design problem with three or more phase materials in the micro models considered in this work, it is straightforward to interpolate the material properties between two neighboring phases (i.e. E_j and E_{j+1}) [75], as

$$E(\rho_{ij}^{mic}) = (\rho_{ij}^{mic})^P E_j + [1 - (\rho_{ij}^{mic})^P] E_{j+1}, \tag{4.9}$$

where P is the penalization exponent. Under this scheme, the elasticity matrix $\mathbf{C}$ in the micro models can be expressed as

$$\mathbf{C}(\rho_{ij}^{mic}) = (\rho_{ij}^{mic})^P \mathbf{C}_j + [1 - (\rho_{ij}^{mic})^P] \mathbf{C}_{j+1} \tag{4.10}$$

where $\mathbf{C}_j$ and $\mathbf{C}_{j+1}$ are respectively the elasticity matrix of the base materials j and $j+1$. As for the macro model, the m-th element elasticity matrix can be expressed as:

$$\mathbf{C}(\rho_m^{mac}) = (\rho_m^{mac})^P \bar{\mathbf{C}}^{H,1} + (1 - (\rho_m^{mac})^P)\bar{\mathbf{C}}^{H,2} \tag{4.11}$$

where $\bar{\mathbf{C}}^{H,1}$ and $\bar{\mathbf{C}}^{H,2}$ are the effective elasticity matrices computed by the homogenization implementation in the micro models 1 and 2, respectively. Based on the classical homogenization method [73, 72], the $\bar{\mathbf{C}}^{H,1}$ and $\bar{\mathbf{C}}^{H,2}$ can be respectively computed as:

$$\bar{\mathbf{C}}^{H,1} = \frac{1}{|\mathrm{Y}|}\int_Y \mathbf{C}^1(\mathbf{I} - \mathbf{bu})d\mathrm{Y} \tag{4.12}$$

and

$$\bar{\mathbf{C}}^{H,2} = \frac{1}{|\mathrm{Y}|}\int_Y \mathbf{C}^2(\mathbf{I} - \mathbf{bu})d\mathrm{Y} \tag{4.13}$$

where $|Y|$ is the total volume of the RVE, I is the identity matrix and $\mathbf{b}$ is the strain-displacement matrix. $\mathbf{C}^1$ and $\mathbf{C}^2$ are the elasticity matrices at a point with relative densities $\rho_{ij}^{mic,1}$ and $\rho_{ij}^{mic,2}$ in Equation (4.10), respectively. $\mathbf{u}$ is the fluctuation of displacement fields caused by imposing uniform strain fields over the RVE, for instance, $\{1,0,0\}^T$, $\{0,1,0\}^T$ and $\{0,0,1\}^T$ in 2D problems.

4.2.2 Sensitivity analysis

In order to calculate the structural compliance as well as conduct the sensitivity analysis, the FE analysis is also performed for the structures at the macro scale. In the macro FE model, the structural compliance is obtained by Equation (4.2), and the sensitivity of the compliance with respect to the macro design variable, ρ_m^{mac}, can be written as

$$\alpha_m^{mac} = \frac{\partial f}{\partial \rho_m^{mac}} = -\mathbf{U}^T \frac{\partial \mathbf{K}}{\partial \rho_m^{mac}}\mathbf{U} = -P(\rho_m^{mac})^{P-1}(\mathbf{U}_m^T \mathbf{K}_m^1 \mathbf{U}_m - \mathbf{U}_m^T \mathbf{K}_m^2 \mathbf{U}_m) \tag{4.14}$$

where $\mathbf{U}_m$ is the displacement vector of the m-th element in the macro model. $\mathbf{K}_m^1$ and $\mathbf{K}_m^2$ are the m-th element stiffness matrices calculated by using $\bar{\mathbf{C}}^{H,1}$ and $\bar{\mathbf{C}}^{H,2}$, respectively. The computation of the $\mathbf{K}_m^1$ and $\mathbf{K}_m^2$ can be expressed as

$$\mathbf{K}_m^1 = \int_{V_m} \mathbf{B}^T \bar{\mathbf{C}}^{H,1}\mathbf{B}dV_m \tag{4.15}$$

and

$$\mathbf{K}_m^2 = \int_{V_m} \mathbf{B}^T \bar{\mathbf{C}}^{H,2}\mathbf{B}dV_m \tag{4.16}$$

As for the micro models, the design variables $\rho_{ij}^{mic,1}$ and $\rho_{ij}^{mic,2}$ are respectively related to all first phase ($\rho_m^{mac} = 1$) and second phase ($\rho_m^{mac} = \rho_{min}$) in the macro model.

Therefore, the sensitivity number of the objective function with respect to the first micro design variables $\rho_{ij}^{mic,1}$ is equal to summation of the derivatives of objective function over all first phase ($\rho_m^{mac} = 1$) as:

$$\begin{aligned}\alpha_{ij}^{mic,1} = \frac{\partial f}{\partial \rho_{ij}^{mic,1}} &= -\sum_{m=1}^{M} (\rho_m^{mac})^P \mathbf{U}_m^T \frac{\partial \mathbf{K}_m}{\partial \rho_{ij}^{mic,1}} \mathbf{U}_m \\ &= -\sum_{m=1}^{M} (\rho_m^{mac})^P \mathbf{U}_m^T \int_{V_m} \mathbf{B}^T \frac{\partial \bar{\mathbf{C}}^H}{\partial \rho_{ij}^{mic,1}} \mathbf{B} dV_m \mathbf{U}_m \end{aligned} \tag{4.17}$$

Similarly, the sensitivity number of the objective function on the second micro design variable $\rho_{ij}^{mic,2}$ is equal to summation of the derivatives of the objective function over all second phase ($\rho_m^{mac} = \rho_{min}$) in the macro model as:

$$\begin{aligned}\alpha_{ij}^{mic,2} = \frac{\partial f}{\partial \rho_{ij}^{mic,2}} &= -\sum_{m=1}^{M} (1-\rho_m^{mac})^P \mathbf{U}_m^T \frac{\partial \mathbf{K}_m}{\partial \rho_{ij}^{mic,2}} \mathbf{U}_m \\ &= -\sum_{m=1}^{M} (1-\rho_m^{mac})^P \mathbf{U}_m^T \int_{V_m} \mathbf{B}^T \frac{\partial \bar{\mathbf{C}}^H}{\partial \rho_{ij}^{mic,2}} \mathbf{B} dV_m \mathbf{U}_m \end{aligned} \tag{4.18}$$

With the help of material interpolation scheme in Equations (4.9) and (4.10), the derivative of homogenized elasticity matrices with respect to the design variables $\rho_{ij}^{mic,1}$ and $\rho_{ij}^{mic,2}$ can be expressed as following using the adjoint variable method [88]:

$$\begin{aligned}\frac{\partial \bar{\mathbf{C}}^{H,1}}{\partial \rho_{ij}^{mic,1}} &= \frac{1}{|\mathrm{Y}|} \int_{\mathrm{Y}} (\mathbf{I} - \mathbf{bu}) \frac{\partial \mathbf{C}^1}{\rho_{ij}^{mic,1}} (\mathbf{I} - \mathbf{bu}) d\mathrm{Y} \\ &= -\frac{P(\rho_{ij}^{mic,1})^{P-1}}{|\mathrm{Y}|} \int_{\mathrm{Y}} (\mathbf{I} - \mathbf{bu})(\mathbf{C}_j^1 - \mathbf{C}_{j-1}^1)(\mathbf{I} - \mathbf{bu}) d\mathrm{Y} \end{aligned} \tag{4.19}$$

and

$$\begin{aligned}\frac{\partial \bar{\mathbf{C}}^{H,2}}{\partial \rho_{ij}^{mic,2}} &= \frac{1}{|\mathrm{Y}|} \int_{\mathrm{Y}} (\mathbf{I} - \mathbf{bu}) \frac{\partial \mathbf{C}^2}{\rho_{ij}^{mic,2}} (\mathbf{I} - \mathbf{bu}) d\mathrm{Y} \\ &= -\frac{P(\rho_{ij}^{mic,2})^{P-1}}{|\mathrm{Y}|} \int_{\mathrm{Y}} (\mathbf{I} - \mathbf{bu})(\mathbf{C}_j^2 - \mathbf{C}_{j-1}^2)(\mathbf{I} - \mathbf{bu}) d\mathrm{Y} \end{aligned} \tag{4.20}$$

It is worth noting that the effective material properties calculated from the micro models by the numerical homogenization are integrated to the macrostructural FE analysis to bridge the macroscopic and microscopic scales. On the other hand, the sensitivity

numbers in the micro models use the displacement fields of the macrostructure, indicating that the macrostructural response affects the optimal design of multi-phase material microstructures reversely. As a result, all three FE analysis models interact with each other, and the topological design of composite macrostructure and the underlying multi-phase material microstructures are carried out concurrently.

4.3 BESO method and numerical implementation

4.3.1 Sensitivity numbers

The sensitivity information in the BESO method can be used to represent a relative ranking of each individual element. Thus, the sensitivity number of the m-th element in the macro model for minimizing the structural compliance can be re-written as

$$\alpha_m^{mac} = -\frac{1}{P}\frac{\partial f}{\partial \rho_m^{mac}} \tag{4.21}$$

Similarly, the two sensitivity numbers in the micro models can be re-written as

$$\alpha_{ij}^{mic,1} = -\frac{1}{P}\frac{\partial f}{\partial \rho_{ij}^{mic,1}} \tag{4.22}$$

and

$$\alpha_{ij}^{mic,2} = -\frac{1}{P}\frac{\partial f}{\partial \rho_{ij}^{mic,2}} \tag{4.23}$$

Using Equations (4.14)-(4.20), the three sensitivity numbers can be obtained correspondingly.

In order to avoid the common numerical instabilities such as checkerboard pattern and mesh-dependency in topology optimization process, the filter scheme is employed to smooth the elemental sensitivity as:

$$\alpha_m^{mac} = \frac{\sum_{q=1}^{N_e} w_{mq}\alpha_q^{mac}}{\sum_{q=1}^{N_e} w_{mq}},\ w_{mq} = \max(0, r_{\min}^{mac} - \Delta(m,q)) \tag{4.24}$$

where w_{mq} is a linear weight factor determined according to the prescribed filter radius $r_{\min}^{mac}$ and the element center-to-center distance $\Delta(m,q)$ between elements m and q. To improve the convergence of the proposed method, the sensitivity numbers can be further averaged with their historical information in previous iteration step [76]:

$$(\alpha_m^{mac})^{(iter)} = \frac{(\alpha_m^{mac})^{(iter)} + (\alpha_m^{mac})^{(iter-1)}}{2}, \tag{4.25}$$

Note that the micro sensitivity numbers $\alpha_{ij}^{mic,1}$ and $\alpha_{ij}^{mic,2}$ can also be filtered according to Equation (4.24) with filter radius r_{min}^{mic} and averaged with their corresponding historical information in the same way.

4.3.2 Variables updating

In the presented BESO method for multi-phase topology optimization, the volume constraints of the different constitutive phases/composites in the micro and macro models are satisfied iteratively. In the macro model, the target volume of the first composite phase for the current iteration can be defined as

$$(V^{mac})^{iter} = \max\left\{V_1^{mac}, (1-c_{\text{er}})V^{(iter-1)}\right\}, \tag{4.26}$$

where c_{er} is the evolution rate which can be pre-decided by designers, and V_1^{mac} is the prescribed volume for the first composite phase.

For the micro models, the sensitivity numbers $\alpha_{ij}^{mic,1}$ and $\alpha_{ij}^{mic,2}$ are denoted as α_{ij}^{mic} in the following for convenience. Note that the sensitivity number α_{ij}^{mic} is defined in the whole domain of the RVE even though it is only used for interchanging base materials j and $j+1$. Consider n ordered base materials used in each micro model, there are $n-1$ ordered groups of materials and $n-1$ groups of sensitivity numbers to make adjustments between neighboring base materials. Taking $n=3$ as an example, the value of j can take vaule of 1 and 2 which means there are two groups of sensitivity numbers in each micro model named as α_{i1}^{mic} and α_{i2}^{mic}. The optimization procedure in micro design models starts from an initial design which is nearly full base material 1 but with small amounts of base material 2. The transitions of base materials 1 and 2 are performed according to the sensitivity number α_{i1}^{mic} and the target volume of base material 2 for the current iteration as

$$(V_2^{mic})^{iter} = \min\left\{V_{2*}^{mic}, (1+c_{\text{er}})(V_2^{mic})^{(iter-1)}\right\}, \tag{4.27}$$

where V_{2*}^{mic} denotes the prescribed volume of phase 2 in the micro models. From the Equation (4.27), it is seen that the volume fraction of phase 2 increases until the prescribed volume of phase 2 is satisfied. Then, the volume fraction of phase 2 remains unchanged and the volume fraction of phase 1 continues to decrese which means that the volume fraction of phase 3 begins to increase. As previously mentioned, the material interchange only occurs between two neighboring phases, i.e. the transition between phases 1 and 3 is interchanged through phase 2 firstly. The transition of phases 2 and 3 in the micro models is performed according to the sensitivity number $\alpha_{i2}^{mic,1}$ and the target volume of phase 3 for the current iteration. The target volume fraction

of phase 3 for the current iteration can be defined in the same way as phase 2 in Equation (4.27). Therefore, the volume fraction of phase 3 is monotonically increasing until the prescribed volume fraction of phase 3 is satisfied. The interchanging process is terminated when the volume constraints of all phases are satisfied. In addition, when the number of phases n is larger than 3, a similar procedure can be applied to make adjustment between phases [75].

To sum up, the optimization procedure iteratively conducts the FEA in the micro and macro models to update the material distribution in the RVEs and macrostructures until the volume constraints in both models are reached and the following convergence criterion is satisfied [76]:

$$\frac{|\sum_{q=1}^{Q}(f_{iter-q+1}-f_{iter-Q-q+1})|}{\sum_{q=1}^{Q} f_{iter-q+1}} \leq \tau. \tag{4.28}$$

where f denotes the objective function, Q is the integral number and τ is a specified small tolerance value.

4.3.3 Numerical implementation

Taking $n = 3$ as an example, the whole numerical implementation procedure for the concurrent topological design of composite macrostructures and the underlying multi-phase material microstructures in this work is outlined as follows. It is worth noting that when the number of phases n is larger than 3, a similar procedure can be applied to make adjustment between material phases in the micro models.

1. Define design parameters such as materials properties of the phases, prescribed volume of stiffer phase at macro scale V_1^{mac}, prescribed volumes of base materials $V_{j*}^{mic,1}$ and $V_{j*}^{mic,2}$ $(j = 1, 2, 3)$ at micro scale, the filter radii r_{min}^{mac} and r_{min}^{mic} at two scales. Construct initial designs of the macrostructure and of the multi-phase material RVE, respectively.

2. Carry out the numerical homogenization on material RVEs and calculate the effective elasticity matrices $\bar{\mathbf{C}}^{H,1}$ and $\bar{\mathbf{C}}^{H,2}$ based on Equations (4.12) and (4.13), respectively.

3. Substitute the obtained homogenized materials properties into the macroscopic FEA model. Solve the FE equilibrium equation in Equation (4.3) to obtain the objective function f.

4. Computer the sensitivities of the objective function with respect to the macro and micro design variables, i.e. α_m^{mac} by using (4.14) and $\alpha_{i1}^{mic,1}$ and $\alpha_{i1}^{mic,2}$ by using

Equations (4.17) and (4.18), respectively. Calculate sensitivity number α_{i2}^{mic} if the target volume fraction of phase 2 at micro scale is satisfied.

5. Process all calculated sensitivity numbers in both macro and micro models with filtering and history-averaging as formulated in Section 4.3.1.

6. Update design variables according to the elemental sensitivities and target volumes for the current iteration in each model. If all volume constraints of composite phases at macro scale and of constitutive materials at micro scale are satisfied as well as the convergence criterion as shown in Equation (4.28) is met, output results and stop. If not, go to Step 2.

4.4 Concurrent optimization for structural stiffness

In this section, several 2D and 3D numerical examples are presented to demonstrate the validity of the proposed framework for concurrent topology optimization of composite macrostructures and their multi-phase materials. The RVEs are discretized into 100×100 four-node quadrilateral (Q4) elements for the 2D cases and $30 \times 30 \times 30$ brick elements for the 3D cases. The filter radii for the micro models r_{min}^{mic} are set to 7 and 2 in 2D and 3D examples, respectively. The elements in 2D and 3D macrostructures are assigned with the dimensions 1×1 mm^2 and $1 \times 1 \times 1$ mm^3, respectively. The filter radii in 2D and 3D macro models are set to 6 and 3, respectively. All base materials used in two micro models have the same Poisson's ratio as $\nu = 0.3$.

4.4.1 Design of a 2D cantilever beam

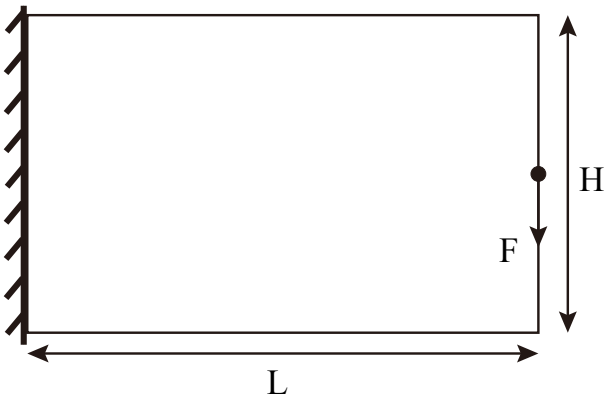

FIGURE 4.2: Geometrical dimension and boundary conditions for a 2D cantilever beam.

In the first example, we design a 2D cantilever beam and the underlying multi-phase material microstructures comcurrently. The dimension of the macrostructural

cantilever beam is $L \times H = 100 \times 60$ mm^2 as shown in Figure 4.2. Assuming three-phase material design is addressed in both two micro models, thus there are totally six phases taking part in the concurrent design process. The Young's moduli of three material phases in the micro model 1 are $E_1^1 = 100$ MPa, $E_2^1 = 10$ MPa and $E_3^1 = 1$ MPa, and the Young's moduli in micro model 2 are $E_1^2 = 0.1$ MPa, $E_2^2 = 0.01$ MPa and $E_3^2 = 0.001$ MPa, respectively. These materials are named as the first group of phases in the following. The prescribed volume constraints of phases 1, 2 and 3 in each micro model are all set to be one-third of the design domain. The target volumes of each phase in the macro model are also set to 50%. It is noted that with the presented concurrent design optimization model, any volume fraction of each constituent material/composite in the micro and macro models can be choosed by the designers.

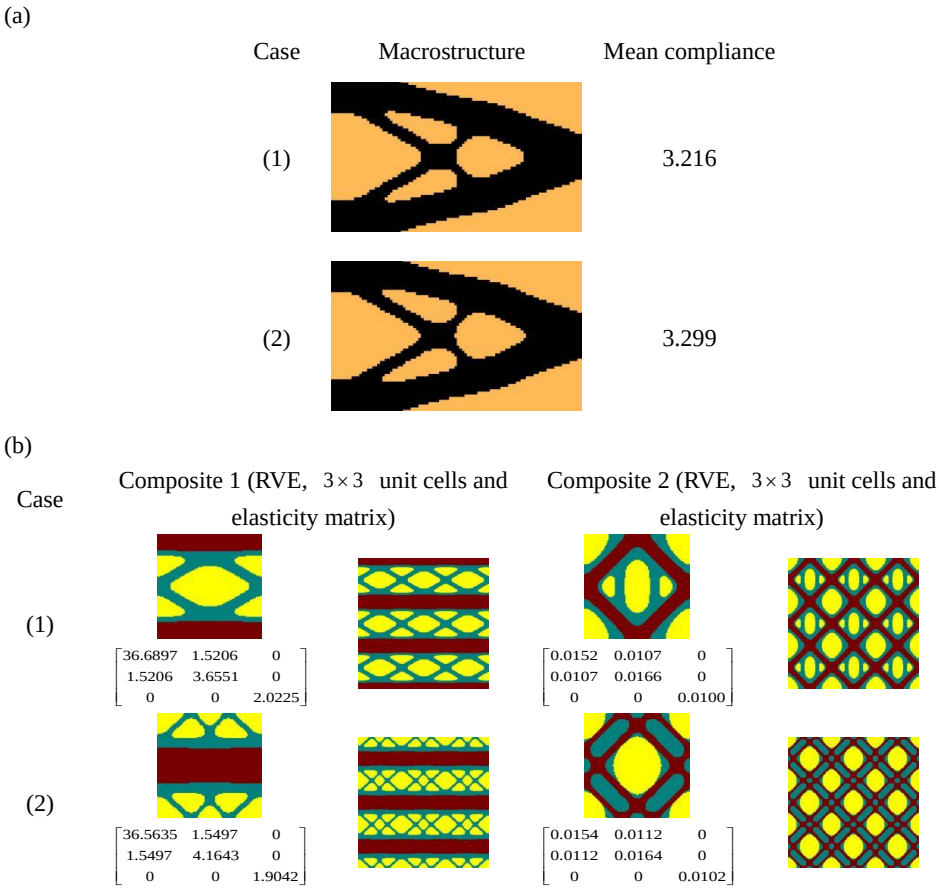

FIGURE 4.3: Summary of two concurrent designs of the 2D cantilever beam considering two different initial configurations: (a) macrostructures and compliances; and (b) microstructures and elasticity matrices.

Before performing the concurrent topological design, two initial guess designs are considered: initial design 1 is full of first constitutive material/composite except for

four center elements for second constitutive material/composite, as illustrated in Figure 3.1 (a); initial design 2 shows the design domain is full of first constitutive material/composite except for four corner elements for second constitutive material/composite as shown in Figure 3.1 (b). Figure 4.3 shows a summary of two final designs of the 2D cantilever beam and material microstructures by considering two different initial designs. The two cases in Figure 4.3 are: (1) the initial design 1 is adopted for both macrostructure and microscopic RVEs before the optimization procedure; (2) the initial design 2 is adopted for both models. Optimal designs of two-phase macrostructures with the resulted structural compliance f are shown in Figure 4.3 (a), where first phase (composite 1) is shown in black and second phase (composite 2) in light yellow. The optimal designs of two kinds of three-phase composite microstructures together with the homogenized elasticity matrices are given in Figure 4.3 (b), where phase 1 is shown in red, phase 2 in green and phase 3 in yellow.

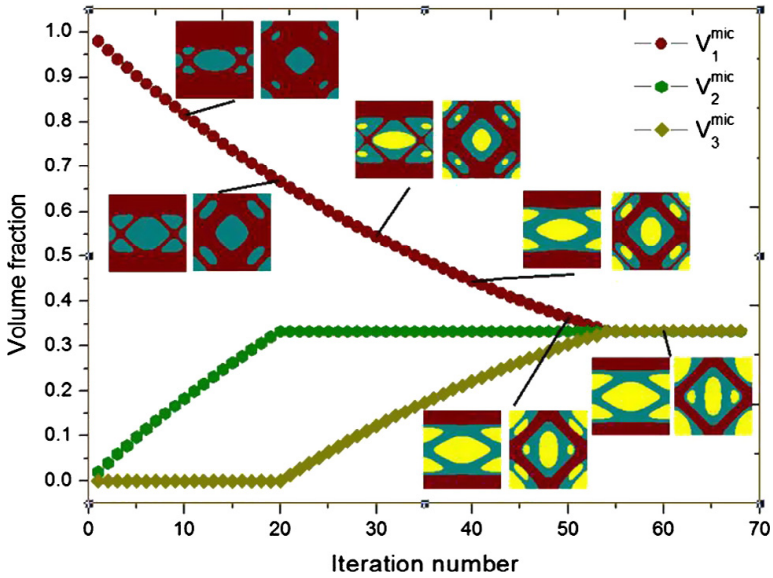

FIGURE 4.4: Iteration processes of microstructural topology and volume fractions.

We can see from the Figure 4.3 that the optimal design of the macrostructure is independent on initial configurations, while they affect the final distribution of the consitutive materials in the RVEs. Even so, the homogenized elasticity matrices of two composites in case (1) are similar with the corresponding terms in the case (2). This result is consistent with the common knowledge of the inverse homogenization design that different microstructures can possess the same physical properties [144], as also can been observed in Chapter 3.1.3. In addition, the final structural compliances in the two cases are approximately equal to each other. The iteration processes of RVEs and volume fractions of phases in case (1) are illustrated in Figure 4.4. It is seen that at the

earlier stage of the whole optimization procedure, the volume fraction of phase 3 goes to zero until the volume constraint of phase 2 is satisfied. Then, the volume fraction of phase 2 remains constant and the volume fraction of phase 3 increases. Finally, all volume fractions of different phases converge to the same final value equal to one-third.

4.4.2 Design of a 2D MBB beam

In this second example, we study the design a 2D Messerschmitt-Bölkow-Blohm (MBB) beam and its multi-phase material microstructures concurrently. As shown in Figure 4.5, the geometrical dimensions of the MBB beam are $L \times H = 200 \times 50$ mm. Firstly, we solve the concurrent design problem with three-phase materials in the micro models, and the Young's moduli of all phase materials are exactly the same as in the first example in Section 4.4.1. In addition, the volume constraints in both micro and macro models are also the same as in the first example. To start the concurrent optimization procedure, initial design 1 as formulated in Section 4.4.1 (see also in Figure 3.1) is adopted for both micro models, and the macrostructure is fill with first phase. The summary of optimization results for both macroscopic structures and micro RVEs is illustrated in Figure 4.6. It is seen that the optimal RVEs and microstructures in this case are all anisotropic, comparing with the optimal results in the first example where the final microstructures are orthotropic. It illustrates that the macrostructural responses or boundary conditions affect the optimal result of the material microstructures. In this case, the whole concurrent design procedure converges after 69 iterations.

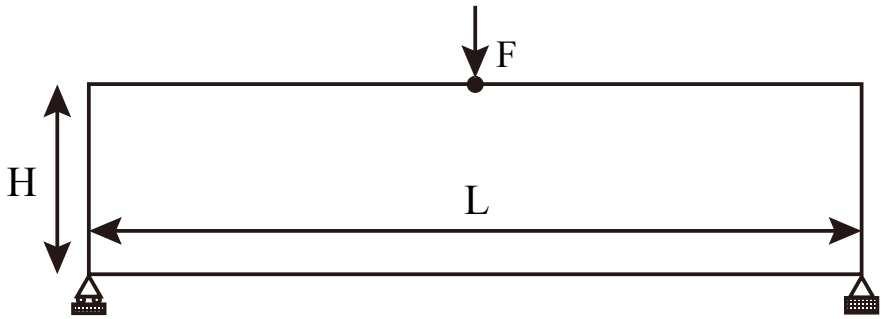

FIGURE 4.5: Geometrical dimension and boundary conditions for a 2D MBB beam.

In order to investigate the effect of inhomogeneity degree of the adopted consititutive materials, a second group of phase materials with different elastic contrast is considered here. In this group, Young's moduli of three phases in micro model 1 are $E_1^1 = 4$ MPa, $E_2^1 = 2$ MPa and $E_3^1 = 1$ MPa, Young's moduli in micro model 2 are $E_1^2 = 0.5$ MPa, $E_2^2 = 0.25$ MPa, $E_3^2 = 0.125$ MPa, respectively. The volume constraints in the micro and macro models are set the same as before. The summary of optimal

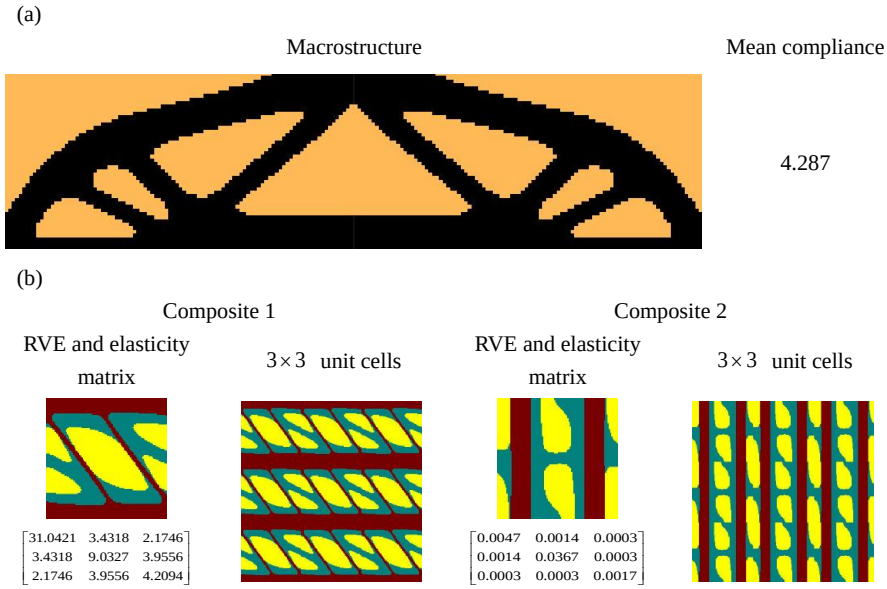

FIGURE 4.6: Summary of final designs for the 2D MBB beam with first group of base materials: (a) macrostructure and compliance and (b) microstructures and elasticity matrices.

results for both three-phase RVEs and the concurrently changed MBB beam are shown in Figure 4.7. It is seen that the distribution of constitutive materials in the RVEs and of the resulting composites in the macrostructures are totally different as compared with those in Figure 4.6. This results are reasonable since the load-bearing abilities of all phase materials are changed, resulting in different optimal distributions of constitutive materials or phases. In this case, the whole concurrent design optimization procedure is converged after 64 iterations.

To further illustrate the proposed concurrent design framework, two composite phases in the macrostructure composed of four constitutive materials are considered here. The Young's moduli of four phase materials in the micro model 1 are $E_1^1 = 16$ MPa, $E_2^1 = 8$ MPa, $E_3^1 = 4$ MPa. and $E_4^1 = 2$ MPa, Young's moduli in the micro model 2 are $E_1^2 = 1$ MPa, $E_2^2 = 0.5$ MPa, $E_3^2 = 0.25$ MPa. and $E_4^2 = 0.125$ MPa, respectively. Therefore, there are in total eight material phases taking part in the concurrent design process in this case. In the micro models, each material phase is distributed with the same volume fraction, i.e. volume fractions of four phases are all specified as 25%. The volume usages for the first and second composite phases in the macro model are also set to equal to each other as 50%. After 80 iterations, the final designs in this case are shown in Figure 4.8. The optimal design of the macrostructure is shown in Figure 4.8 (a), where the second phase of macrostructure is shown in light blue. In Figure 4.8 (b), the phases 1, 2, 3 and 4 in each micro model are respectively shown in dark blue (darkest region), light blue, yellow and red. The two kinds of four-phase composites are both

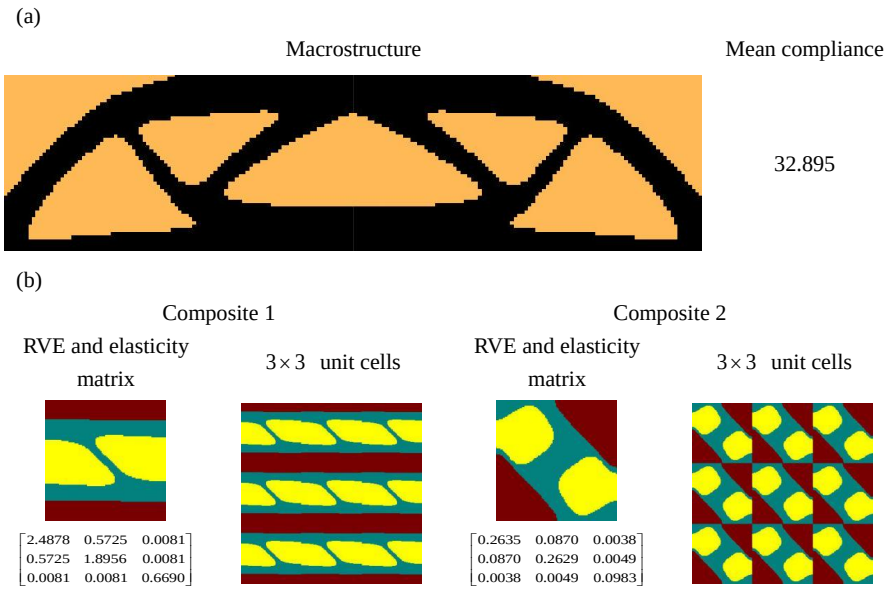

FIGURE 4.7: Summary of final designs for the 2D MBB beam with second group of base materials: (a) macrostructure and compliance; and (b) microstructures and elasticity matrices.

anisotropic as can be observed from their effective elasticity matrices. Comparing with the final results in the last example, the distribution of two composite phases in the macrostrucure is similar, and the stiffer constitutive materials in the first micro model are also distributed in horizontal direction to resist the concentrated load.

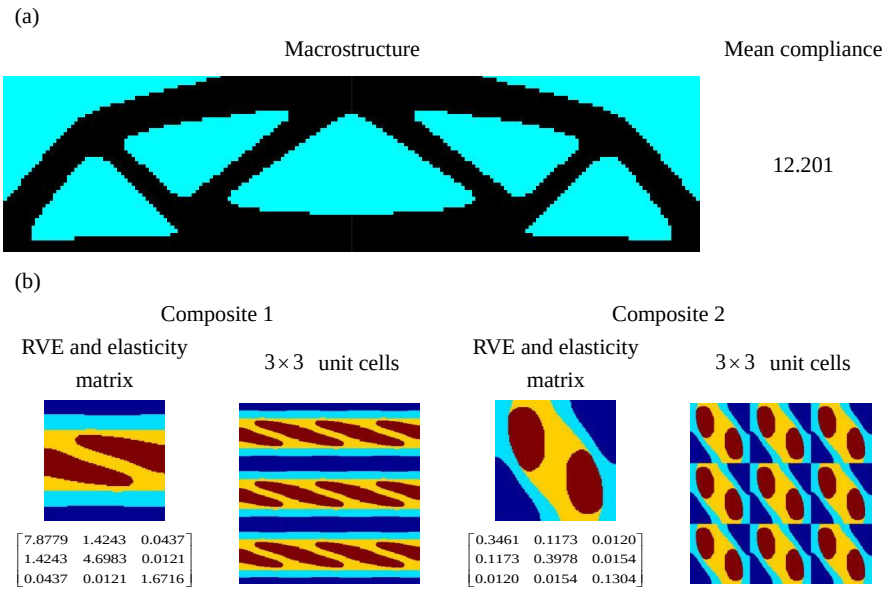

FIGURE 4.8: Summary of final designs for the 2D MBB beam with eight phases: (a) macrostructure and compliance; and (b) microstructures and elasticity matrices.

4.4.3 Design of a 3D cantilever beam

In this example, we study the design of a 3D cantilever beam and its underlying multi-phase materials. The design dimensions of the macrostructure are $L \times H \times W = 60 \times 20 \times 4$ as shown in Figure 4.9. The left side of the macrostructure is fixed, and a unit concentrated load is applied at the middle point of right bottom edge. The first group of phases given in the first example (see Section 4.4.1) is employed, and the volume fractions of phases 1, 2 and 3 are respectively prescribed as 50%, 30% and 20% in each micro model. In the macro model, volume fraction of the first composite phase in the macrostructure is set to be 50%. To start the concurrent optimization procedure, an initial design which is fully composed of first constitutive material/composite except for eight center elements for second constitutive material/composite is adopted both for macro and micro models. The optimal design of the macrostructure is given in Figure 4.10, where the first and second phases of the macrostructure are shown in green and blue, respectively. Note that the geometry of the first composite phase shown in Figure 4.10 (b) is similar with the result obtained from traditional topological design of the same cantilever beam [98]. The final structural compliance is $f = 0.144$ mm^2/N. Optimal designs of three-phase composites 1 and 2 together with the corresponding homogenized elasticity matrices are given in Figures 4.11 and 4.12 respectively, where the phases 1, 2 and 3 are respectively shown in red, blue and green. As can be observed, the stiffest phase materials are mainly distributed in x- and y- directions to resist the concentrated load, and laminated plate structures are generated. Finally, the whole concurrent design process for the 3D cantilever beam is convergent after only 44 iterations.

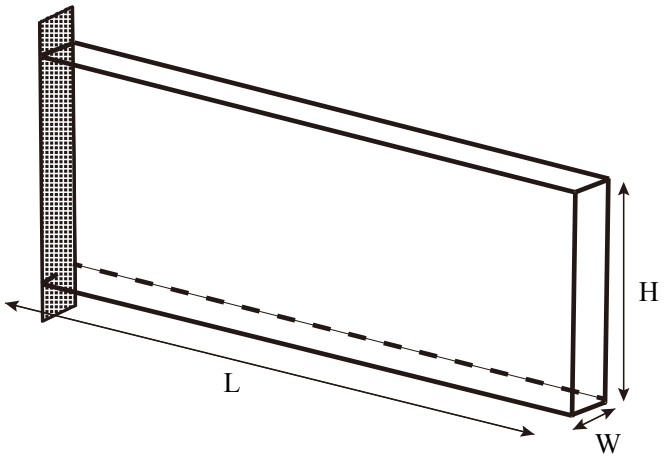

FIGURE 4.9: Geometrical dimension and boundary conditions for a 3D cantilever beam.

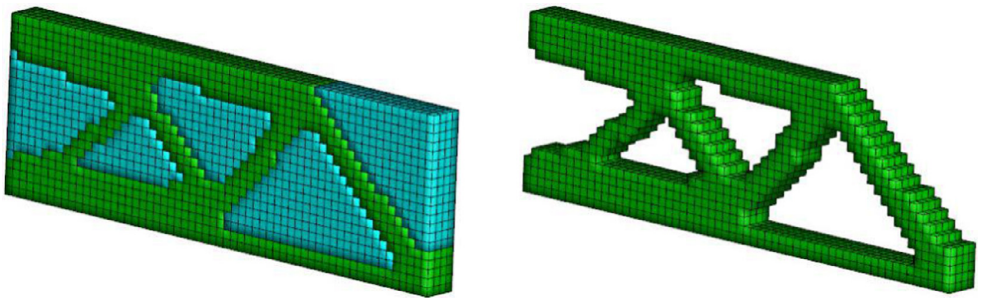

(a) Macrostructure (b) Macrostructure (first phase only)

FIGURE 4.10: Optimal design of macrostructure for the 3D cantilever beam.

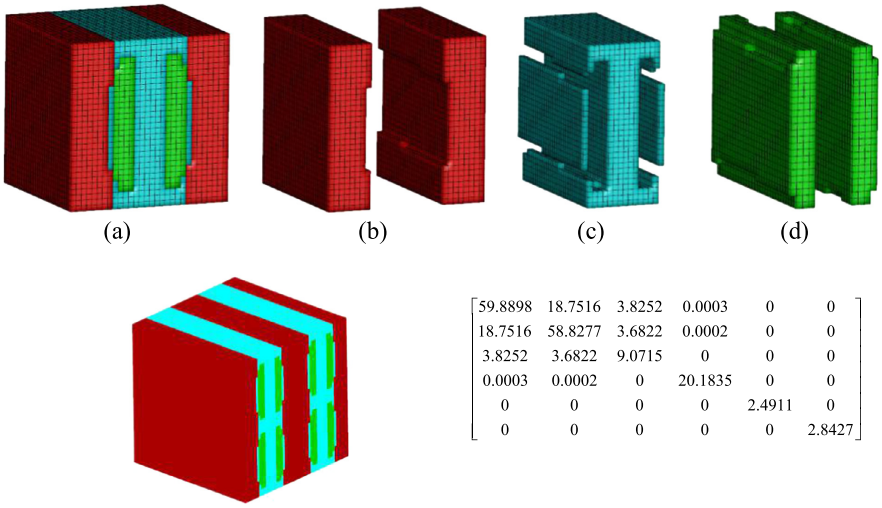

FIGURE 4.11: Optimized material microstructures of composite 1 for the 3D cantilever beam: (a) micro RVE (b) phase 1 only; (c) phase 2 only; (d) phase 3 only; (e) $2 \times 2 \times 2$ unit cells; and (f) homogenization elasticity matrix.

4.4.4 Design of a 3D MBB beam

In this example, the concurrent design of a 3D MBB beam and its multi-material microstructures subject to multiple external forces is given. The dimensions of the macrostructure are $L \times H \times W = 80 \times 20 \times 12$ mm shown in Figure 4.13. Here, there are four unit concentrated forces loaded at the top face of the considered macrostructure. The first group of phases formulated in the Section 4.4.1 are still considered here, and the material volume fractions of phases 1, 2 and 3 in each micro model are restricted to 30%, 40% and 30%, respectively. Volume constraint of the first phase in the macro model is set to 30%. To start the concurrent optimization procedure, the same initial design in

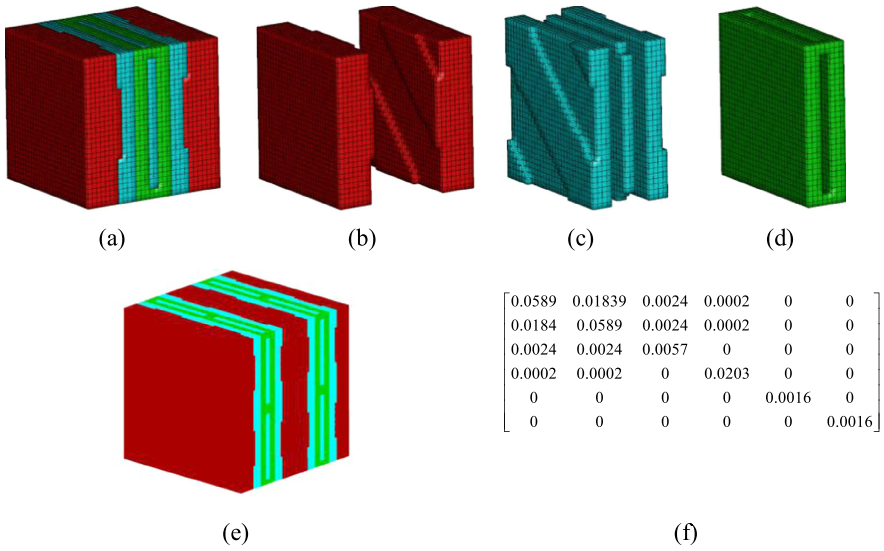

FIGURE 4.12: Optimized material microstructures of composite 2 for the 3D cantilever beam; (a) micro RVE (b) phase 1 only; (c) phase 2 only; (d) phase 3 only; (e) $2 \times 2 \times 2$ unit cells; and (f) homogenization elasticity matrix.

the last example is adopted for the macrostructure and material RVEs. After 71 iterations, all phases target volumes are well satisfied and the macrostructural compliance converges to $f = 1.653$ mm^2/N. The optimal design of the macrostructure is given in Figure 4.14 (a), and the generated geometry of the first phase in the macrostructure shown in Figure 4.14 (b) is comparable with the final result from mono-scale design of the same structure [98]. The optimal distribution of adopted constitutive materials in composites 1 and 2 are illustrated in Figures 4.15 and 4.16, respectively. It is seen that the material distribution in composites 1 and 2 are totally different, and distinctive interfaces between different constitutive materials in both macrroscopic structure and micro RVEs emerged.

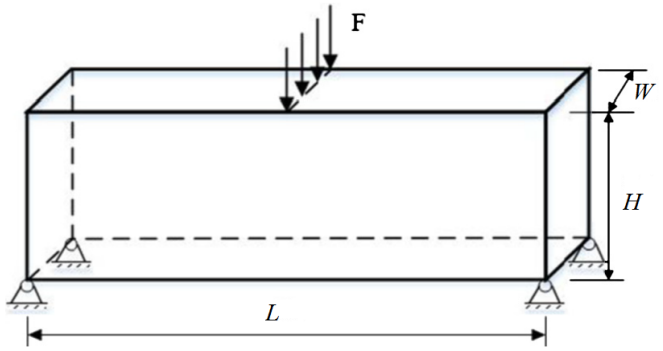

FIGURE 4.13: Geometrical dimension and boundary conditions for a 3D MBB beam.

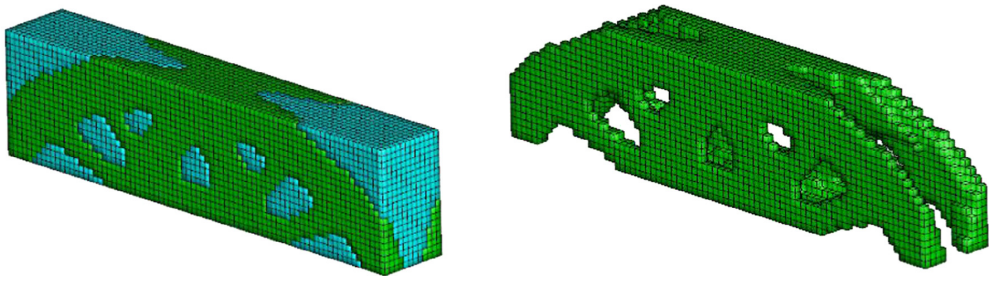

(a) Macrostructure (b) Macrostructure (first phase only)

FIGURE 4.14: Optimal design of macrostructure for the 3D MBB beam..

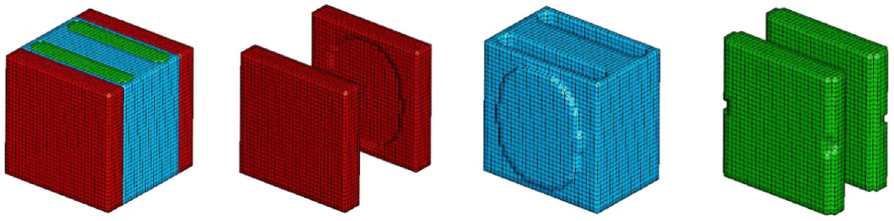

(a) (b) (c) (d)

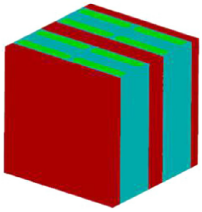

$$\begin{bmatrix} 37.7269 & 11.8732 & 2.0351 & 0 & 0 & 0 \\ 11.8732 & 38.1514 & 2.1297 & 0 & 0 & 0 \\ 2.0351 & 2.1297 & 5.0720 & 0 & 0 & 0 \\ 0 & 0 & 0 & 12.9231 & 0 & 0 \\ 0 & 0 & 0 & 0 & 1.5533 & 0 \\ 0 & 0 & 0 & 0 & 0 & 1.3470 \end{bmatrix}$$

(e) (f)

FIGURE 4.15: Optimized material microstructures of composite 1 for the 3D MBB beam; (a) micro RVE (b) phase 1 only; (c) phase 2 only; (d) phase 3 only; (e) $2 \times 2 \times 2$ unit cells; and (f) homogenization elasticity matrix.

4.5 Concluding remarks

In this Chapter, we have extended the topology optimization to concurrent design of composite structures and the underlying multi-phase material microstructures. Configurations of the composite macrostructures and of the material RVEs are optimized concurrently such that the resulting macrostructure has the minimum compliance. Several 2D and 3D numerical examples have shown that the presented concurrent design framework can provide efficient composite macrostructures with underlying three or more phases material microstructures in terms of stiffness. The generated interfaces between different constitutive materials/composites are clear and distinctive which potentially facilitates the manufacturing requirements. The present framework has also shown high stability during the design procedure and requires a small number of iterations for convergence. It is also worth mentioning that the presented concurrent optimization model can be extended to the topological design of composite structures

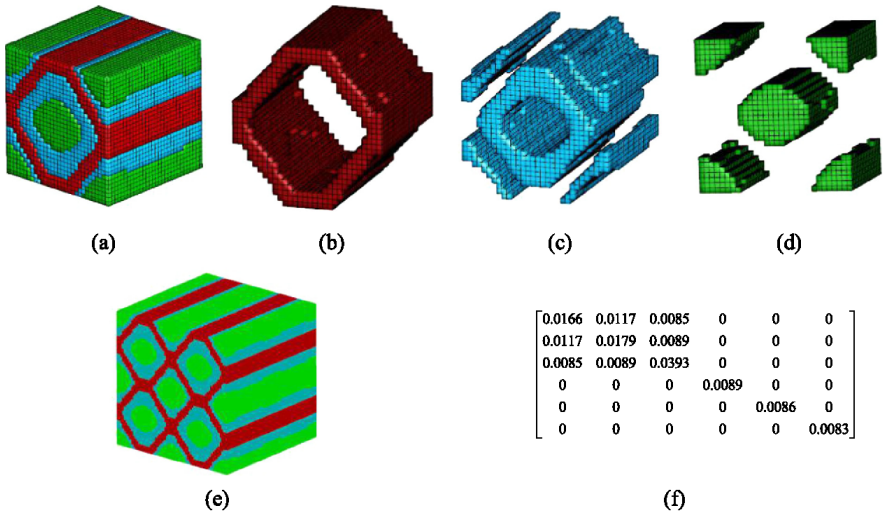

FIGURE 4.16: Optimized material microstructures of composite 2 for the 3D MBB beam; (a) micro RVE; (b) phase 1 only; (c) phase 2 only; (d) phase 3 only; (e) $2 \times 2 \times 2$ unit cells; and (f) homogenization elasticity matrix.

and the underlying multi-functional materials, which are normally composed of multi-phase materials, for different objectives or multi-objective functions. In the next Chapter, rather than assuming that the macroscopic and microscopic scales are separated, the topology optimization will be extended to multiscale design of materials and structures without scale separations.

Chapter 5

Multiscale topology optimization in the context of non-separated scales

In topology optimization applied to material or multiscale design modeling, the homogenization method is often adopted to link the microscopic and macroscopic scales. However, the assumption of scale separation is often assumed in the classical homogenization theory. This assumption states that the characteristic length of the microstructural details are much smaller than the dimensions of the structure, or that the characteristic wavelength of the applied load is much larger than that of the local fluctuation of mechanical fields [58]. In additive manufacturing of architecture materials like lattice structures, the manufacturing process might induce limitations on the size of local details, which can lead to a violation of scale separation when the characteristic size of the periodic unit cells within the lattice are not much smaller than that of the structure. In such case, classical homogenization methods may lead to inaccurate description of the effective behavior as non local effects, or strain-gradient effects, may occur within the structure. On the other hand, using a fully detailed description of the lattice structure in an optimization framework could be computationally very costly.

In Section 5.1 we first develop a multiscale topology optimization procedure for periodic structures based on the classical homogenization theory in the context of non-separated scales. The dimensions of the unit cell range from large to small as compared with the dimensions of the whole structure to highlight the size effect.

In Section 5.2, the objective is to develop a new multiscale topology optimization procedure, by using a nonlocal filter-based homogenization scheme, for heterogeneous materials such as lattice materials in the context of non-separated scales. The adopted nonlocal homogenization method takes into account the strain gradient effects combined with a topological optimization scheme of unit cells, in contrast with the optimization scheme based on the classical homogenization in Section 5.1.

In Section 5.3, we present the topological optimization of mesostructures with predefined or optimally designed microscopic unit cells without scale separation. The consistent nonlocal filter-based homogenization method introduced in Section 5.2 is

adopted to take into account the heterogeneities within RVEs and to link the two different scales. The microscopic RVE itself, rather than particular isotropic materials within the finite element in the RVE, is considered as the design variable in the proposed optimization model. A simple stiffness interpolation scheme is introduced to simplify the sensitivity analysis of objective function with respect to the defined design variable.

5.1 Size effect analysis in topology optimization for periodic structures using the classical homogenization

In this section, the size effect in classical homogenization-based topology optimization for periodic structures is investigated, with the size of the periodic cell ranging from large to small as compared with the characteristic length of the whole structure. More specifically, a relocalization scheme is proposed based on the homogenization method to link the two scale fields, allowing performing the topological optimization problem on a coarse mesh. A corresponding reference solution is obtained by fully meshing the heterogeneities in the whole structure. In the following, the classical homogenization technique is reviewed in Section 5.1.1. Details of numerical computation of effective material properties as well as the relocalization scheme are provided. Presented topological optimization model and procedure are given in Section 5.1.2. Numerical experiments are conducted in Section 5.3.2 to fully investigate the size effect of the periodic unit cells.

5.1.1 The classical homogenization method

In this section, the computation of effective or homogenized material properties of heterogeneous composite in the context of linear elasticity is reviewed. The local problem at microscopic scale with different types of boundary conditions is firstly introduced, followed by the numerical implementation to evaluate the effective elastic matrix by means of the classical finite element method (FEM).

5.1.1.1 Localization problem

A heterogeneous structure composed of two-phase composite is considered here as described in Figure 5.1 (a). The RVE shown in Figure 5.1 (b) is associated with a domain Ω and boundary $\partial\Omega$. The objective is to define the effective or homogenized elastic tensor $\bar{\mathbb{C}}^H$. The constitutive material phases are assumed isotropic with constant elastic properties, and the interfaces between the different constitutive phases are assumed to be perfect. Therefore, the local problem assuming that the RVE is subject to homogeneous strains is formulated as follows. Applying a constant macroscopic strain $\bar{\varepsilon}$, find the

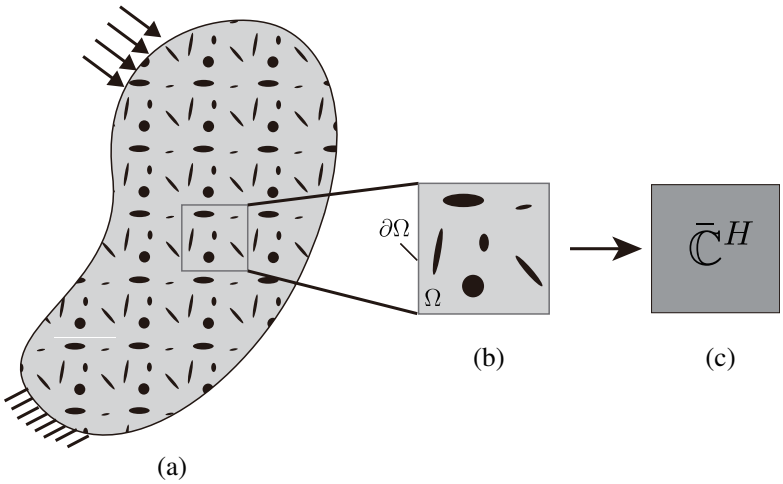

FIGURE 5.1: Illustration of a heterogeneous structure composed of perioidc unit cells: (a) heterogeneous structure; (b) RVE; (c) homogenized material.

displacement field $\boldsymbol{\mu}(\boldsymbol{x})$ in Ω satisfying:

$$\nabla \cdot (\boldsymbol{\sigma}(\boldsymbol{x})) = 0 \quad \text{in } \Omega \tag{5.1}$$

and

$$\boldsymbol{\sigma}(\boldsymbol{x}) = \mathbb{C}(\boldsymbol{x}) : \boldsymbol{\varepsilon}(\boldsymbol{x}) \tag{5.2}$$

with

$$\langle \boldsymbol{\varepsilon} \rangle = \bar{\boldsymbol{\varepsilon}} \quad \text{in } \Omega \tag{5.3}$$

where $\mathbb{C}(\boldsymbol{x})$ is the constant fourth-order elasticity tensor associated with different phases, $\nabla \cdot (\cdot)$ denotes the divergence operator, and $\langle \cdot \rangle$ denotes the space averaging over Ω. Following [184], the split of local strain field into a constant macroscopic strain field $\bar{\boldsymbol{\varepsilon}}$ and a remaing local fluctuation $\tilde{\boldsymbol{\varepsilon}}$ is assumed:

$$\boldsymbol{\varepsilon}(\boldsymbol{x}) = \bar{\boldsymbol{\varepsilon}}(\boldsymbol{x}) + \tilde{\boldsymbol{\varepsilon}}(\boldsymbol{x}) \tag{5.4}$$

Taking average of the above equation, we have

$$\langle \boldsymbol{\varepsilon}(\boldsymbol{x}) \rangle = \bar{\boldsymbol{\varepsilon}} + \langle \tilde{\boldsymbol{\varepsilon}}(\boldsymbol{x}) \rangle = \bar{\boldsymbol{\varepsilon}} + \frac{1}{|\Omega|} \int_{\Omega} \tilde{\boldsymbol{\varepsilon}}(\boldsymbol{x}) d\Omega = \bar{\boldsymbol{\varepsilon}} + \frac{1}{2|\Omega|} \int_{\Omega} \{\nabla(\tilde{\boldsymbol{u}}(x)) + \nabla^T(\tilde{\boldsymbol{u}}(x))\} d\Omega \tag{5.5}$$

where $\tilde{\boldsymbol{u}}$ is the unknown fluctuation displacement as $\tilde{\boldsymbol{u}} = \boldsymbol{u}(\boldsymbol{x}) - \bar{\boldsymbol{\varepsilon}}\boldsymbol{x}$. Using the divergence theorem, we have

$$\langle \boldsymbol{\varepsilon}(\boldsymbol{x}) \rangle - \bar{\boldsymbol{\varepsilon}} = \frac{1}{2|\Omega|} \int_{\partial\Omega} \{\tilde{\boldsymbol{u}}(x) \otimes \mathbf{n} + \mathbf{n} \otimes (\tilde{\boldsymbol{u}}(x)\} d\Gamma \tag{5.6}$$

Note that the condition (5.3) can be satisfied by solving the present local problem Equations (5.1)-(5.2) with appropriate boundary conditions. In other words, the right-hand side of Equation (5.6) should be equal to zero. It can be verified with the following two possible conditions:

$$\tilde{\boldsymbol{u}}(\boldsymbol{x}) = 0 \ \text{ on } \partial\Omega \quad \text{or} \quad \tilde{\boldsymbol{u}}(\boldsymbol{x}) \ \text{ is periodic on } \partial\Omega \tag{5.7}$$

Following [184], the corresponding two types of boundary conditions can be obtained by integrating Equation (5.4) with repect to $\boldsymbol{x}$. The first is called Kinematically Uniform Boundary Conditions (KUBC) and is expressed as

$$\boldsymbol{u}(\boldsymbol{x}) = \bar{\boldsymbol{\varepsilon}}\boldsymbol{x}, \forall \boldsymbol{x} \in \partial\Omega \tag{5.8}$$

where the displacement is imposed directly at boundary points. In the second type of boundary conditions which is named Periodic Boundary Condition (PER), the displacement field over the boundary $\partial\Omega$ takes the form

$$\boldsymbol{u}(\boldsymbol{x}) = \bar{\boldsymbol{\varepsilon}}\boldsymbol{x} + \tilde{\boldsymbol{u}}, \forall \boldsymbol{x} \in \partial\Omega \tag{5.9}$$

where the fluctuation term $\tilde{\boldsymbol{u}}(\boldsymbol{x})$ is periodic on $\partial\Omega$, i.e. it takes the same values on two points of opposite faces over $\partial\Omega$. It should be mentioned that an alternative localization problem assuming that the RVE is subjected to a constant stress field can also be used to predict the effective material properties. For detailed information about stress averaging theorem as well as the corresponding boundary conditions one can refer to [184]. In this work, the second type of boundary conditions is adopted to solve the present localization problem. It is also worth noting that even though only two-phase RVE are considered here, the procedure can be straightforwardly extended to an arbitrary number of phases.

5.1.1.2 Definition and computation of the effective material properties

With the superposition principle, the solution of the local problem in Equations (5.1)-(5.2) can be viewed as a linear combination of 3 independent components of the strain tensor in 2D:

$$\boldsymbol{u}(\boldsymbol{x}) = \boldsymbol{u}^{(11)}(\boldsymbol{x})\bar{\varepsilon}_{11} + \boldsymbol{u}^{(22)}(\boldsymbol{x})\bar{\varepsilon}_{22} + 2\boldsymbol{u}^{(12)}(\boldsymbol{x})\bar{\varepsilon}_{12} \tag{5.10}$$

where $\boldsymbol{u}^{(ij)}(\boldsymbol{x})$ is the displacement field obtained by solving the local problem (Equations (5.1)-(5.2)) together with the PER (Equation (5.9)) using

$$\bar{\boldsymbol{\varepsilon}} = \frac{1}{2}(e_i \otimes e_j + e_j \otimes e_i) \tag{5.11}$$

where e_i $(i = 1, 2)$ are unitary basis vectors. To be specific, $\boldsymbol{u}^{(11)}$, $\boldsymbol{u}^{(22)}$ and $\boldsymbol{u}^{(12)}$ are respectively obtained by solving the local problem with

$$\bar{\varepsilon} = \begin{bmatrix} 1 & 0 \\ 0 & 0 \end{bmatrix}, \quad \bar{\varepsilon} = \begin{bmatrix} 0 & 0 \\ 0 & 1 \end{bmatrix}, \quad \bar{\varepsilon} = \begin{bmatrix} 0 & 1/2 \\ 1/2 & 0 \end{bmatrix} \tag{5.12}$$

Setting $\boldsymbol{\varepsilon}^{(ij)}(\boldsymbol{x}) = \varepsilon(\boldsymbol{u}^{(ij)}(\boldsymbol{x}))$, we have:

$$\varepsilon(\boldsymbol{x}) = \boldsymbol{\varepsilon}^{(11)}(\boldsymbol{x})\bar{\varepsilon}_{11} + \boldsymbol{\varepsilon}^{(22)}(\boldsymbol{x})\bar{\varepsilon}_{22} + 2\boldsymbol{\varepsilon}^{(12)}(\boldsymbol{x})\bar{\varepsilon}_{12} \tag{5.13}$$

This expression can be re-written in a compact form as

$$\boldsymbol{\varepsilon}(\boldsymbol{x}) = \mathbb{A}(\boldsymbol{x}) : \bar{\boldsymbol{\varepsilon}}, \quad \forall \boldsymbol{x} \in \Omega \tag{5.14}$$

where $\mathbb{A}(\boldsymbol{x})$ is the fourth-order localization tensor relating microscopic and macroscopic strains with

$$A_{ijkl}(\boldsymbol{x}) = \varepsilon_{ij}^{(kl)}(\boldsymbol{x}) \tag{5.15}$$

Using the classical Hooke's law, we have

$$\sigma_{pq}(\boldsymbol{x}) = C_{pqij}(\boldsymbol{x})A_{ijkl}(\boldsymbol{x})\bar{\varepsilon}_{(kl)} \tag{5.16}$$

or

$$\boldsymbol{\sigma}(\boldsymbol{x}) = \mathbb{C}(\boldsymbol{x}) : \mathbb{A}_{ijkl}(\boldsymbol{x}) : \bar{\boldsymbol{\varepsilon}} \tag{5.17}$$

By taking the spatial average over Ω, the constitutive relationship at macroscopic scale can be formulated as:

$$\bar{\boldsymbol{\sigma}} = \bar{\mathbb{C}}^H : \bar{\boldsymbol{\varepsilon}} \tag{5.18}$$

with

$$\bar{\mathbb{C}}^H = \langle \mathbb{C}(\boldsymbol{x}) : \mathbb{A}(\boldsymbol{x}) \rangle \tag{5.19}$$

Using classical displacement-based FEM, a matrix $\boldsymbol{U}$ containing in each row the nodal displacement solution of the above 3 local problems in one element is defined. Therefore, the matrix form of the localization tensor $\mathbb{A}$ in Equation (5.14) or (5.15) can be written as

$$\boldsymbol{A}(\boldsymbol{x}) = \boldsymbol{B}(\boldsymbol{x})\boldsymbol{U} \tag{5.20}$$

where $\boldsymbol{B}$ is the strain matrix. The matrix form of the effective elasicity tensor $\bar{\mathbb{C}}^H$ in Equation (5.19) is then given by:

$$\bar{\boldsymbol{C}}^H = \frac{1}{V}\int_{\Omega} \boldsymbol{C}(\boldsymbol{x})\boldsymbol{B}(\boldsymbol{x})\boldsymbol{U}\, d\Omega \tag{5.21}$$

5.1.1.3 Numerical implementation for the local problem with PER

Following [184], a technique based on Lagrange multipliers to enforce the PER in 2D cases is presented here. From Equation 5.9, the displacement on the opposite faces of the RVE is expressed as

$$\begin{cases} u_i^{k+} = \bar{\varepsilon}_{ij} x_j^{k+} + \tilde{u}_i^* \\ u_i^{k-} = \bar{\varepsilon}_{ij} x_j^{k-} + \tilde{u}_i^* \end{cases} \tag{5.22}$$

where superscripts "$k+$" and "$k-$" denote nodes on the pair of opposite surfaces of the cell. $\tilde{u}_i^*$ is the periodic fluctuation field which can be eliminated by comparing the difference between the displacements:

$$u_i^{k+} - u_i^{k-} = \bar{\varepsilon}_{ij}(x_j^{k+} - x_j^{k-}) = R^{k+k-} \tag{5.23}$$

Therefore, in order to enforce the periodic boundary conditions using the Lagrange multipliers method, the constraint equations can be written as following :

$$\boldsymbol{P}\boldsymbol{u} - \boldsymbol{R} = 0 \tag{5.24}$$

The discrete form is written as

$$C_i^{k+k-} = P_{ij} u_j - R_i^{k+k-} = 0 \tag{5.25}$$

where $\boldsymbol{P}$ is a matrix relating the whole indices of coupled nodes on opposite faces of the RVE, which is completely filled with the numbers 1, 0 and -1. It is noted that there are two constraint equations for each pair of nodes on the boundaies in the case here. The constrained minimization problem then can be stated as

$$\inf_{\substack{\boldsymbol{u} \\ C_i=0,\ i=1,\ldots,n_c}} \frac{1}{2}\boldsymbol{u}^T \boldsymbol{K}\boldsymbol{u} \tag{5.26}$$

where $\boldsymbol{u}$ is the global vector of required displacement, and n_c is the number of constraint equations. Introducing the vector of Lagrange multipliers Λ associated with the adopted periodicity constraints, the above equation can be re-written as

$$\mathcal{L} = \frac{1}{2}\boldsymbol{u}^T \boldsymbol{K}\boldsymbol{u} + \Lambda \cdot (\boldsymbol{P}\boldsymbol{u} - \boldsymbol{R}) \tag{5.27}$$

The stationary of $\mathcal{L}$ is found by

$$\begin{cases} D_{\delta \boldsymbol{u}} \mathcal{L} = 0 \\ D_{\delta \Lambda} \mathcal{L} = 0 \end{cases} \tag{5.28}$$

Therefore, we have:

$$\begin{cases} \delta \boldsymbol{u}^T \boldsymbol{K} \boldsymbol{u} + \Lambda \cdot \boldsymbol{P} \delta \boldsymbol{u} = 0 \\ \delta \Lambda^T \boldsymbol{P} \boldsymbol{u} = \delta \Lambda^T \boldsymbol{R} \end{cases} \tag{5.29}$$

Since the arbitrariness of $\delta \boldsymbol{u}$ and $\delta \Lambda$, the following linear system can be obtained:

$$\begin{bmatrix} \boldsymbol{K} & \boldsymbol{P}^T \\ \boldsymbol{P} & 0 \end{bmatrix} \begin{bmatrix} \boldsymbol{u} \\ \Lambda \end{bmatrix} = \begin{bmatrix} 0 \\ \boldsymbol{R} \end{bmatrix} \tag{5.30}$$

where $\boldsymbol{K}$ is the global stiffness matrix after dicretizing the elastic problem (5.1) without enfocring the Dirichlet boundary conditions, and the vector $\boldsymbol{R}$ can be trivially obtained through Equation (5.23).

5.1.2 Topology optimization model and procedure

5.1.2.1 Optimization model and sensitivity number

In this work, the macroscopic structure is assumed to be composed of microscopic substructures/RVEs periodically. Effective material properties of the considered heterogeneous microstructures are calculated based on the above formulated homogenization method, even though the length scale of the microscopic RVE is comparable to the higher scale structures. The topology of the RVE is tailored by means of topology optimization such that the obtained structure has the optimal stiffness with certain amount of materials. The final goal is to inverstigate the size effect of the RVE when micro and macro scales are clearly non-separated. Therefore, this work aims to answer the following question: When the ratio between the size of the RVE and the size of the real macrostructure is used, the classical homogenization method can be used as an effective tool for multiscale topology optimization of periodic structures without scale separation. This topology optimization problem can be stated mathmatically as follows:

$$\text{Find} : \{\boldsymbol{\rho}^{(1)}, \ldots, \boldsymbol{\rho}^{(N_s)}\} \tag{5.31}$$

$$\text{Minimize} : f_c(\boldsymbol{\rho}, \bar{\mathbf{u}}) = \bar{\mathbf{F}}^T \bar{\mathbf{u}} \tag{5.32}$$

$$\text{Subject to} : \bar{\mathbf{K}} \bar{\mathbf{u}} = \bar{\mathbf{F}} \tag{5.33}$$

$$: V(\boldsymbol{\rho}) = \sum \rho_e^{(k)} v_e^{(k)} = V_{\text{req}}, \ k = 1, \ldots, N_s \tag{5.34}$$

$$: \rho_e^{(1)} = \cdots = \rho_e^{N_s}, \ e = 1, \ldots, N_e \tag{5.35}$$

$$: \rho_e^{(k)} = \rho_{min} \text{ or } 1, \ e = 1, \ldots, N_e, \ k = 1, \ldots, N_s \tag{5.36}$$

where f_c is the objective function of macrostructural compliance. $\bar{\mathbf{F}}$ and $\bar{\mathbf{u}}$ are the global load and displacement vectors, respectively. V_{req} is the required/prescribed volume of solid material in each RVE. N_{s} is the number of the periodic unit cells within the structure. Note that the constraint $\rho_e^{(1)} = \cdots = \rho_e^{N_{\text{s}}},\ e = 1, \ldots, N_e$ is prescibed to make sure the structure is composed of periodic microstructures with the existence of the RVE, which means that the pseudo densities of elements (ρ_{min} or 1 in Equation (5.36)) at the corresponding locations in each substructure are the same. N_e is the number of finite elements in each RVE.

During the process of evolutionary-type structural optimization, the elements are removed or added based on their sensitivity numbers. Therefore, the elements at the same locations in different substructures are removed or added simultaneously. However, the strain/stress distribution in different substructures/microscopic unit cells may not be the same in most cases. To enforce the periodic array of the microscopic unit cells, the element sensitivity numbers at the same location in each unit cell need to be consistent. They are then defined as the summation of the sensitivity of corresponding elements in all unit cells. In conventional evolutionary structural optimization method (see e.g. [37] and [76]), the element sensitivity number is defined as the change of the structural compliance or total strain energy since the removal of that element which is then equal to the elemental strain energy. Therefore, the elemental sensitivity number in this scheme can be expressed as the variation of the overall structural compliance due to the removal of $e-$th elements in all substructures:

$$\alpha_e^{cla} = \begin{cases} \sum_{k=1}^{N_s} \int_{\Omega_e^k} \boldsymbol{\sigma}^{cla}(\boldsymbol{x}) \boldsymbol{\varepsilon}^{cla}(\boldsymbol{x}) d\Omega_e^k, & \text{for } \rho_e^{(k)} = 1 \\ 0\,, & \text{for } \rho_e^{(k)} = \rho_{min}. \end{cases} \tag{5.37}$$

where $\boldsymbol{\sigma}^{cla}(\boldsymbol{x})$ and $\boldsymbol{\varepsilon}^{cla}(\boldsymbol{x})$ are the re-localized stress and strain fields based on the classical homogenization method. Details about computation of the re-localized stress and strain as well as the assembly of global stiffness matrix $\bar{\mathbf{K}}$ in (5.33) are formulated in the next section.

5.1.2.2 Finite element meshes and relocalization scheme

In order to assemble the stiffness matrix $\bar{\mathbf{K}}$ in Equation (5.33) at the macroscopic scale, the local problem (5.1)-(5.3) should be solved to obtain the effective material properties at the lower scale. In this scheme, a fine mesh is adopted at microscopic scale to account for all heterogeneous details within the RVE. However, coarse meshes are used to carry out the finite element analysis for macrostructure so as to save computational expense. Specific finite element meshes for both macroscopic and microscopic problems can be seen in the section of numerical examples. It is noted that the sensitivity number in

Equation (5.37) is formulated at the finest microscopic mesh, therefore, a relocalization process is required after solving the structural problem based on coarse meshes at the higher scale to obtain the sensitivities in (5.37).

With the calculated effective material properties $\bar{\boldsymbol{C}}^H$ of the RVE (see Section 5.1.1), the global stiffness matrix $\bar{\mathbf{K}}$ can be assembled in a standard finite element way as:

$$\bar{\mathbf{K}} = \sum_k \int_{\Omega^k} \boldsymbol{B}^T(\boldsymbol{x}) \bar{\boldsymbol{C}}^H \boldsymbol{B}(\boldsymbol{x}) d\Omega, \tag{5.38}$$

where $\boldsymbol{B}$ and $\bar{\boldsymbol{C}}^H$ are the strain matrix and the effective elastic matrix within the coarse mesh element at the macro scale, respectively. With the solution of the macroscopic problem based on the coarse mesh at hand, the microscopic strain and stress fields can be reconstructed by using the localization operator in each RVE as

$$\varepsilon^{cla}(\boldsymbol{x}) = \mathbb{A}(\boldsymbol{x}) : \bar{\varepsilon}(\bar{\mathbf{u}}(\boldsymbol{x})), \quad \forall \boldsymbol{x} \in \Omega \tag{5.39}$$

and

$$\boldsymbol{\sigma}^{cla}(\boldsymbol{x}) = \mathbb{C}(\boldsymbol{x}) : \mathbb{A}(\boldsymbol{x}) : \bar{\boldsymbol{\varepsilon}}(\bar{\mathbf{u}}(\boldsymbol{x})), \quad \forall \boldsymbol{x} \in \Omega \tag{5.40}$$

where the strain value $\bar{\varepsilon}(\bar{\mathbf{u}}(\boldsymbol{x}))$ is defined as $\bar{\varepsilon}(\bar{\mathbf{u}}(\boldsymbol{x})) = \frac{1}{2}(\nabla(\bar{\mathbf{u}}(\boldsymbol{x})) + \nabla^T(\bar{\mathbf{u}}(\boldsymbol{x})))$. The localization operator $\mathbb{A}$ has been obtained previously by solving the RVE problem (5.1)-(5.3) (see Section 5.1.1). Therefore, the sensitivity number formulated in (5.37) can be calculated to perform the topology optimization. We note that the sensitivity number can be naturally obtained by a reference solution when all heterogeneities are fully meshed. However, this could result in a huge amount of calculations, especially in topology optimization where the finite element analysis needs to be carried out in each iteration. In the section of examples, the optimized topologies of RVE as well as the resulted stiffness based on the presented method and on the reference solution will be compared to investigate the size effect of the RVE, with the size ranging from large to small as compared with the structure dimensions.

5.1.2.3 Optimization procedure

The BESO method starts from an initial guess of the design domain and tailors the topology according to the sensitivity numbers iteratively. In this work, the structural problem is solved on the coarse mesh to save the computational cost, and a relocalized scheme based on the classical homogenization is adopted to relocalize the microscopic fields so as to compute the sensitivity number from Equation (5.37). Overall optimization procedure of the multiscale topology optimization for periodic structures in the context of non-separated scales using the classical homogenization scheme is formulated as follows.

1. Set a coarse mesh associated with the structure, such that each substructure/unit cell is meshed with the same number of coarse elements. Set another fine mesh related to the microscopic scale to discretize the RVE microstructure.

2. Assign the pesudo densities $(\rho_{min}\ or\ 1)$ to fine mesh elements in the RVE to construct an initial design before optimization.

3. Perform the classical homogenization method on the RVE to obtain the localization tensor $\mathbb{A}$ and the effective elastic tensor $\bar{\mathbb{C}}^H$, as summarized in Section 5.1.1.

4. Solve the structure problem on the coarse mesh with the effective material property.

5. Based on the solution from the structure problem, relocalize the microscopic strain and stress fields by (5.39) and (5.40), respectively.

6. Compute the elemental sensitivity number using (5.37), and process the sensitivity number with filtering and history-averaging as Equations (3.12) and (3.14), respectively.

7. Remove inefficient materials from the RVE according to the modified sensitivity number to satisfy the volume constraint at the current iteration as Equation (3.15).

8. Repeat 3-7 until the material constraint V_{req} is satisfied and the convergence criterion as (3.16) is reached:

It is worth noting that the present homogenization method allows starting the optimization process from a homogeneous design with $\rho_e = 1, \forall e$, since the microscale fields are relocalized at the nodes of the coarsh mesh of the higher scale. As a result, there is no mandatory requirement to set one or several holes for initiating the procedure which is the case in most inverse homogenization schemes for topological design of material microstructures [144, 193, 170, 79].

5.1.3 Numerical examples

In this section, several numerical experiments are presented to investigate the size effect of unit cell in the classical homogenization-based topology optimization of lattice/periodic structures. The dimensions of the unit cell ranges from large to small as compared with the dimensions of the structure in different cases. The examples consist in comparing the optimized topologies by the presented homogenization method, which is solved on the coarse mesh, with the reference solution where all heterogeneities

are fully meshed. Regular meshes with 4-node elements have been adopted for all examples. Plane stress conditions are assumed. At the initiation of the topology optimization, the material distribution is homogeneous with $\rho_e = 1, \forall e$ within the RVE. The material constituting the architectured structure is assumed to be isotropic, with Young's and Poisson's coefficients given respectively by $E_m = 1000$ MPa and $\nu_m = 0.3$. During the topology optimization procedure, the interior of emerged holes is meshed with highly compliant material to maintain regular meshes, and fictitious material properties for the holes are taken as $E_i = 10^{-6}$ MPa and $\nu_i = 0.3$. The target volume fraction for the optimized topology of the RVE in all examples is 0.5.

5.1.3.1 Doubly-clamped elastic domain

In this first example, we investigate the topology optimization of periodic doubly-clamped square elastic domain as illustrated in Figure 5.2. The horizontal and vertical displacements of both left and right ends of the beam are fixed. A concentrated force $F = 100$ N is loaded on the centre point of this beam. The side of the square beam is $L = 1000$ mm. The structure is a lattice composed of $N_s = \eta \times \eta$ unit cells repeated periodically, with η represents the number of unit cells along each space direction. A coarse mesh composed of 5×5 elements is associated to the unit cells at the structural scale. The fine mesh on the RVE is composed of 40×40 elements to solve the local problem. 5 cases are studied: (i) $\eta = 2$; (ii) $\eta = 4$; (iii) $\eta = 8$; (iv) $\eta = 16$; (v) $\eta = 20$. These different cases correspond to the following coarse meshes for the structure: (i) 10×10 elements; (ii) 20×20 elements; (iii) 40×40 elements; (iv) 80×80 elements; and (v) 100×100 elements. The reference solution is obtained by discretizing the structure with the fine mesh for accouting for all heterogeneities, resulting into the following regular meshes for the different studied cases: (i) 80×80 elements; (ii) 160×160 elements; (iii) 320×320 elements; (iv) 640×640 elements; and (v) 800×800 elements. It is reminded that the present homogenization method allows re-localizing the microscopic fileds. Then, the homogenization-based topological optimization procedure only uses the values at the nodes of the coarse mesh, reducing drastically the computational time.

Figure 5.3 shows the different optimized topologies of the lattice structure for several numbers of unit cells along each direction to inversigate the size effect of the unit cell. Figure 5.3 (a) shows the final optimized geometry of the lattice obtained by the reference solution while Figure 5.3 (b) shows the final optimized geometry of the lattice obtained by the present homogenization method. Figure 5.3 (c) and (d) show the optimized geometry of one unit cell for comparison. Along rows (i) - (v), the number of unit cells repeated along each direction is increased and the ratio between the dimensions of the unit cells and the dimensions of the whole structure are decreased. We observe from Figure 5.3 (i) to (v) that the optimized topology converges rapidly. We can

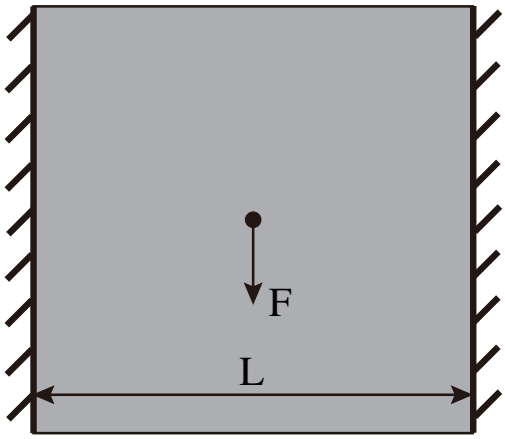

FIGURE 5.2: Doubly-clamped square elastic domain composed of periodic microscale unit cells: geometry and boundary conditions.

also note that even for the case (i) where the two scales can clearly not be separated, both methods lead to the same topology, which was not expected. To further illustrate the size effect of unit cell, we compare the compliances for optimized geometries of the lattice when using the reference solution or present homogenization-based method in Figure 5.4 (a). We can see that with the decrease of the unit cell size, the gap in resulted compliances is getting smaller and smaller. We also note that when the number of unit cells is large, both methods lead to the same compliance. To quantify the computational saving, the numbers of degree of freedoms (DOFs) to be solved in two different solutions are compared in Figure 5.4 (b). It is observed that the number of DOFs in the homogenization method is almost negligible compared with the reference solution, especially when the number of unit cells is large. Even so, the homogenization method could generate the optimized lattice structures with the same topology as well as the same stiffness as the reference solution.

5.1.3.2 L-shaped structure

In the previous example, the boundary conditions of the macrostructure were symmetrical, resulting in the optimal topological configuration of RVE being orthogonal and in a fast convergence. In this example, a more complicated L-shaped structure is investigated. The geometry of the problem is depicted in Figure 5.5, where the dimension of the macroscopic structure is $L = 1000$ mm. The top end of the L-shape structure is fixed, and the concentrated force is taken as $F = 100$ N (see Figure 5.5). The mesh used at the fine scale within the RVE is composed of 40×40 elements. A coarse mesh composed of 5×5 is associated to the unit cells at the structural scale. As in the previous example, the number of unit cells composing the beam is varied to study the size effect of the unit cell. Then, the following numbers of unit cells along each direction

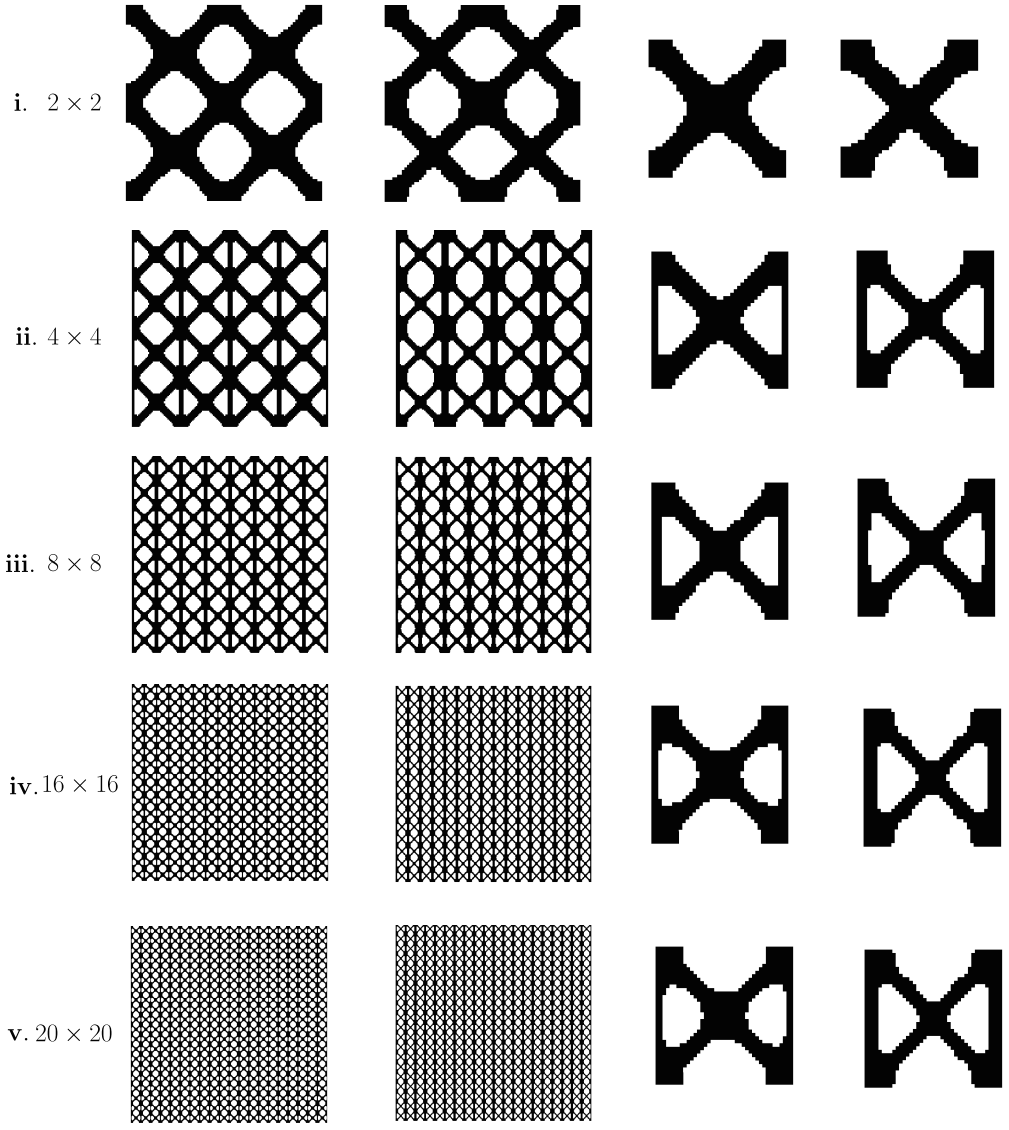

FIGURE 5.3: Optimized topologies for the double-clamped beam: columns (a), (b) compare the global lattice topologies when using the reference solution or homogenization-based method; columns (c) and (d) show the corresponding unit cell. Rows (i) to (v) correspond to increasing the number of unit cells in the lattice.

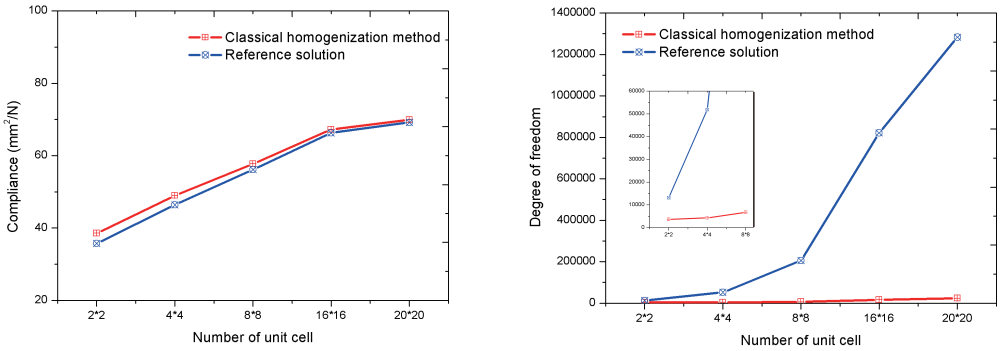

(a) (b)

FIGURE 5.4: Resulted compliance and solved DOFs by topological optimization using reference solution (blue curve) and homogenization method (red curve). Results are plotted as a function of the number of unit cells.

are investigated: (i) 2×2; (ii) 4×4; (iii) 8×8; (iv) 16×16; and (v) 20×20. Since the structure is not square, the number of unit cells in $x-$ and $y-$ directions is not the same, e.g. there are only three unit cells for the case (i). Then, the following numbers of DOFs are solved, respectively: (i) 3554; (ii) 4044; (iii) 5924; (iv) 13,284; (v) 18,764. As a comparison, the numbers of DOFs need to be solved using reference meshes are respectively: (i) 9922; (ii) 39,042; (iii) 154,882; (iv) 616,962; (v) 963,203. We can note that using the present technique, the topology optimization procedure only uses the nodal values of the coarsh mesh, thus drastically reducing the computational costs.

As in the first example, Figure 5.6 shows the different optimized topologies of the lattice structure for several number of unit cells along each direction using reference solution and homogenization method. We can observe from Figures. 5.6 (i) and (v) that the optimized topologies have huge difference between two different solutions. However, with the large number of unit cells, the topology of optimized structure by the homogenization method is also convergent to the reference solution. We compare the compliance for the optimized geometries of the lattice using two solutions in Figure 5.7 (a). In this case, using the homogenization method, the obtained resulting compliance is much larger than the reference solution for the case (i). As expected, the compliance converges to the same value with the decrease of unit cell size. As an illustration, the DOFs need to be solved in two optimized models are compared in Figure 5.7 (b). Here again, the homogenization topology optimization method based on the coarse meshes reduces computational time significantly.

5.1.3.3 MBB beam

In this last example, we investigate the topology optimization of a periodic Messerschmitt-Bölkow-Blohm (MBB) beam subjected to a concentrated load, where the aspect ratio

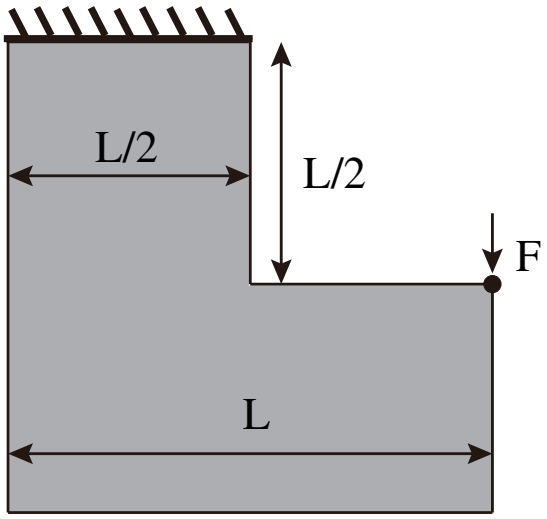

FIGURE 5.5: L-shaped beam composed of periodic microscale unit cells: geometry and boundary conditions.

of the beam is chosen as 4. The geometry of the problem is depicted in Figure 5.8. The concentrated force load is applied at the centre of the bottom end of the domain with a magnitude $F = 100$ N. The dimensions are $L \times H = 4000 \times 1000$ mm. Since the symmetry of boundary conditions, only the right half of the MBB beam is investigated. Therefore, assuming that the half structure consists of $N_s = s_x \times s_y$ unit cells repeated periodically, with s_x and s_y denoting the number of unit cells along $x-$ and $y-$ directions, respectively. In this example, we keep $s_x = 2s_y$. 6 cases are studied: (i) $s_x \times s_y = 2 \times 1$; (ii) $s_x \times s_y = 4 \times 2$; (iii) $s_x \times s_y = 8 \times 4$; (iv) $s_x \times s_y = 16 \times 8$; (v) $s_x \times s_y = 20 \times 10$; (vi) $s_x \times s_y = 24 \times 12$. These different cases correspond to the following coarse meshes for the structure: (i) 10×5 elements; (ii) 20×10 elements; (iii) 40×20 elements; (iv) 80×40 elements; (v) 100×50 elements; (vi) 120×60 elements. As in the previous examples, the topology optimization problem of periodic structure is solved using the reference mesh (fully accounting for the heterogeneities). In the reference model, the different cases have the following fine meshes for the structure: (i) 80×40 elements; (ii) 160×80 elements; (iii) 320×160 elements; (iv) 620×320 elements; (v) 800×400 elements; (vi) 960×480 elements, respectively.

Figure 5.9 shows the different optimized topologies of the lattice structure for several number of unit cells along each direction, using the homogenization-based and reference methods. Here again, the optimized topologies are different in the first few cases, while both methods lead to the same topology with the large number of unit cells. We also compare the compliances for optimized geometries of the lattice using the homogenization-based and reference solutions. It is observed that obtained resulting compliance using classical homogenization is much larger than reference solution for the case (i) where the scales can clearly not be separated. However, as expected,

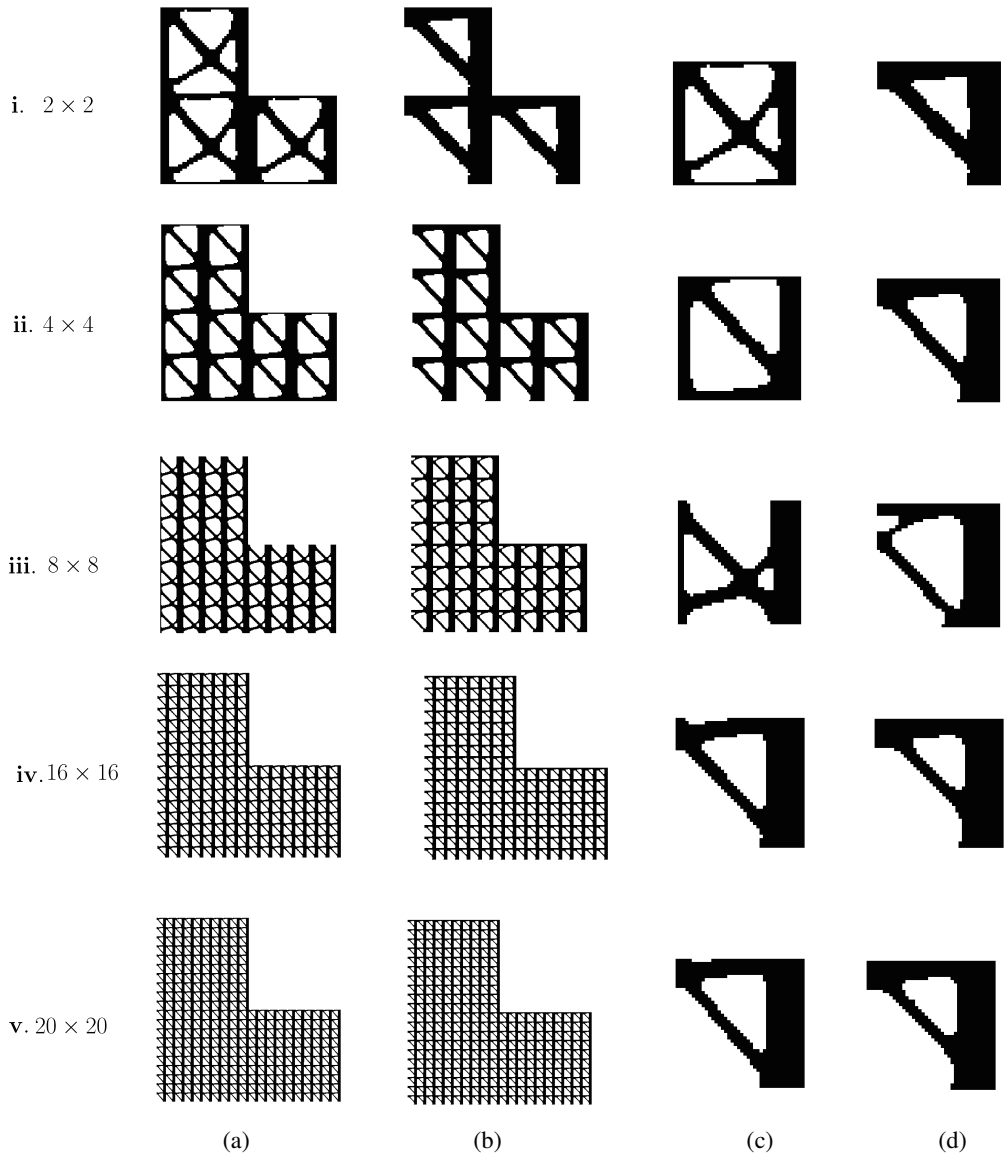

FIGURE 5.6: Optimized topologies for the L-shaped beam: columns (a), (b) compare the global lattices topologies when using the reference solution or homogenization-based method; columns (c) and (d) show the corresponding unit cell. Rows (i) to (v) correspond to increasing the number of unit cells in the lattice.

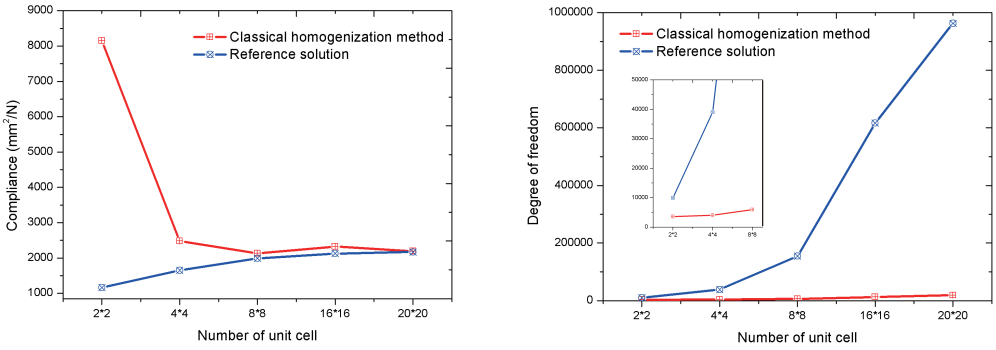

FIGURE 5.7: Resulted compliance and solved DOFs by topological optimization using reference solution (blue curve) and homogenization method (red curve). Results are plotted as a function of the number of unit cells.

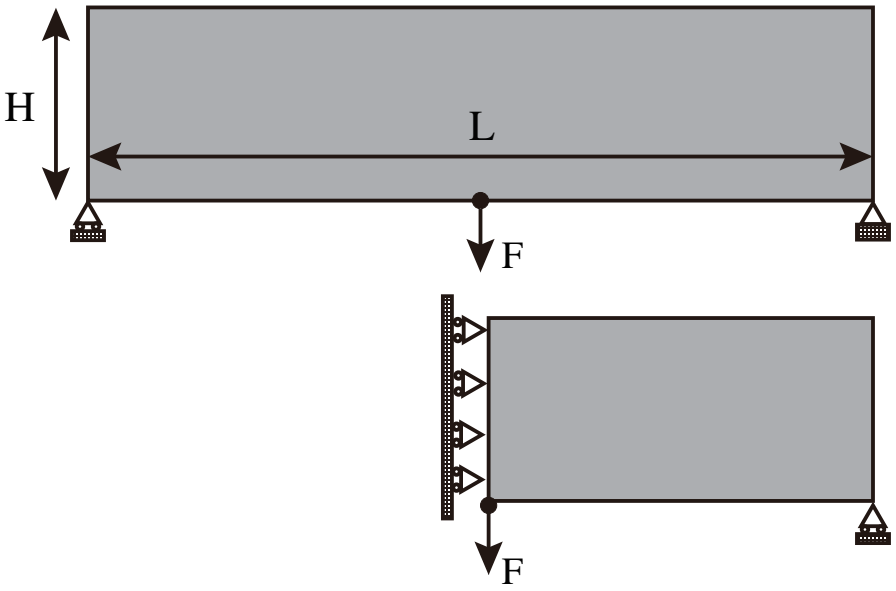

FIGURE 5.8: MBB beam composed of periodic microscale unit cells: geometry and boundary conditions.

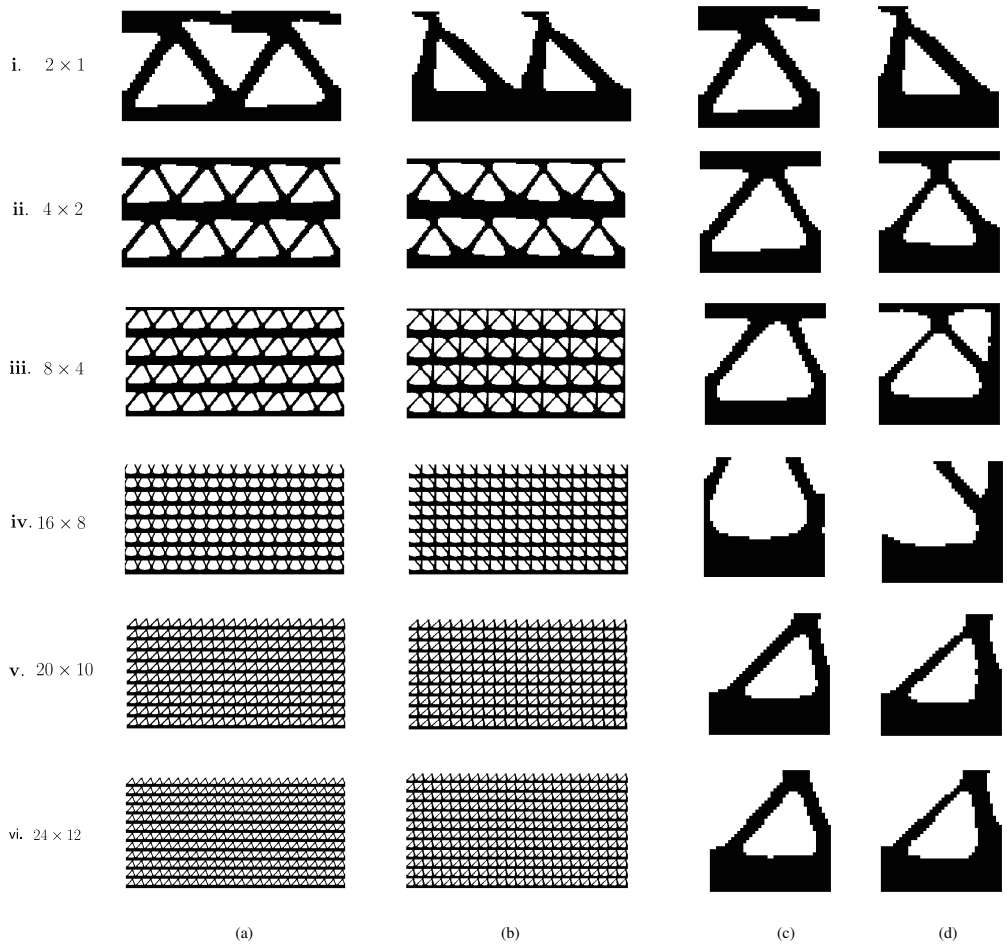

FIGURE 5.9: Optimized topologies for the half MBB beam: columns (a), (b) compare the global lattice topologies when using the reference solution and homogenization-based method; columns (c) and (d) show the corresponding unit cell. Rows (i) to (v) correspond to increasing the number of unit cells in the lattice.

both methods lead to the same value of the compliance when the number of unit cell in short side is larger than 8. We also compare the DOFs solved in two methods in Figure 5.10. It is then suggested that the present classical homogenization method can be chosen for topology optimization of periodic structures with large number of unit cells.

5.2 Topology optimization of periodic structures taking into account strain gradient

This section presents a new multiscale topology optimization for periodic structures, by using a consistent nonlocal filter-based homogenization scheme to account for strain

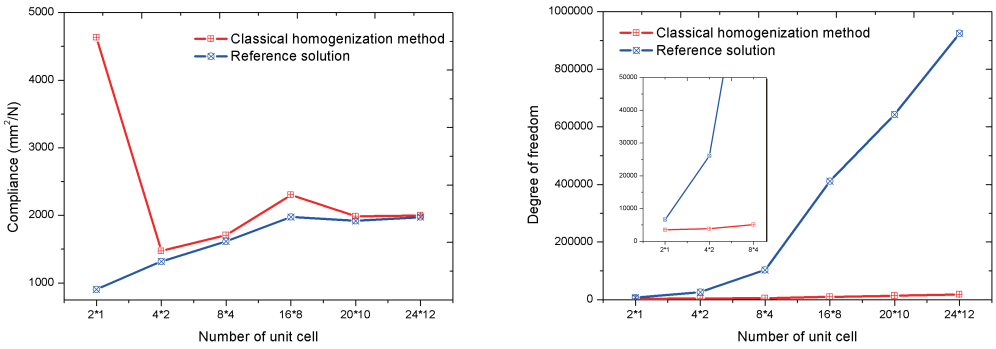

FIGURE 5.10: Resulted compliance and number of DOFs using reference solution (blue curve) and homogenization method (red curve). Results are plotted as a function of the number of unit cells.

gradient effects when the two scales are non-separated. Whereas several computational homogenization methods taking into account strain gradient effects are available (see e.g. [53, 131, 89]), we have used the technique developed in [185, 186, 152]. The major advantage of this technique is that it can take into account an arbitrary level of strain gradient without higher order elements, in a classical finite element framework. A review of the computational homogenization techniques used to take into account the strain gradient effects based on least-square polynomial filters is provided in Section 5.2.1. The procedure combining this nonlocal homogenization method with the topological optimization procedure is described in section 5.2.2. The nonlocal homogenization method is validated in Section 5.2.3 and the proposed methodology is applied to lattice structures in Section 5.2.4 to study the gain of taking into account the strain gradient effects as compared to a topology optimization combined with classical homogenization in the context of non-separated scales.

5.2.1 Nonlocal filter-based homogenization for non-separated scales

5.2.1.1 Definition of local and mesoscopic fields through the filter

In this section, we first briefly review the homogenization method that we use to take into account strain gradient effects. The method, called filter-based homogenization method, was introduced in [185] and later extended in [186, 152]. The main idea is to construct a mesoscopic non local homogenized model using computations on the Representative Volume Element (RVE) by replacing averaging operators in the homogenization theory by linear numerical filters. In this framework, a convenient numerical model based on a coarse mesh of the heterogeneous structure can be constructed, while keeping the possibility of re-localizing all microstructural mechanical fields.

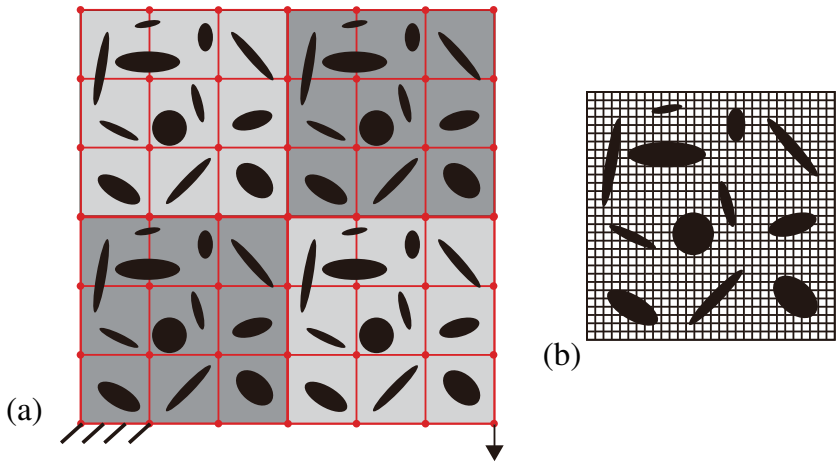

FIGURE 5.11: (a) Coarse mesh covering the structure and unit cells; (b) Fine mesh over the unit cell.

We consider two scales, one called microscopic scale, associated to fine scale strain and stress fields $\boldsymbol{\varepsilon}(\boldsymbol{x})$ and $\boldsymbol{\sigma}(\boldsymbol{x})$, and another one called *mesoscopic scale*, associated to strain and stress fields at the upper scale, denoted by $\hat{\boldsymbol{\varepsilon}}(\boldsymbol{x})$ and $\hat{\boldsymbol{\sigma}}(\boldsymbol{x})$. Note that the *mesoscopic* fields have a characteristic wavelength which is not necessarily much larger than that of the microscopic fluctuations fields. As illustrated in Figure 5.11, structures considered in the present work are assumed to be composed of periodic substructures or unit cells. The length scale of microscopic unit cell is comparable to the structural length scale such that the scale separation cannot be assumed. A coarse mesh is associated with the whole structure, and each substructure/unit cell is meshed with the same number of coarse elements. In addition, the microscopic structure (unit cell) is meshed using a fine mesh related to the microscopic scale. The mesoscopic strain and stress fields $\hat{\boldsymbol{\varepsilon}}$ and $\hat{\boldsymbol{\sigma}}$ are then approximated on the coarse mesh (see Figure 5.11(a)), whereas the microscopic fields $\boldsymbol{\varepsilon}$ and $\boldsymbol{\sigma}$ are evaluated on the fine mesh (see Figure 5.11(b)). The size of the fine grid is assumed to be small enough to catch all the fluctuations of the microstructure at the smallest scale.

Mesoscopic and microscopic fields are related by:

$$\begin{cases} \hat{\boldsymbol{\varepsilon}} = \mathcal{F}\{\boldsymbol{\varepsilon}(\boldsymbol{x})\}, \\ \hat{\boldsymbol{\sigma}} = \mathcal{F}\{\boldsymbol{\sigma}(\boldsymbol{x})\}, \end{cases} \tag{5.41}$$

where $\mathcal{F}$ is a linear operator, acting as a low-pass filter on the fine scale fluctuations. This operator is associated to a characteristic length h related to the field fluctuations observed at the mesoscopic scale. In order to construct a theory able to describe continuously mesoscopic fields from the microscale up to the macroscale, and precisely overcome the limitations of scale separation, the following properties are required for

the filter [185, 186, 152]:

$$\begin{cases} \lim\limits_{h\to 0} \mathcal{F}\{h, \varepsilon(\boldsymbol{x})\} = \varepsilon(\boldsymbol{x}), \\ \lim\limits_{h\to \infty} \mathcal{F}\{h, \varepsilon(\boldsymbol{x})\} = \langle \varepsilon(\boldsymbol{x}) \rangle, \\ \mathcal{F}\left\{\mathcal{F}\{\varepsilon(\boldsymbol{x})\}\right\} = \mathcal{F}\{\varepsilon(\boldsymbol{x})\}, \end{cases} \tag{5.42}$$

where $\langle . \rangle$ denotes averaging operator.

A least-square polynomial filter introduced in [186], which consists in a least-square projection of the microscopic strain field over a piece-wise polynomial basis, is adopted in this work. By this filter process, the mesoscopic fields are expressed as

$$\begin{cases} \hat{\varepsilon}_{ij}(\boldsymbol{x}) = \sum_{p=1}^{P} M^p(\boldsymbol{x}) \hat{\varepsilon}_{ij}^p, \\ \hat{\sigma}_{ij}(\boldsymbol{x}) = \sum_{p=1}^{P} M^p(\boldsymbol{x}) \hat{\sigma}_{ij}^p, \end{cases} \tag{5.43}$$

where $M^p(\boldsymbol{x})$ are piecewise polynomial basis (e.g. finite element shape functions) associated to nodes $p, p = 1, ..., P$ of a coarse mesh covering the domain where the microscopic fields are described. Given the fine scale strain field on a discrete fine mesh composed of N nodes $\boldsymbol{x}^m, m = 1, 2, ..., N$, the unknown coefficients $\hat{\varepsilon}_{ij}^p$ are required to minimize the distance between the approximation and the given fine scale strain field in the least-square sense. Let us define U such that

$$U = \sum_{m=1}^{N} \left(\sum_{p=1}^{P} M^p(\boldsymbol{x}^m) \hat{\varepsilon}_{ij}^p - \varepsilon_{ij}(\boldsymbol{x}^m) \right)^2 . \tag{5.44}$$

Optimality conditions give

$$\frac{dU}{d\hat{\varepsilon}_{ij}^q} = 0, \quad q = 1, 2, ..., N, \tag{5.45}$$

leading to

$$2 \sum_{m=1}^{N} M^q(\boldsymbol{x^m}) (\sum_{p=1}^{P} M^p(\boldsymbol{x^m}) \hat{\varepsilon}_{ij}^p - \varepsilon_i j(\boldsymbol{x}^m)) = 0, \quad q = 1, 2, .., N, \tag{5.46}$$

or

$$\sum_{p=1}^{P} \left(\sum_{m=1}^{N} M^p(\boldsymbol{x}^m) M^q(\boldsymbol{x}^m) \right) \hat{\varepsilon}_{ij}^p = \sum_{m} M^q(\boldsymbol{x}^m) \varepsilon_{ij}(\boldsymbol{x}^m). \tag{5.47}$$

Then the coefficients $\varepsilon_{ij}^p, p = 1, 2, ..., N$ are found by solving the following system:

$$\boldsymbol{A}\mathrm{u} = \boldsymbol{b}, \tag{5.48}$$

where

$$A_{pq} = \sum_{m=1}^{N} M^p(\boldsymbol{x}^m) M^q(\boldsymbol{x}^m), \quad b_q = \sum_{m=1}^{N} M^p(\boldsymbol{x}^m) \varepsilon_{ij}(\boldsymbol{x}^m), \tag{5.49}$$

and where $\mathrm{u} = [\hat{\varepsilon}_{ij}^1, \hat{\varepsilon}_{ij}^2, ..., \hat{\varepsilon}_{ij}^N]$.

5.2.1.2 Microscopic unit cell calculations

Let us consider a unit cell $\Omega \subset \mathbb{R}^d$ as defined in Section 2.1, d being the dimension of the space, with boundary $\partial\Omega$. The unit cell is related to microscopic scale where the fields are described at the finest scale. The local problem on the unit cell for non-separated scales is defined as follows: assuming known an applied non-constant mesoscopic strain field $\hat{\boldsymbol{\varepsilon}}(\boldsymbol{x})$, find $\boldsymbol{\varepsilon}(\boldsymbol{x})$ satisfying;

$$\nabla \cdot (\boldsymbol{\sigma}(\boldsymbol{x})) = 0 \quad \text{in } \Omega \tag{5.50}$$

and

$$\boldsymbol{\sigma}(\boldsymbol{x}) = \mathbb{C}(\boldsymbol{x}) : \boldsymbol{\varepsilon}(\boldsymbol{x}), \tag{5.51}$$

with

$$\mathcal{F}\{\boldsymbol{\varepsilon}(\boldsymbol{x})\} = \hat{\boldsymbol{\varepsilon}}(\boldsymbol{x}) \quad \text{in } \Omega, \tag{5.52}$$

where $\mathbb{C}(\boldsymbol{x})$ is a fourth-order elasticity tensor, and $\nabla \cdot (.)$ denotes the divergence operator. Instead of requiring that the spatial average of the strain fields matches the mesoscopic one as in the classical homogenization, the condition (5.52) states that the filtered part of the compatible strain field must match the given non-uniform mesoscopic strain field $\hat{\boldsymbol{\varepsilon}}(\boldsymbol{x})$. This problem is then different from the local problem in classical homogenization.

Following [185], the microscopic strain field is split into a filtered (mesoscopic) part and a remaining fluctuation $\tilde{\boldsymbol{\varepsilon}}(\boldsymbol{x})$:

$$\boldsymbol{\varepsilon}(\boldsymbol{x}) = \hat{\boldsymbol{\varepsilon}}(\boldsymbol{x}) + \tilde{\boldsymbol{\varepsilon}}(\boldsymbol{x}). \tag{5.53}$$

Introducing (5.51) and (5.53) into (5.50) and using the property (5.42)(c), the new localization problem is obtained as:

$$\nabla \cdot (\mathbb{C}(\boldsymbol{x}) : \tilde{\boldsymbol{\varepsilon}}(\boldsymbol{x})) = -\nabla \cdot (\mathbb{C}(\boldsymbol{x}) : \hat{\boldsymbol{\varepsilon}}(\boldsymbol{x})) \quad \text{in } \Omega \tag{5.54}$$

with

$$\mathcal{F}\{\tilde{\boldsymbol{\varepsilon}}(\boldsymbol{x})\} = 0 \quad \text{in } \Omega. \tag{5.55}$$

To enforce the non-trivial condition (5.52), an auxiliary strain field $\boldsymbol{e}(x)$ is defined by $\tilde{\boldsymbol{\varepsilon}}(\boldsymbol{x}) = \boldsymbol{e}(\boldsymbol{x}) - \mathcal{F}(\boldsymbol{e}(\boldsymbol{x}))$. Invoking again the property (5.42)(c), we have:

$$\mathcal{F}\{\tilde{\boldsymbol{\varepsilon}}(\boldsymbol{x})\} = \mathcal{F}\left\{\boldsymbol{e}(\boldsymbol{x}) - \mathcal{F}\{\boldsymbol{e}(\boldsymbol{x})\}\right\} = \mathcal{F}\{\boldsymbol{e}(\boldsymbol{x})\} - \mathcal{F}\left\{\mathcal{F}\{\boldsymbol{e}(\boldsymbol{x})\}\right\} = 0. \tag{5.56}$$

The new local problem (5.54) then can be re-written by seeking $\boldsymbol{e}(\boldsymbol{x})$ satisfying

$$\nabla \cdot (\mathbb{C}(\boldsymbol{x}) : [\boldsymbol{e}(\boldsymbol{x}) - \mathcal{F}\{\boldsymbol{e}(\boldsymbol{x})\}]) = -\nabla \cdot (\mathbb{C}(\boldsymbol{x}) : \hat{\varepsilon}(\boldsymbol{x})) \quad \text{in } \Omega. \tag{5.57}$$

Condition (5.55) implies that

$$\langle \tilde{\boldsymbol{\varepsilon}}(\boldsymbol{x}) \rangle = 0 \tag{5.58}$$

which is satisfied for any value of the spatial average $\langle \boldsymbol{e}(\boldsymbol{x}) \rangle$. So, we choose $\langle \boldsymbol{e}(\boldsymbol{x}) \rangle = 0$, and this equation is classically verified for the two possible sets of boundary conditions:

$$\boldsymbol{u}^e(\boldsymbol{x}) = 0 \ \text{ on } \partial\Omega, \tag{5.59}$$

or

$$\boldsymbol{u}^e(\boldsymbol{x}) = 0 \quad \text{periodic on } \partial\Omega, \tag{5.60}$$

where $\boldsymbol{u}^e$ is a compatible displacement field such that $\boldsymbol{e}(\boldsymbol{x}) = \boldsymbol{\varepsilon}(\boldsymbol{u}^e(\boldsymbol{x}))$, with $\boldsymbol{\varepsilon}(.) = \frac{1}{2}(\nabla(.) + \nabla^T(.))$.

To summarize, the new problem is defined by Eq.(5.54) with boundary conditions (5.59) or (5.60). In the present work, the first set of boundary conditions is adopted. The presence of the nonlocal operator in the left-hand term of (5.57) induces a numerical difficulty, as the stiffness matrix associated with this linear operator is fully populated. Following [186, 152], the following iterative scheme is defined to alleviate this difficulty: starting from an initialized solution $\boldsymbol{e}^0(\boldsymbol{x})$, e.g. $\boldsymbol{e}^0(\boldsymbol{x}) = 0$, we seek the field $\boldsymbol{e}^{n+1}(\boldsymbol{x})$ at each iteration n of the following scheme:

$$\nabla \cdot (\mathbb{C}(\boldsymbol{x}) : \boldsymbol{e}^{n+1}(\boldsymbol{x})) = \nabla \cdot (\mathbb{C}(\boldsymbol{x}) : \mathcal{F}\{\boldsymbol{e}^n(\boldsymbol{x})\} - \nabla \cdot (\mathbb{C}(\boldsymbol{x}) : \hat{\varepsilon}(\boldsymbol{x})) \tag{5.61}$$

until a convergence criterion is reached. At convergence, the strain field is recovered as follows:

$$\boldsymbol{\varepsilon}(\boldsymbol{x}) = \hat{\boldsymbol{\varepsilon}}(\boldsymbol{x}) + \boldsymbol{e}^{n+1}(\boldsymbol{x}) - \mathcal{F}\{\boldsymbol{e}^{n+1}(\boldsymbol{x})\}. \tag{5.62}$$

Following [152], we assume that the mesoscopic strain field derives from a mesoscopic displacement field $\hat{\boldsymbol{u}}(\boldsymbol{x})$ related to the mesoscopic scale as follows:

$$\hat{\varepsilon}_{ij}(\boldsymbol{x}) = \frac{1}{2}\left(\frac{\partial \hat{u}_i(\boldsymbol{x})}{\partial x_j} + \frac{\partial \hat{u}_j(\boldsymbol{x})}{\partial x_i}\right). \tag{5.63}$$

The mesoscopic displacement field is interpolated on the coarse mesh by finite element shape functions as:

$$\hat{u}_i(\boldsymbol{x}) \simeq \sum_p M^p(\boldsymbol{x})\hat{u}_i^p, \tag{5.64}$$

where $M^p(\boldsymbol{x})$ is the finite element shape function associated with the node p and $\hat{u}_i^p$ are the nodal components of $\hat{\boldsymbol{u}}(\boldsymbol{x})$ on the coarse mesh. Then, the corresponding strain field is given by:

$$\hat{\varepsilon}_{ij}(\boldsymbol{x}) \simeq \sum_{p=1}^{P} \frac{1}{2}\left(\frac{\partial M^p(\boldsymbol{x})}{\partial x_j}\hat{u}_i^p + \frac{\partial M^p(\boldsymbol{x})}{\partial x_i}\hat{u}_j^p\right), \tag{5.65}$$

where P is the number of nodes on the coarse mesh of the unit cell. This equation can be re-written as:

$$\hat{\varepsilon}_{ij}(\boldsymbol{x}) \simeq \sum_{p=1}^{P} \frac{1}{2}\left(\frac{\partial M^p(\boldsymbol{x})}{\partial x_j}\delta_{ik} + \frac{\partial M^p(\boldsymbol{x})}{\partial x_i}\delta_{jk}\right)\hat{u}_k^p. \tag{5.66}$$

From the superposition principle, the solution of the local problem is then a linear combination of the components of nodal displacements components $\hat{u}_k^p$ on the coarse mesh:

$$\varepsilon_{ij}(\boldsymbol{x}) \simeq \sum_{p=1}^{P} \mathcal{D}_{ijk}^p(\boldsymbol{x})\hat{u}_k^p. \tag{5.67}$$

Introducing the vector forms for the second-order tensors $\boldsymbol{\varepsilon}$ and $\boldsymbol{\sigma}$: $[\boldsymbol{\varepsilon}] = [\varepsilon_{11}, \varepsilon_{22}, 2\varepsilon_{12}]^T$, $[\boldsymbol{\sigma}] = [\sigma_{11}, \sigma_{22}, \sigma_{12}]^T$, Eq. (5.67) can be re-written into the matrix form in 2D as follows:

$$[\boldsymbol{\varepsilon}](\boldsymbol{x}) = \sum_p \begin{bmatrix} D_{11}^p(\boldsymbol{x}) & D_{12}^p(\boldsymbol{x}) \\ D_{21}^p(\boldsymbol{x}) & D_{22}^p(\boldsymbol{x}) \\ D_{31}^p(\boldsymbol{x}) & D_{32}^p(\boldsymbol{x}) \end{bmatrix} \begin{bmatrix} \hat{u}_1^p \\ \hat{u}_2^p \end{bmatrix}, \tag{5.68}$$

where the column $[D_{11}^p(\boldsymbol{x}), D_{21}^p(\boldsymbol{x}), D_{31}^p(\boldsymbol{x})]$ is the strain vector obtained from solving the local problem with $\hat{\boldsymbol{\varepsilon}}(\boldsymbol{x})$ given by the expression (5.66) with $\hat{u}_1^p = 1$ and $\hat{u}_2^p = 0$. The column $[D_{12}^p(\boldsymbol{x}), D_{22}^p(\boldsymbol{x}), D_{32}^p(\boldsymbol{x})]$ is the strain vector obtained from solving the local problem with $\hat{\boldsymbol{\varepsilon}}(\boldsymbol{x})$ given by the expression (5.66) with $\hat{u}_1^p = 0$ and $\hat{u}_2^p = 1$. We show how to compute the $\mathbf{D}^p(\boldsymbol{x})$ in the following.

The corresponding weak form of the localization problem expressed in (5.61) can be formulated as: find $\boldsymbol{u}(\boldsymbol{x})$ satisfying periodic boundary condition (5.59), such that

$\forall \delta \boldsymbol{u} \in H^1(\Omega)$:

$$\begin{aligned} \int_\Omega \boldsymbol{\varepsilon}\left([\boldsymbol{u}^e]^{n+1}\right) : \mathbf{C}(\boldsymbol{x}) : \boldsymbol{\varepsilon}(\delta \boldsymbol{u}(\boldsymbol{x}))d\Omega = \\ \int_\Omega \mathcal{F}\left\{\boldsymbol{\varepsilon}\left([\boldsymbol{u}^e]^{n+1}(\boldsymbol{x})\right)\right\} : \mathbf{C}(\boldsymbol{x}) : \boldsymbol{\varepsilon}(\delta \boldsymbol{u}(\boldsymbol{x}))d\Omega - \int_\Omega \hat{\boldsymbol{\varepsilon}}(\boldsymbol{x}) : \mathbf{C}(\boldsymbol{x}) : \boldsymbol{\varepsilon}(\delta \boldsymbol{u}(\boldsymbol{x}))d\Omega, \end{aligned} \tag{5.69}$$

where $H^1(\Omega)$ is the usual Sobolev space. Using a classical FEM discretization over the fine mesh, we have:

$$\mathbf{K}\mathbf{U}^{n+1} = \mathbf{f}^n + \hat{\mathbf{f}}, \tag{5.70}$$

with

$$\mathbf{K} = \int_\Omega \mathbf{B}^T(\boldsymbol{x})\mathbf{C}(\boldsymbol{x})\mathbf{B}(\boldsymbol{x})d\Omega, \tag{5.71}$$

where $\mathbf{B}$ denotes the matrix of shape functions derivatives, $\mathbf{C}$ is the matrix form associated with the fourth-order tensor $\mathbb{C}(\boldsymbol{x})$ in (5.51) and $\hat{\mathbf{f}}$ is the body force vector associated to the prescribed non-uniform strain $\hat{\varepsilon}(\boldsymbol{x})$, which corresponds to an unitary displacement of one node of the coarse mesh as follows:

$$\hat{\mathbf{f}} = -\int_\Omega \mathbf{B}^T(\boldsymbol{x})\mathbf{C}(\boldsymbol{x})[\hat{\boldsymbol{\varepsilon}}(\boldsymbol{x})]d\Omega \tag{5.72}$$

where $[\hat{\boldsymbol{\varepsilon}}(\boldsymbol{x})]$ is the vector form associated with $\hat{\boldsymbol{\varepsilon}}(\boldsymbol{x})$ and

$$\mathbf{f}^n = \int_\Omega \mathbf{B}^T(\boldsymbol{x})\mathbf{C}(\boldsymbol{x})\left[\mathcal{F}\left\{\boldsymbol{\varepsilon}\left([\boldsymbol{u}^e]^n(\boldsymbol{x})\right)\right\}\right]d\Omega. \tag{5.73}$$

Note that in all $2 \times P$ problems as well as for all iterations of the iterative procedure, the same stiffness matrix $\mathbf{K}$ is involved, which then only needs to be computed and decomposed once. Finally, we obtain:

$$\begin{bmatrix} D^p_{11}(\boldsymbol{x}) & D^p_{12}(\boldsymbol{x}) \\ D^p_{21}(\boldsymbol{x}) & D^p_{22}(\boldsymbol{x}) \\ D^p_{31}(\boldsymbol{x}) & D^p_{32}(\boldsymbol{x}) \end{bmatrix} = \begin{bmatrix} \varepsilon^{(1)}_{11}(\boldsymbol{x}) & \varepsilon^{(2)}_{11}(\boldsymbol{x}) \\ \varepsilon^{(1)}_{22}(\boldsymbol{x}) & \varepsilon^{(2)}_{22}(\boldsymbol{x}) \\ \varepsilon^{(1)}_{12}(\boldsymbol{x}) & \varepsilon^{(2)}_{12}(\boldsymbol{x}) \end{bmatrix}. \tag{5.74}$$

Then, we have the following relationships:

$$[\boldsymbol{\varepsilon}(\boldsymbol{x})] = \sum_{p=1}^{P} \mathbf{D}^p(\boldsymbol{x})\hat{\mathbf{u}}^p, \tag{5.75}$$

$$[\boldsymbol{\sigma}(\boldsymbol{x})] = \sum_{p=1}^{P} \mathbf{C}(\boldsymbol{x})\mathbf{D}^p(\boldsymbol{x})\hat{\mathbf{u}}^p. \tag{5.76}$$

Applying the linear filter $\mathcal{F}$, we have

$$[\hat{\boldsymbol{\sigma}}(\boldsymbol{x})] = \sum_p \hat{\mathbf{G}}^p(\boldsymbol{x})\hat{\mathbf{u}}^p, \tag{5.77}$$

with

$$\hat{\mathbf{G}}^p(\boldsymbol{x}) = \mathcal{F}\{\mathbf{C}(\boldsymbol{x})\mathbf{D}^p(\boldsymbol{x})\}. \tag{5.78}$$

As a result, the obtained constitutive relationship at the mesoscopic scale has been derived by a fully microscopically-based framework without any empirical assumptions. A simple classical displacement-based finite element strategy is adopted to implement the numerical scheme without requiring higher-order elements.

The overall algorithm for the microscopic unit cell computations is summarized as follows:

For each point p of the coarse mesh covering the unit cell:

1. Solve the local problem (5.57) with boundary conditions (5.59) by using the FEM discretization over the fine mesh until convergence is reached.
2. Compute microscopic strain field $\boldsymbol{\varepsilon}(\boldsymbol{x})$ using (5.62).
3. Compute $\mathbf{D}^p(\mathbf{x})$ using (5.74) and store it.
4. Compute $\hat{\mathbf{G}}^p(\boldsymbol{x})$ using (5.78) and store it. Only nodal values of $\hat{\mathbf{G}}^p(\boldsymbol{x})$ at the nodes of the coarse mesh need to be stored. The full spatial description in the unit cell can be recovered through finite element shape functions as: $\hat{\mathbf{G}}^p(\boldsymbol{x}) = \sum_i M^i(\boldsymbol{x})[\hat{\mathbf{G}}^p]_i$, where $[\hat{\mathbf{G}}^p]_i$ are the nodal values of $\hat{\mathbf{G}}^p(\boldsymbol{x})$ on the coarse mesh.

Once these tensors computed and stored, for an arbitrary distribution of nodal values of the mesoscopic displacement field $\hat{\mathbf{u}}^p$ over the coarse mesh, we can compute:

1. The reconstructed local stress field $\sigma(\boldsymbol{x})$ using (5.76).
2. The mesoscopic stress field $\hat{\sigma}(\boldsymbol{x})$ using (5.77)-(5.78).

5.2.1.3 Mesoscopic structure calculations

Let us consider a mesoscopic structure defined in a domain $\hat{\Omega} \subset \mathbb{R}^d$ with boundary $\partial\hat{\Omega}$. The structure is associated to the mesoscopic scale, that is, the strain and stress fields are described at the characteristic wavelength associated to the filter $\mathcal{F}$ allowing to define them on the coarse mesh. The structure is subdivided into periodic substructures corresponding to unit cells $\Omega^k (k = 1, ..., N_s)$, with N_s the number of substructures, as depicted in Figure 5.11. The boundary $\partial\hat{\Omega}$ is composed of Dirichlet and Neumann

parts, denoted respectively $\partial\hat{\Omega}_u$ and $\partial\hat{\Omega}_t$, where the displacements and tractions are prescribed.

The equilibrium equation is expressed by

$$\nabla \cdot (\hat{\boldsymbol{\sigma}}(\boldsymbol{x})) + \hat{\mathbf{f}} = 0 \quad \text{in } \hat{\Omega} \tag{5.79}$$

with boundary conditions as:

$$\hat{\mathbf{u}}(\boldsymbol{x}) = \mathbf{u}^d \quad \text{on } \partial\hat{\Omega}_u \tag{5.80}$$

and

$$\hat{\boldsymbol{\sigma}} \cdot \mathbf{n} = \mathbf{f}^d \quad \text{on } \partial\hat{\Omega}_t \tag{5.81}$$

completed with the mesoscopic constitutive law (5.77)-(5.78), where $\mathbf{u}^d$ and $\mathbf{f}^d$ are respectively the prescribed displacement and forces.

The weak form corresponding to the mesoscopic problem (5.79)-(5.81) is given as follows: find $\hat{\mathbf{u}} \in H^1(\Omega)$ satisfying the boundary condition (5.80) such that

$$\int_{\hat{\Omega}} [\hat{\boldsymbol{\sigma}}(\hat{\mathbf{u}})] \cdot [\hat{\boldsymbol{\varepsilon}}(\delta\hat{\mathbf{u}})] d\Omega = \int_{\partial\hat{\Omega}_t} \hat{\mathbf{F}} \cdot \delta\hat{\mathbf{u}} d\Gamma + \int_{\hat{\Omega}} \hat{\mathbf{f}} \cdot \delta\hat{\mathbf{u}} d\Omega = \delta\hat{W}^{ext} \tag{5.82}$$

where $\hat{\boldsymbol{\varepsilon}}(\delta\hat{\mathbf{u}})$ is approximated on the coarse mesh using classical FEM shape functions

$$[\hat{\boldsymbol{\varepsilon}}](\delta\hat{\mathbf{u}}) = \mathbf{B}\delta\hat{\mathbf{u}}^e \tag{5.83}$$

and $\delta\hat{\mathbf{u}}^e$ are nodal values of $\delta\hat{\mathbf{u}}$ on the coarse mesh. Then we have

$$\sum_k \int_{\hat{\Omega}^k} \sum_{p \in \hat{\Omega}^k} \hat{\mathbf{G}}^p(\boldsymbol{x}) \hat{\mathbf{u}}^p \cdot \mathbf{B}(\boldsymbol{x}) \delta\hat{\mathbf{u}}^e d\Omega = \delta\hat{W}^{ext}, \tag{5.84}$$

which leads to the linear system of equations

$$\hat{\mathbf{K}}\hat{\mathbf{u}} = \hat{\mathbf{F}} \tag{5.85}$$

with

$$\hat{\mathbf{K}} = \sum_k \sum_{p \in \hat{\Omega}^k} \int_{\hat{\Omega}^k} \mathbf{B}^T(\boldsymbol{x}) \hat{\mathbf{G}}^p(\boldsymbol{x}) d\Omega \tag{5.86}$$

and

$$\hat{\mathbf{F}} = \int_{\partial\hat{\Omega}} \mathbf{N}^T \cdot \hat{\mathbf{f}} d\Omega + \int_{\partial\hat{\Omega}_t} \mathbf{N}^T \cdot \bar{\mathbf{F}} d\Gamma. \tag{5.87}$$

The mesoscopic problem can be solved on a coarse mesh only, but the technique can provide all re-localized fine scale fields in the heterogeneous structure, as described in Section 5.2.1.2.

5.2.2 Topology optimization procedure

5.2.2.1 Model definition and sensitivity numbers

In this section, the BESO method for topology optimization is extended to strain gradient effects by incorporating the non-local model presented in the previous section, and applied to lattices structure composed of periodic unit cells. Then, the topology of all unit cells is the same, but takes into account the response of the whole structure to maximize its stiffness. The structural stiffness maximization problem can be formulated using the design variable $\rho_e^{(k)}$, where k and e denote the substructure number and the element number in each substructure, respectively, as

$$\text{Find} : \{\boldsymbol{\rho}^{(1)}, \dots, \boldsymbol{\rho}^{(N_s)}\} \tag{5.88}$$

$$\text{Minimize} : f_{\mathrm{c}}(\boldsymbol{\rho}, \hat{\mathbf{u}}) = \hat{\mathbf{F}}^T \hat{\mathbf{u}} \tag{5.89}$$

$$\text{subject to} : \hat{\mathbf{K}}\hat{\mathbf{u}} = \hat{\mathbf{F}}, \tag{5.90}$$

$$: V(\boldsymbol{\rho}) = N_s \sum \rho_e^{(k)} v_e^{(k)} = V_{\mathrm{req}}, \tag{5.91}$$

$$: \rho_e^{(1)} = \cdots = \rho_e^{(N_s)},\ e = 1, \dots, N_e, \tag{5.92}$$

$$: \rho_e^{(k)} = \rho_{min} \text{ or } 1,\ e = 1, \dots, N_{\mathrm{e}},\ k = 1, \dots, N_s \tag{5.93}$$

where f_{c} is known as the compliance functional, and $\hat{\mathbf{F}}$ and $\hat{\mathbf{u}}$ are respectively the applied load and displacement vectors defined at the mesoscopic scale in section 5.2.1.3. The above stiffness matrix $\hat{\mathbf{K}}$ is assembled using (5.86), where $\hat{\mathbf{G}}^p$ is obtained using (5.78). It should be noted that the computation of both tensors $\hat{\mathbf{G}}^p$ and $\hat{\mathbf{D}}^p$ in (5.78) is both based on a fully microscopic framework accounting for all heterogeneities at the microscale. In (5.91), $v_e^{(k)}$ is the volume of the $e-$th element in the $k-$th unit cell, and N_e is the number of elements in the microscale fine mesh for each substructure. Similar to the optimization model defined in Section 5.1 using the classical homogenization method, the condition $\rho_e^{(1)} = \cdots = \rho_e^{(N_s)},\ e = 1, \dots, N_e$ ensures that the pseudo densities (ρ_{min} or 1) of elements at the corresponding locations in each substructure are the same. Therefore, the sensitivity number in this scheme can also be expressed as the variation of the overall structural compliance due to the removal of $e-$th elements in all substructures:

$$\alpha_e = \begin{cases} \sum_{k=1}^{N_s} \int_{\Omega_e^k} \boldsymbol{\sigma}(\boldsymbol{x})\boldsymbol{\varepsilon}(\boldsymbol{x}) d\Omega_e^k, & \text{for } \rho_e^{(k)} = 1 \\ 0\ , & \text{for } \rho_e^{(k)} = \rho_{min}, \end{cases} \tag{5.94}$$

where $\boldsymbol{\sigma}$ and $\boldsymbol{\varepsilon}$ are respectively microscopic stress and strain fields in the $e-$th element of the $k-$th substructure Ω_e^k, which are evaluated directly from the obtained mesoscopic displacement field on the coarse mesh as formulated in section 5.2.1. By the

presented nonlocal homogenization scheme, the re-localized strain and stress fields are obtained using (5.75) and (5.76). Then, only computations on the coarse mesh are required, but all local fields can be reconstructed. As shown in the Section 5.1, this is highly advantageous by reducing the computational costs in the topology optimization procedure, using only the coarse mesh nodal values of displacements.

5.2.2.2 Overall optimization procedure

To summarize, the objective function is computed by solving the mesoscopic problem on a coarse mesh only and the microscopic strain and stress fields (fine scale) are re-localized by means of the localization operators calculated on the unit cells. The microstructural topology of the RVE is tailored to find the optimal material layout at microscale such that the resulting overall structure has the maximum stiffness within a prescribed amount of material. Finally, the overall multiscale topology optimization procedure for designing the periodic microscopic structures without scale separation using a filter-based homogenization scheme is described as follows.

1. Set a coarse mesh associated with the structure, such that each substructure/unit cell is meshed with the same number of coarse elements. Set another fine mesh related to the microscopic scale to discretize the microstructure of RVE .
2. Assign the pseudo densities $(\rho_{min}\ or\ 1)$ to fine mesh elements in the RVE to construct an initial design before optimization.
3. Perform the microscopic unit cell computations as described in Section 5.2.1.2.
4. Solve the mesoscopic structure problem as summarized in Section 5.2.1.3.
5. Based on the nodal displacement solution from the mesoscopic problem on the coarse mesh, evaluate the local strain field by (5.75) and the local stress field by (5.76).
6. Compute the elemental sensitivity number using (5.94) and modify it by using (3.12) and (3.14).
7. Update the structural topology in RVE with (3.15).
8. Repeat 3-7 until the material constraint V_{req} is satisfied and the convergence criterion (3.16) is reached.

5.2.3 Validation of the nonlocal homogenization approach

Even though the nonlocal approach described in section 5.2.1 has been validated through various examples in previous works (see e.g. [152]), we present in this section a short

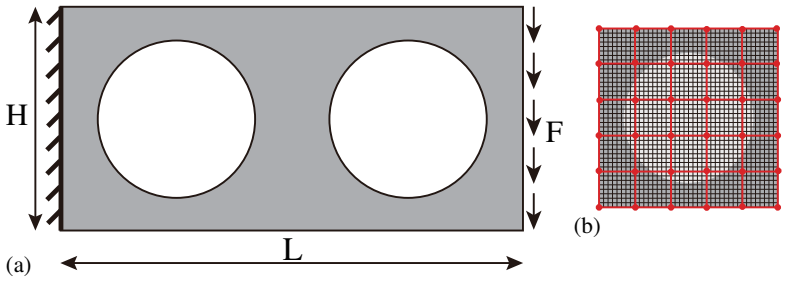

FIGURE 5.12: Cantilever lattice structure composed of periodic unit cells subjected to distributed force: (a) geometry and boundary conditions of the beam; (b) coarse and fine meshes associated to the unit cell.

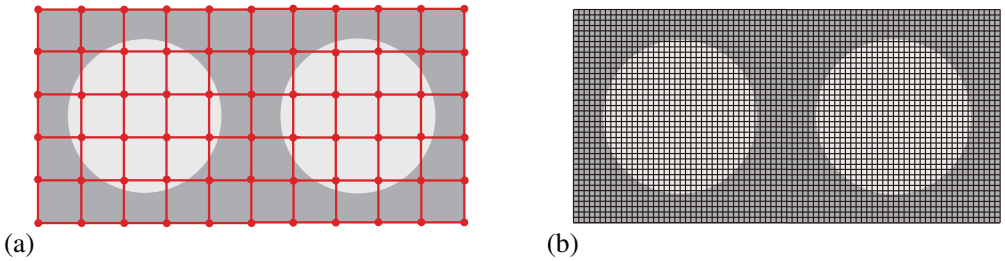

FIGURE 5.13: Meshes of the whole structure for computing (a) the mesoscopic problem and (b) the reference solution.

validation test for the sake of self-consistency of the thesis. The validation test consists in comparing the re-localized field obtained by the present non-local homogenization method on a coarse mesh with a reference solution where all heterogeneities are fully meshed. We consider a structure depicted in Figure 5.12 (a). The dimensions of the structure are $L \times H = 200 \times 100$ mm. The boundary conditions are described in Figure 5.12 (a). The prescribed force is $F = 2$ kN. The unit cell is depicted in Figure 5.12 (b). The central hole radius is such that the porosity is equal to 0.6. The material constituting the architectured structure is assumed to be isotropic, with Young's and Poisson's coefficients given respectively by $E_m = 1000$ MPa and $\nu_m = 0.3$. As the topology optimization is more conveniently applied with a regular mesh, the interior of the hole is meshed and associated with a fictive, highly compliant material with Young's and Poisson's coefficients given respectively by $E_i = 10^{-6}$ MPa and $\nu_i = 0.3$. Plain stress are assumed.

The unit cell is discretized with 50×50 regular four-node bilinear elements for the fine scale mesh. A coarse 5×5 mesh is used to construct the localization operators of the nonlocal homogenized model, as described in section 5.2.1.2. The structure is discretized by a coarse mesh including 10×5 nodes. The reference solution is obtained by discretizing the structure with a regular 100×50 bilinear elements mesh (see Figure 5.13 (b). The results are presented in Figures. 5.14 and 5.15, where the ε_{11} and σ_{11} components of the strain and stress fields are plotted for both reference solution and for the

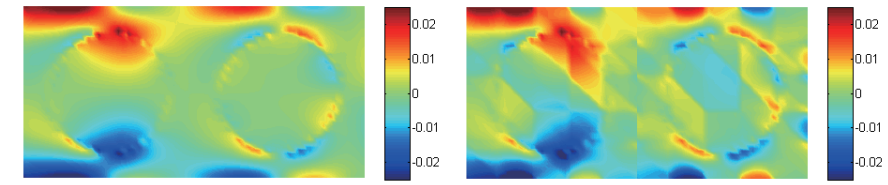

FIGURE 5.14: (a) Reference solution and (b) re-localized strain field ε_{11} obtained from the nonlocal homogenization method (computed on the coarse mesh).

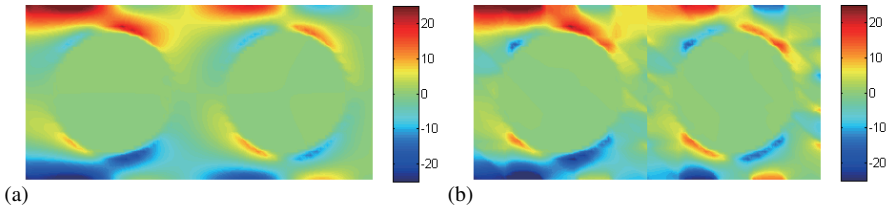

FIGURE 5.15: (a) Reference solution and (b) re-localized stress field σ_{11} obtained from the nonlocal homogenization method (computed on the coarse mesh).

re-localized fields obtained by the homogenized model (solved on the coarse mesh). We can note a satisfying agreement between both solutions, illustrating that the nonlocal homogenized model can be employed for the topology optimization for taking into account strain gradients while only relying on a coarse mesh. Such procedure will be described in the next section.

5.2.4 Numerical examples

In this section, several numerical examples are presented to illustrate the capabilities of the proposed topology optimization in a strain gradient context. For all next examples, regular meshes with 4-node elements have been used. The plane stress assumption has been adopted. Here again, to maintain regular meshes during the topology optimization procedure, the regular mesh covers the holes and the related elements are associated to highly compliant properties. It is noted that even though the present method was validated in the last section, the reference solution is adopted during the optimization process to cooperatively adjust the direction of topology evolution. The Young's and Poisson's ratio for the material ($\rho_e = 1$) are respectively $E_m = 1000$ MPa and $\nu_m = 0.3$. The fictitious material properties for the holes ($\rho_e = \rho_{min}$) are taken as $E_i = 10^{-6}$ MPa and $\nu_m = 0.3$. At the initiation of the topology optimization, the material distribution is homogeneous with $\rho_e = 1$.

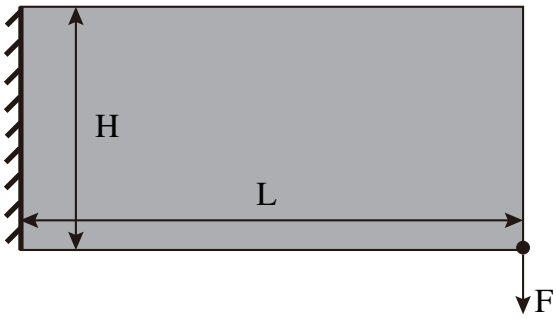

FIGURE 5.16: Cantilever beam lattice structure composed of periodic microscale unit cells: geometry and boundary conditions.

5.2.4.1 Cantilever beam with a concentrated load

In this first example, we investigate the topology optimization of a periodic lattice structure subjected to concentrated load. To study the influence of strain gradient effects, the dimensions of the unit cell range from large to small as compared with the dimensions of the structure. The geometry of the problem is described in Figure 5.16. The $x-$ and $y-$ displacements of the left end of the beam are both fixed.

A concentrated force load is applied on the bottom corner of the right end of the domain with a magnitude $F = 100$ N. The aspect ratio of the cantilever beam is chosen as 2 to highlight the strain gradient effects. The dimensions are $L \times H = 2000 \times 1000$ mm. The structure is a lattice composed of $N_s = s_1 \times s_2$ unit cells repeated periodically along each space direction, with s_1 and s_2 denoting the number of substructures along $x-$ and $y-$ directions, respectively. A coarse mesh composed of 5×5 elements is associated to the unit cells at the mesoscopic scale. The fine scale mesh on the RVE is composed of 50×50 elements to perform the microscopic unit cell computations. In this example, we keep $s_1 = 2s_2$ (see Figure 5.17). 5 cases are studied: (i) $s_1 \times s_2 = 2 \times 1$; (ii) $s_1 \times s_2 = 4 \times 2$; (iii) $s_1 \times s_2 = 8 \times 4$; (iv) $s_1 \times s_2 = 16 \times 8$; (v) $s_1 \times s_2 = 20 \times 10$ (Figure 5.17). These different cases correspond to the following coarse meshes for the structure: (i) 10×5 elements; (ii) 20×10 elements; (iii) 40×20 elements; (iv) 80×40 elements; and (v) 100×50 elements. It is worth reminding that the present homogenization method allows re-localizing the microscale fields. As a result, the total sensitivity number can be reduced by using the local operators in each subdomain. The target volume fraction for the optimized topology of the unit cells is 0.5.

Figure 5.17 shows different optimized topologies of the lattice structure for several numbers of unit cells along each direction and using the present method to take into account strain gradient and classical homogenization. Figure 5.17 (a) shows the final optimized geometry of the lattice taking into account strain gradient while Figure 5.17 (b) shows the final optimized geometry of the lattice without taking into account the

strain gradient. Figure 5.17 (c) and (d) only shows the optimized geometry of a single unit cell for comparison. Along rows (i) - (v), the number of unit cells repeated along each direction is increased and the ratio between the dimensions of the unit cells and the dimensions of the whole structure are decreased. Then for row (i) the scales are not separated while for row (v) the scales can be considered as separated. We can observe from Figures. 5.17 (i) and (v) that both topological strategies taking into account the strain gradient or not lead to different geometries of unit cells. We can also note that when scales are separated (row (v)), both methods lead to the same topology, which is expected. To quantify the gains obtained by the present method, we compare the compliances for optimized geometries of the lattice when the strain gradient is taken into account or not in Figure 5.18. We can see that using the present nonlocal homogenization method, the obtained resulting compliance is lower than using classical homogenization (then ignoring strain gradient effects), inducing a significant gain in the resulting stiffness of the lattice. We also note that when the number of unit cells is large, then both methods lead to the same compliance, which is also consistent as the scale are in this case separated.

In this work, standard BESO method is adopted to solve the proposed optimization problem. This method updates the topology of the RVE by removing certain amount of material step by step, in order to finally meet the volume constraint. Normally, the evolutionary volume ratio is set to 2% [76, 77] which means that 2% solid elements within the design domain are deleted from the previous design iteration. This value cannot be too large to avoid accidentally deleting too many solid elements at each iteration [76, 77]. However, if it is too small, more iterations are needed from the initial design to reach the final volume constraint. Taking the case (i) in this numerical experiment as an example, when we set the evolutionary volume ratio as 1%, the different optimized topologies of the lattice structure using the present method and classical homogenization are shown in Fig. 5.19. We can see that there is no noticeable difference of the topologies in Fig. 5.19 and Fig. 5.17 row (i). However, the solution in Fig. 5.19 requires twice the number of iterations since a small value of evolutionary volume ratio is adopted. In addition, a specified small number τ given in Eq. (3.16) is used to stop the optimization procedure when the volume constraint is satisfied and objective function is kept constant. In this case, when we set a smaller τ 0.1%, the optimized topologies for the cantilever beam lattice structure are shown in Fig. 5.20. We can see no change in the topology and thus no sensitivity on τ in this case.

As an illustration, we depict in Figure 5.21 the evolution of the microstructure topology for the case of non-separated scales (1×2 unit cells) using the present homogenization method for taking into account strain gradient effects. These evolutions correspond to different iterations in the topology optimization procedure. It is worth reminding that the present optimization method is able to start from an initial guess

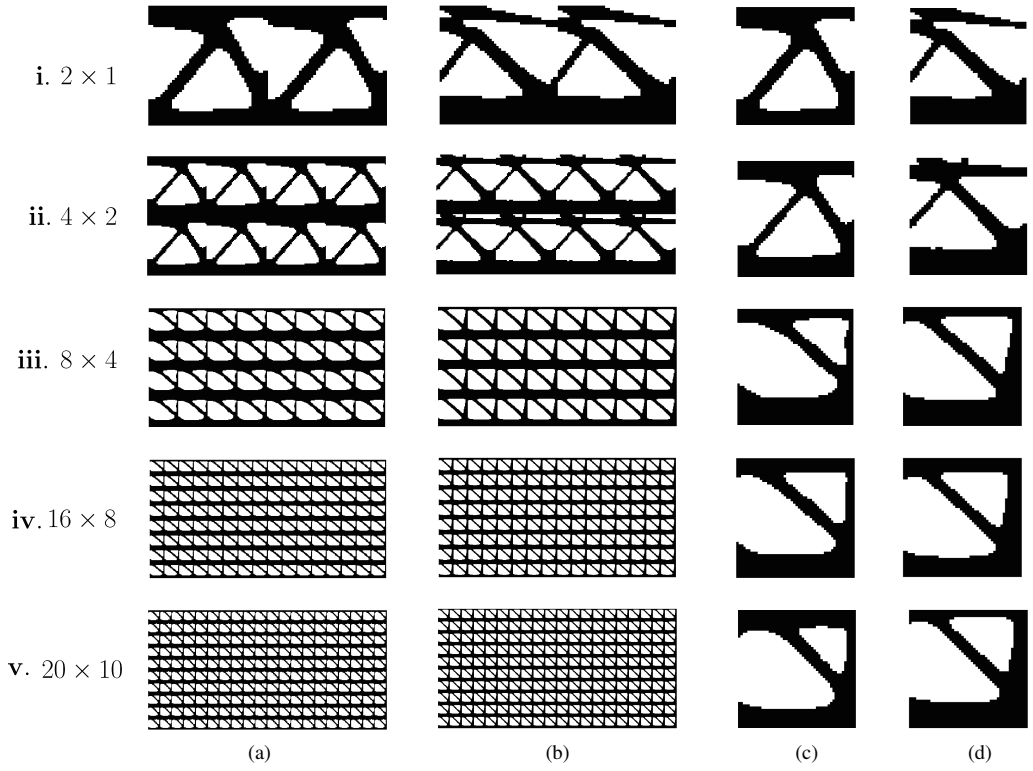

FIGURE 5.17: Optimized topologies for the cantilever beam lattice structure: columns (a), (b) compare the global lattices topologies when taking into account strain gradient or not in the optimization procedure; columns (c) and (d) show the corresponding unit cell. Rows (i) to (v) correspond to increasing the number of unit cells in the lattice leading to (i) non-separated scales; (v) separated scales.

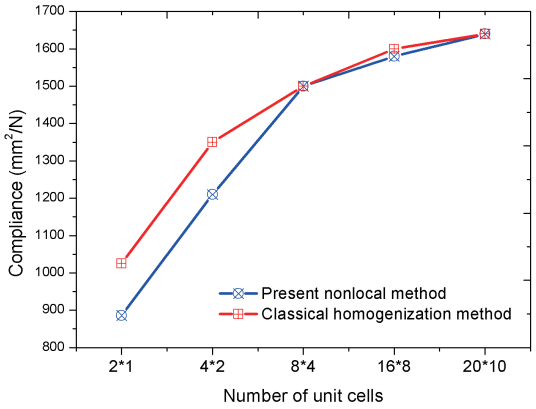

FIGURE 5.18: Compliance obtained by topological optimization when taking into account strain gradient effects (blue curve) and without taking into account strain gradient (red curve). Results are plotted as a function of the number of unit cells, and large number of unit cells leads to scale separation.

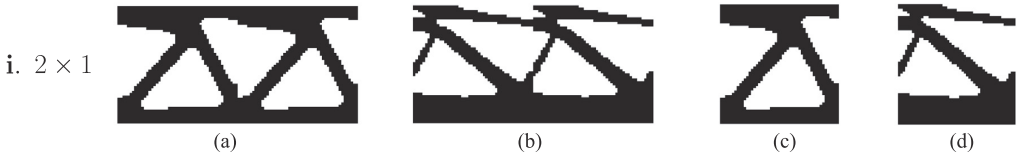

FIGURE 5.19: Optimized topologies for the cantilever beam lattice structure using small evolutionary volume ratio c_{er}: columns (a), (b) compare the global lattice topologies when taking into account strain gradient or not in the optimization procedure; columns (c) and (d) show the corresponding unit cell.

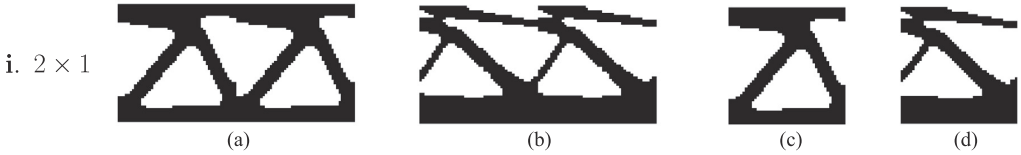

FIGURE 5.20: Optimized topologies for the cantilever beam lattice structure using small r: columns (a), (b) compare the global lattice topologies when taking into account strain gradient or not in the optimization procedure; columns (c) and (d) show the corresponding unit cell.

FIGURE 5.21: Evolution of the optimized topology of the unit cell for the cantilever beam lattice with $N_s = 2 \times 1$ periodic cells: (a) iteration 0; (b) iteration 10; (c) iteration 20; (d) iteration 30; (e) iteration 40 (final topology).

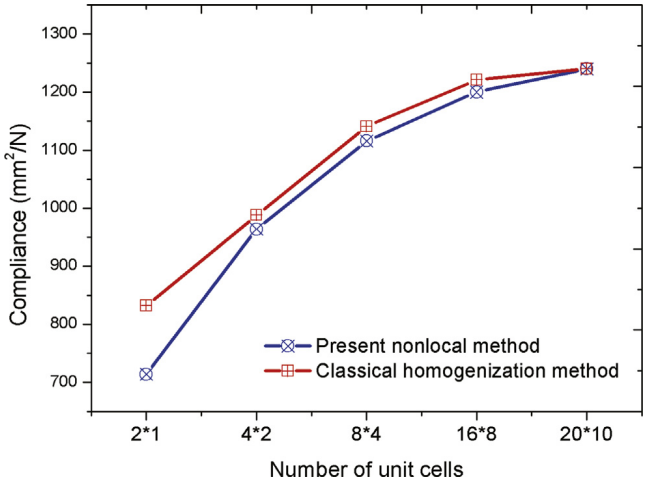

FIGURE 5.22: Compliance obtained by topological optimization when taking into strain gradient effects (blue curve) and without taking into account strain gradient (red curve). Results are plotted as a function of the number of unit cells, and large number of unit cells leads to scale separation.

without holes, which is not the case in most multiscale optimization methods available which require one or several holes for initiating the procedure.

It is noted that any volume fraction constraint can be selected by the designer in the present optimization procedure. In this example, when we set the volume fraction value to 0.6, the compliances for optimized geometries of the lattice when the strain gradient is taken into account or not are compared in Fig. 5.22. We can see that using the present nonlocal homogenization method, the obtained resulting compliance in this case is also lower than using classical homogenization, resulting in a higher stiffness of the structure. In addition, when the number of unit cells is large, then both methods lead to the same compliance, which is also consistent with the case when the volume constraint is set as 0.5.

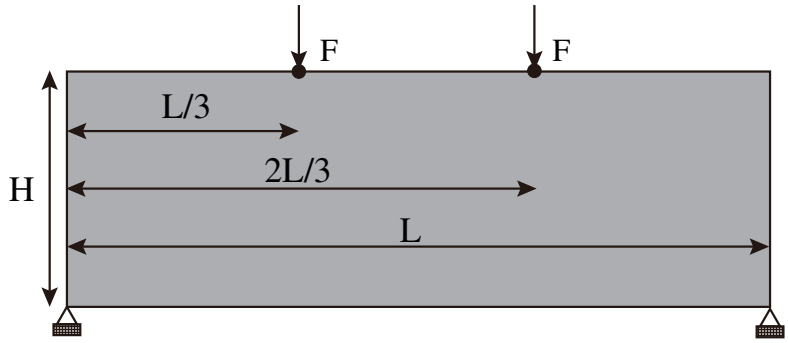

FIGURE 5.23: Four-point bending beam lattice structure composed of periodic unit cells: geometry and boundary conditions.

5.2.4.2 Four-point bending lattice structure

In this second example, a lattice structure is subjected to four-point bending. The geometry of the problem is depicted in Figure 5.23. The dimensions of the lattice structure along $x-$ and $y-$ are $L = 3000$ mm and $H = 1000$ mm, respectively. The left and right bottom corner nodes are fixed in both $x-$ and $y-$ directions. On the upper end concentrated forces are applied (see Figure 5.23).

The loading force is taken as $F = 100$ N. The mesh used for the fine scale within the RVE is composed of 40×40 elements. The target volume fraction for the optimized topology of unit cells is 0.6. As in the previous example, the number of unit cells composing the lattice is varied to study the effects of the scale separation. Then, the following numbers of unit cells along each directions are investigated: (i) 3×1; (ii) 6×2; (iii) 15×5; (iv) 30×10; and (v) 48×16. The corresponding coarse meshes are composed of respectively (i) 15×5 elements; (ii) 30×10 elements; (iii) 75×25 elements; (iv) 150×50 elements and (v) 240×80 elements. It is worth noting that in the last case, solving the topology optimization problem with a direct meshing of the microstructure would involve 2,462,722 degrees of freedom. Using the present technique, the topological optimization procedure only uses the nodes of the coarse mesh through the homogenized nonlocal model and then drastically reduces the computational costs. For the last case, the coarse mesh only contains $39,042$ degrees of freedom.

As in the previous example, Figure 5.24 shows the different optimized topologies of the lattice structure for several number of unit cells along each direction and using on one hand the present method to take into account strain gradient and classical homogenization. We can observe from Figures. 5.24 (i) and (v) the different topologies when strain gradient is taken into account or not. Here again, when scales are separated (row (v)), both methods lead to the same topology. We compare the compliances for optimized geometries of the lattice when the strain gradient is taken into account or not in Figure 5.25. Using the present nonlocal homogenization method, the obtained

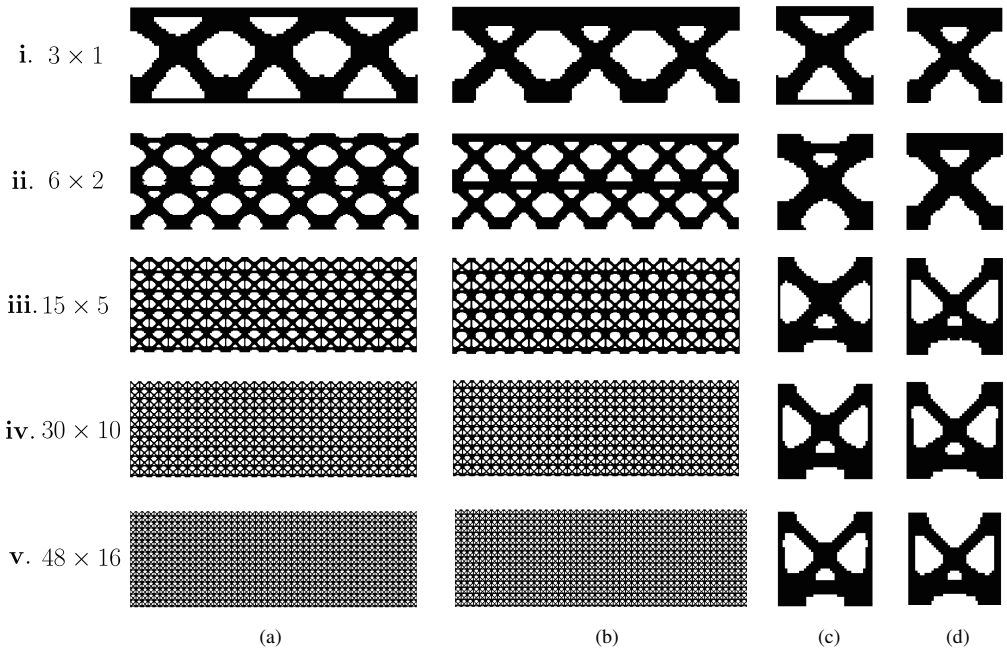

FIGURE 5.24: Optimized topologies for the four-point bending beam lattice structure: columns (a), (b) compare the global lattices topologies when taking or not into account strain gradient in the optimization procedure; columns (c) and (d) show the corresponding unit cell. Rows (i) to (v) correspond to increasing the number of unit cells in the lattice leading to (i) non-separated scales; (v) separated scales.

resulting compliance is here again lower than using classical homogenization (then ignoring strain gradient effects), inducing a significant gain in the resulting stiffness (or a decrease in the compliance) of the lattice. The evolution of the topology of the unit cell for the case (v) is shown in Figure 5.26. The whole multiscale topological design process converges after 34 iterations in this case. These results show that when scales are not separated, the present topology optimization based on a homogenization method taking into account strain gradient brings an added value by inducing a larger stiffness of the final lattice.

5.3 Topology optimization of structures with fixed periodic microstructures

This section extends the topology optimization to structural design with fixed/given periodic cells at the microscopic scale in the context of non-separated scales. The nonlocal filter-based homogenization method introduced in Section 5.2 is adopted to deal with the heterogeneities of the given RVE and perform the multiscale computations.

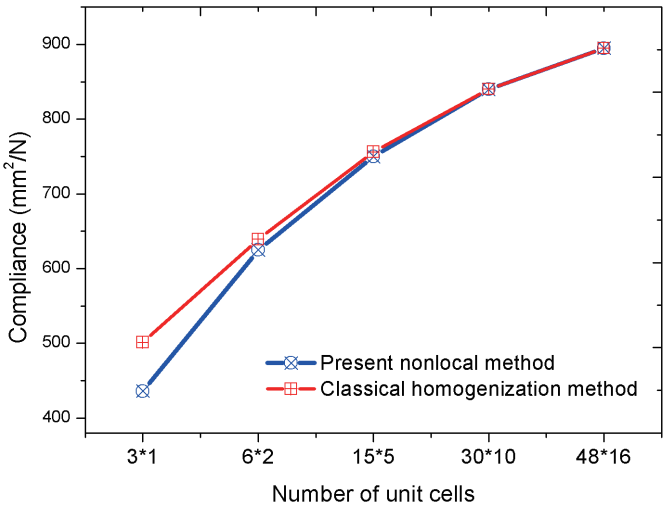

FIGURE 5.25: Compliance obtained by topological optimization when taking into strain gradient effects (blue curve) and without taking into account strain gradient (red curve) for the four-point bending beam. Results are plotted as a function of the number of unit cells, and large number of unit cells leads to scale separation.

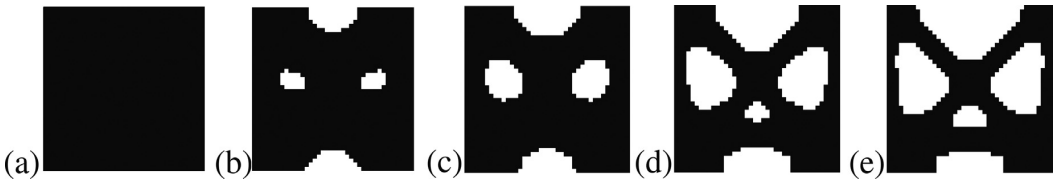

FIGURE 5.26: Evolution of the optimized topology of the unit cell for the four-point bending beam with $N_s = 48 \times 16$ periodic cells: (a) iteration 0; (b) iteration 5; (c) iteration 10; (d) iteration 20; (e) iteration 34 (final topology).

The topology optimization framework defining the microscopic RVE itself as the design variable is defined. Therefore, the local/microscopic computation only needs to be performed once over the RVE to account for the full microscopic heterogeneities, and topology of considered mesostructures is tailored in terms of the stiffness. In the following, the topology optimization model and the sensitivity analysis are given in Section 5.3.1. In Section 5.3.2, several numerical examples are presented to validate the proposed multiscale topology optimizaiton framework for designing the mesoscopic structures.

5.3.1 Optimization model and procedure

In this Section, the optimization problem aims to find the optimal topology of mesoscopic structure or the layout of previously defined substructures/microscopic unit cells so as to maximize the overall structural stiffness for the given amount of the substructures. It is assumed that the stiffness matrix of each subtructure is dependent on a binary design variable ρ_k, where ρ_k is equal to 1 or ρ_{min}, corresponding to existing or void substructure in the mesoscopic model, respectively. Therefore, the substructural stiffness can be expressed as

$$\hat{\mathbf{K}}_k(\rho_k) = (\rho_k)^P \hat{\mathbf{K}}_0 \tag{5.95}$$

where $\hat{\mathbf{K}}_0$ is the stiffness matrix for the solid substructures, P is the exponent of penalization. Note that the above interpolation is similar/identical to the SIMP model [141] except that the referred model is applied to isotropic materials, while the interpolation model in this work is defined directly on the substructure. This is because the substructure itself is defined as the design variable rather than the particular materials/elements. Therefore, with the volume constraint of previously defined substructures, the structural stiffness maximization problem herein can be formulated using the design variable ρ_k as

$$\text{Find} : \{\rho_k\} \tag{5.96}$$

$$\text{Minimize} : f_c(\rho_k, \hat{\mathbf{u}}) = \hat{\mathbf{F}}^T \hat{\mathbf{u}} \tag{5.97}$$

$$\text{subject to} : \hat{\mathbf{K}}\hat{\mathbf{u}} = \hat{\mathbf{F}} \tag{5.98}$$

$$: V(\rho_k) = \sum_k \rho_k v_k = V_{\text{req}} \tag{5.99}$$

$$: \rho_k = \rho_{min} \text{ or } 1, \; k = 1, \ldots, N_s \tag{5.100}$$

where f_c is known as the compliance functional, $\hat{\mathbf{F}}$ and $\hat{\mathbf{u}}$ are respectively the applied load and displacement vectors defined at the mesoscopic scale. The global stiffness matrix $\hat{\mathbf{K}}$ can be assembled from the stiffness of substructure $\hat{\mathbf{K}}_k$ shown in (5.95) in a

standard finite element way. The term v_k is the volume of the $k-$ substructure, and V_{req} is the target volume of the solid substructures depending on the number of the solid substructures over the whole mesoscopic structure.

In order to solve the above topology optimization problem, the sensitivity of the objective funtion f_{c} with respect to the design variable ρ_k should be explicited. With the help of the stiffness interpolation scheme (5.95), the derivation of the structural compliance against the design variable ρ_k can be expressed as

$$\frac{\partial f_{\text{c}}}{\partial \rho_k} = \hat{\mathbf{F}}^T \frac{\partial \hat{\mathbf{u}}}{\partial \rho_k} = \hat{\mathbf{F}}^T \hat{\mathbf{K}}^{-1} \left(\frac{\partial \hat{\mathbf{F}}}{\partial \rho_k} - \frac{\partial \hat{\mathbf{K}}}{\partial \rho_k} \hat{\mathbf{u}} \right) = -\hat{\mathbf{u}}^T \frac{\partial \hat{\mathbf{K}}}{\partial \rho_k} \hat{\mathbf{u}} = -P(\rho_k)^{P-1} \hat{\mathbf{u}}_k^T \hat{\mathbf{K}}_0 \hat{\mathbf{u}}_k \quad (5.101)$$

where $\hat{\mathbf{u}}_k$ is the displacement vector of the $k-$th substructure in the mesoscopic model. As mentioned, the stiffness matrix $\hat{\mathbf{K}}_0$ of solid subtructures is obtained by a fully microscopically-based framework with heterogeneous details over the RVE (see Section 5.2.1.2).

Then, the substructural sensitivity number in (5.101) can be obtained after further carrying out the mesoscopic structural computations on the coarse mesh (see also definition in Section 5.2.1.3). In order to adopt the evolutionary-type structural optimization methods, the obtained substructural sensitivity number, which denotes the ranking of substructures for updating the design variable ρ_k, is firstly modified by multiplying by a constant $-\frac{1}{P}$

$$\alpha_k = -\frac{1}{P} \frac{\partial f_{\text{c}}}{\partial \rho_k} = (\rho_k)^{P-1} \hat{\mathbf{u}}_k^T \hat{\mathbf{K}}_0 \hat{\mathbf{u}}_k \quad (5.102)$$

In order to avoid checkerboard patterns, the above formulated sensitivity number is smoothed by means of a filtering scheme 3.12. Due to the discrete nature of the design variable, and to avoid oscillations in evolutionary history of the design objective value so as to improve the convergence, the current sensitivity number is further averaged with its historical information as in 3.14.

Before executing the evolutionary procedure based on the computed substructural sensitivity number, the target volume of solid substructures for the current iteration needs to be assigned as 3.15. Once the volume constraint V_{req} is reached, the volume fraction of substructures will be kept constant and the optimization algorithm alters only the topology. The optimization procedure will iteratively conduct the mesoscopic structural computations and update the topology of mesoscopic structure until the volume constraint V_{req} is reached and the convergence criterion 3.16 is satisfied.

To sum up, the overall multiscale topology optimization procedure for designing the mesoscopic heterogeneous structures with fixed microscopic unit cells in the context of non-separated scales is described as follows.

1. Give the geometry of the RVE, set a fine mesh to discretize the RVE at the microscopic scale. Set another coarse mesh associated with the heterogeneous structure, such that each substructure/unit cell is meshed with the same number of coarse elements.

2. Solve once the microscopic/local probelm over the RVE to establish the consitutive law and link the microscopic and mesoscopic scales as summarized in Section 5.2.1.2.

3. Solve the mesoscopic structure problem as summarized in Section 5.2.1.3.

4. Based on the stiffness matrix of solid substructures/unit cells and the nodal displacement solution from the mesoscopic problem over the coarse mesh, evaluate the sensitivity of each substructure/unit cell by (5.101).

5. Modify the substructural sensitivity number by Equation (5.102) and smooth it by using Equations (3.12) and (3.14).

6. Update the topology of considered mesoscopic structure according to (3.15).

7. Repeat 3-6 until the volume constraint V_{req} is satisfied and the convergence criterion (3.16) is reached.

5.3.2 Numerical examples

In this section, several numerical examples for designing the topology of heterogeneous mesostructures using predefined microscopic substructures/unit cells are presented. Before starting the whole optimization procedure, the geometry of microscopic RVE should be firstly provided. For all adopted microscopic cells in this work, the local solid material and void phases at the micro scale are treated as isotropic with Young's coefficients $E_s = 1000$ MPa and $E_i = 10^{-6}$ MPa, respectively. Poisson's coefficient is $\nu = 0.3$. In order to ensure the consistency of all numerical examples and fairly compare the resultant designs, the volume fractions of the solid materials in all adopted RVEs are set as 60%. At the higher scale, the volume fraction of the solid microscopic cells gradually decreases from an initial 100% to target 50%, which means that the local solid isotropic material occupies 30% of the whole structural domain area for the resultant designs. Plane stress condition is assumed for all examples.

5.3.2.1 A double-clamped beam

The boundary conditions of the mesoscopic double-clamped beam in this first example are depicted in Figure 5.3 in Section 5.1. The structure is made up of a square domain, where the left and right ends are both fixed. A concentrated force $F = 1$ KN is located

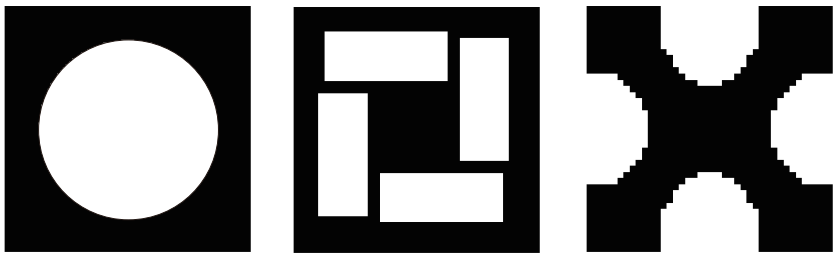

FIGURE 5.27: Illustration of three microscopic unit cells for the double-clamped beam:(a) unit cell A; (B) unit cell B; (c) unit cell C.

at the centre point of the double-clamped beam, and the side of the beam is $L = 1000$ mm. To start the developed design optimization model, three guess designs of the microscopic RVE are considered as illustrated in Figure 5.27: unit cell A is full of solid material except for a centered hole with diameter corresponding to the volume fraction of solid phases 60%; unit cell B is an anisotropic structure with four void rectangles to meet the same volume fraction of solid phases; unit cell C is a simple crossed structure. For each microscopic unit cell, a coarse mesh 4×4 is associated at the mesoscopic scale, while the microscopic mesh is composed of 40×40 regular four-node bilinear elements. Firstly, the considered double-clamped structure is initially divided into $N_s = s_x \times s_y$ repeatable unit cells, where s_x and s_y denote the number of substructures along $x-$ and $y-$ directions, respectively. In this example, three cases with the following numbers of $s_x \times s_y$ unit cells are considered: (i) 20×20; (ii) 40×40; (iii) 80×80. Therefore, these configurations correspond to coarse meshes for the whole structure of 80×80 elements, 160×160 elements, and 320×320 elements, respectively. Therefore, at the end of the design optimization, the number of solid microscopic cells for the resultant structures should be respectively 200, 800, and 3200 to meet the target volume fraction 50%.

Figure 5.28 shows the optimized double-clamped beam using specific microscopic unit cells with different coarse meshes at the mesoscopic scale, i.e. different numbers of substructures adopted. Each row in Figure 5.28 shows the final optimized geometries of the double-clamped beam, with the increased numbers of unit cells repeated along each direction, while each column shows the final optimized geometries of the double-clamped beam using different microscopic unit cells. As shown in Figures 5.28 (Ai), (Bi), and (Ci), the resultant topologies are totally different since different microscopic cells are adopted. The symmetrical mesostructures are generated when adopting microscopic cells A and C, while the resultant structure is asymmetric with unit cell B. This phenomenon is reasonable since the cell B itself is not symmetrical. With increasing the number of microscopic cells, the optimized designs with unit cells A and C are kept the same as a cross structure. It is noted that the final optimized geometries are

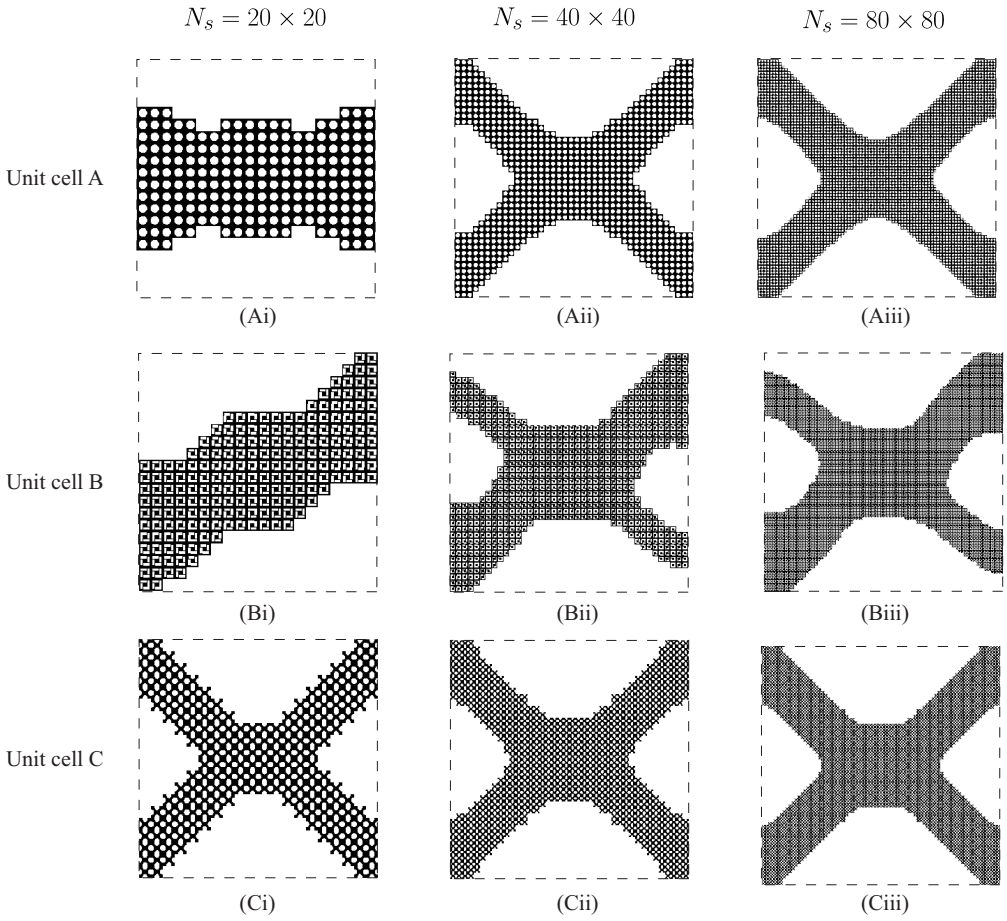

FIGURE 5.28: Optimized heterogeneous double-clamped structures using specified unit cells and different coarse meshes at mesoscopic scale.

FIGURE 5.29: Illustration of three microscopic unit cells for the cantilever beam:(a) unit cell A; (B) unit cell B; (c) unit cell C.

totally different for cases (Ai) and (Aii), which demonstrates the necessity of subdividing the mesostructure using different numbers of microscopic cells. The same effect is observed for optimized geometries in Figures (Bi) and (Bii).

5.3.2.2 A cantilever beam

The second example aims to topologically design a mesoscopic cantilever beam subjected to a concentrated load with different microscopic cells. The problem geometry of the mesoscopic beam is shown in Figure 5.5. The left side of the considered beam is fixed and a concentrated force $F = 100$ N is located on the bottom point of the right end of the domain. The dimensions of the beam are $L \times H = 2000 \times 1000$ mm. Similar to the previous example, three RVEs are considered as shown in Figure 5.29. Unit cells A and B have respectively a circle and rectangle area as void phase to meet the volume fraction of solid phase of 60%, and unit cell C is optimally obtained by the design procedure in the Section 5.2 for the periodic cantilever beam with the same volume constraint of the solid phase.

The mesh of microscopic RVE is composed of 50×50 square shaped bilinear elements at the microscale and 5×5 elements at the mesoscopic scale. In order to demonstrate the proposed design framework, the following numbers of substructures $s_x \times s_y$ are separately considered here: (i) 20×10; (ii) 40×20; (iii) 80×40. As the successive increasing number of periodic unit cells in each direction, the above cases reduce to coarse mesh with (i) 100×50 elements; (ii) 200×100 elements; (iii) 400×200 elements at the mesoscopic scale, respectively. The optimized geometries of mesoscopic cantilever beam with specific microstructures for above different cases are given in Figure 5.30. It is seen that the geometries of optimized mesostructures are totally different with the adoption of different microscopic RVEs, which further demonstrates the effectiveness of the proposed mutiscale design framwork. The final compliances of the optimized structures are shown also in Figure 5.30. As expected, with the same number of unit cells in each direction, the mesostructures composed of optimally designed microscopic cell C always have the higher stiffness than other solutions. Figure 5.31 shows the evolution of the topology of the mesoscopic cantilever beam for the case (Cii). These evolutions correspond to different iterations in the topology optimization procedure, and the whole design optimization process converges after 40 iterations in this case.

5.4 Concluding remarks

In this section, we have presented a topological optimization method for lattice structures in the case when scales are not separated, i.e. when the characteristic dimensions of the unit cells are not much lower than the dimensions of the structure. This case can occur in many situations, for example in additive manufacturing processes where very large times can be necessary to produce lattice structures with very small dimensions. In this context, the assumption of scale separation might be violated. Firstly, we have

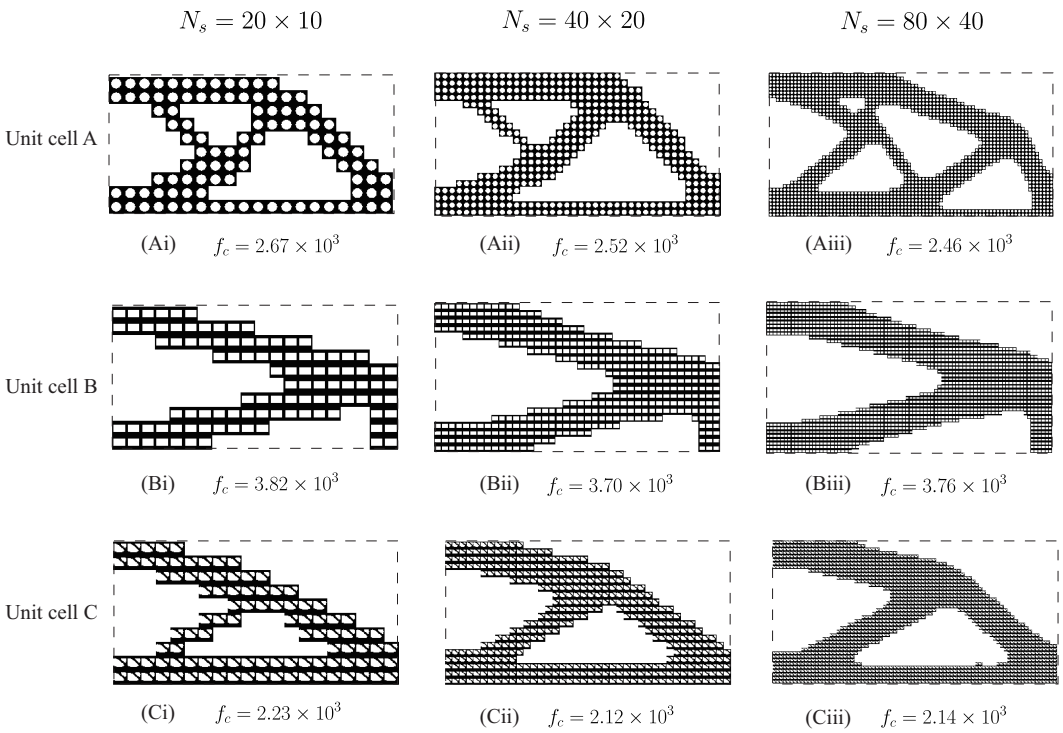

FIGURE 5.30: Optimized heterogeneous cantilever beams using specified unit cells and different coarse meshes at mesoscopic scale.

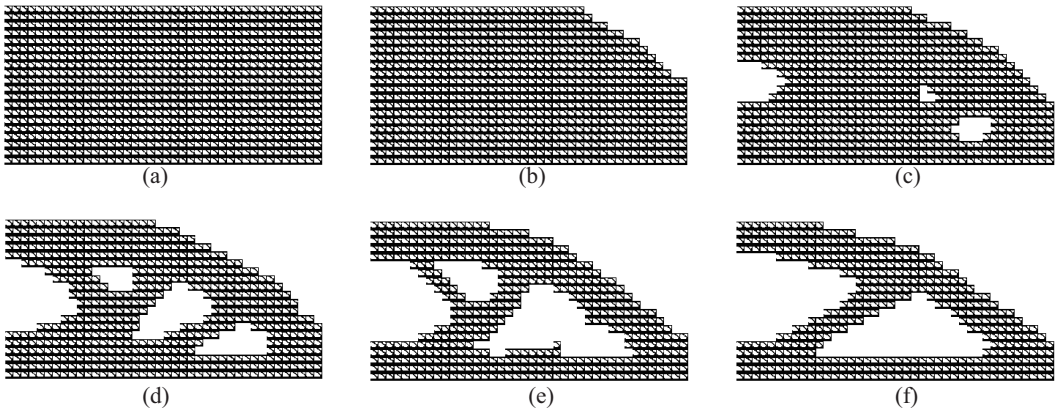

FIGURE 5.31: Evolution of the optimized cantilever beam for the case (Cii): (a) iteration 0; (b) iteration 5; (c) iteration 10; (d) iteration 20; (e) iteration 30; (f) iteration 40 (final topology).

proposed a topology optimization for periodic structures based on the classical homogenization method but in the context of non-separated scales. The present method uses a coarse mesh corresponding to a homogenized medium based on the classical numerical homogenization, allowing reducing the micro fields to perform the topology optimization. On the other hand, topology optimization using a fully detailed description of the heterogeneous structure is performed as a comparison. Size effect of the periodic unit

cell is investigated to analyse the effectiveness of the present topology optimization based on classical homogenization method. We have shown that the present topology optimization will lead to optimized structure with higher compliance when the scales can clearly not be separated (few number of unit cells). Furthermore, with the increase of number of unit cells, the number of degrees of freedom to be solved can be drastically reduced as compared with the reference solution. In other words, for a large number of unit cells, the present method takes less time to obtain the optimized lattice structure without losing any stiffness. In addition, we have proposed another similar topology optimization framework which is also based on a coarse mesh to reduce the computational times, while taking into account all structural details and the strain gradient effects by a non-local homogenization method. We have shown that taking into account strain gradient effects can lead to a significant increase in the stiffness of the lattice associated with the optimized topology.

Finally, we have extended the topology optimization framework to design the geometry of mesoscopic structures with specific microscopic unit cells. The microscopic substructure/RVE can be selected through existing materials, artificial definitions, or optimal designs. Several interesting mesoscopic structures composed of customized RVEs are obtained for specific volume constraints and boundary conditions. Numerical examples have shown that structural geometries of the predefined RVE have major influence on the optimal solutions of the mesoscopic structures, demonstrating the effectiveness and significance of the proposed topological design framework. In order to further release design freedom within multiscale design scheme, the design model could be extended to a concurrent topology optimization framework for heterogeneous materials and structures in the context of non-separated scales, involving the topological design of the microscopic unit cells simultaneously.

Part III

Phase field modeling and fracture resistance design

Chapter 6

Phase field for crack propagation in linear viscoelastic materials

Heterogeneous materials like concrete are important constitutive materials of civil structures whose main role is to ensure high level of performance regarding the required middle to long-term containment function. As such, creep and microcracking are known as significant factors affecting the mechanical properties and the long term behavior of concrete, and may reduce the safety of civil facilities. The accurate modelling of these phenomena including their coupled effects have then to receive a special attention. We propose in this Chapter to apply the relatively recent method making use of a phase field approach to reproduce the initiation and propagation of microcracking in heterogeneous materials. This method relies on a diffuse description of the microcrack surfaces by one scalar variable whose values result from a specific balance equation. As a main contribution, it is extended here and coupled to a linear viscoelastic behavior to mimic the creep (and possibly shrinkage) of the heterogeneous materials. A classical generalized Maxwell model is adopted for modelling this viscoelastic behavior.

In the following, an energy-based formulation is first developed in Section 6.1 to express the equations governing both viscoelastic mechanical and phase field problems. In this first attempt, only cracking due to extensions is considered. In Section 6.2, the classical generalized Maxwell model is adopted for modelling this viscoelastic behavior. The overall algorithm using the staggered solution scheme for phase field crack propagation is given in Section 6.3. Finally, several 2D and 3D numerical examples of heterogeneous concrete samples made up of elastic aggregates dispersed in a mortar matrix concentrating the viscoelastic behavior are presented in Section 6.4.

6.1 Extension of the phase field method to viscoelasticity

In this section we describe an extension of the phase field model for fracture to linear viscoelastic materials. An energy-based formulation is first developed in Section 6.1.1.

Viscoelastic mechanical and phase field problems are formulated in Section 6.1.2 and 6.1.3, respectively.

6.1.1 Variational principle

For a viscoelastic cracked body defined in a domain $\Omega \subset \mathbb{R}^3$ containing sharp cracks denoted collectively as Γ, we define the total energy of the system as:

$$E = \int_\Omega \Psi(\varepsilon, \alpha^V, \Gamma) d\Omega + \int_\Omega \phi^V(\dot{\alpha^V}) d\Omega + G_c \int_\Gamma d\Gamma \tag{6.1}$$

where $\Psi(\varepsilon, \alpha^V, \Gamma)$ is the elastic strain density function, $\phi^V(\dot{\alpha^V})$ is a dissipative potential and G_c is the critical energy release rate in the sense of Griffith. The associated regularized form is given by:

$$E = \int_\Omega \Psi(\varepsilon, \alpha^V, d) d\Omega + \int_\Omega \phi^V(\dot{\alpha^V}) d\Omega + G_c \int_\Omega \gamma(d, \nabla d) d\Omega \tag{6.2}$$

where γ is a crack density function, and

$$\Psi = g(d)\tilde{\Psi}^+(\varepsilon^+) + \tilde{\Psi}^-(\varepsilon^-), \quad \phi^V = g(d)\tilde{\phi}^V \tag{6.3}$$

where $g(d)$ is a degradation function such that $g(0) = 1$, $g(1) = 0$ and $g'(1) = 0$ and $\tilde{\Psi}^+(\varepsilon^+)$ and $\tilde{\Psi}^+(\varepsilon^-)$ denote parts of the strain density related to tensile and compressive parts of the strain tensor, respectively (see [108]). We define the set of internal variables $\alpha^V = \{\varepsilon_1^V, \varepsilon_2^V, ..., \varepsilon_N^V\}$,

Such that

$$\varepsilon^e = \varepsilon - \sum_{i=1}^{N} \varepsilon_i^V \tag{6.4}$$

where ε_i^V denote dissipative viscous strains. The driving forces associated with ε_i^V are defined as

$$\mathcal{A}_i = \frac{\partial \Psi}{\partial \varepsilon_i^V} \tag{6.5}$$

or

$$\mathcal{A}_i = -\frac{\partial \phi^V}{\partial \dot{\varepsilon}_i^V} \tag{6.6}$$

Combining both above equations, we obtain:

$$\frac{\partial \Psi}{\partial \varepsilon_i^V} + \frac{\partial \phi^V}{\partial \dot{\varepsilon}_i^V} = 0 \tag{6.7}$$

The variational approach to fracture as proposed in Bourdin, Francfort and Marigo [54, 25, 26] and developed in a convenient algorithmic setting by Miehe [108] is adopted

here. The phase field formulation implies: (a) minimization of the total energy with respect to the displacement field $\mathbf{u}$ and (b) minimization of the energy with respect to the scalar field d describing the crack surface in a smooth manner. This second minimization is subjected to an inequality constraint: $\dot{d} \geq 0$. To formulate this minimization problem in a simpler setting, we introduce a time-stepping $\mathcal{T} = \{t^0, t^1, ..., t^n, t^{n+1}, ..., t^N\}$. At each time step t^{n+1}, the problem is to find the displacement fields $\mathbf{u}^{n+1}$ and d^{n+1} such that

$$\mathbf{u}^{n+1}, d^{n+1} = \underset{\substack{\mathbf{u}\in\mathcal{K}_A \\ 0\leq d^n \leq d^{n+1}}}{\text{Argmin}}\, E \tag{6.8}$$

where $\mathcal{K}_A$ is a set of kinematically admissible fields. One possible algorithm to solve this problem is to use sequential solving of both minimization problems as

$$D_{\delta\mathbf{u}}\mathcal{L} = 0 \tag{6.9}$$

$$D_{\delta d}\mathcal{L} = 0, \;\; 0 \leq d^n \leq d^{n+1} \tag{6.10}$$

where $D_\delta v f(\mathbf{u})$ is the Gateaux derivative.

The first equation (6.9) defines the mechanical problem while the second one (6.10) defines the phase field problem. These two problems are coupled as both involve the fields $\mathbf{u}$ and d.

6.1.2 Mechanical problem

Eq. (6.9) can be developed as

$$\int_\Omega \frac{\partial \Psi}{\partial \varepsilon}(\varepsilon, \alpha^V, d) : \varepsilon(\delta\mathbf{u}))d\Omega = 0 \tag{6.11}$$

where

$$\sigma = \frac{\partial \Psi}{\partial \varepsilon}(\varepsilon, \alpha^V, d) \tag{6.12}$$

and (6.7) can be used to define the evolution law for α^V. The Euler -Lagrange equation associated with (6.11) is given by:

$$\nabla \cdot \sigma = 0, \;\; \sigma\mathbf{n} = \overline{F} \text{ over } \partial\Omega_F, \;\; \mathbf{u} = \overline{\mathbf{u}} \text{ over } \partial\Omega_u \tag{6.13}$$

6.1.3 Phase field problem

The first equation in (6.10) can be developed as:

$$\int_\Omega \frac{\partial \Psi}{\partial d}\delta d \, d\Omega + \int_\Omega \frac{\partial \phi^V}{\partial d}\delta d \, d\Omega + G_c \int_\Omega D_{\delta d}\gamma d\Omega = 0 \tag{6.14}$$

Choosing

$$\gamma = \frac{1}{2\ell}d^2 + \frac{\ell}{2}\nabla d \cdot \nabla d \tag{6.15}$$

we obtain

$$\int_\Omega \left\{ \frac{\partial \Psi}{\partial d}\delta d + \frac{\partial \phi^V}{\partial d}\delta d + \frac{G_c}{\ell}\left(d\delta d + \ell \nabla d \cdot \nabla(\delta d)\right) \right\} d\Omega = 0, \tag{6.16}$$

or

$$\int_\Omega \left\{ \left(\frac{\partial \Psi}{\partial d} + \frac{\partial \phi^V}{\partial d} + \frac{G_c}{\ell}d \right)\delta d + \ell G_c \nabla d \cdot \nabla(\delta d) \right\} d\Omega = 0 \tag{6.17}$$

$$= \int_\Omega \left\{ \left(g'(d)\left[\tilde{\Psi}^+ + \tilde{\phi}^V\right] + \frac{G_c}{\ell} \right)\delta d + \ell G_c \nabla d \cdot \nabla(\delta d) \right\} d\Omega = 0 \tag{6.18}$$

Choosing $g(d) = (1-d)^2$, we obtain:

$$= \int_\Omega \left\{ \left(-2(1-d)\left[\tilde{\Psi}^+ + \tilde{\phi}^V\right] + \frac{G_c}{\ell}d \right)\delta d + G_c \ell \nabla d \cdot \nabla(\delta d) \right\} d\Omega = 0 \tag{6.19}$$

or

$$\int_\Omega \left(2\left[\tilde{\Psi}^+ + \tilde{\phi}^V\right] + \frac{G_c}{\ell} \right) d\delta d + G_c \ell \nabla d \cdot \nabla(\delta d) d\Omega = \int_\Omega 2\left[\tilde{\Psi}^+ + \tilde{\phi}^V\right]\delta d d\Omega \tag{6.20}$$

The associated Euler-Lagrange equations are given by:

$$\left(2\left[\tilde{\Psi}^+ + \tilde{\phi}^V\right] + \frac{G_c}{\ell} \right) d - \ell G_c \Delta d = 2\left[\tilde{\Psi}^+ + \tilde{\phi}^V\right], \;\; \nabla d \cdot \mathbf{n} = 0 \text{ over } \partial\Omega_G, \;\; d = 1 \text{ over } \Gamma \tag{6.21}$$

where Δd denotes the Laplacian operator. Enforcing the irreversibility condition can be prescribed in several ways (see e.g. [92, 108], e.g. by enforcing the Dirichlet condition $d = 1$ at the nodes where the phase field has reached a value of $d = 1$. In addition, we adopt the formulation of Miehe [108] by introducing a history function $\mathcal{H}$ which substitutes $\tilde{\Psi}$ to handle loading and unloading and defined as:

$$\mathcal{H}(\mathbf{x}, t) = \max_{\tau \in [0,t]} \left\{ \tilde{\Psi}^+(\mathbf{x}, \tau) + \tilde{\phi}^+(\mathbf{x}, \tau) \right\} \tag{6.22}$$

which leads to:

$$\left(2\mathcal{H} + \frac{G_c}{\ell}\right) d + \ell G_c \Delta d = 2\mathcal{H}, \quad \nabla d \cdot \mathbf{n} = 0 \text{ on } \partial\Omega_G \quad d = 1 \text{ on } \Gamma \tag{6.23}$$

6.2 Generalized Maxwell viscoelastic model

We now specify the equations of the generalized Maxwell model. For the sake of simplification, we do not consider here tensile and compressive decomposition of the strain tensor (i.e. assume that the loads do not induce auto-contact within the cracks). In addition, still for for the sake of simplification, the model used here mixes both deviatoric and hydrostatic parts within the same model, while in more realistic models deviatoric and hydrostatic parts of the viscous strains are separated for the strain tensor, or only the deviatoric part is involved. With these simplifications in mind, we define:

$$\Psi = \frac{1}{2}(1-d)^2 \mathbb{C} : (\varepsilon - \sum_{i=1}^{n} \varepsilon_i^V) : (\varepsilon - \sum_{i=1}^{n} \varepsilon_i^V) \tag{6.24}$$

The dissipative potential is given by:

$$\phi^V = g(d)\tilde{\phi}^V, \quad \tilde{\phi}^V = \sum_{i=1}^{n} \phi_i^V \tag{6.25}$$

where

$$\phi_i^V = \mu_i \tau_i \left|\dot{\varepsilon}_i^V\right|^2 \tag{6.26}$$

Then,

$$\frac{\partial \phi_i^V}{\partial \dot{\varepsilon}_i^V} = (1-d)^2 2\mu_i \tau_i \dot{\varepsilon}_i^V \tag{6.27}$$

and

$$\frac{\partial \Psi}{\partial \varepsilon_i^V} = -(1-d)^2 \mathbb{C} : (\varepsilon - \sum_{i=1}^{n} \varepsilon_i^V) \tag{6.28}$$

Using (6.7), we have:

$$2\mu_i \tau_i \dot{\varepsilon}_i^V = \mathbb{C} : (\varepsilon - \sum_{i=1}^{n} \varepsilon_i^V) \tag{6.29}$$

which provides an evolution law for $\dot{\varepsilon}_i^V$.

Defining:

$$\dot{\varepsilon}_i^V = \frac{\left\{\varepsilon_i^V\right\}^{n+1} - \left\{\varepsilon_i^V\right\}^n}{\Delta t} \tag{6.30}$$

we obtain:

$$\left\{\varepsilon_i^V\right\}^{n+1} = \left\{\varepsilon_i^V\right\}^n + \frac{\mathbb{C} : (\varepsilon^{n+1} - \sum_{i=1}^n \left\{\varepsilon_i^V\right\}^n)}{2\mu_i\tau_i}\Delta t \tag{6.31}$$

6.3 Overall algorithm

The overall algorithm to solve the problem of fracture in a viscoelastic solid is defined as follows. At each loading step t^n, given: $\left\{\varepsilon_i^V\right\}^n$ and d^n:

1. Solve the mechanical problem (6.11) for $\mathbf{u}^{n+1}$;
2. Compute $\left\{\varepsilon_i^V\right\}^{n+1}$ using (6.31);
3. Compute $\mathcal{H}^{n+1}$ usig (6.22);
4. Solve the phase field problem (6.20) for d^{n+1};
5. Set $d^n = d^{n+1}$, $\left\{\varepsilon_i^V\right\}^n = \left\{\varepsilon_i^V\right\}^{n+1}$, $\mathbf{u}^n = \mathbf{u}^{n+1}$.

6.4 Numerical examples

6.4.1 A homogeneous 2D plate

The problem setting of a 2D plate with one pre-existing crack notch is illustrated in Fig. 6.1(a). The plate is homogeneous with material properties given in Table 6.1. The dimensions of the plate are 50×100 mm which is uniformly discretized into 60×120 square shaped bilinear elements. Plane strain conditions are adopted. The lower end of the plate is fixed vertically and free horizontally, while the left bottom corner node is fixed in both directions to avoid rigid body motions. The upper end of the plate incremental displacement $\Delta\bar{\mathbf{u}} = 0.002$ mm is prescribed for each loading/time step. Different time intervals, i.e., $\Delta t = 0.25s$, $\Delta t = 0.5s$, and $\Delta t = 1s$, are respectively defined to investigate the time effects on the considered viscoelastic cracked body. The incremental loading process continues until the reaction forces is below a prescribed criterion value indicating that the structure is completely broken.

The final crack patterns of the above formulated three cases as well as the corresponding load-displacement curves are given in Fig. 6.2. For a specific displacement value of the upper end of the plate, for instance, $\bar{U} = 0.106$ mm, the corresponding crack patterns of the three cases are illustrated in Fig. 6.3. For a specific time point after

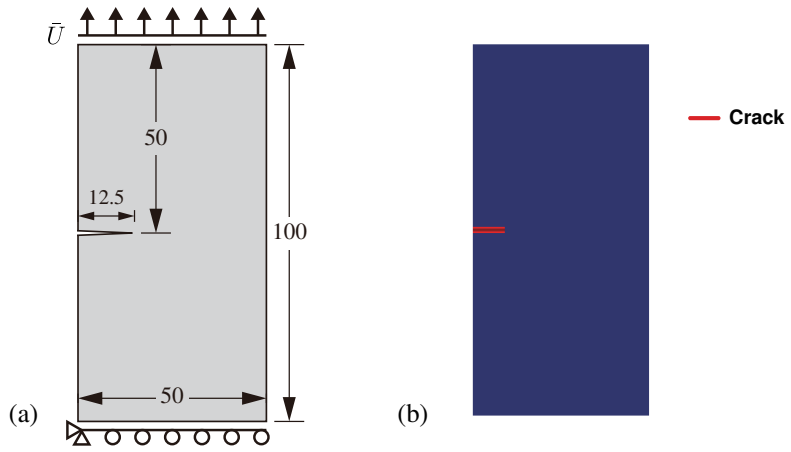

FIGURE 6.1: A plate with one pre-existing crack notch subjected to incremental traction loads: (a) problem geometry; (b) initial crack.

loading, for instance, $\mathcal{T} = 16.25s$, the corresponding crack patterns of the three cases are illustrated in Fig. 6.4.

TABLE 6.1: Material properties

Name	Symbol	Value	Unit
Young's modulus	E	3	GPa
Poisson's ratio	ν	0.3	[-]
Fracture toughness	G_c	3.3×10^{-3}	KN/mm
Relaxation time	τ	5.882	s

6.4.2 A heterogeneous 2D composite plate

The problem setting of this example is the same as the previous one, while the considered plate is composed of two different materials, i.e. matrix and inclusion phases, as shown in Fig. 6.5. The material properties of two phases are given in Table 6.2. The incremental displacement load is set as $\Delta\bar{\mathbf{u}} = 0.005$ mm, and these cases with different time intervals $\Delta t = 0.25s$, $\Delta t = 0.5s$, and $\Delta t = 1s$ are defined, respectively. The final crack patterns as well as the corresponding load-displacement curves are given in Fig. 6.6. For a specific displacement value of the upper end of the plate, for instance, $\bar{U} = 0.165$ mm, the corresponding crack patterns are illustrated in Fig. 6.7. For a specific time point after loading, for instance, $\mathcal{T} = 12s$, the corresponding crack patterns are illustrated in Fig. 6.8.

6.4.3 A heterogeneous 3D composite plate

The problem setting of a 3D plate with one pre-existing crack notch surface is shown in Fig. 7.16. The material properties are given in Table 6.3. The dimensions of the 3D plate

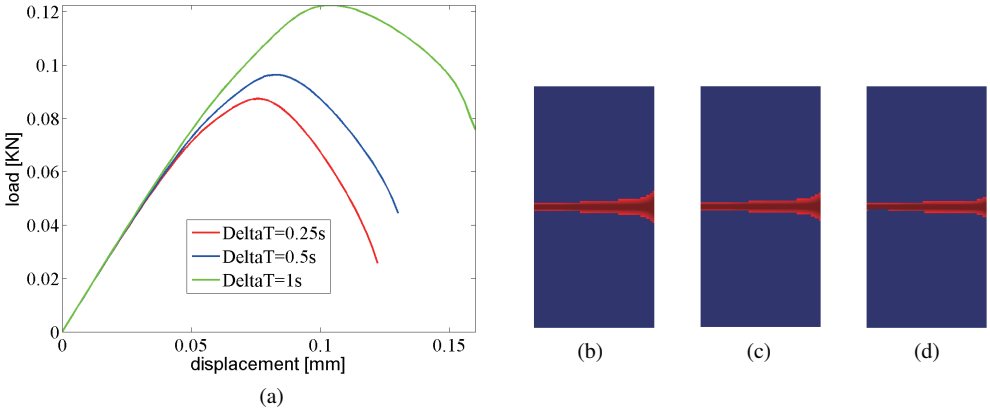

FIGURE 6.2: (a) Force-displacement curves for three cases, (b) final crack pattern for $\Delta t = 0.25s$, (c) final crack pattern for $\Delta t = 0.5s$, (d) final crack pattern for $\Delta t = 1s$.

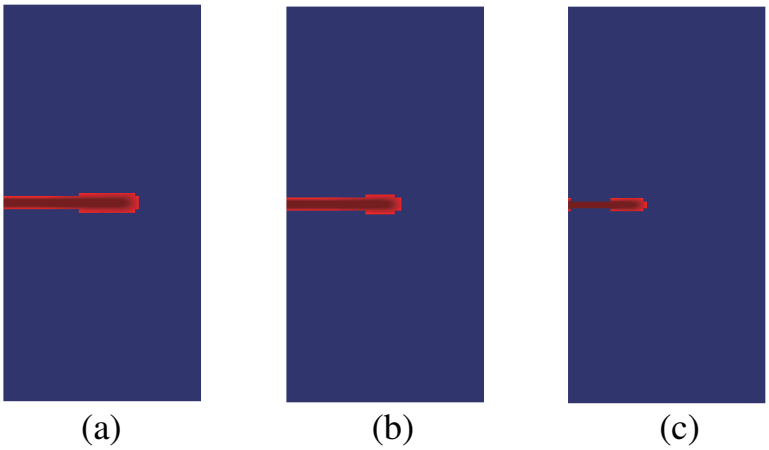

FIGURE 6.3: Three crack patterns for a specific $\bar{U}$ ($\bar{U} = 0.106$ mm): (a) $\Delta t = 0.25s$, (b) $\Delta t = 0.5s$, and (c) $\Delta t = 1s$.

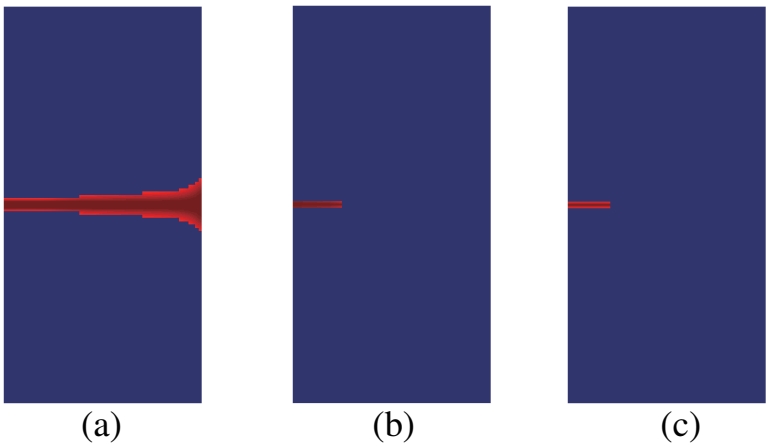

FIGURE 6.4: Three crack patterns for a specific $\mathcal{T}$ ($\mathcal{T} = 16.25s$): (a) $\Delta t = 0.25s$, (b) $\Delta t = 0.5s$, and (c) $\Delta t = 1s$.

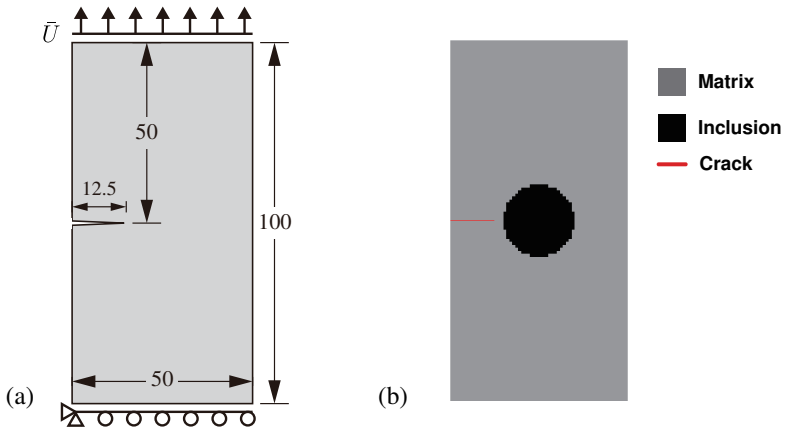

FIGURE 6.5: A composite plate with pre-existing crack notch subjected to incremental traction loads: (a) problem geometry; (b) initial crack.

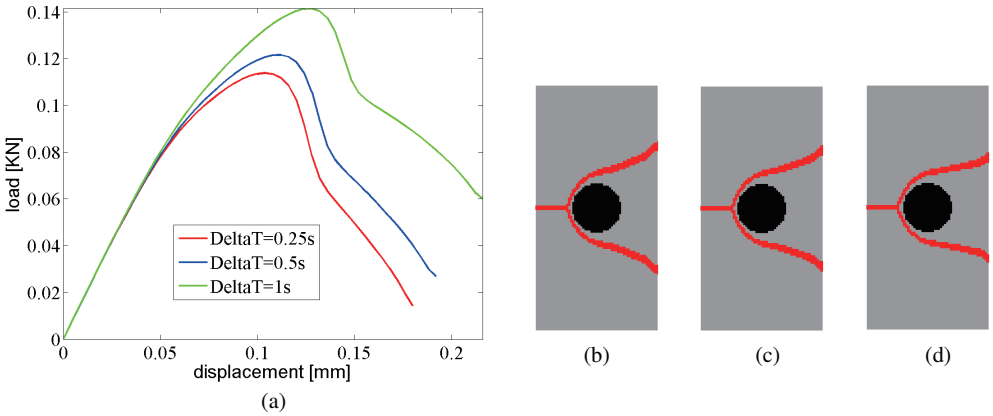

FIGURE 6.6: (a) Force-displacement curves for three cases, (b) final crack pattern for $\Delta t = 0.25s$, (c) final crack pattern for $\Delta t = 0.5s$, (d) final crack pattern for $\Delta t = 1s$.

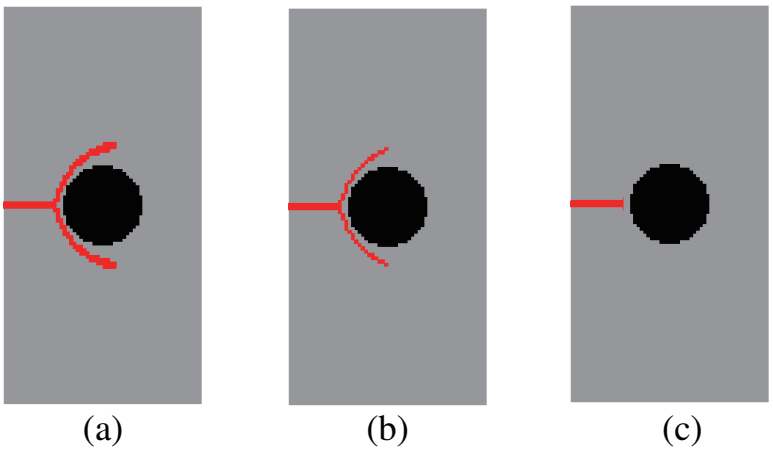

FIGURE 6.7: Three crack patterns for a specific $\bar{U}$ ($\bar{U} = 0.165$ mm): (a) $\Delta t = 0.25s$, (b) $\Delta t = 0.5s$, and (c) $\Delta t = 1s$.

TABLE 6.2: Material properties of matrix and inclusion phases

Name	Symbol	Value	Unit
Young's modulus of inclusion	E^{inc}	20	GPa
Young's modulus of matrix	E^{mat}	3	GPa
Poisson's ratio	ν	0.3	[-]
Fracture toughness of matrix	G_c^{mat}	3.3×10^{-3}	KN/mm
Fracture toughness of inclusion	G_c^{inc}	4.5×10^{-3}	KN/mm
Relaxation time of both phases	τ	5.882	s

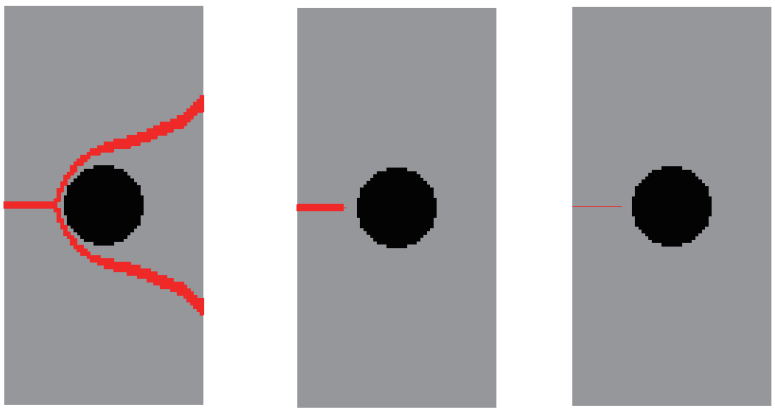

FIGURE 6.8: Three crack patterns for a specific $\mathcal{T}$ ($\mathcal{T} = 12s$): (a) $\Delta t = 0.25s$, (b) $\Delta t = 0.5s$, and (c) $\Delta t = 1s$..

are $50 \times 100 \times 6.67$ mm, and the whole volume domain is discretized into $60 \times 120 \times 8$ eight-node cubic elements. The lower end of the plate is fixed vertically while free horizontally. The central node on the right end edge is fixed in all directions to avoid rigid body motions. The upper end of the plate incremental displacement loads with $\Delta\bar{\mathbf{u}} = 0.005$ mm for each loading/time step is prescribed. Different times intervals, i.e. $\Delta t = 0.25s$, $\Delta t = 0.5s$, and $\Delta t = 1s$ are defined to investigate the time effects of the considered viscoelastic cracked body, respectively. The incremental loading process continues until the reaction forces is below a prescribed criterion value indicating that the structure is completely broken.

The final crack patterns of the above formulated three cases as well as the corresponding load-displacement curves are given in Fig. 6.9. For a specific displacement value of the upper end of the plate, for instance, $\bar{U} = 0.13$ mm, the corresponding crack patterns are illustrated in Fig. 6.10. For a specific time point after loading, for instance, $\mathcal{T} = 7s$, the corresponding crack patterns are illustrated in Fig. 6.11.

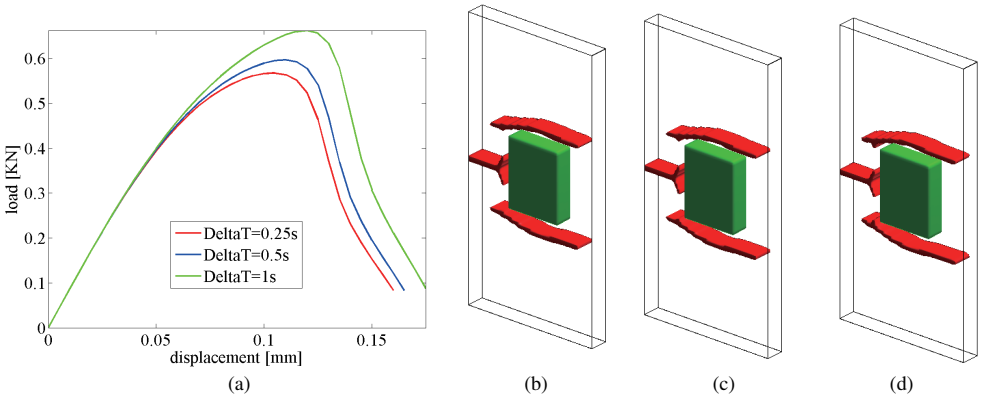

FIGURE 6.9: (a) Force-displacement curves for three cases, (b) final crack pattern for $\Delta t = 0.25s$, (c) final crack pattern for $\Delta t = 0.5s$, (d) final crack pattern for $\Delta t = 1s$.

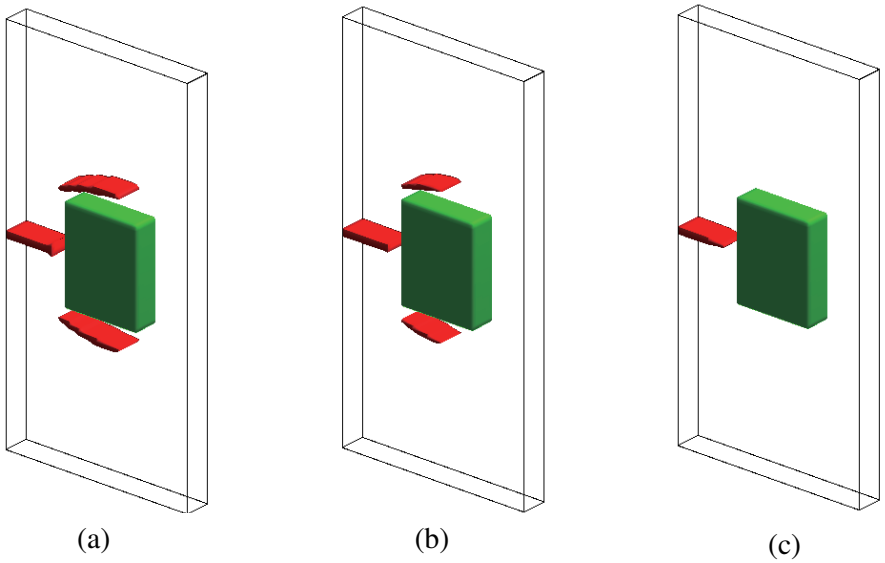

FIGURE 6.10: Three crack patterns for a specific $\bar{U}$ ($\bar{U} = 0.13$ mm): (a) $\Delta t = 0.25s$, (b) $\Delta t = 0.5s$, and (c) $\Delta t = 1s$.

TABLE 6.3: Material properties of matrix and inclusion phases for a 3D plate

Name	Symbol	Value	Unit
Young's modulus of inclusion	E^{inc}	20	GPa
Young's modulus of matrix	E^{mat}	3	GPa
Poisson's ratio	ν	0.3	[-]
Fracture toughness of matrix	G_c^{mat}	3.3×10^{-3}	KN/mm
Fracture toughness of inclusion	G_c^{inc}	7.5×10^{-3}	KN/mm
Relaxation time of both phases	τ	5.882	s

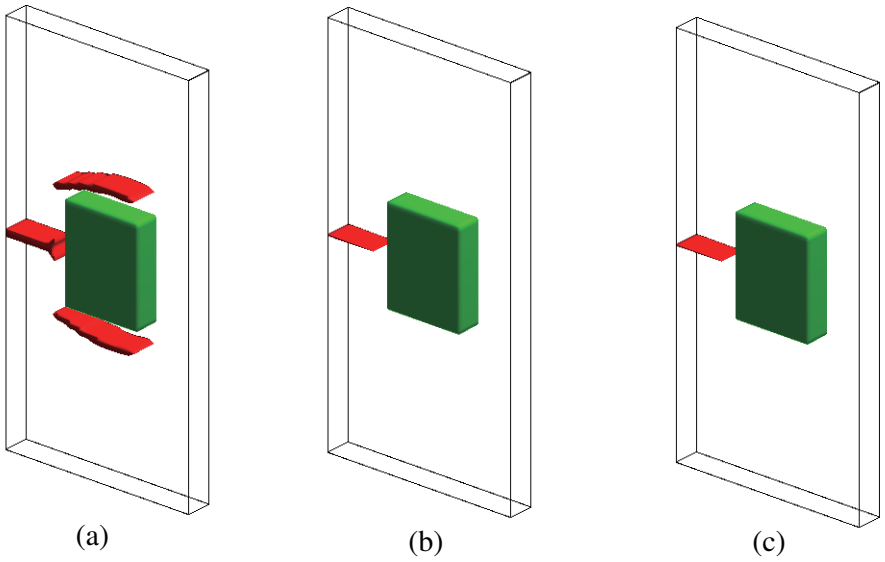

FIGURE 6.11: Three crack patterns for a specific $\mathcal{T}$ ($\mathcal{T} = 7s$): (a) $\Delta t = 0.25s$, (b) $\Delta t = 0.5s$, and (c) $\Delta t = 1s$..

6.5 Concluding remarks

In this Chapter, we have proposed a first attempt for the extension of the phase field method to viscoelastic materials. An energy-based formulation has been developed to express the equations governing viscoelastic phase field problems, and a classical generalized Maxwell model has been implemented for modelling the viscoelastic behavior. Both 2D and 3D heterogeneous materials subjected to loading with various durations have been analyzed with regard to different crack patterns. The presented work can be effectively extended to combine the topological design framework of heterogeneous materials proposed in Chapter 7, aiming to maximize the fracture resistance of linear viscoelastic materials.

Chapter 7

Topology optimization for maximizing the fracture resistance

Mechanical and physical properties of complex heterogeneous materials are determined on one hand by the composition of their constituents, but can on the other hand be drastically modified, at a constant volume fraction of heterogeneities, by their geometrical shape and by the presence of interfaces. As shown in Chapter 3, topological optimization of microstructures can help designing materials with higher effective properties while satisfying the prescribed volume fraction of constituents, or to obtain new properties which are not naturally available (metamaterials). Recently, the development of 3D printing techniques and other additive manufacturing processes have made possible to manufacture directly the designed materials from a numerical file, opening routes for totally new designs (see e.g. [133]). Among all properties of interest, accounting for material failure is of essential importance in the design of composite materials. As illustrated in Fig. 7.1, it is desired to improve the fracture resistance in terms of the required mechanical work for complete failure through an optimal placement of the inclusion phase. However, optimization design of composite materials accounting for fracture resistance remains relatively unexplored so far, mainly due to the lack of robust numerical methods for fracture propagation, until recently. One major challenge is to use topological optimization to improve the fracture resistance of heterogeneous materials, taking into account the heterogeneities and their interfaces in the material.

In Section 7.1, we first propose a numerical framework for optimizing the fracture resistance of quasi-brittle composites through a modification of the topology of the inclusion phase. The phase field method to fracturing is adopted within a regularized description of discontinuities, allowing to take into account cracking in regular meshes, which is highly advantageous for topology optimization purpose. A computationally efficient adjoint sensitivity formulation is derived to account for the whole fracturing process, involving crack initiation, propagation and complete failure of the specimen. The effectiveness of developed framework is illustrated through a series of 2D and 3D benchmark tests.

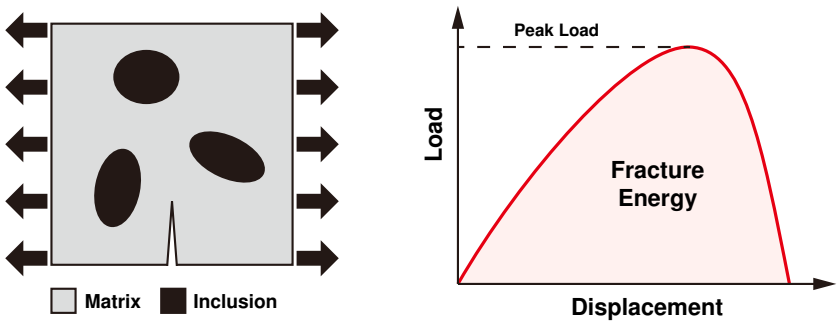

FIGURE 7.1: Illustration of a pre-cracked composite and fracture energy.

In Section 7.2, we present a topology optimization of particle-matrix composites for optimal fracture resistance taking into account interfacial damage. A phase field method for fracture capable of describing interactions between bulk brittle fracture and interfacial damage is adopted within a diffuse approximation of discontinuities. Efficient design sensitivity analysis is performed by using the adjoint method, and the optimization problem is solved by an extended BESO method. The sensitivity formulation accounts for the whole fracturing process involving cracks nucleation, propagation and interaction, either from the interfaces and then through the solid phases, or in the opposite direction. The spatial distribution of material phases is optimally designed to improve the fractural resistance. We demonstrate through several examples that the fracture resistance of the composite can be significantly increased at constant volume fraction of inclusions by the topology optimization process.

In Section 7.3, we extend the topology optimization framework proposed in Section 7.2 to maximizing the fracture resistence of periodic composites. The optimization problem aims to find the optimal material distribution of constant volume fraction of inclusions within the periodic unit cell, so as to maximize the fracture resistence of the periodic composites. Therefore, element sensitivity number in a single cell is defined as the summation of the sensitivity of corresponding elements in all cells to acount for the fracture response of whole periodic composite structure. Numerical examples demonstrate that the fracture resistance of the periodic composite structures can be improved significantly by redistributing the inclusion phases within the unit cell. In addition, the optimized inclusion phase is applied to larger periodic samples to further demonstrate the effectiveness of the proposed topology optimization framework.

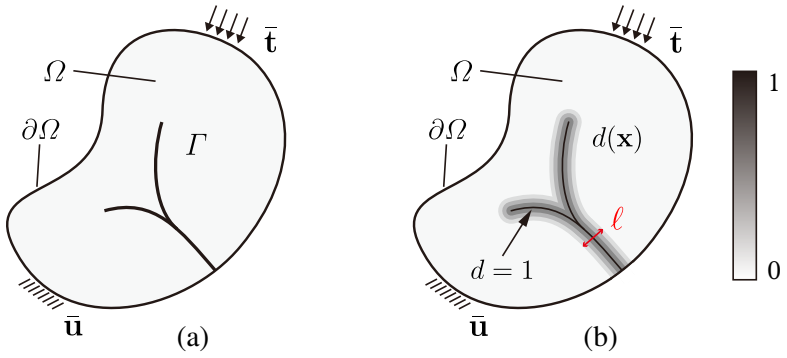

FIGURE 7.2: Illustration of phase field crack modeling: (a) a sharp crack surface Γ embedded within the solid Ω; (b) the regularized representation of the crack by the phase field $d(\mathbf{x})$.

7.1 Topology optimization for optimal fracture resistance of quasi-brittle composites

This section presents a topological design framework for fracture resistance of quasi-brittle composites, accounting for complete fracturing process. Extended BESO method is formulated and employed to find the optimal distribution of inclusion phase, given a target volume fraction of inclusion and seeking a maximal fracture resistance. In the following, Section 7.1.1 first reviews the phase field method for the modeling of crack propagation as developed by Miehe et al. [108, 110]. Section 7.1.2 presents the topology optimization method for design of quasi-brittle composites with fracture resistance. Section 7.1.3 validates the proposed design framework through a series of 2D and 3D benchmark tests.

7.1.1 Phase field modeling of crack propagation

Let $\Omega \in \mathbb{R}^D$ be an open domain describing a cracked solid as depicted in Fig. 7.2 , with $D \in [2, 3]$ being the space dimension. The external boundary of Ω is denoted by $\partial\Omega \in \mathbb{R}^{D-1}$. Cracks which may propagate within the solid are collectively denoted by Γ. In this work, we adopt the framework proposed in [116, 6, 111, 108, 110] for a regularized representation of discontinuities. In this regularized framework, the propagating cracks are approximately represented by an evolving scalar phase field $d(\mathbf{x}, t)$, where the diffusion is characterized by a length scale parameter ℓ.

7.1.1.1 Phase field approximation of cracks

The scalar crack phase field $d(\mathbf{x}, t)$ can be determined through solving the following boundary value problem subject to Dirichlet boundary conditions ($d = 1$) on the crack

(see [111] for more details):

$$\begin{cases} d(\mathbf{x},t) - \ell^2 \nabla^2 d(\mathbf{x},t) = 0, \ \text{ in } \Omega \\ d(\mathbf{x},t) = 1, \ \text{ on } \Gamma \\ \nabla d(\mathbf{x},t) \cdot \mathbf{n} = 0, \ \text{ on } \partial\Omega, \end{cases} \tag{7.1}$$

where $\nabla^2(.)$ is the Laplacian operator, ℓ is a length scale parameter that governs the width of the regularization zone and gives for $\ell \to 0$ the exact sharp crack in Γ in (7.1), and $\mathbf{n}$ is the unit outward normal vector to $\partial\Omega$. In the following, we denote the crack phase field $d(\mathbf{x},t)$ by d to alleviate the notations. It has been shown that the system of equations (7.1) corresponds to the Euler-Lagrange equation associated with the variational problem:

$$d = \text{Arg}\{\inf_{d \in S} \Gamma(d)\}, \quad \Gamma(d) = \int_\Omega \gamma(d) \, \mathrm{d}V, \tag{7.2}$$

where $S = \{d \mid d(\mathbf{x}) = 1, \forall \mathbf{x} \in \Gamma\}$, and γ is the crack surface density function per unit volume defined by:

$$\gamma(d) = \frac{1}{2\ell} d^2 + \frac{\ell}{2} \nabla d \cdot \nabla d. \tag{7.3}$$

The functional $\Gamma(d)$ represents the total length of the crack in 2D and the total crack surface area in 3D. A detailed explanation of (7.63) can be found in [111].

7.1.1.2 Thermodynamics of the phase field crack evolution

The variational approach to fracture mechanics provided by Francfort and Marigo [54] introduces the following energy functional for a cracked body:

$$J(\mathbf{u}, \Gamma) = \int_\Omega W_u(\boldsymbol{\varepsilon}(\mathbf{u})) \, \mathrm{d}V + \int_\Gamma g_c \, \mathrm{d}A, \tag{7.4}$$

in which W_u is the energy density function where $\boldsymbol{\varepsilon} = \frac{1}{2}(\nabla \mathbf{u} + \nabla^T \mathbf{u})$ are the strain and $\mathbf{u}$ the displacement fields. The first term on the right hand side of (7.4) corresponds to the elastic energy stored in the cracked solid. The second term on the right hand side of (7.4) corresponds to the energy required to create the crack according to the Griffith criterion with g_c the critical fracture energy density, also named as Griffith's critical energy release rate.

In the adopted regularized framework, the phase field $d(\mathbf{x})$ is introduced for the representation of cracks. Then above functional (7.4) is substituted by the following one:

$$J(\mathbf{u}, d) = \int_\Omega W_u(\boldsymbol{\varepsilon}, d) \, \mathrm{d}V + \int_\Omega g_c \gamma(d) \, \mathrm{d}V, \tag{7.5}$$

where $\gamma(d)$ is the surface density defined in (7.63). From (7.5), the energy potential or free energy W can be identified as:

$$W(\boldsymbol{\varepsilon}, d) = W_u(\boldsymbol{\varepsilon}, d) + g_c\gamma(d). \tag{7.6}$$

Following [111], the elastic energy W_u is defined in the following form that assumes isotropic elastic behavior of the solid and accounts for damage induced by traction only, through:

$$W_u(\boldsymbol{\varepsilon}, d) = ((1-d)^2 + \kappa)\psi^+(\boldsymbol{\varepsilon}) + \psi^-(\boldsymbol{\varepsilon}), \tag{7.7}$$

where $\kappa \ll 1$ is a small positive parameter introduced to prevent the singularity of the stiffness matrix due to fully broken parts, ψ^+ and ψ^- are the tensile and compressive strain energies,

$$\psi^{\pm} = \lambda\langle \mathrm{tr}[\boldsymbol{\varepsilon}]\rangle_{\pm}^2/2 + \mu \mathrm{tr}[\boldsymbol{\varepsilon}^{\pm}]^2, \tag{7.8}$$

with λ and μ the Lamé coefficients of the solid. Only tensile damage degradation is taken into account in the elastic energy (7.7) through a decomposition of the elastic strain ε into tensile and compressive parts [111]:

$$\boldsymbol{\varepsilon} = \boldsymbol{\varepsilon}^+ + \boldsymbol{\varepsilon}^- \quad \text{with} \quad \boldsymbol{\varepsilon}^{\pm} = \sum_{i=1}^{3} \langle \varepsilon^i \rangle_{\pm} \mathbf{n}^i \otimes \mathbf{n}^i. \tag{7.9}$$

In the above, $\langle x \rangle_{\pm} = (x \pm |x|)/2$, and ε^i and $\mathbf{n}^i$ are the eigenvalues and eigenvectors of $\boldsymbol{\varepsilon}$. The evolution of the damage variable $d(\mathbf{x}, t)$ can be determined by the variational derivative of the free energy W. In a rate-independent setting with the consideration of the reduced Clausius-Duhem inequality, the evolution criterion is provided by the Kuhn-Tucker conditions [111, 124]:

$$\dot{d} \geq 0; \quad -\delta_d W \leq 0; \quad \dot{d}[-\delta_d W] = 0, \tag{7.10}$$

yielding

$$-\delta_d W = 2(1-d)\psi^+(\boldsymbol{\varepsilon}) - g_c\delta_d\gamma = 0, \tag{7.11}$$

with the functional derivative [111]

$$\delta_d\gamma = d/\ell - \ell\Delta d. \tag{7.12}$$

Following [108], the maximum tensile strain energy is stored to account for loading and unloading histories and the damage evolution criterion (7.11) can then be expressed in the following form:

$$\frac{g_c}{\ell}[d - \ell^2\nabla^2 d] = 2(1-d) \max_{t\in[0,T]} \{\psi^+(\mathbf{x}, t)\}. \tag{7.13}$$

The criterion (7.13) is a monotonously increasing function of the strain $\boldsymbol{\varepsilon}(\mathbf{x}, t)$ that induces unnecessary stress degradation even at low strain values. To avoid this issue, an energetic damage evolution criterion with threshold has been introduced in [110, 112, 109], yielding

$$\psi_c[d - \ell^2 \nabla^2 d] = (1 - d) \max_{t \in [0,T]} \{\langle \psi^+(\mathbf{x}, t) - \psi_c \rangle_+\}, \tag{7.14}$$

in which ψ_c is a specific fracture energy density of the solid, which can be further related to a critical fracture stress σ_c by:

$$\psi_c = \frac{1}{2E} \sigma_c^2, \tag{7.15}$$

where E is the Young's modulus (see more details in [110]). The above crack evolution criterion (7.14) can be further stated as

$$\psi_c[d - \ell^2 \nabla^2 d] = (1 - d)\mathcal{H}(\mathbf{x}, t), \tag{7.16}$$

with the introduction of a strain energy history function [109]

$$\mathcal{H}(\mathbf{x}, t) = \max_{t \in [0,T]} \{\langle \psi^+(\mathbf{x}, t) - \psi_c \rangle_+\}. \tag{7.17}$$

7.1.1.3 Weak forms of displacement and phase field problems

In the absence of body forces, the linear momentum balance equation for the solid medium reads

$$\nabla \cdot \boldsymbol{\sigma} = \mathbf{0}, \tag{7.18}$$

where according to the definitions in (7.7) and (7.8), the stress tensor $\boldsymbol{\sigma}$ equals

$$\boldsymbol{\sigma} = \frac{\partial W_u}{\partial \boldsymbol{\varepsilon}} = \{(1 - d)^2 + \kappa\}\{\lambda \langle \mathrm{tr}[\boldsymbol{\varepsilon}] \rangle_+ \mathbf{1} + 2\mu \boldsymbol{\varepsilon}^+\} + \lambda \langle \mathrm{tr}[\boldsymbol{\varepsilon}] \rangle_- \mathbf{1} + 2\mu \boldsymbol{\varepsilon}^-, \tag{7.19}$$

in which $\mathbf{1}$ is the second-order identity tensor and $\kappa \ll 1$ is a small positive parameter introduced to prevent the singularity of the stiffness matrix due to fully broken parts. Multiplying the governing equation (7.18) by kinematically admissible test functions for the displacement $\delta\mathbf{u}$, integrating the resulting expression over the domain Ω, and using the divergence theorem together with boundary conditions yields the associated weak form:

$$\int_\Omega \boldsymbol{\sigma} : \boldsymbol{\varepsilon}(\delta\mathbf{u}) \, \mathrm{d}V = \int_{\partial\Omega_t} \bar{\mathbf{t}} \cdot \delta\mathbf{u} \, \mathrm{d}A, \tag{7.20}$$

in which $\bar{\mathbf{t}}$ is the applied traction on the Neumann boundary $\partial\Omega_t$ (see Fig. 7.2). The weak form (7.20) is completed with Dirichlet boundary conditions defined on $\partial\Omega_u$.

The associated weak form for the crack phase field evolution (7.16) can be obtained in a similar fashion:

$$\int_{\Omega} \{\{\mathcal{H} + \psi_c\} d\delta d + \psi_c \ell^2 \nabla d \cdot \nabla(\delta d)\} \, \mathrm{d}V = \int_{\Omega} \mathcal{H} \delta d \, \mathrm{d}V, \tag{7.21}$$

in which $\delta d \in H_0^1(\Omega)$, $d \in H^1(\Omega)$ and satisfying the Dirichlet boundary conditions on Γ.

7.1.1.4 Finite element discretization

In this work, we adopt the same finite element discretization for the approximation of the displacement field $\mathbf{u}$ and the crack phase field d. We can express the two finite element approximate fields $(\mathbf{u}^h, d^h)$ as:

$$\mathbf{u}^h(\mathbf{x}) = \mathbf{N}_u(\mathbf{x})\mathbf{d}_u, \; d^h(\mathbf{x}) = \mathbf{N}_d(\mathbf{x})\mathbf{d}_d \tag{7.22}$$

and their gradients as

$$\nabla \mathbf{u}^h(\mathbf{x}) = \mathbf{B}_u(\mathbf{x})\mathbf{d}_u, \; \nabla d^h(\mathbf{x}) = \mathbf{B}_d(\mathbf{x})\mathbf{d}_d, \tag{7.23}$$

where $\mathbf{N}_u$ and $\mathbf{B}_u$ denote matrices of shape functions and shape functions derivatives associated to displacements, and $\mathbf{N}_d$ and $\mathbf{B}_d$ denote matrices of shape functions and shape functions derivatives associated to phase field variable. Here, $\{\mathbf{d}_u, \mathbf{d}_d\}$ denote the vectors of the nodal values of the finite element mesh for displacement and crack phase fields, respectively.

Introducing the above discretization into the weak form (7.20), we obtain the following discrete system of equations:

$$\mathbf{K}_u \mathbf{d}_u = \mathbf{f}_u, \tag{7.24}$$

with the external force vector $\mathbf{f}_u$

$$\mathbf{f}_u = \int_{\partial\Omega_t} \mathbf{N}_u \bar{\mathbf{t}} \, \mathrm{d}A, \tag{7.25}$$

and the stiffness matrix $\mathbf{K}_u$

$$\mathbf{K}_u = \int_{\Omega} \mathbf{B}_u^T \mathbf{D} \mathbf{B}_u \, \mathrm{d}V, \tag{7.26}$$

where $\mathbf{D}$ is the constitutive matrix corresponding to the definition in (7.19), given by:

$$\mathbf{D} = \frac{\partial[\boldsymbol{\sigma}]}{\partial[\boldsymbol{\varepsilon}]} = (1-d)^2\{\lambda \mathcal{R}^+[\mathbf{1}][\mathbf{1}]^T + 2\mu \mathbf{P}^+\} + \{\lambda \mathcal{R}^-[\mathbf{1}][\mathbf{1}]^T + 2\mu \mathbf{P}^-\}, \tag{7.27}$$

where $[\boldsymbol{\sigma}]$ and $[\boldsymbol{\varepsilon}]$ are the vector forms corresponding to the second order tensors of stress $\boldsymbol{\sigma}$ and strain $\boldsymbol{\varepsilon}$. $\mathcal{R}^{\pm}$ and $\mathbf{P}^{\pm}$ are two operators for the decomposition of strain into the tensile and compressive parts (see e.g., [124]). The matrices $\mathbf{P}^{\pm}$ are such that:

$$[\varepsilon^{+}] = \mathbf{P}^{+}[\boldsymbol{\varepsilon}] \quad \text{and} \quad [\varepsilon^{-}] = \mathbf{P}^{-}[\boldsymbol{\varepsilon}]. \tag{7.28}$$

The discretization of the phase field problem (7.21) leads to the following discrete system of equations:

$$\mathbf{K}_d \mathbf{d}_d = \mathbf{f}_d \tag{7.29}$$

where

$$\mathbf{K}_d = \int_{\Omega} \{\{\mathcal{H} + \psi_c\}\mathbf{N}_d^T \mathbf{N}_d + \psi_c \ell^2 \mathbf{B}_d^T \mathbf{B}_d\} \, \mathrm{d}V \tag{7.30}$$

and

$$\mathbf{f}_d = \int_{\Omega} \mathbf{N}_d^T \mathcal{H} \, \mathrm{d}V, \tag{7.31}$$

in which $\mathcal{H}$ is strain energy history function defined in (7.72).

In the present work, a staggered solution scheme is employed following [108], where at each time increment the phase field problem is solved for fixed displacement field known from the previous time step t^n. The mechanical problem is then solved given the phase field at the new time step t^{n+1}. The overall algorithm is described as follows:

1. Set the initial fields $d(t_0)$, $\mathbf{u}(t_0)$, and $\mathcal{H}(t_0)$ at time t_0.
2. **Loop** over all time increments: at each time t_{n+1}:
   (a) Given $d(t_n)$, $\mathbf{u}(t_n)$, and $\mathcal{H}(t_n)$:
   (b) Compute the history function $\mathcal{H}(t_{n+1})$ according to (7.72).
   (c) Compute the crack phase field $d(t_{n+1})$ by solving (7.29).
   (d) Compute $\mathbf{u}(t_{n+1})$ with the current crack $d(t_{n+1})$ by solving (7.24).
   (e) $(.)_n \leftarrow (.)_{n+1}$ and go to (a).
3. **End**.

7.1.2 Topology optimization model for fracture resistance

The extended bi-directional evolutionary structural optimization (BESO) method developed in [55, 174] for the design of elastoplastic structures is adopted in this work to carry out topology optimization. Composites made of two material phases, matrix phase and inclusion phase, are considered. The spatial layout of inclusion phase is optimized by the extended BESO method to yield composite with a higher fracture resistance.

7.1.2.1 Model definitions

The design domain Ω is discretized into N_e finite elements and each element e is assigned with a topology design variable ρ_e. The N_e-dimensional vector containing the design variables is denoted as $\boldsymbol{\rho} = (\rho_1, \ldots, \rho_{N_\mathrm{e}})^T$. Following [75], the design variables and the multiple material interpolation model are defined as

$$\rho_e = 0 \text{ or } 1, \quad e = 1, 2, \ldots, N_\mathrm{e} \tag{7.32}$$

and

$$\begin{cases} E_e = \rho_e E_\mathrm{inc} + (1 - \rho_e) E_\mathrm{mat} \\ \sigma_{c,e} = \rho_e \sigma_{c,\mathrm{inc}} + (1 - \rho_e) \sigma_{c,\mathrm{mat}}, \end{cases} \tag{7.33}$$

where E_e and $\sigma_{c,e}$ are the Young's modulus and the critical fracture stress of the e-th element. $\{E_\mathrm{inc}, \sigma_{c,\mathrm{inc}}\}$ and $\{E_\mathrm{mat}, \sigma_{c,\mathrm{mat}}\}$ are the Young's moduli and the critical fracture stresses of the inclusion and the matrix phases, respectively. Attention needs to be recalled that "$E_\mathrm{inc} > E_\mathrm{mat}$" is assumed when carrying out topology optimization with multiple materials using the BESO method [75]. The Poisson's ratios of the two material phases are assumed identical. The design variables can thus be interpreted as an indicator such that the value of one corresponds to the inclusion phase, whereas zero corresponds to the matrix phase.

For stability considerations, it is conventional to adopt displacement-controlled loading for nonlinear designs (e.g., [106, 137, 78, 55, 174]). For a prescribed displacement load, the fracture resistance maximization is equivalent to the maximization of the mechanical work expended in the course of the fracturing process as illustrated in Fig. 7.1. In practice, the total mechanical work J, is approximated by numerical integration using the trapezoidal rule, i.e.

$$J \approx \frac{1}{2} \sum_{i=1}^{n_\mathrm{load}} \left(\mathbf{f}_u^{(i)} + \mathbf{f}_u^{(i-1)} \right)^T \Delta \mathbf{d}_u^{(i)}. \tag{7.34}$$

Here n_load is the total number of displacement increments, $\Delta \mathbf{d}_u^{(i)}$ is the i-th increment of the nodal displacement vector and $\mathbf{f}_u^{(i)}$ is the external nodal force vector (comprising surface tractions and reaction forces) at the i-th load increment.

During the optimization process the volume fraction of the inclusion phase is prescribed. Then the optimization problem discretized can be formulated as [e.g., 78, 55,

174]

$$\begin{aligned} \max_{\boldsymbol{\rho}}: \quad & J(\boldsymbol{\rho}, \mathbf{d}_u, \mathbf{d}_d) \\ \text{subject to}: \quad & \mathbf{K}_u^{(i)} \mathbf{d}_u^{(i)} = \mathbf{f}_u^{(i)}, i = 1, \ldots, n_{\text{load}} \\ : \quad & V(\boldsymbol{\rho}) = \sum \rho_e v_e = V_{\text{req}} \\ : \quad & \rho_e = 0 \text{ or } 1, e = 1, \ldots, N_{\text{e}}. \end{aligned} \tag{7.35}$$

Here v_e is the volume of the e-th element, $V(\rho)$ and V_{req} are the total and required material volumes, respectively. The stiffness matrix $\mathbf{K}_u^{(i)}$ at the i-th load increment is constructed following (7.26) and (7.27).

It may be recalled that by this model the discrete topology design variable $\rho_e \in \{0; 1\}$ indicates merely the associated material phase (matrix/inclusion) of the e-th element. This assumption omits naturally the definition of supplementing pseudo-relationships between intermediate densities and their constitutive behaviors as is the case in density-based models (e.g., [137, 22, 86]) resulting in algorithmic advantages (see also [55, 174]).

7.1.2.2 Sensitivity analysis

In order to perform the topology optimization, the sensitivity of the objective function J with respect to topology design variables $\boldsymbol{\rho}$ needs to be provided. Following the "hard-kill" BESO procedure [75, 175], the topology evolution is driven merely by the sensitivities of the solid phase ($\boldsymbol{\rho} = 1$, the inclusion phase in the current context), whilst the sensitivities of the void phase with ($\boldsymbol{\rho} = 0$, the matrix phase) are set to zero.

The derivation of the sensitivity requires using the adjoint method (see, e.g., [29, 36]). Lagrange multipliers $\boldsymbol{\mu}^{(i)}$, $\boldsymbol{\lambda}^{(i)}$ of the same dimension as the vector of unknowns $\mathbf{d}_u$ are introduced in order to enforce zero residual $\mathbf{r}$ at times t_{i-1} and t_i for each term of the quadrature rule (7.34). Then the objective function J can be rewritten in the following form without modifying the original objective value as

$$J^* = \frac{1}{2} \sum_{i=1}^{n_{\text{load}}} \left\{ \left(\mathbf{f}_u^{(i)} + \mathbf{f}_u^{(i-1)} \right)^T \Delta \mathbf{d}_u^{(i)} + \left(\boldsymbol{\lambda}^{(i)} \right)^T \mathbf{r}^{(i)} + \left(\boldsymbol{\mu}^{(i)} \right)^T \mathbf{r}^{(i-1)} \right\}. \tag{7.36}$$

Due to the asserted static equilibrium the residuals $\mathbf{r}^{(i)}$ and $\mathbf{r}^{(i-1)}$ have to vanish. The objective value is, thus, invariant with respect to the values of the Lagrange multipliers $\boldsymbol{\lambda}^{(i)}$ and $\boldsymbol{\mu}^{(i)}$ ($i = 1, \ldots, n_{\text{load}}$), i.e.

$$J^* \left(\boldsymbol{\rho}; \left\{ \boldsymbol{\lambda}^{(i)}, \boldsymbol{\mu}^{(i)} \right\}_{i=1,\ldots,n_{\text{load}}} \right) = J\left(\boldsymbol{\rho}\right). \tag{7.37}$$

This equivalence holds also for the sensitivity with respect to changes of the topology design variable ρ_e on element e

$$\frac{\partial J^*}{\partial \rho_e} = \frac{\partial J}{\partial \rho_e}. \tag{7.38}$$

In the following the derivative $\partial J^*/\partial \rho_e$ is computed with properly determined values of $\boldsymbol{\lambda}^{(i)}$ and $\boldsymbol{\mu}^{(i)}$ leading to certain simplifications of the derivation. To formally describe these derivations, we introduce a partitioning of all degrees of freedom (DOF) into essential (index E; associated with Dirichlet boundary conditions) and free (index F; remaining DOF) entries. For a vector $\mathbf{w}$ and a matrix $\mathbf{M}$ we have

$$\mathbf{w} \sim \begin{bmatrix} \mathbf{w}_{\mathrm{E}} \\ \mathbf{w}_{\mathrm{F}} \end{bmatrix} \quad \text{and} \quad \mathbf{M} \sim \begin{bmatrix} \mathbf{M}_{\mathrm{EE}} & \mathbf{M}_{\mathrm{EF}} \\ \mathbf{M}_{\mathrm{FE}} & \mathbf{M}_{\mathrm{FF}} \end{bmatrix} \tag{7.39}$$

In the present context, the displacements $\mathbf{d}_{u,\mathrm{E}}$ on the Dirichlet boundary are prescribed and, hence, they are independent of the current value of $\boldsymbol{\rho}$. This implies that

$$\frac{\partial \Delta \mathbf{d}_u}{\partial \rho_e} = \frac{\partial}{\partial \rho_e} \begin{bmatrix} \Delta \mathbf{d}_{u,\mathrm{E}} \\ \Delta \mathbf{d}_{u,\mathrm{F}} \end{bmatrix} = \begin{bmatrix} \mathbf{0} \\ \partial \{\Delta \mathbf{d}_{u,\mathrm{F}}\}/\partial \rho_e \end{bmatrix} \tag{7.40}$$

holds for arbitrary load time increments, i.e. for $\mathbf{d}_u = \mathbf{d}_u^{(i)}$ or $\mathbf{d}_u = \mathbf{d}_u^{(i-1)}$. The components $\mathbf{f}_{u,\mathrm{F}}$ of the force vector $\mathbf{f}_u$ vanish at all load time increments and the only (possibly) non-zero components are the reaction forces $\mathbf{f}_{u,\mathrm{E}}$

$$\mathbf{f}_u^{(i)} = \begin{bmatrix} \mathbf{f}_{u,\mathrm{E}}^{(i)} \\ \mathbf{0} \end{bmatrix} \tag{7.41}$$

Equations (7.40) and (7.41) imply

$$\{\mathbf{f}_u^{(j)}\}^T \frac{\partial \Delta \mathbf{d}_u^{(i)}}{\partial \rho_e} = 0. \tag{7.42}$$

Hence for arbitrary load increment indices $i, j = 1, \ldots, n_{\mathrm{load}}$, we have

$$\frac{\partial}{\partial \rho_e} \{\{\mathbf{f}_u^{(j)}\}^T \Delta \mathbf{d}_u^{(i)}\} = \{\frac{\partial \mathbf{f}_u^{(j)}}{\partial \rho_e}\}^T \Delta \mathbf{d}_u^{(i)}. \tag{7.43}$$

With the property of (7.43) at hand, the derivative of the modified design objective in (7.38) is given by:

$$\frac{\partial J^*}{\partial \rho_e} = \frac{1}{2} \sum_{i=1}^{n_{\mathrm{load}}} \{\frac{\partial \{\mathbf{f}_u^{(i)} + \mathbf{f}_u^{(i-1)}\}^T}{\partial \rho_e} \Delta \mathbf{d}_u^{(i)} + \{\boldsymbol{\lambda}^{(i)}\}^T \frac{\partial \mathbf{r}^{(i)}}{\partial \rho_e} + \{\boldsymbol{\mu}^{(i)}\}^T \frac{\partial \mathbf{r}^{(i-1)}}{\partial \rho_e}\}. \tag{7.44}$$

Recall the equilibrium equation at each load time increment is given by (7.105), the derivatives of $\mathbf{r}^{(j)}$ at the equilibrium of the j-th load increment with respect to ρ_e can be expanded as

$$\frac{\partial \mathbf{r}^{(j)}}{\partial \rho_e} = \frac{\partial \mathbf{f}_u^{(j)}}{\partial \rho_e} - \frac{\partial \mathbf{K}_u^{(j)}}{\partial \rho_e}\mathbf{d}_u^{(j)} - \mathbf{K}_u^{(j)}\frac{\partial \mathbf{d}_u^{(j)}}{\partial \rho_e}. \tag{7.45}$$

With the expression (7.45), (7.109) can be reformulated as

$$\begin{aligned}\frac{\partial J^*}{\partial \rho_e} = \frac{1}{2}\sum_{i=1}^{n_{\text{load}}}\Big\{ &\{\frac{\partial \mathbf{f}_u^{(i)}}{\partial \rho_e}\}^T\{\Delta\mathbf{d}_u^{(i)} + \boldsymbol{\lambda}^{(i)}\} + \{\frac{\partial \mathbf{f}_u^{(i-1)}}{\partial \rho_e}\}^T\{\Delta\mathbf{d}_u^{(i)} + \boldsymbol{\mu}^{(i)}\} \\ &- \{\boldsymbol{\lambda}^{(i)}\}^T\{\frac{\partial \mathbf{K}_u^{(i)}}{\partial \rho_e}\mathbf{d}_u^{(i)} + \mathbf{K}_u^{(i)}\frac{\partial \mathbf{d}_u^{(i)}}{\partial \rho_e}\} - \{\boldsymbol{\mu}^{(i)}\}^T\{\frac{\partial \mathbf{K}_u^{(i-1)}}{\partial \rho_e}\mathbf{d}_u^{(i-1)} + \mathbf{K}_u^{(i-1)}\frac{\partial \mathbf{d}_u^{(i-1)}}{\partial \rho_e}\}\Big\}.\end{aligned} \tag{7.46}$$

As mentioned previously, the aim is to find proper values of the Lagrange multipliers $\boldsymbol{\lambda}^{(i)}$ and $\boldsymbol{\mu}^{(i)}$ such that the sensitivities can be explicitly and efficiently computed. From the consideration of (7.41), the first two terms can be omitted by setting

$$\boldsymbol{\lambda}_{\text{E}}^{(i)} = -\Delta\mathbf{d}_{u,\text{E}}^{(i)} \quad \text{and} \quad \boldsymbol{\mu}_{\text{E}}^{(i)} = -\Delta\mathbf{d}_{u,\text{E}}^{(i)}. \tag{7.47}$$

Accounting further for the structure of the sensitivities of $\mathbf{d}_u$ in (7.40) and for the symmetry of the stiffness matrices we have

$$\begin{aligned}\frac{\partial J^*}{\partial \rho_e} = -\frac{1}{2}\sum_{i=1}^{n_{\text{load}}}\Big\{ &\{\boldsymbol{\lambda}^{(i)}\}^T\frac{\partial \mathbf{K}_u^{(i)}}{\partial \rho_e}\mathbf{d}_u^{(i)} + \{\mathbf{K}_{u,\text{FE}}^{(i)}\boldsymbol{\lambda}_{\text{E}}^{(i)} + \mathbf{K}_{u,\text{FF}}^{(i)}\boldsymbol{\lambda}_{\text{F}}^{(i)}\}^T\frac{\partial \Delta\mathbf{d}_{u,\text{F}}^{(i)}}{\partial \rho_e} \\ &+ \{\boldsymbol{\mu}^{(i)}\}^T\frac{\partial \mathbf{K}_u^{(i-1)}}{\partial \rho_e}\mathbf{d}_u^{(i-1)} + \{\mathbf{K}_{u,\text{FE}}^{(i-1)}\boldsymbol{\mu}_E^{(i)} + \mathbf{K}_{u,\text{FF}}^{(i-1)}\boldsymbol{\mu}_F^{(i)}\}^T\frac{\partial \Delta\mathbf{d}_{u,\text{F}}^{(i-1)}}{\partial \rho_e}\Big\}.\end{aligned} \tag{7.48}$$

In order to avoid the evaluation of the unknown derivatives of $\mathbf{d}_{u,\text{F}}^{(i)}$ and $\mathbf{d}_{u,\text{F}}^{(i-1)}$, the values of $\boldsymbol{\lambda}_{\text{F}}^{(i)}$ and $\boldsymbol{\mu}_{\text{F}}^{(i)}$ are sought as following by solving the adjoint systems with the prescribed values $\boldsymbol{\lambda}_{\text{E}}^{(i)} = -\Delta\mathbf{d}_{u,\text{E}}^{(i)}$ and $\boldsymbol{\mu}_{\text{E}}^{(i)} = -\Delta\mathbf{d}_{u,\text{E}}^{(i)}$ at the essential nodes:

$$\boldsymbol{\lambda}_{\text{F}}^{(i)} = \{\mathbf{K}_{u,\text{FF}}^{(i)}\}^{-1}\mathbf{K}_{u,\text{FE}}^{(i)}\Delta\mathbf{d}_{u,\text{E}}^{(i)}, \tag{7.49}$$

and

$$\boldsymbol{\mu}_{\text{F}}^{(i)} = \{\mathbf{K}_{u,\text{FF}}^{(i-1)}\}^{-1}\mathbf{K}_{u,\text{FE}}^{(i-1)}\Delta\mathbf{d}_{u,\text{E}}^{(i)}. \tag{7.50}$$

The two relations (7.49) and (7.50) together with (7.47) completely determine the values of the Lagrange multipliers $\boldsymbol{\lambda}^{(i)}$ and $\boldsymbol{\mu}^{(i)}$. It is obvious that the first adjoint system of (7.49) is in fact self-adjoint such that no additional calculation is needed and

$\boldsymbol{\lambda}^{(i)} = -\Delta\mathbf{d}_u^{(i)}$. Note in addition that because the proportional loading is increased at a constant rate, i.e.

$$\Delta\mathbf{d}_{u,\mathrm{E}}^{(i)} = \frac{\Delta t^{(i)}}{\Delta t^{(i-1)}}\Delta\mathbf{d}_{u,\mathrm{E}}^{(i-1)}, \tag{7.51}$$

the solution of the second linear system (7.50) can also be omitted by means of the recursion formula

$$\boldsymbol{\mu}_{\mathrm{F}}^{(i)} = \frac{\Delta t^{(i)}}{\Delta t^{(i-1)}}\boldsymbol{\lambda}_{\mathrm{F}}^{(i-1)}. \tag{7.52}$$

Substituting the two Lagrange multipliers into (7.48), the objective derivative $\partial J^*/\partial\rho_e$ can be eventually computed via

$$\frac{\partial J^*}{\partial\rho_e} = \frac{1}{2}\sum_{i=1}^{n_{\mathrm{load}}}\left\{\{\boldsymbol{\lambda}^{(i)}\}^T\frac{\partial\mathbf{K}_u^{(i)}}{\partial\rho_e}\mathbf{d}_u^{(i)} + \{\boldsymbol{\mu}^{(i)}\}^T\frac{\partial\mathbf{K}_u^{(i-1)}}{\partial\rho_e}\mathbf{d}_u^{(i-1)}\right\} \tag{7.53}$$

in which

$$\frac{\partial\mathbf{K}_u^{(j)}}{\partial\rho_e} = \mathbf{k}_{e,\mathrm{inc}}^{(j)} - \mathbf{k}_{e,\mathrm{mat}}^{(j)}, \quad j = 1, 2, \ldots, n_{\mathrm{load}} \tag{7.54}$$

according to the defined multiple material interpolation model in (7.33), where $\mathbf{k}_{e,\mathrm{inc}}^{(j)}$ and $\mathbf{k}_{e,\mathrm{mat}}^{(j)}$ are the element stiffness matrices at the j-th load time calculated from using Young's moduli E_{inc} and E_{mat}, respectively.

7.1.2.3 Extended BESO method

The extended BESO method recently developed in [174] augments the original proposition in [78] through an additional damping treatment of sensitivity numbers, so as to improve the robustness and the effectiveness of the method, particularly in dealing with nonlinear designs in presence of dissipative effects.

By the extended BESO method, the target volume of material $V^{(k)}$ at the current design iteration (k-th) is determined by

$$V^{(k)} = \max\left\{V_{\mathrm{req}}, (1 - c_{\mathrm{er}})V^{(k-1)}\right\}, \tag{7.55}$$

in which the evolutionary ratio c_{er} determines the percentage of material to be removed from the design of the previous iteration. Once the final required material volume V_{req} is reached, the optimization algorithm alters only the topology but keeps the volume fraction constant.

At each design iteration, the sensitivity numbers which denote the relative ranking of the element sensitivities are used to determine material phase exchange. When uniform meshes are used, the sensitivity number for the considered objective is defined as

following using the element sensitivity computed from (7.53)

$$\alpha_e = \begin{cases} \{\frac{\partial J^*}{\partial \rho_e}\}^\eta, & \text{for } \rho_e = 1 \\ 0\,, & \text{for } \rho_e = 0. \end{cases} \tag{7.56}$$

in which η is a numerical damping coefficient (the same as the one applied in the Optimality Criteria method for density-based methods [141]). When $\eta = 1$, we recover the conventional sensitivity numbers for linear elastic designs [77, 175]. In the presence of dissipative effects, the sensitivity numbers vary by several orders of magnitude resulting in instabilities of the topology evolution process, especially when removing certain structural branches (see, e.g., [55, 174]). For this reason, the sensitivity numbers are damped in this work with "$\eta = 0.5$" as suggested in [174].

In order to avoid mesh-dependency and checkerboard patterns, sensitivity numbers are firstly smoothed by means of a filtering scheme [141]

$$\alpha_e = \frac{\sum_{j=1}^{N_e} w_{ej}\alpha_j}{\sum_{j=1}^{N_e} w_{ej}}, \tag{7.57}$$

where w_{ej} is a linear weight factor

$$w_{ej} = \max(0, r_{\min} - \Delta(e, j)), \tag{7.58}$$

determined according to the prescribed filter radius $r_{\min}$ and the element center-to-center distance $\Delta(e, j)$ between elements Ω_e and Ω_j. Attention needs to be recalled that the filter (7.57) is also responsible for material exchange from the matrix phase ($\rho_e = 0$) to the inclusion phase ($\rho_e = 1$) by attributing filtered sensitivity number values to design variables that are associated to the matrix phase.

Due to the discrete nature of the BESO material model, the current sensitivity numbers need to be averaged with their historical information to improve the design convergence [76]

$$\alpha_e^{(k)} \leftarrow \frac{(\alpha_e^{(k)} + \alpha_e^{(k-1)})}{2}. \tag{7.59}$$

The update of the topology design variables is realized by means of two threshold parameters $\alpha_{\text{del}}^{\text{th}}$ and $\alpha_{\text{add}}^{\text{th}}$ for material removal and addition, respectively [78, 55]

$$\rho_e^{(k+1)} = \begin{cases} 0 & \text{if } \alpha_e \le \alpha_{\text{del}}^{\text{th}} \text{ and } \rho_e^{(k)} = 1, \\ 1 & \text{if } \alpha_{\text{add}}^{\text{th}} < \alpha_e \text{ and } \rho_e^{(k)} = 0, \\ \rho_e^{(k)} & \text{otherwise.} \end{cases} \tag{7.60}$$

The present scheme indicates that inclusion elements are exchanged to matrix elements when their sensitivity numbers are less than $\alpha_{\text{del}}^{\text{th}}$ and matrix elements are reversed to inclusion elements when their sensitivity numbers are greater than $\alpha_{\text{add}}^{\text{th}}$. The parameters $\alpha_{\text{del}}^{\text{th}}$ and $\alpha_{\text{add}}^{\text{th}}$ are obtained from the following iterative algorithm which was first proposed in [78] and recently adopted in [55, 174]:

1. Let $\alpha_{\text{add}}^{\text{th}} = \alpha_{\text{del}}^{\text{th}} = \alpha_{\text{th}}$, where the value α_{th} is determined iteratively such that the required material volume usage is met at the current iteration.

2. Compute the admission ratio c_{ar}, which is defined as the volume of the recovered elements ($\rho_e = 0 \to 1$) divided by the total volume of the current design iteration. If $c_{\text{ar}} \leq c_{\text{ar}}^{\max}$, the maximum admission ratio, then skip the next steps; otherwise, $\alpha_{\text{del}}^{\text{th}}$ and $\alpha_{\text{add}}^{\text{th}}$ are redetermined in the next steps.

3. Determine $\alpha_{\text{add}}^{\text{th}}$ iteratively using only the sensitivity numbers of the matrix elements ($\rho_e = 0$) until the maximum admission ratio is met, i.e., $c_{\text{ar}} \approx c_{\text{ar}}^{\max}$.

4. Determine $\alpha_{\text{del}}^{\text{th}}$ iteratively using only the sensitivity numbers of the inclusion elements ($\rho_e = 1$) until the required material volume usage is met at the current iteration.

The introduction of $c_{\text{ar}}^{\max}$ stabilizes the topology optimization process by controlling the number of elements reversed from matrix to inclusion. In the present work, $c_{\text{ar}}^{\max}$ is set to a value greater than 1% so that it does not suppress the merit of the reverse procedure.

7.1.3 Numerical examples

In this section, we show the performance of the proposed design framework through a series of 2D and 3D benchmark tests. In all 2D examples, uniform meshes of quadrilateral bilinear elements with the plane strain assumption are employed. Similarly, uniform mesh of eight-node cubic elements are adopted for the 3D design case. The same finite element discretization is adopted for both displacement and crack phase fields. The characteristic length scale parameter for the phase field regularization appearing in (7.1) is set to be twice that of the typical finite element size $\ell = 2h^e$. For the sake of clear visualization, only the crack phase field with the values over 0.4 is plotted. The material properties of the inclusion and the matrix phases are given in Table 7.1 according to [123].

With regard to topology optimization, all parameters involved in the extended BESO method as presented in Section 7.1.2.3 are held constant in all following examples. The evolutionary rate c_{er}, which determines the relative percentage of material to

be removed at each design iteration, is set to $c_{\text{er}} = 4\%$ (exception for the third example $c_{\text{er}} = 6\%$). The maximum admission ratio corresponding to the maximum percentage of recovered material that is allowed per iteration is set to $c_{\text{ar}}^{\max} = 2\%$. The filter radius is set to be twice that of the typical finite element size $r_{\min} = 2h^e$.

TABLE 7.1: Material properties of the inclusion and the matrix [123].

Name	Symbol	Value	Unit
Young's modulus of inclusion	E_{inc}	52	GPa
Young's modulus of matrix	E_{mat}	10.4	GPa
Poisson's ratio of both phases	ν	0.3	[-]
Critical fracture stress of inclusion	$\sigma_{c,\text{inc}}$	30	MPa
Critical fracture stress of matrix	$\sigma_{c,\text{mat}}$	10	MPa

7.1.3.1 Design of a 2D reinforced plate with one pre-existing crack notch

The problem setting of the 2D plate with one pre-existing crack notch is illustrated in Fig. 7.3(a). The dimensions of the plate are 50×100 mm. The whole plate is uniformly discretized into 60×120 square shaped bilinear elements. Plane strain assumption is adopted. The lower end of the plate is fixed vertically while free horizontally. The left bottom corner node is fixed in both directions to avoid rigid body motions. The upper end of the plate incremental displacement loads with $\Delta\bar{\mathbf{u}} = 0.01$ mm for the first five load increments and $\Delta\bar{\mathbf{u}} = 0.002$ mm for the following load increments are prescribed. The incremental loading process continues until the reaction force is below a prescribed criterion value indicating that the structure is completely broken.

Fig. 7.3(b) is the initial guess design with the inclusion phase occupying 10% of the domain area. By the extended BESO method, the inclusion phase area is gradually reduced to a target area fraction, 5% of the domain area. The pre-existing crack notch is simulated by prescribing Dirichlet conditions on the crack phase field with $d = 1$ along the crack. The surrounding area of the initial crack notch (up to 2 times of the length scale parameter ℓ) is treated as a non-designable region to avoid nonphysical designs with the inclusion material added within the already existing crack. The evolution of inclusion typologies together with their final crack patterns and the design objective history are shown in Fig. 7.4. It can be observed from Fig. 7.4 that the fracture resistance of the composite structure gently improves whilst the area fraction of the inclusion phase gradually decreases from initial 10% to 5%. It means that for the same fracture resistance performance, the required usage of inclusion phase can be largely saved via an optimal spatial distribution design.

Detailed propagation of the phase field crack of the optimally designed composite structure with a single pre-existing crack notch subject to incremental traction loads is given in Fig. 7.5. The crack propagates into the inner supporting structure made of the

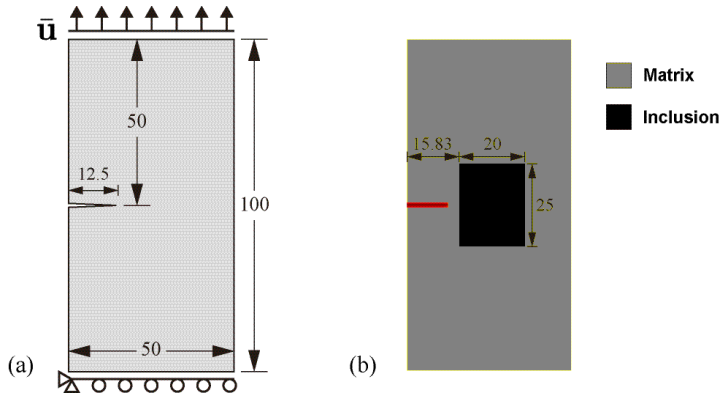

FIGURE 7.3: A 2D plate with one pre-existing crack notch subject to incremental traction loads: (a) problem depiction, (b) initial guess design.

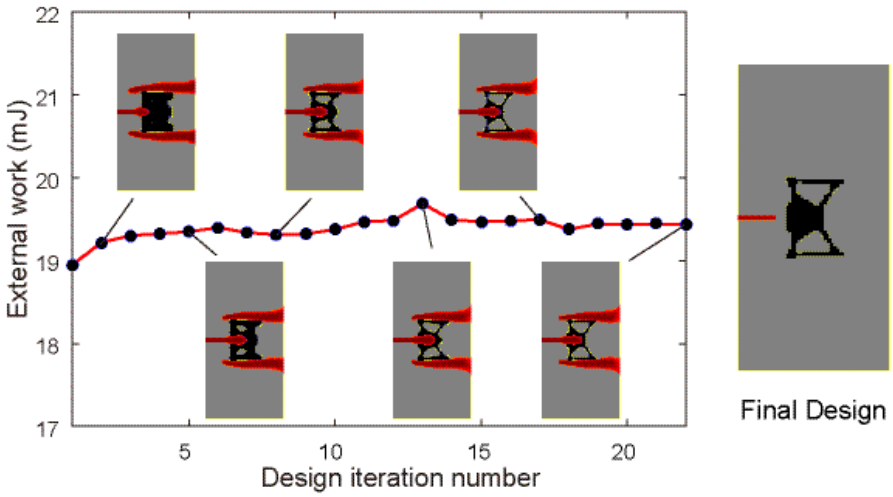

FIGURE 7.4: History of the evolution of inclusion typologies and their final crack patterns.

inclusion phase during the initial incremental loads. Two other cracks initiate around the upper and lower left corners of the inner supporting structure and continue to propagate horizontally until the structure is fully broken.

The fracture resistance of the optimally designed composite structure is validated through a comparison study. Starting from the same initial guess design (Fig. 7.3(b)), topology optimization using the same parameter setting has been carried out considering only linear elastic behavior without accounting for crack propagation, i.e. linear design, yielding two parallel bars along the vertical loading direction from the left design in Fig. 7.6. A complete fracturing simulation is carried out then on the linearly designed composite structure accounting for crack propagation. From both load-displacement curves and design objective values, the crack design is 15% more resistant to fracture than the linear design.

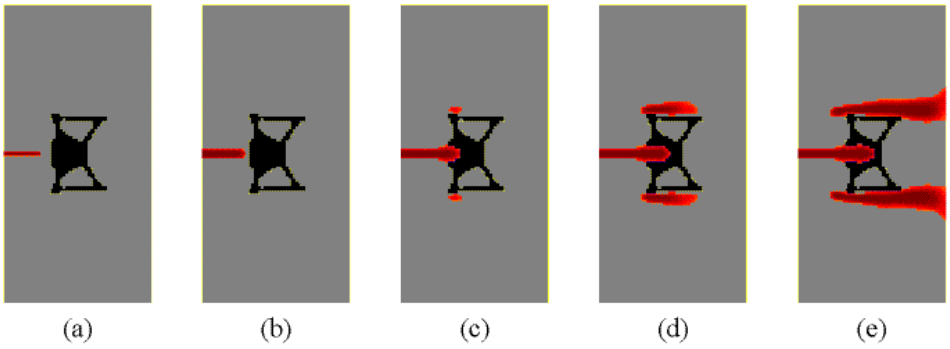

FIGURE 7.5: Crack propagation of the optimally designed composite structure with a single pre-existing crack notch subject to incremental traction loads: (a) $\bar{\mathbf{u}} = 0$ mm, (b) $\bar{\mathbf{u}} = 0.060$ mm, (c) $\bar{\mathbf{u}} = 0.076$ mm, (d) $\bar{\mathbf{u}} = 0.082$ mm, (e) $\bar{\mathbf{u}} = 0.092$ mm.

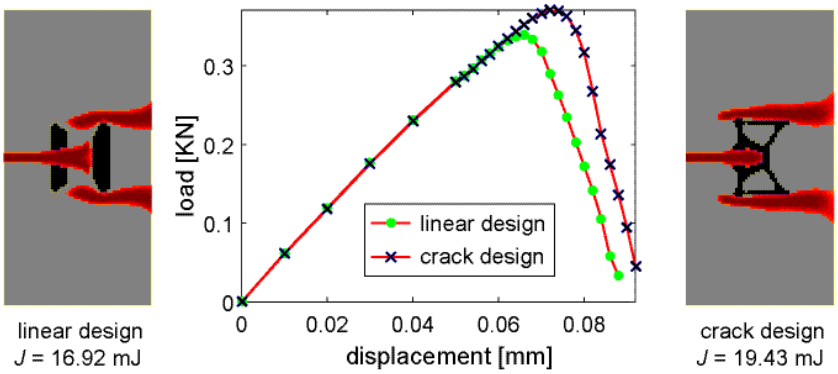

FIGURE 7.6: Fracture resistance comparison of two composite structures with a single pre-existing crack notch subject to incremental traction loads.

We would like to recall that the adopted BESO method is a heuristic scheme which does not necessarily guarantee a global optimum design. In the case of linear elasticity, the method has been proved to be insensitive to the two chosen initial starting topologies for structural stiffness maximization design [76]. However, such independency is not guaranteed when it comes to severe nonlinear problems as in the current case, i.e., different starting topologies may lead to different local optimum designs. Meanwhile, though the BESO method allows for both material removal and addition, their efficiencies are different. As stated in Section 7.1.2.3, sensitivity numbers are only evaluated for the inclusion elements and are set to zero for the matrix elements. It is only due to the filtering scheme (7.57) that sensitivity numbers on the matrix elements neighboring to inclusion-matrix interface are evaluated. Therefore, it is in usual more efficient to perform a gradual material reduction starting from a larger initial domain. Meanwhile the recovery/addition serves as a complementary mechanism for minor adjustment [175].

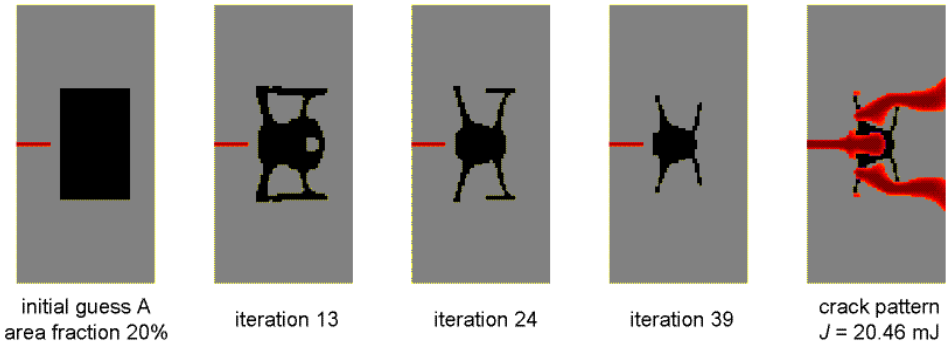

FIGURE 7.7: Evolution of inclusion topologies from an inital guess design with the inclusion phase occupying 20% area fraction of the domain and the final crack pattern.

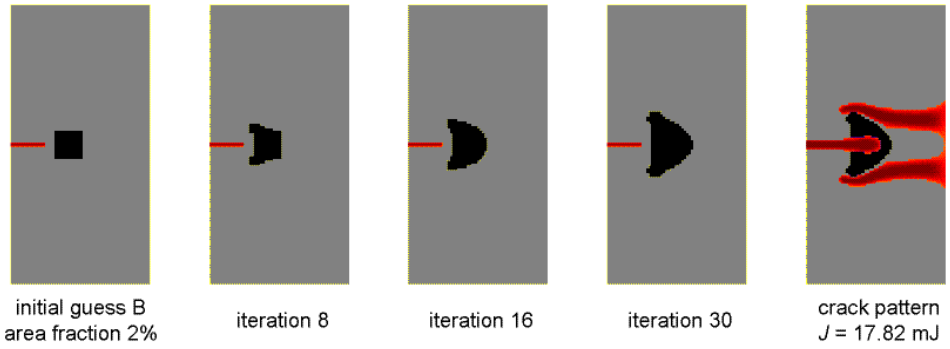

FIGURE 7.8: Evolution of inclusion topologies from an inital guess design with the inclusion phase occupying 2% area fraction of the domain and the final crack pattern.

For the purpose of comparison, we have redesigned the first example from two alternative initial topologies as shown in Figs. 7.7 and 7.8. For both cases, the resulted final inclusion topologies are local optimum designs and are different from the previous design in Fig. 7.4. Note that in order to start with initial guess B with a lower inclusion area fraction, (7.57) needs to be modified for material addition and the maximum admission ratio $\alpha_{\text{add}}^{\text{th}}$ should be exempted from the design. By comparing the values of the required work for complete fracture, a larger initial inclusion domain would result in a better design, however at the expense of a higher computing effort.

7.1.3.2 Design of a 2D reinforced plate with two pre-existing crack notches

A 2D plate with two pre-existing crack notches in Fig. 7.9(a) is considered for design. Apart from the two pre-existing crack notches, the other problem settings are defined the same as in the previous example. An initial guess design with the inclusion phase occupying 15% of the domain area is assumed as shown in Fig. 7.9(b). It is expected to optimally reduce the inclusion phase area fraction from 15% to 8% by using the

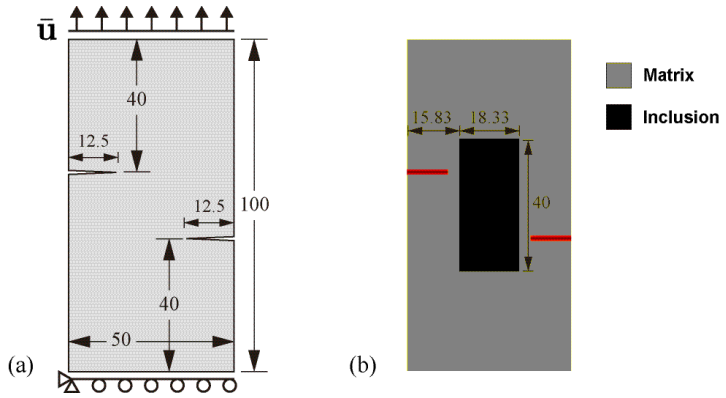

FIGURE 7.9: Illustration of a 2D plate with two pre-existing crack notches subject to incremental traction loads: (a) problem depiction, (b) initial guess design.

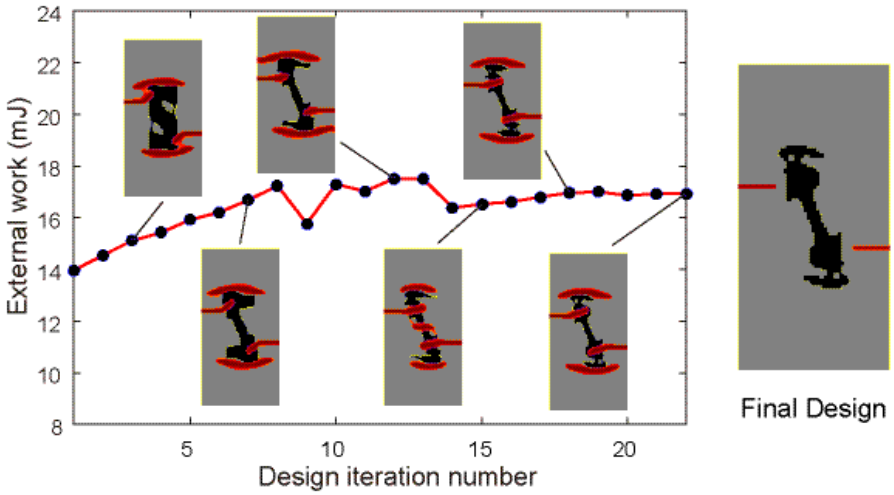

FIGURE 7.10: History of the evolution of inclusion typologies and their final crack patterns.

developed method. The pre-existing two crack notches are simulated by prescribing Dirichlet conditions with $d = 1$ along the crack. The surrounding area of the two initial crack notches is treated as a non-designable region to avoid nonphysical designs with the inclusion material added within the already existing crack. .

Fig. 7.10 shows the evolution of inclusion topologies together with their final crack patterns and the design objective history. Similar to the previous example, the fracture resistance of the composite structure gently improves whilst the area fraction of the inclusion gradually decreases from initial 14.67% to 8%, indicating that for the same fracture resistance performance, the required usage of inclusion phase material can be largely saved via an optimal spatial distribution design. Due to the anti-symmetry of the problem setting, cracks appear anti-symmetrically in the upper and lower parts of the structure. Fig. 7.11 shows detailed propagation of the phase field crack of the

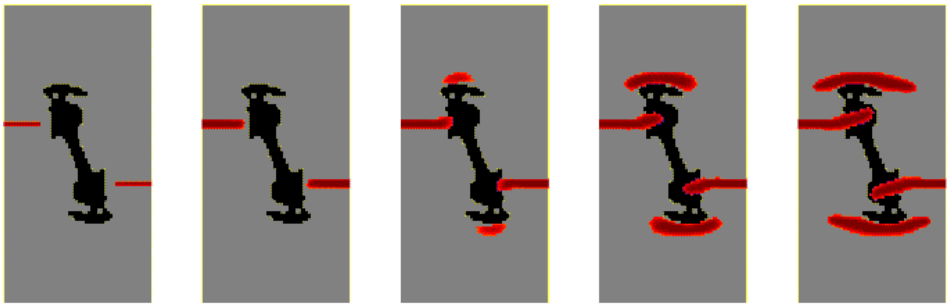

FIGURE 7.11: Crack propagation of the optimally designed composite structure with two pre-existing crack notches subject to incremental traction loads: (a) $\bar{\mathbf{u}} = 0$ mm, (b) $\bar{\mathbf{u}} = 0.060$ mm, (c) $\bar{\mathbf{u}} = 0.072$ mm, (d) $\bar{\mathbf{u}} = 0.080$ mm, (e) $\bar{\mathbf{u}} = 0.094$ mm.

optimally designed composite structure with two pre-existing crack notches subject to incremental traction loads. The two initial cracks propagate into the inner supporting structure made of the inclusion phase during the initial incremental loads. Then, two other cracks initiate at the upper and lower left surfaces of the inner supporting structure. All four cracks then continue to propagate until the structure is fully broken.

Similar to the previous example, a comparison study is also performed to validate the performance of the fracture resistance of the optimally designed composite structure. Topology optimization is carried out considering only linear elastic behavior without accounting for crack propagation starting from the same initial guess design (Fig. 7.9(b)) and using the same design parameters. Linear design without accounting for crack propagation results in two longer parallel bars compared to the linear design obtained in the previous example (due to increased inclusion usage) as shown in Fig. 7.12. The linearly designed composite structure is then subjected to a full fracturing simulation and its load-displacement curve is compared with the one of the crack design. From both load-displacement curves and design objective values, the fracture resistance of the crack design has been obviously increased by over 40% in comparison to the linear design.

7.1.3.3 Design of a 2D reinforced plate with multiple pre-existing cracks

This example addresses a multi-objective design using the developed method to improve the fracture resistance of a 2D reinforced plate trying to accommodate the geometry of the inclusion to several different distributions of cracks, and at the same time to deal with possible random creation of cracks within the structures. For the illustrative purposes, only 3 configurations are used here as shown in Fig. 7.13. All problem settings are defined the same as in the previous two examples except for the use of a finer

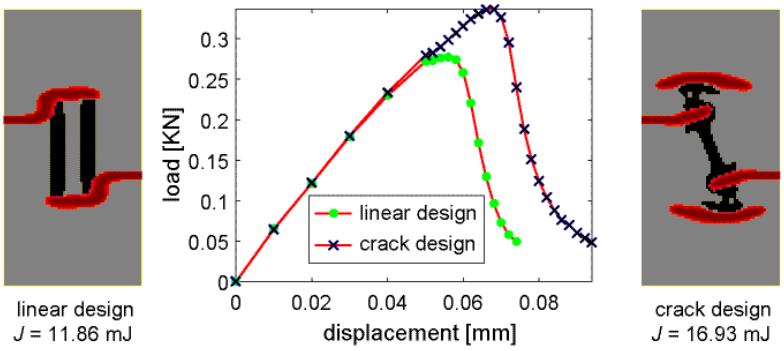

FIGURE 7.12: Fracture resistance comparison of two composite structures with two pre-existing crack notches subject to incremental traction loads.

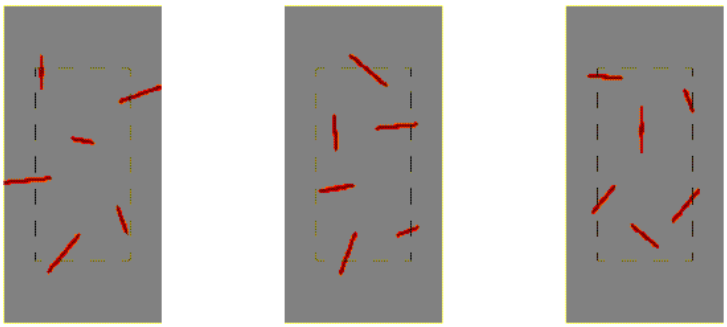

FIGURE 7.13: Three 2D plates with multiple pre-existing cracks (cases 1-3 from left to right).

finite element discretization. Considering the simulation accuracy involving multiple cracks, a finer discretization with 100×200 square shaped bilinear elements is adopted in this design. Following the same design procedure as presented in the first two examples, the area fraction of inclusion is gradually reduced from initial 28% to 8%. The initial distribution of inclusion phase is assumed to be a square shape enveloping all inner cracks of three cases as shown by the dashed lines in Fig. 7.13.

The optimally designed distribution topology of inclusion phase is given in Fig. 7.14 and their final crack patterns are shown in Fig. 7.15. It can be observed that the inclusion phase is distributed preferably at places such that can prevent the further propagation of critical cracks. Attention needs to be recalled that due to the regularized description of cracks using the phase field method, the surrounding region of all initial cracks is assumed to be non-designable. Otherwise the inclusion phase would fill all fictitious cracks, resulting in nonphysical designs.

FIGURE 7.14: Optimally designed inclusion distribution topology for three 2D plates with multiple pre-existing cracks (cases 1-3 from left to right).

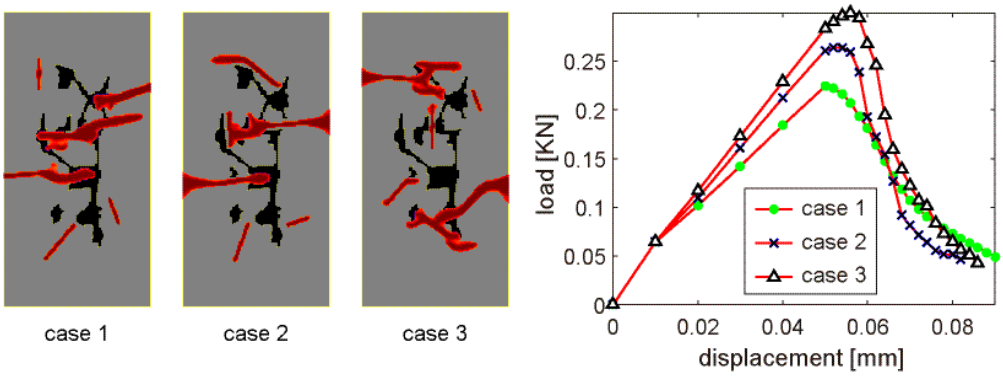

FIGURE 7.15: Final crack patterns of the three optimally designed 2D plates with multiple pre-existing cracks and their load-displacement curves.

7.1.3.4 Design of a 3D reinforced plate with a single pre-existing crack notch surface

A 3D plate with a single pre-existing crack notch surface as shown in Fig. 7.16 is considered for design to further validate the developed method. The dimensions of the 3D plate are $50 \times 100 \times 6.67$ mm. The whole volume domain is discretized into $60 \times 120 \times 8$ eight-node cubic elements. Similar to the 2D case in Section 7.1.3.1, the lower end of the plate is fixed vertically while free horizontally. The central node on the right end edge is fixed in all directions to avoid rigid body motions. The upper end of the plate incremental displacement loads with $\Delta\bar{\mathbf{u}} = 0.01$ mm for first seven load increments and $\Delta\bar{\mathbf{u}} = 0.002$ mm for the following load increments are prescribed. The incremental loading process continues until the reaction force is below a prescribed criterion value indicating that the structure is completely broken. The pre-existing crack notch surface is simulated by prescribing Dirichlet conditions $d = 1$ along the crack surface. The surrounding volume of the initial crack surface (up to 2 times the length scale parameter ℓ) is treated as a non-designable region to avoid nonphysical designs.

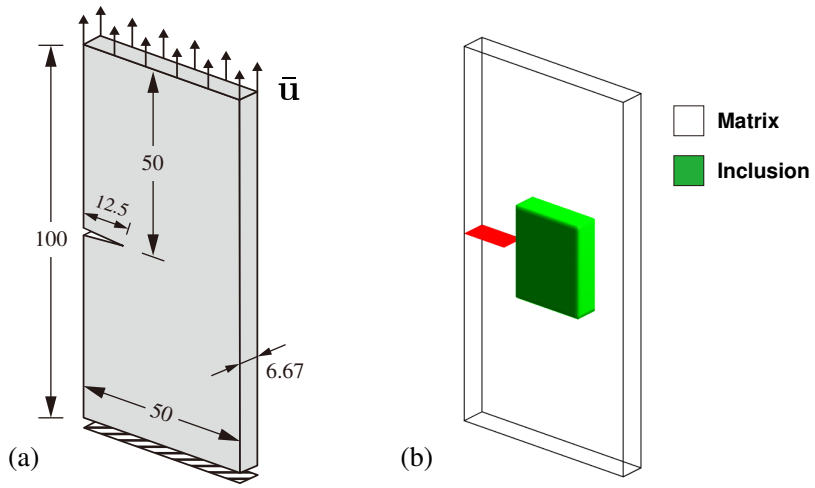

FIGURE 7.16: A 3D plate with a single pre-existing crack notch subject to a traction load: (a) problem depiction, (b) initial guess design.

Fig. 7.16(b) gives the initial guess design with the inclusion phase occupying 10% of the domain volume. By the developed method, the inclusion phase area is gradually reduced to the target volume fraction, 5% of the domain volume. The evolution of the spatial distribution topology of inclusion phase together with their final crack patterns and the design objective history are given in Fig. 7.17. The resultant hollow distribution topology design is similar to the one obtained in the 2D case in Section 7.1.3.1. It can be observed from Fig. 7.17 that unlike the 2D cases, the fracture resistance of the composite structure in the 3D case is obviously improved during the removal of material volume. From the 3D design, it is more obvious that for the same or even higher fracture resistance performance, the required usage of inclusion phase can be largely saved via an optimal spatial distribution design. This is because there exist much more inefficient material in the 3D case than the 2D case, such as within the hollow, which could be clearly removed without weakening the fracture resistance of the composite structure. Detailed phase field crack propagation of the optimally designed 3D composite structure is given in Fig. 7.18, where the crack propagation trajectory is similar to the corresponding 2D case in Section 7.1.3.1.

7.2 Topology optimization for optimal fracture resistance taking into account interfacial damage

It is observed in last section that the crack propagation resistance was only evaluated on the basis of phase distribution. In most heterogeneous quasi-brittle materials (e.g. ceramic matrix composites, cementitious materials), the interfacial damage plays a central role in the nucleation and propagation of microcracks [95, 158, 125, 120]. In this

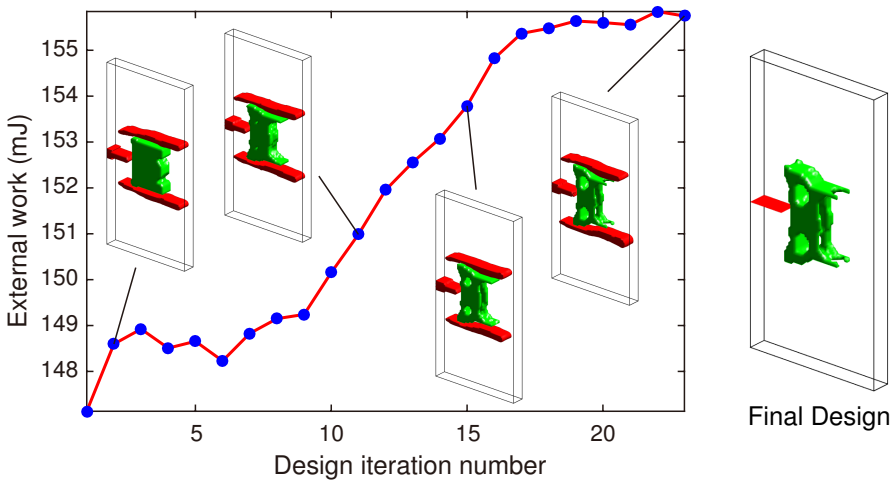

FIGURE 7.17: History of the evolution of inclusion typologies and their final crack patterns.

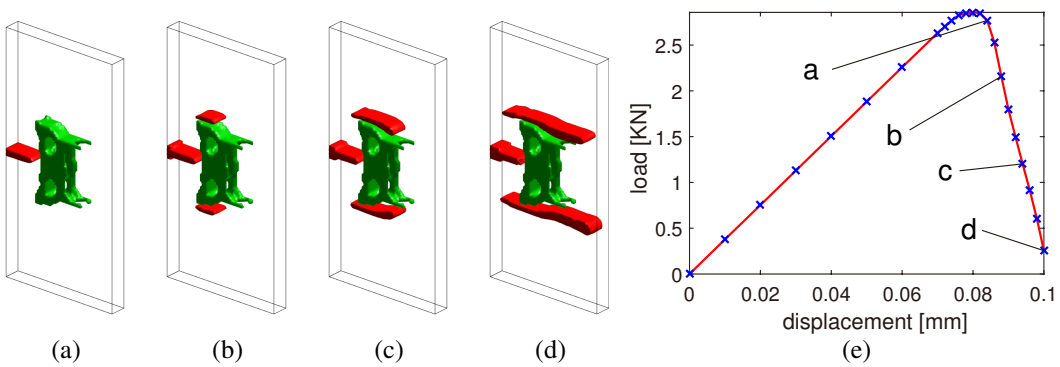

FIGURE 7.18: Crack propagation of the optimally designed 3D composite structure with a single pre-existing crack notch subject to incremental traction loads: (a) $\bar{\mathbf{u}} = 0.084$ mm, (b) $\bar{\mathbf{u}} = 0.088$ mm, (c) $\bar{\mathbf{u}} = 0.094$ mm, (d) $\bar{\mathbf{u}} = 0.010$ mm, (e) load-displacement curve.

section, the main objective is to extend the framework developed in the last section for defining through topological optimization the optimal phase distribution in a two-phase composite with respect to fracture resistance, taking into account crack nucleation both in the matrix and in the interfaces. The layout of this section is organized as follows. Section 7.2.1 gives the detailed phase field framework incorporating bulk fracture and cohesive interface. Numerical details and FEM discretization details are presented. In Section 7.2.2, we formulate the topology optimization model, containing detailed sensitivity derivation as well as the updating scheme with a damping on the sensitivity numbers. In Section 7.2.3, several numerical benchmark tests are presented to demonstrate the potential of the proposed method.

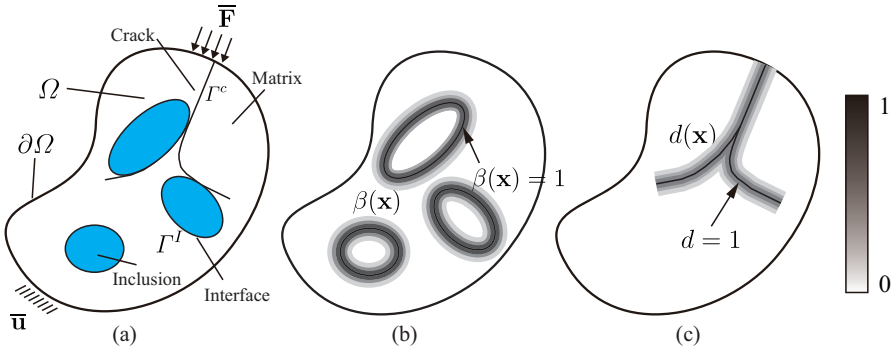

FIGURE 7.19: Illustration of the regularized representation of cracks and interfaces: (a) a solid containing interfaces and cracks; (b) regularized representation of the interfaces; (c) regularized representation of the cracks.

7.2.1 Phase field modeling of bulk crack and cohesive interfaces

In this section we describe the numerical method which is used by the topological optimization algorithm to obtain the fracture energy of the sample. The technique is based on the phase field model for fracture extended to interfacial damage by Nguyen et al. [123], and allows simulating the initiation and propagation of a multiple cracks network in heterogeneous microstructures. The main concepts and details are recalled in the following.

7.2.1.1 Regularized representation of discontinuous field

Let $\Omega \in \mathbb{R}^d$ be an open domain describing a solid with external boundary $\partial\Omega$. The solid contains internal material interfaces between different phases, collectively denoted by Γ^I. During the loading, cracks may propagate within the solid and can pass through the material interfaces as depicted in Fig. 7.19 (a). The crack surfaces are denoted by Γ^c. In this work, we adopt smeared representations of both cracks and material interfaces, i.e., the cracks are approximated by an evolving phase field $d(\mathbf{x}, t)$. Interfaces between different material phases are described by a fixed scalar phase field $\beta(\mathbf{x})$. The material interfaces do not evolve during the loading. The regularized parameters describing the actual widths of the smeared cracks and material interfaces are respectively denoted by ℓ_d and ℓ_β. In the following, the same regularization length $\ell = \ell_\beta = \ell_d$ is adopted for cracks and material interfaces for the sake of simplicity.

Given a non-evolving sharp crack defined on a surface Γ^c, a regularized (smeared) representation of the corresponding damage $d(\mathbf{x})$ (see Fig. 7.19 (c)) can be obtained by solving the Equation (7.1).

In Nguyen et al. [123], an *interface* phase field has been introduced to describe in the same manner the discontinuities related to the damage of interfaces, obtained by

solving the problem:

$$\begin{cases} \beta(\mathbf{x}) - \ell^2 \nabla^2 \beta(\mathbf{x}) = 0, \ \text{ in } \Omega \\ \beta(\mathbf{x}) = 1, \ \text{ on } \Gamma^I \\ \nabla\beta(\mathbf{x}) \cdot \mathbf{n} = 0, \ \text{ on } \partial\Omega. \end{cases} \tag{7.61}$$

Eq. (7.61) corresponds to the Euler-Lagrange equation associated with the variational problem

$$\beta(\mathbf{x}, t) = \text{Arg}\{\inf_{\beta \in S_\beta} \Gamma^\beta(\beta)\}, \quad \Gamma^\beta(\beta) = \int_\Omega \gamma_\beta(\beta) \, \mathrm{d}\Omega \tag{7.62}$$

where $S_\beta = \{\beta \mid \beta(\mathbf{x}) = 1, \forall \mathbf{x} \in \Gamma^I\}$, Γ^β represents the total interface length, and γ_β is defined by

$$\gamma_\beta(\beta) = \frac{1}{2l}\beta(\mathbf{x})^2 + \frac{\ell}{2}\nabla\beta(\mathbf{x}) \cdot \nabla\beta(\mathbf{x}). \tag{7.63}$$

For $\ell \to 0$ the above variation principle leads to a sharp interface description. This function will be used as an indicator to particularize the damage model to the interfaces or to the bulk in the formulation described in following sections.

In addition, it is necessary to introduce an approximation for the displacement jump at the interfaces, to associate a damage model specific to the interfaces and different from the bulk. For this purpose, the following approximation has been proposed [123] using Taylor expansion of the displacement field around a point $\mathbf{x}$ located on the interface:

$$[\![\mathbf{u}(\mathbf{x})]\!] \simeq \mathbf{w}(\mathbf{x}) = \mathbf{u}(\mathbf{x} + \frac{h}{2}\mathbf{n}^I) - \mathbf{u}(\mathbf{x} - \frac{h}{2}\mathbf{n}^I) = h\nabla(\mathbf{u}(\mathbf{x}))\mathbf{n}^\mathbf{I}, \tag{7.64}$$

where $\mathbf{w}(\mathbf{x})$ denotes the smoothed displacement jump approximation and $\mathbf{n}^I$ is an approximation of the normal to the interface Γ^I at a point $\mathbf{x}$. Several techniques are possible to define this normal. For example, in [123], a level-set technique has been proposed (see more details in the mentioned paper). In [159], another definition using the possible modification of the interface by the damage related to bulk cracks was introduced.

7.2.1.2 Energy functional

The following total energy functional is introduced for the solid body related to both cracks and interfaces:

$$E = \int_\Omega W_u^e(\boldsymbol{\varepsilon}^e(\mathbf{u}, \beta), d) d\Omega + \int_\Omega [1 - \beta(\mathbf{x})] g_c \gamma_d(d) d\Omega + \int_\Omega \psi^I(\mathbf{w}) \gamma_\beta(\beta) d\Omega, \tag{7.65}$$

where g_c is the toughness and ψ^I is a strain density function depending on the displacement jump across the interface Γ^I. Above, $\boldsymbol{\varepsilon}^e$ is the bulk part of the infinitesimal

strain tensor $\boldsymbol{\varepsilon}$ which satisfies the following relationship:

$$\boldsymbol{\varepsilon} = \boldsymbol{\varepsilon}^e + \bar{\boldsymbol{\varepsilon}}, \tag{7.66}$$

where $\bar{\boldsymbol{\varepsilon}}$ is the strain part induced by the smoothed jump at the interfaces such that $\bar{\boldsymbol{\varepsilon}} \to 0$ away from the interfaces (see [159]), in which case we recover the energy functional for a cracked body without considering the interface behavior:

$$E = \int_\Omega W_u^e(\boldsymbol{\varepsilon}^e(\mathbf{u}), d)d\Omega + \int_\Omega g_c\gamma_d(d)d\Omega. \tag{7.67}$$

From Eq. (7.65), the free energy W can be identified as

$$W = W_u^e(\boldsymbol{\varepsilon}^e(\mathbf{u}, \beta), d) + [1-\beta(\mathbf{x})]g_c\gamma_d(d) + \psi^I(\mathbf{w}, \boldsymbol{\alpha})\gamma_\beta(\beta). \tag{7.68}$$

The principle of maximum dissipation requires that dissipation $\mathcal{A}\dot{d}$ attains maximum under the constraint, i.e. $\dot{d} > 0, F = 0$. Therefore,

$$F = -\frac{\partial W}{\partial d} = -\frac{\partial W_u^e}{\partial d} - (1-\beta)g_c\delta\gamma(d) = 0 \tag{7.69}$$

with the functional derivative [108]

$$\delta\gamma(d) = \frac{d}{\ell} - \ell\Delta d. \tag{7.70}$$

It follows that when $\dot{d} > 0$, then

$$-2(1-d)\psi_e^+ + (1-\beta)g_c\delta\gamma(d) = 0, \tag{7.71}$$

To handle loading and unloading, the strain history function adopted in [108, 123] is employed here:

$$\mathcal{H}(\mathbf{x}, t) = \max_{\tau\in[0,t]}\{\psi_e^+(\mathbf{x}, t)\} \tag{7.72}$$

and (7.71) is substituted by

$$-2(1-d)\mathcal{H} + (1-\beta)g_c\delta\gamma(d) = 0. \tag{7.73}$$

7.2.1.3 Displacement and phase field problems

Using (7.70), the evaluation of the crack field $d(\mathbf{x},\mathbf{t})$ can be determined by solving the following phase field problem

$$\begin{cases} 2(1-d)\mathcal{H} - (1-\beta)\frac{g_c}{\ell}(d-\ell^2\nabla^2 d) = 0, \ \text{ in } \Omega \\ d(\mathbf{x}) = 1, \ \text{ on } \Gamma^c \\ \nabla d(\mathbf{x})\cdot\mathbf{n} = 0, \ \text{ on } \partial\Omega. \end{cases} \tag{7.74}$$

The associated weak form is obtained as (see [123]):

$$\int_\Omega \left\{(2\mathcal{H} + [1-\beta]\frac{g_c}{\ell})d\delta d + [1-\beta]g_c\ell\nabla d\cdot\nabla(\delta d)\right\} d\Omega = \int_\Omega 2\mathcal{H}\delta d d\Omega. \tag{7.75}$$

Using the variational principle for minimizing the total energy E with respect to the displacement $\mathbf{u}$, the weak form associated with the displacement problem can be formulated as

$$\int_\Omega \frac{\partial W_u^e}{\partial \boldsymbol{\varepsilon}^e} : \boldsymbol{\varepsilon}^e(\delta\mathbf{u})d\Omega + \int_\Omega \frac{\partial \psi^I(\mathbf{w})}{\delta \mathbf{w}}\cdot\partial\mathbf{w}\gamma_\beta(\beta)d\Omega = \int_\Omega \mathbf{f}\cdot\delta\mathbf{u}d\Omega + \int_{\partial\Omega_F}\bar{\mathbf{F}}\cdot\delta\mathbf{u}d\Gamma = \delta W^{ext}. \tag{7.76}$$

In the absence of body forces, Eq.(7.76) can be re-written as

$$\int_\Omega \boldsymbol{\sigma}^e : \boldsymbol{\varepsilon}^e(\delta\mathbf{u})d\Omega + \mathbf{t}(\mathbf{w})\cdot\delta\mathbf{w}\gamma_\beta(\beta)d\Omega - \int_\Omega \boldsymbol{\sigma}^e : \nabla^s\delta\mathbf{u}d\Omega = 0, \tag{7.77}$$

where $\boldsymbol{\sigma}^e = \frac{\partial \mathbf{w}_e}{\partial \boldsymbol{\varepsilon}^e}$ is the Cauchy stress, and $\mathbf{t}(\mathbf{w})$ is the traction vector acting on the interface Γ^I oriented by $\mathbf{n}^I$ and $\delta\mathbf{w} = h\nabla(\delta\mathbf{u})\mathbf{n}^I$. Using $\boldsymbol{\sigma}^e\mathbf{n} = \mathbf{t}$, the above equation can be further re-written as

$$\int_\Omega \boldsymbol{\sigma}^e : \{\boldsymbol{\varepsilon}^e(\delta\mathbf{u}) + \mathbf{n}\otimes\delta\mathbf{w}\gamma_\beta(\beta) - \nabla^s\delta\mathbf{u}\}\, d\Omega \tag{7.78}$$

which is satisfied for an admissible strain field:

$$\boldsymbol{\varepsilon}^e = \nabla^s\mathbf{u} - \mathbf{n}\otimes^S\mathbf{w}\gamma_\beta \tag{7.79}$$

where $(\nabla^s\mathbf{u})_{ij} = (u_{i,j}+u_{j,i})/2$ and $(\mathbf{n}\otimes^S\mathbf{w})_{ij} = (n_i\mathbf{w}_j + \mathbf{w}_i n_j)$. $\bar{\boldsymbol{\varepsilon}}$ can be identified as $\bar{\boldsymbol{\varepsilon}} = \mathbf{n}\otimes^S\mathbf{w}\gamma_\beta$.

With the above description of strain energy function, the Cauchy stress now reads:

$$\boldsymbol{\sigma}^e = \frac{\partial\psi_e^+}{\partial\boldsymbol{\varepsilon}^e}[g(d)+k] + \frac{\partial\psi_e^-}{\partial\boldsymbol{\varepsilon}^e} = [(1-d)^2+k]\left\{\lambda\langle tr\boldsymbol{\varepsilon}^e\rangle_+\mathbf{1} + 2\mu\boldsymbol{\varepsilon}^{e+}\right\} + \lambda\langle tr\boldsymbol{\varepsilon}^e\rangle_-\mathbf{1} + 2\mu\boldsymbol{\varepsilon}^{e-}. \tag{7.80}$$

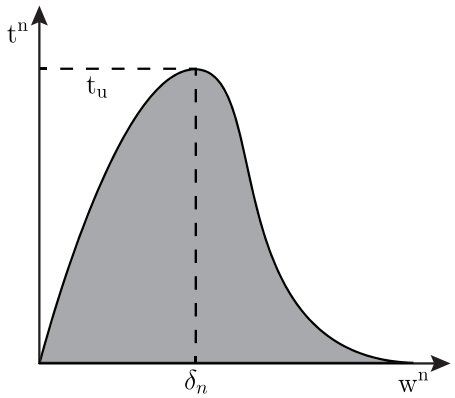

FIGURE 7.20: Illustration of the cohesive model for the interfaces.

The general form of the traction vector $\mathbf{t}(\mathbf{w})$ in Eq. (7.77) is given by

$$\mathbf{t}(\mathbf{w}) = [t^n, t^t]^T \tag{7.81}$$

where t^n and t^t denote respectively normal and tangential parts of the traction vector $\mathbf{t}$ across the interface oriented by its normal $\mathbf{n}^I$. In the presented work, a simplified nonlinear elastic cohesive model is used. We have shown that the framework proposed in [123] allows avoiding the use of internal variables related to the interface damage to handle loading and unloading by exploiting the damage phase field itself as the history variable. In addition, by only taking into account the normal traction, i.e. $\mathbf{t}(\mathbf{w})\cdot\mathbf{n}^I = t^n$, the cohesive law can be written as

$$t^n = g_c^I(\frac{w^n}{\delta^n})exp(-\frac{w^n}{\delta^n}) \tag{7.82}$$

where $w^n = \mathbf{w}\cdot\mathbf{n}^I$. For this model, we obtain $\mathbf{K}_I = \frac{\partial \mathbf{t}(\mathbf{w})}{\partial \mathbf{w}}$. The relationship between δ^n, the toughness g_c^I and th fracture strength t_u is given by $\delta^n = g_c^I/(t_u e)$, with $e = exp(1)$ (see Fig. 7.20).

Even though the phase field problem is linear in the staggered scheme, i.e. for a fixed value to $\mathbf{u}$, it should be mentioned that for a fixed crack phase field value d, the mechanical problem (7.76) is nonlinear since the computation of eigenvalues of $\boldsymbol{\varepsilon}^e$ and the interface cohesive model in (7.82). A linear procedure to solve this nonlinear problem by the Newton method is introduced in the following. From (7.76) and (7.80), the balance equation can be rewritten as

$$\mathcal{R} = \int_\Omega \boldsymbol{\sigma}^e : \boldsymbol{\varepsilon}^e(\delta\mathbf{u})d\Omega + \int_\Omega \gamma_\beta(\mathbf{x})\mathbf{t}(\mathbf{w},\alpha)\cdot\delta\mathbf{w}d\Omega - \int_\Omega \mathbf{f}\cdot\delta\mathbf{u}d\Omega - \int_{\partial\Omega_F} \bar{\mathbf{F}}\cdot\mathbf{u}d\Gamma = 0, \tag{7.83}$$

where $\boldsymbol{\varepsilon}^e(\delta\mathbf{u}) = \nabla^s\delta\mathbf{u} - \mathbf{n}\otimes^S\mathbf{w}\gamma_\beta$. In a standard Newton method, the displacements are updated for each loading by solving the following tangent equation:

$$D_{\Delta u}\mathcal{R}(\mathbf{u}^k, d) = -\mathcal{R}(\mathbf{u}^k, d) = 0, \tag{7.84}$$

where $\mathbf{u}^k$ is the displacement solution from the k-th iteration. The displacements at the current iteration are given by

$$\mathbf{u}^{k+1} = \mathbf{u}^k + \Delta\mathbf{u}. \tag{7.85}$$

From (7.84), we obtain

$$D_{\Delta\mathbf{u}}\mathcal{R}(\mathbf{u}^k) = \int_\Omega \frac{\partial\boldsymbol{\sigma}^e}{\partial\boldsymbol{\varepsilon}^e} : \boldsymbol{\varepsilon}^e(\Delta\boldsymbol{\varepsilon}) : \boldsymbol{\varepsilon}^e(\delta\boldsymbol{\varepsilon}) + \int_\Omega \frac{\partial\mathbf{t}(\mathbf{w})}{\partial\mathbf{w}} : \Delta\mathbf{w} : \delta\mathbf{w}d\Omega \tag{7.86}$$

with

$$\Delta\mathbf{w}(\mathbf{x}) = h\nabla\Delta\mathbf{u}(\mathbf{x})\frac{\nabla\phi(\mathbf{x})}{||\nabla\phi(\mathbf{x})||} \tag{7.87}$$

and

$$\frac{\partial[\boldsymbol{\sigma}^e]}{\partial[\boldsymbol{\varepsilon}^e]} = \mathbf{C}(\mathbf{u}, d) = [(1-d)^2+k]\left\{\lambda R^+[\mathbf{1}]^T[\mathbf{1}] + \mathbf{2}\mu\mathbf{P}^+\right\} + \left\{\lambda R^-[\mathbf{1}]^\mathbf{T}[\mathbf{1}] + \mathbf{2}\mu\mathbf{P}^-\right\} \tag{7.88}$$

where $[\boldsymbol{\sigma}^e]$ and $[\boldsymbol{\varepsilon}^e]$ are the vector forms for the second-order tensors $\boldsymbol{\sigma}^e$ and $\boldsymbol{\varepsilon}^e$, respectively and $\mathbf{C}$ is the matrix form corresponding to the fourth-order tensor $\mathbb{C}$.

7.2.1.4 Finite element discretization and numerical implementation

A staggered solution procedure is adopted in this work, where the phase field and the mechanical problems are solved alternatively. At each increment, given the displacement field from the mechanical problem, the phase field problem is linear using a shifted algorithm (see more details in [124]). Using FEM, the phase field and phase field gradient in one element are approximated by:

$$d(\mathbf{x}) = \mathbf{N}_d(\mathbf{x})\mathbf{d}^e, \nabla d(\mathbf{x}) = \mathbf{B}_d(\mathbf{x})\mathbf{d}^e, \tag{7.89}$$

where $\mathbf{d}_e$ are nodal phase field values in one element, $\mathbf{N}_d(\mathbf{x})$ and $\mathbf{B}_d(\mathbf{x})$ are matrices of shape functions and of shape functions derivatives associated to phase field variable, respectively. Introducing the above FEM discretization into the weak form (7.75), the following linear discrete system of equations can be obtained:

$$\mathbf{K}_d\tilde{\mathbf{d}} = \mathbf{F}_d \tag{7.90}$$

where

$$\mathbf{K}_d = \int_\Omega \left\{ (\frac{g_c}{\ell}(1-\beta) + 2\mathcal{H})\mathbf{N}_d^{\mathbf{T}}\mathbf{N}_d + (1-\beta)g_c\ell\mathbf{B}_d^T\mathbf{B}_d \right\} d\Omega \tag{7.91}$$

and

$$\mathbf{F}_d = \int_\Omega 2\mathbf{N}_d^T\mathcal{H}(\mathbf{u}_n)d\Omega. \tag{7.92}$$

Similarly, the displacement field and incremental displacement field can be expressed using the FEM approximations

$$\mathbf{u} = \mathbf{N}\mathbf{u}^e, \Delta\mathbf{u} = \mathbf{N}\Delta\mathbf{u}^e \tag{7.93}$$

where $\mathbf{N}$ denotes the matrix of shape functions associated to displacement variables, $\mathbf{u}^e$ and $\Delta\mathbf{u}^e$ are nodal displacement components and nodal incremental displacement components in one element. Furthermore, we have

$$[\boldsymbol{\varepsilon}](\Delta\mathbf{u}) = \mathbf{B}_u\Delta\mathbf{u}^e \tag{7.94}$$

where $\mathbf{B}_u$ is a matrix of shape function derivatives. From (7.64), the diffuse jump approximation vector and its incremental counterparts can be discretized as

$$\mathbf{w} = h\mathbf{N}\tilde{\mathbf{B}}_u\mathbf{u}^e, \Delta\mathbf{w} = h\mathbf{N}\tilde{\mathbf{B}}_u\Delta\mathbf{u}^e \tag{7.95}$$

where

$$\mathbf{N} = \begin{bmatrix} n_1 & n_2 & 0 & 0 \\ 0 & 0 & n_1 & n_2 \end{bmatrix}, \tag{7.96}$$

and n_1 and n_2 are the $x-$ and $y-$ components of the normal vector. The smoothed jump strain at the interfaces is defined by

$$[\bar{\boldsymbol{\varepsilon}}] = \begin{bmatrix} \bar{\varepsilon}_{11} \\ \bar{\varepsilon}_{22} \\ \sqrt{2}\bar{\varepsilon}_{12} \end{bmatrix} = \gamma_\beta(\mathbf{x}) \begin{bmatrix} \omega_1 n_1 \\ \omega_2 n_2 \\ \frac{1}{\sqrt{2}}(\omega_1 n_2 + \omega_2 n_1) \end{bmatrix}. \tag{7.97}$$

Then

$$[\bar{\boldsymbol{\varepsilon}}(\Delta u)] = h\gamma_\beta(\mathbf{x})\mathbf{M}\tilde{\mathbf{B}}_\mathbf{u}\boldsymbol{\Delta}\mathbf{u}^\mathbf{e} \tag{7.98}$$

with

$$\mathbf{M} = \begin{bmatrix} n_1^2 & n_1 n_2 & 0 & 0 \\ 0 & 0 & n_1 n_2 & n_2^2 \\ \frac{1}{\sqrt{2}}n_1 n_2 & \frac{1}{\sqrt{2}}n_2^2 & \frac{1}{\sqrt{2}}n_1^2 & \frac{1}{\sqrt{2}}n_1 n_2 \end{bmatrix}. \tag{7.99}$$

With the above FEM discretization, the tangent problem reduces to the following linear system of algebraeic equations

$$\mathbf{K}_{tan}\Delta\tilde{\mathbf{u}} = -\mathbf{R}(\tilde{\mathbf{u}}^k), \tag{7.100}$$

where

$$\mathbf{K}_{tan} = \int_\Omega [\mathbf{B}_u^T - h\gamma_\beta(\mathbf{x})\tilde{B}_u^T\mathbf{M}^T]\mathbf{C}(\mathbf{x})[\mathbf{B}_u - h\gamma_\beta(\mathbf{x})\tilde{B}_u\mathbf{M}]d\Omega + \int_\Omega h^2\gamma_\beta(\mathbf{x})\tilde{B}_u^T\mathbf{N}^T\mathbf{K}_I\mathbf{N}\tilde{B}_u d\Omega, \tag{7.101}$$

and

$$\begin{aligned}\mathbf{R} = &\int_\Omega [\mathbf{B}_u^T - h\gamma_\beta(\mathbf{x})\tilde{\mathbf{B}}_u^T\mathbf{M}^T]\mathbf{C}(\mathbf{x})[\mathbf{B}_u - h\gamma_\beta(\mathbf{x})\tilde{B}_u\mathbf{M}](\mathbf{u}^e)^k d\Omega \\ &+ \int_\Omega h\gamma_\beta(\mathbf{x})\tilde{B}_u^T\mathbf{N}^T\mathbf{t}(\mathbf{w}^k)d\Omega + \int_\Omega \mathbf{f}\mathbf{N}^T d\Omega + \int_\Omega \bar{\mathbf{F}}\mathbf{N}^T d\Gamma.\end{aligned} \tag{7.102}$$

The overall algorithm is described as follows.

1. Set the initial displacement field $\mathbf{u}_0(\mathbf{x})$, the phase field $d_0(\mathbf{x})$, and the strain-history function $\mathcal{H}_0$.
2. Compute the phase field $\beta(\mathbf{x})$.
3. **For** all loading increments: (at each time t_{n+1}), given d_n, $\mathbf{u}_n$, and $\mathcal{H}_n(\mathbf{x})$.
   (a) Compute the history function $\mathcal{H}(t_{n+1})$ according to (7.72).
   (b) Compute the crack phase field $d_{n+1}(\mathbf{x})$ by solving linear problem (7.90).
   (c) Compute $\mathbf{u}_{n+1}(\mathbf{x})$:
      i. Initialize $\mathbf{u}_k = \mathbf{u}_n$
      While $||\Delta\mathbf{u}_{k+1}|| > \epsilon, \epsilon \ll 1$:
      ii. Compute $\Delta\mathbf{u}_{k+1}^e$ by (7.100).
      iii. Update $\mathbf{u}_{k+1} = \mathbf{u}_k + \Delta\mathbf{u}_{k+1}^e$.
      iv. $(.)_{n+1} \rightarrow (.)_n$ and go to (a).
      End

   End

7.2.2 Topology optimization method

In this section, we present the topological optimization method based on the bi-directional evolutionary structural optimization (BESO) [76]. In the proposed procedure, the geometry of constant volume of inclusion phases is optimized so as to maximize the fracture resistance of the sample. This procedure involves evaluating the sensitivity of the whole fracturing process (initiation of multiple cracks, propagation and complete failure of the sample) with respect to changes in the geometry.

7.2.2.1 Model definitions

Similar to Section 7.1.2, the total number of finite elements in the considered domain Ω is denoted as N_e and each element e is assigned with a topology design variable ρ_e. Following the multiple material interpolation model in [75, 41], we have

$$E_e = \rho_e E_{\text{inc}} + (1 - \rho_e) E_{\text{mat}} \tag{7.103}$$

where E_{inc} and E_{mat} are the Young's moduli of the inclusion and matrix phases, respectively. The density value takes zero or one corresponding to the matrix and the inclusion phase, respectively.

Following the Eq. (7.34), the objective function J equivalent to the total mechanical work during the fracturing process is calculated by using numerical integration, i.e.

$$J \approx \frac{1}{2} \sum_{n=1}^{n_{\text{load}}} \left(\mathbf{f}_{\text{ext}}^{(n)} + \mathbf{f}_{\text{ext}}^{(n-1)} \right)^T \Delta \mathbf{u}^{(n)}, \tag{7.104}$$

and will be used as our definition of fracture resistance in the following. Above, n_{load} is the total number of displacement increments, $\Delta \mathbf{u}^{(n)}$ is the n-th nodal displacement component and $\mathbf{f}_{\text{ext}}^{n}$ is the external nodal force at the n-th load increment.

During the design optimization, the material volume fractions of matrix and of inclusion phases are prescribed. Then, the topology optimization problem subjected to balance equation and inclusion volume constraint can be formulated as

$$\begin{aligned} \max_{\boldsymbol{\rho}} : \quad & J(\boldsymbol{\rho}, \mathbf{u}, \mathbf{d}, \boldsymbol{\beta}) \\ \text{subjected to} : \quad & \mathcal{R} = 0 \\ : \quad & V(\boldsymbol{\rho}) = \textstyle\sum \rho_e v_e = V_{\text{req}} \\ : \quad & \rho_e = 0 \text{ or } 1, e = 1, \ldots, N_{\text{e}}. \end{aligned} \tag{7.105}$$

In the above, v_e is the volume of e-th element, $V(\boldsymbol{\rho})$ and V_{req} are the total and required material volumes, respectively and $\mathcal{R}$ denotes the nodal residual force:

$$\mathcal{R} = \mathbf{f}_{\text{ext}} - \mathbf{f}_{\text{int}}. \tag{7.106}$$

In (7.106), $\mathbf{f}_{\text{int}}$ is defined in each element as the internal force vector given in terms of the associated topology design variable ρ_e and the Cauchy stress as:

$$\mathbf{f}_{\text{int}} = \sum_{e=1}^{N_e} \rho_e \int_{\Omega_e} \mathbf{B}^T \boldsymbol{\sigma}^e d\Omega_e. \tag{7.107}$$

7.2.2.2 Sensitivity analysis

In order to compute the sensitivity of the objective function J with respect to topology design variables $\boldsymbol{\rho}$, two Lagrangian multipliers $\boldsymbol{\mu}^{(n)}$, $\boldsymbol{\lambda}^{(n)}$ are introduced to enforce zero residual $\mathcal{R}$ at time t_{n-1} and t_n for each term of the total mechanical work (7.104). Similar to Section 7.1.2, the two Lagrangian multipliers have the same dimension as the vector of unknowns $\mathbf{u}$. Therefore, the objective function J can be rewritten in the following form without modifying the original objective value as

$$\widehat{J} = \frac{1}{2}\sum_{n=1}^{n_{\text{load}}} \left\{ \left(\mathbf{f}_{\text{ext}}^{(n)} + \mathbf{f}_{\text{ext}}^{(n-1)}\right)^T \Delta\mathbf{u}^{(n)} + \left(\boldsymbol{\lambda}^{(n)}\right)^T \mathcal{R}^{(n)} + \left(\boldsymbol{\mu}^{(n)}\right)^T \mathcal{R}^{(n-1)} \right\}. \tag{7.108}$$

Introducing a partitioning of all degrees of freedom (DOF) into essential (index E; associated with Dirichlet boundary conditions) and free (index F; remaining DOF) entrie and following the same procedure in Section 7.1.2, the derivative of the modified design objective in (7.108) can be rewritten as:

$$\frac{\partial\widehat{J}}{\partial\rho_e} = \frac{1}{2}\sum_{n=1}^{n_{\text{load}}} \left\{ \left(\frac{\partial\mathbf{f}_{\text{ext}}^{(n)}}{\partial\rho_e} + \frac{\partial\mathbf{f}_{\text{ext}}^{(n-1)}}{\partial\rho_e} \right)^T \Delta\mathbf{u}^{(n)} + \left(\boldsymbol{\lambda}^{(n)}\right)^T \frac{\partial\mathcal{R}^{(n)}}{\partial\rho_e} + \left(\boldsymbol{\mu}^{(n)}\right)^T \frac{\partial\mathcal{R}^{(n-1)}}{\partial\rho_e} \right\}. \tag{7.109}$$

Recalling the balance equation at each load time increment in (7.83), the derivatives of $\mathcal{R}^{(m)}$ at the equilibrium of the m-th load increment with respect to ρ_e can be expanded as

$$\frac{\partial\mathcal{R}^m}{\partial\rho_e} = \frac{\partial\mathbf{f}_{\text{ext}}^m}{\partial\rho_e} - \int_{\Omega_e} \mathbf{B}^T (\sigma^e)^{(m)} d\Omega_e - \mathbf{K}_{tan}^{(m)} \frac{\partial\Delta\mathbf{u}^{(m)}}{\partial\rho_e} \tag{7.110}$$

where

$$\mathbf{K}_{\text{tan}}^{(m)} = -\frac{\partial\mathcal{R}^{(m)}}{\partial\mathbf{u}^{(m)}} \tag{7.111}$$

is the tangent stiffness matrix of the nonlinear mechanical system at the balance equation of the $m-$th load increment. With the expression (7.110), (7.109) can be reformulated as

$$\begin{aligned} \frac{\partial\widehat{J}}{\partial\rho_e} = \frac{1}{2}\sum_{n=1}^{n_{\text{load}}} \Bigg\{ & \left(\frac{\partial\mathbf{f}_{\text{ext}}^{(n)}}{\partial\rho_e} \right)^T \left(\Delta\mathbf{u}^{(n)} + \boldsymbol{\lambda}^{(n)} \right) + \left(\frac{\partial\mathbf{f}_{\text{ext}}^{(n-1)}}{\partial\rho_e} \right)^T \left(\Delta\mathbf{u}^{(n)} + \boldsymbol{\mu}^{(n)} \right) \\ & - \left(\boldsymbol{\lambda}^{(n)}\right)^T \left(\int_{\Omega_e} \mathbf{B}^T (\boldsymbol{\sigma}^e)^{(n)} d\Omega_e + \mathbf{K}_{tan}^{(n)} \frac{\partial\Delta\mathbf{u}^{(n)}}{\partial\rho_e} \right) \\ & - \left(\boldsymbol{\mu}^{(n)}\right)^T \left(\int_{\Omega_e} \mathbf{B}^T (\boldsymbol{\sigma}^e)^{(n-1)} d\Omega_i + \mathbf{K}_{tan}^{(n-1)} \frac{\partial\Delta\mathbf{u}^{(n-1)}}{\partial\rho_e} \right) \Bigg\} \end{aligned} \tag{7.112}$$

The first two terms in (7.112) can be omitted by setting

$$\boldsymbol{\lambda}_{\mathrm{E}}^{(n)} = -\Delta\mathbf{u}_{\mathrm{E}}^{(n)} \quad \text{and} \quad \boldsymbol{\mu}_{\mathrm{E}}^{(n)} = -\Delta\mathbf{u}_{\mathrm{E}}^{(n)}. \tag{7.113}$$

With the symmetry of the stiffness matrices, we have

$$\begin{aligned}\frac{\partial\widehat{J}}{\partial\rho_e} = \frac{1}{2}\sum_{n=1}^{n_{\mathrm{load}}}\Bigg\{ & -\left(\boldsymbol{\lambda}^{(n)}\right)^T\int_{\Omega_e}\mathbf{B}^T(\boldsymbol{\sigma}^e)^{(n)}d\Omega_e - \left(\boldsymbol{\mu}^{(n)}\right)^T\int_{\Omega_i}\mathbf{B}^T(\boldsymbol{\sigma}^e)^{(n-1)}d\Omega_i \\ & -\left(\mathbf{K}_{\mathrm{tan,FE}}^{(n)}\boldsymbol{\lambda}_E^{(n)} + \mathbf{K}_{\mathrm{tan,FF}}^{(n)}\boldsymbol{\lambda}_F^{(n)}\right)^T\frac{\partial\Delta\mathbf{u}_{\mathrm{F}}^{(n)}}{\partial\rho_e} \\ & -\left(\mathbf{K}_{\mathrm{tan,FE}}^{(n-1)}\boldsymbol{\mu}_E^{(n)} + \mathbf{K}_{\mathrm{tan,FF}}^{(n-1)}\boldsymbol{\mu}_F^{(n)}\right)^T\frac{\partial\Delta\mathbf{u}_{\mathrm{F}}^{(n-1)}}{\partial\rho_e}\Bigg\}.\end{aligned} \tag{7.114}$$

To avoid the evaluation of the unknown derivatives of $\mathbf{u}_{\mathrm{F}}^{(n)}$ and $\mathbf{u}_{\mathrm{F}}^{(n-1)}$, i.e. eliminating the last two lines of (7.114), the values of $\boldsymbol{\lambda}_{\mathrm{F}}^{(n)}$ and $\boldsymbol{\mu}_{\mathrm{F}}^{(n)}$ are sought as following by solving the adjoint systems with the prescribed values $\boldsymbol{\lambda}_{\mathrm{E}}^{(n)} = -\Delta\mathbf{u}_{\mathrm{E}}^{(n)}$ and $\boldsymbol{\mu}_{\mathrm{E}}^{(n)} = -\Delta\mathbf{u}_{\mathrm{E}}^{(n)}$ at the essential nodes:

$$\boldsymbol{\lambda}_{\mathrm{F}}^{(n)} = \left(\mathbf{K}_{\mathrm{tan,FF}}^{(n)}\right)^{-1}\mathbf{K}_{\mathrm{tan,FE}}^{(i)}\Delta\mathbf{u}_{\mathrm{E}}^{(n)}, \tag{7.115}$$

and

$$\boldsymbol{\mu}_{\mathrm{F}}^{(n)} = \left(\mathbf{K}_{\mathrm{tan,FF}}^{(n-1)}\right)^{-1}\mathbf{K}_{\mathrm{tan,FE}}^{(n-1)}\Delta\mathbf{u}_{\mathrm{E}}^{(n)}. \tag{7.116}$$

The two relations (7.115) and (7.116) together with (7.113) fully determine the values of the Lagrange multipliers $\boldsymbol{\lambda}^{(n)}$ and $\boldsymbol{\mu}^{(n)}$. Finally, the objective function gradient $\partial\widehat{J}/\partial\rho_e$ can be computed via

$$\frac{\partial\widehat{J}}{\partial\rho_e} = -\frac{1}{2}\sum_{n=1}^{n_{\mathrm{load}}}\left\{\left(\boldsymbol{\lambda}^{(n)}\right)^T\int_{\Omega_i}\mathbf{B}^T(\boldsymbol{\sigma}^e)^{(n)}d\Omega_i + \left(\boldsymbol{\mu}^{(n)}\right)^T\int_{\Omega_i}\mathbf{B}^T(\boldsymbol{\sigma}^e)^{(n-1)}d\Omega_i\right\}. \tag{7.117}$$

As shown also in Section 7.1.2, in order to improve the robustness and efficiency of the method, especially in dealing with nonlinear designs, the above obtained sensitivity numbers are firstly modified using an additional damping treatment as in Eq. (7.56). To avoid checkerboard patterns, sensitivity numbers are further smoothed by means of a filtering scheme as Eq. (7.57). Finally, due to the discrete nature of the BESO material model, the current sensitivity numbers are needed to be averaged with their historical information to improve the design convergence as in Eq. (7.59).

It is noted that the material volume fraction of reinforced inclusion phases in this work is kept constant during the optimization process. Interfaces between different

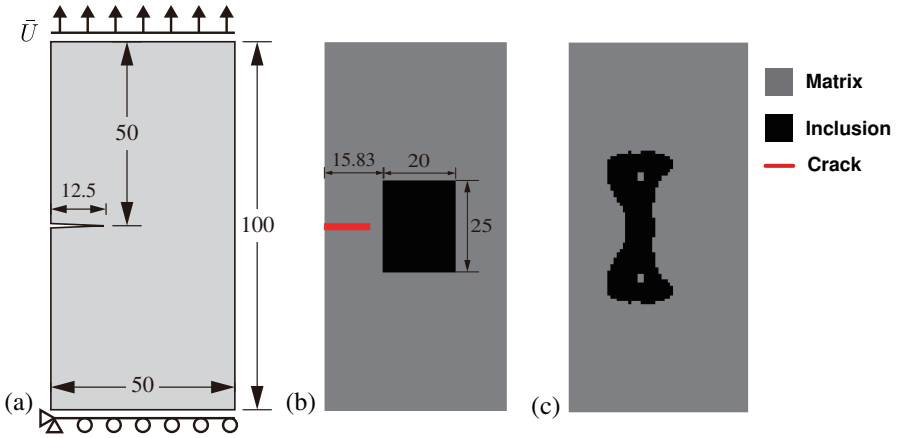

FIGURE 7.21: A plate with one pre-existing crack notch subjected to incremental traction loads: (a) problem geometry; (b) initial guess design; (c) final design.

material phases or even the topology of the reinforced inclusion materials will be tailored through the redistribution of the quantitative inclusion phases. The extended BESO method is adopted to solve the optimization problem by using the modified sensitivity numbers, which account for the whole fracturing process, involving crack nucleation, propagation and interaction until complete failure of the considered heterogeneous materials, so as to improve the fracture resistance of the specimens.

7.2.3 Numerical examples

In this section, several numerical examples are presented to demonstrate the potential of the proposed topology optimization framework. In all tests, regular meshes using quadrilateral bilinear elements are adopted, and plane strain condition is assumed. The same finite element discretization is adopted for both displacement and crack phase fields. The regularization parameter ℓ describing the width of smeared crack and interface is chosen as two times the finite element size $\ell = 2\ell_e$. The material parameters of each phase are taken as: $E_i = 52$ Gpa, $E_m = 10.4$ Gpa, $v_i = v_m = 0.3$, where the indices i and m correspond to the matrix and inclusion materials, respectively. These parameters are those of a mortar composed of a cement paste (matrix) and sand (inclusion). The toughness is $g_c = g_c^I = 1 \times 10^{-4}$ kN/mm and the interface fracture strength is chosen as $t_u = 10^{-2}$ Gpa.

7.2.3.1 Design of a plate with one initial crack under traction

The geometry of this example is depicted in Fig. 7.21(a). The dimensions of the plate are 50×100 mm, and the domain is uniformly discretized into 60×120 square shaped bilinear elements. The boundary conditions are as follows: on the lower end, the vertical

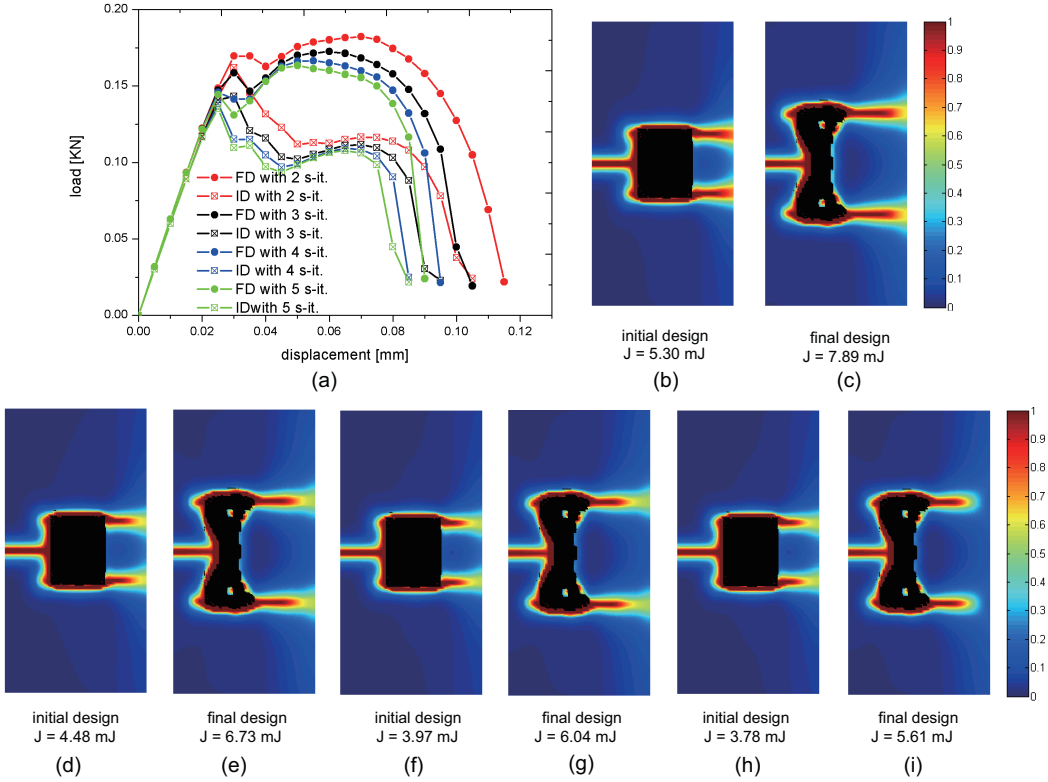

FIGURE 7.22: Fracture resistance comparison of two composite structures with one initial crack subjected to incremental traction loads: (a) load-displacement curves with different numbers of sub-iteration; (b) ID with 2 s-it; (c) FD with 2 s-it; (d) ID with 3 s-it; (e) FD with 3 s-it; (f) ID with 4 s-it; (g) FD with 4 s-it; (h) ID with 5 s-it; (i) FD with 5 s-it (ID/FD:initial/final design,s-it:sub-iteration).

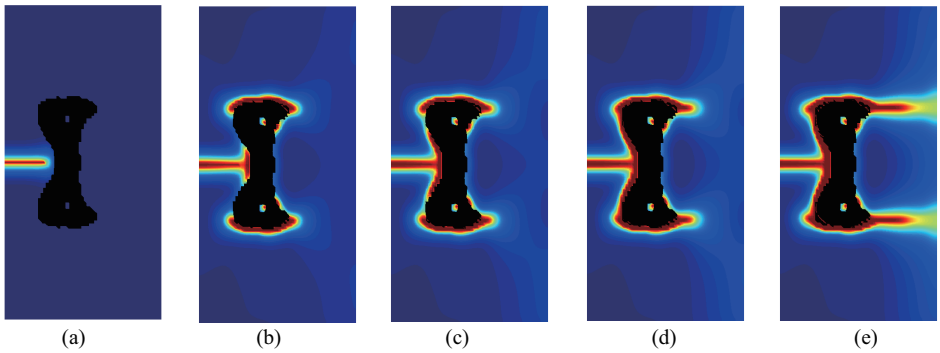

FIGURE 7.23: Crack propagation of the final design composite structure with a single initial crack subjected to incremental traction loads: (a) $\bar{U} = 0$ mm; (b) $\bar{U} = 0.05$ mm; (c) $\bar{U} = 0.06$ mm; (d) $\bar{U} = 0.08$ mm; (e) $\bar{U} = 0.095$ mm.

displacements are fixed while the horizontal displacements are free, and the left bottom corner node is fixed in both directions. On the upper end, the horizontal displacements are free, while the vertical displacements are prescribed with monotonic displacement increments $\bar{U} = 0.005$ mm during the simulation. The incremental loading process continues until the reaction force is below a prescribed value indicating that the structure is completely broken. It is worth noting that during the crack propagation, interfacial damage can occur and interact with the propagation of the pre-existing matrix crack.

Fig. 7.21(b) is the initial guess design and consists of a single square inclusion occupying a volume fraction of 10% of the sample. In all next examples, the material volume fraction of the inclusion phase is maintained constant during the optimization process. By the extended BESO method, the inclusion phase will be redistributed based on sensitivity numbers so as to improve the fracture resistance of the considered structure. The pre-existing crack notch is simulated by prescribing Dirichlet conditions on the crack phase field with $d = 1$ along the crack. The surrounding area of the initial crack notch (up to 2 times of the length scale parameter ℓ) is treated as a non-designable region to avoid non-physical designs with the inclusion material added within the already existing crack (see a discussion in [173]). The final structural topology of the inclusion phase is shown in Fig. 7.21 (c). It can be observed that the material on the right side of the reinforcement inclusion moves up and down on the left side, and holes are generated to tailor the topology of the inclusion phases. The fracture resistance improvement of the resultant composite structure is evaluated by comparing the initial and new designs response in Fig. 7.22. It is worth noting, that in the present work, a staggered procedure has been employed for solving the coupled displacement-phase field problems formulated in section 7.1.1. Then, for one load increment, the number of sub-iterations, i.e. the number of times the displacement and phase field problems are solved alternatively has an effect on the solution. It is worth noting that most authors

(see e.g. [108], and also our own previous works, [124, 123], among many others) only use one sub-iteration by assuming that the load increments are small enough, but this requires a preliminary convergence study. In the following, we have studied the effects of using 2, 3, 4 and 5 sub-iterations in the staggered scheme of the load-displacement response of the structure.

In Fig. 7.22, we denote by "FD" and "ID" Final and Initial Designs, respectively, and "s-it" means sub-iterations. We can observe from Fig. 7.22 (a) that the number of sub-iterations in the whole optimization procedure does have an effect on the final load-displacement curve but almost no effect on the final optimized shape (see Fig. 7.22 (b)-(i)). We note that for 4 sub-iterations, the load-displacement curve has roughly converged. With these observations in mind, we then conduct the whole optimization procedure for obtaining the final design with only 2 sub-iterations to reduce the computational costs, as it has been seen that the number of sub-iterations as small influence on the final shape of the inclusion. Then, we use the obtained final design and re-compute the load-displacement curve with 4 sub-iterations to avoid underestimating the fracture energy. In the present example, we can see from Fig. 7.22 that the total required fracture energies for complete failure is 3.97 mJ for the initial design and 6.04 mJ for the final design, which means that the final structure is 52% more resistant to fracture than the initial guess design.

Detailed propagation of the phase field crack of the final design composite structure with a single pre-existing crack notch subjected to incremental traction loads is given in Fig. 7.23. The initial crack propagates into the inner supporting structure and is blocked by the reinforced inclusion phase during the previous incremental loads. Then, two interface cracks nucleate and propagate along the upper and lower material interfaces. Inclusion materials which are redistributed up and down on the left side try to prevent the vertical propagation of matrix crack. Finally, the interface and matrix cracks intersect and propagat horizontally until the structure is fully broken.

7.2.3.2 Design of a plate without initial cracks for traction loads

The problem setting of this example is the same as in the last section except that there is no initial crack. The geometry of the plate is depicted in Fig. 7.24 (a), where the inclusion phase occupies a volume fraction of 5% of the sample. The optimized geometry of the inclusion phase is depicted in Fig. 7.24 (b). Detailed propagations of the phase field cracks of the initially and finally designed composite structures subjected to incremental traction load are given in Fig. 7.25 and Fig. 7.26, respectively. The cracks are firstly generated around the upper and lower material interfaces for the initial guess design, while they nucleate in the middle of the inner inclusion phase as well as in the interfaces for the new design. Then, similar interface cracks around the upper and

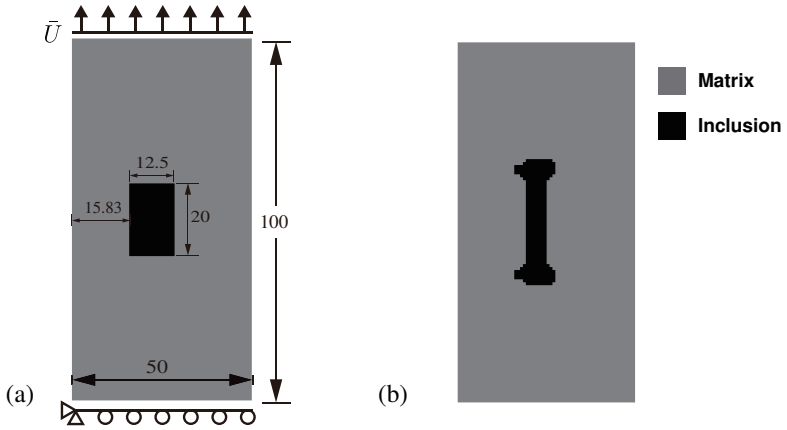

FIGURE 7.24: A plate without initial crack subjected to incremental traction loads: (a) geometry of the initial design; (b) final design.

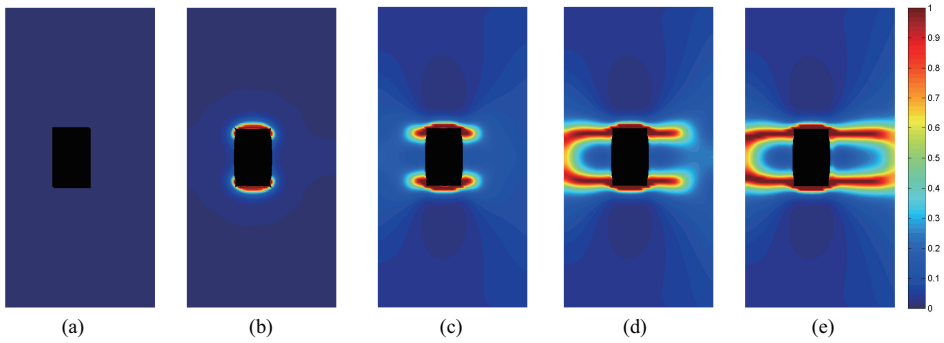

FIGURE 7.25: Crack propagation of the initial design composite structure without initial cracks subjected to incremental traction loads: (a) $\bar{U} = 0$ mm; (b) $\bar{U} = 0.025$ mm; (c) $\bar{U} = 0.065$ mm; (d) $\bar{U} = 0.085$ mm; (e) $\bar{U} = 0.105$ mm.

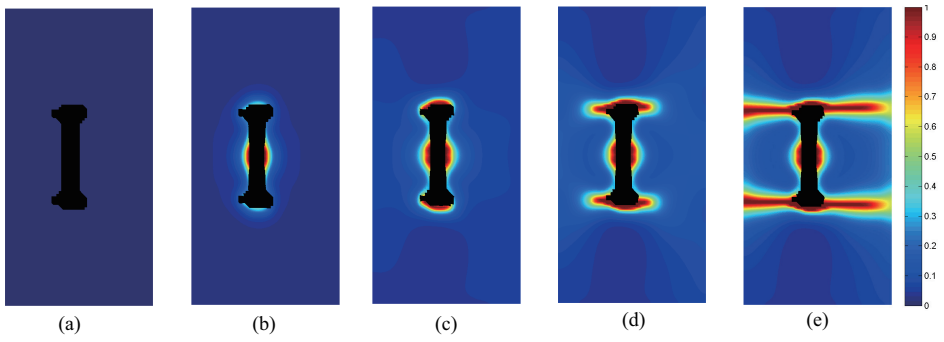

FIGURE 7.26: Crack propagation of the final design composite structure without initial cracks subjected to incremental traction loads: (a) $\bar{U} = 0$ mm; (b) $\bar{U} = 0.035$ mm; (c) $\bar{U} = 0.055$ mm; (d) $\bar{U} = 0.075$ mm; (e) $\bar{U} = 0.105$ mm.

lower material interfaces are generated. Finally, cracks propagate horizontally until the

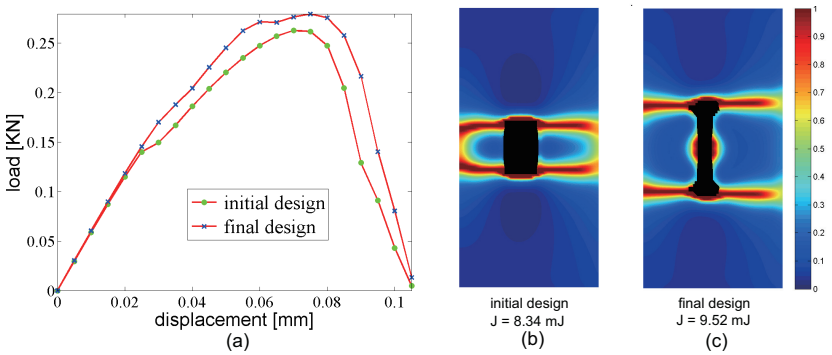

FIGURE 7.27: Fracture resistance comparison of two composite structures without initial crack subjected to incremental traction loads

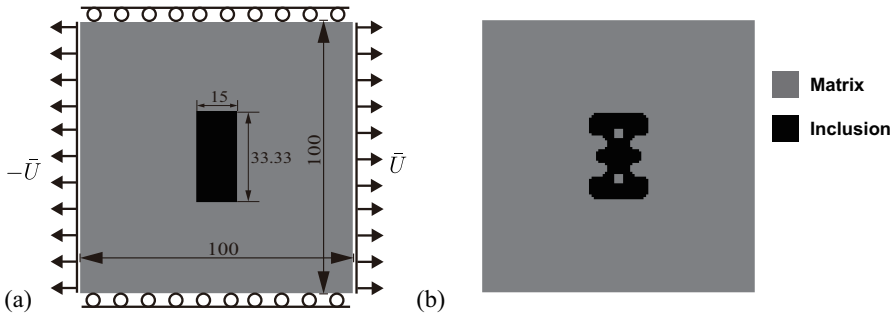

FIGURE 7.28: A square plate without initial crack subjected to uniaxial tension: (a) geometry of the initial design; (b) final design.

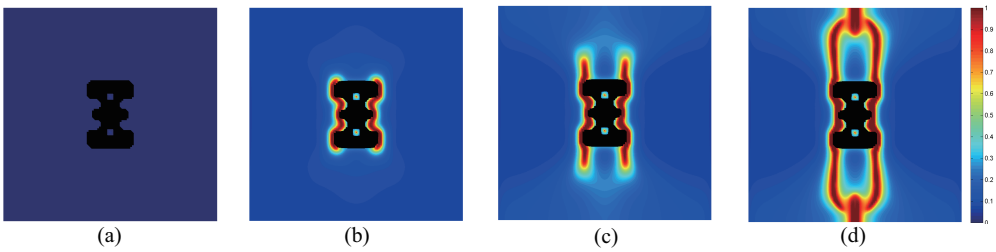

FIGURE 7.29: Crack propagation of the initial design composite structure with without initial cracks subjected to uniaxial tension: (a) $\bar{U} = 0$ mm; (b) $\bar{U} = 0.025$ mm; (c) $\bar{U} = 0.04$ mm; (d) $\bar{U} = 0.08$ mm.

structure is fully broken in both cases. The final crack patterns, the total required fracture energies for complete failure, and the load-displacement curves for the initial and optimized designs are given in Fig. 7.27. In this example, the structure with optimal design is 15% more resistant to fracture than the initial composite structure.

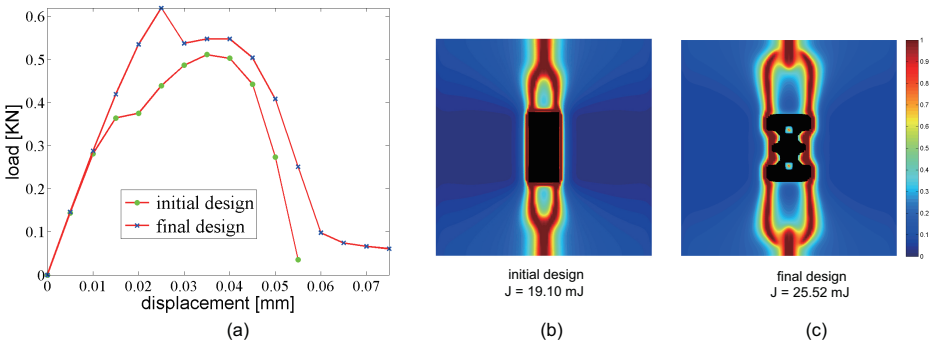

FIGURE 7.30: Fracture resistance comparison of two composite structures without initial cracks subjected to uniaxial tension.

7.2.3.3 Design of a square plate without initial cracks in tensile loading

This example aims to design a square composite plate without initial crack subjected to uniaxial tension. The problem geometry of the square plate is depicted in Fig. 7.28 (a). The dimensions of the plate are 100×100 mm^2, and the domain is uniformly discretized into 120×120 square bilinear elements. The boundary conditions are as follows: on the upper and lower end, the vertical displacements are fixed while the horizontal displacements are free. On the left and right end, the horizontal displacements are prescribed by an increasing uniform value of $\bar{U} = 0.005$ mm during the simulation. The incremental loading process continues until the reaction force is below a prescribed value indicating that the structure is fully broken. The initial guess involves an inclusion representing 5% of the volume fraction as shown in Fig. 7.28 (a). The final design of the inclusion phase is shown in Fig. 7.28 (b). The width of the final design is larger than the initial guess to resist the x-directional tension, and the inclusion phase topology is changed. Detailed propagation of the phase field crack in the composite structures with optimal design is given in Fig. 7.29. Here, the interface cracks firstly initiate at the interface (see Fig. 7.29 (b)). Subsequently, the left and right interface cracks propagate vertically and merge. The complete fracture patterns and design objective values are shown in Fig. 7.30 (b) for the initial design and in Fig. 7.30 (c) for the optimal design. Both responses are compared in Fig. 7.30 (a). Here, the fracture resistance of the final design structure has been increased by 33% as compared to the initial design.

7.2.3.4 Design of a plate with a single initial crack under three-point bending

The purpose of this example is to design a plate subjected to three-point bending with one initial crack. The problem geometry of the square plate is depicted in Fig. 7.31 (a). The dimensions of the plate are 50×100 mm. The domain is uniformly discretized

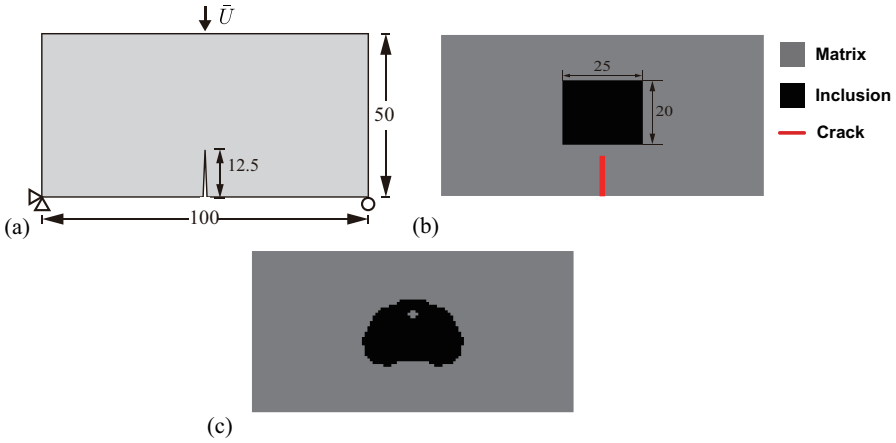

FIGURE 7.31: A plate with one initial crack subjected to three-point bending: (a) geometry and boundary condition; (b) geometry of the initial design and crack; (c) final design.

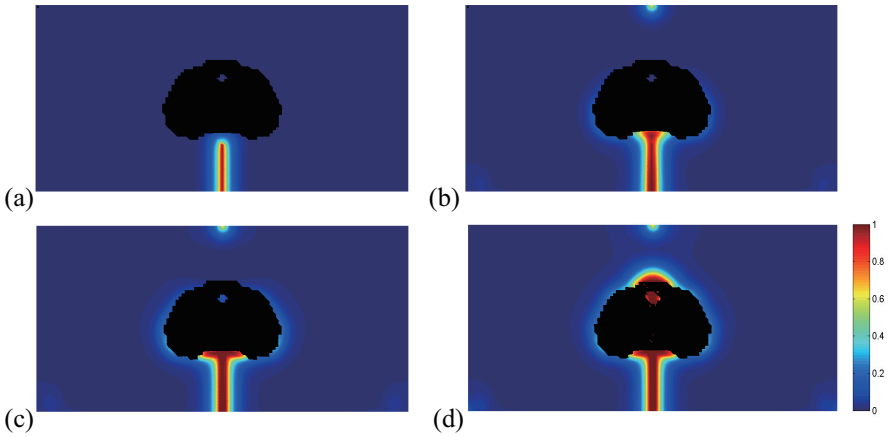

FIGURE 7.32: Crack propagation of the initial design composite structure without initial cracks subjected to three-point bending: (a) $\bar{U} = 0$ mm; (b) $\bar{U} = 0.11$ mm; (c) $\bar{U} = 0.14$ mm; (d) $\bar{U} = 0.16$.

into 60×120 square shape bilinear elements. The load consists into a prescribed displacement at the center of the beam on the top edge. The left bottom corner node is fixed, while node at the right bottom corner the y-displacement is fixed and the x-displacement is free. For this case, an initial pre-existing crack is shown in Fig. 7.31 (b), and the initial guess design with the inclusion phase occupying 10% volume fraction of the domain area. The computation is performed with monotonic displacement increments of $\bar{U} = 0.01$ mm until the reaction force is below a prescribed criterion value. The displacements are prescribed along the y-direction while the displacement along x is free.

The pre-existing crack is simulated by prescribing Dirichlet conditions with $d = 1$

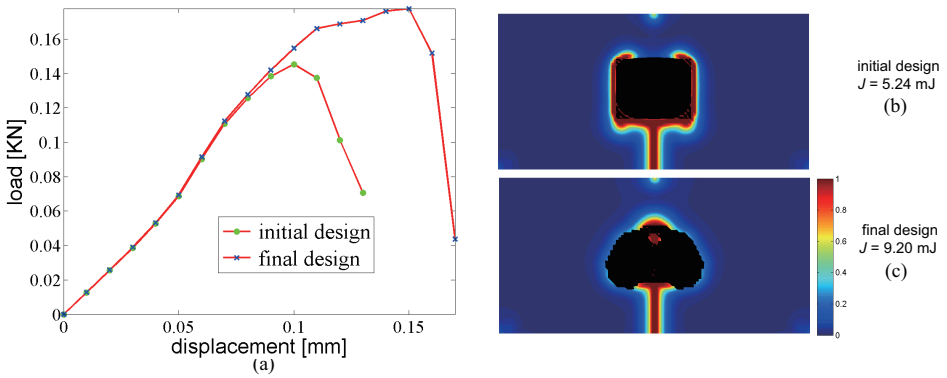

FIGURE 7.33: Fracture resistance comparison of two composite structures with one initial crack subjected to three-point bending.

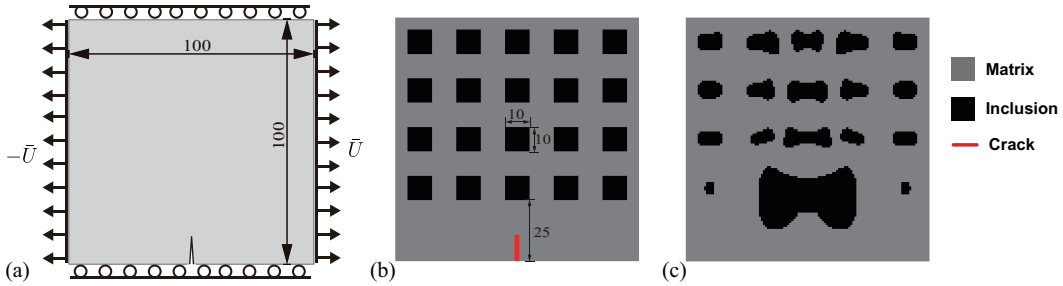

FIGURE 7.34: A plate containing multiple inclusions and a single initial crack for tensile loads: (a) geometry and boundary condition; (b) geometry of the initial design and crack; (c) final design.

along the crack. The surrounding area of the initial crack notch is treated as a non-design region. Fig. 7.31 (c) shows the final design of inclusion topology. Detailed propagation of the phase field crack of the finally designed composite structure with a single pre-existing crack notch subjected to three-point bending with monotonic displacement increments is shown in Fig. 7.32. The initial matrix crack firstly propagates vertically and is blocked by the reinforced inclusion phase materials. During the next steps, it tries to spread along the horizontal direction but is blocked by the inclusion material redistributed by the proposed topological optimization method. Eventually, the matrix crack propagates along the loading direction until the structure is fully broken. The two load-displacement curves are compared in Fig. 7.33 (a). The final crack patterns as well as the total required fracture energies for complete failure for the initial and final designs are shown in Fig. 7.33 (b) and Fig. 7.33 (c), respectively. In this example, the fracture resistance of the final design has been increased by 76% as compared to the initial design.

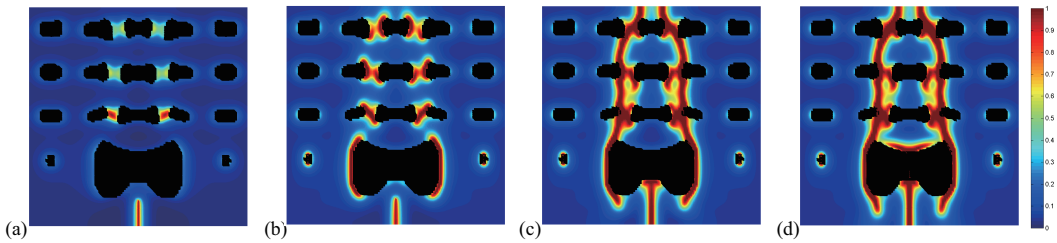

FIGURE 7.35: Crack propagation of the final design composite structure with one initial crack subjected to tensile loads: (a) $\bar{U} = 0.01$ mm; (b) $\bar{U} = 0.02$ mm; (c) $\bar{U} = 0.05$ mm; (d) $\bar{U} = 0.09$ mm.

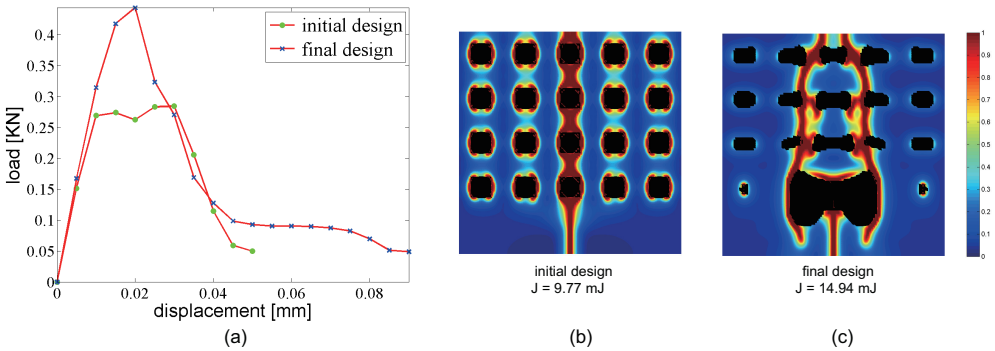

FIGURE 7.36: Fracture resistance comparison of two composite structures containing multiple inclusions and one initial crack subjected to tensile loads

7.2.3.5 Design of a plate containing multiple inclusions

Finally, a plate containing 20 periodically distributed square inclusions is considered. The plate is modeled as a square domain whose side is 100 mm. The length of the inclusions is computed such that the volume fraction of inclusion phase is equal to 20%. The boundary conditions are the same as described in Section 4.3 and are shown in Fig. 7.34 (a): on the lower and upper ends, the y-displacements are fixed, while the x-displacements are free. On the left and right ends, the y-displacements are free, while x-displacements are prescribed, with a uniform increasing value of $\bar{U}$ during the simulation. The computation is performed with monotonic displacement increments $\bar{U} = 0.005$ mm until the structure is completely broken. Here again, the surrounding region of the initial crack is assumed to be non-designable to avoid nonphysical designs. The final design is presented in Fig. 7.34 (c). Detailed propagation of the phase field crack of the final design of the considered composite structure containing multiple inclusions and a single initial crack subjected to tensile loads is shown in Fig. 7.35. It can be observed that the initial crack propagates vertically and new cracks around intermediate interfaces of the structure are generated. The inclusion materials are redistributed to prevent further propagation of critical cracks. In the subsequent loading

steps, the pre-existing crack meets the reinforced inclusion materials and is blocked at the beginning. Then, both matrix and interface cracks propagate toward the vertical direction as well as along the material interfaces until the structure is fully broken. The comparisons of final crack paths, the total required fracture energies for complete failure and load-displacement curves between initial and optimal designs are provided in Fig. 7.36. In this example, the fracture resistance has been increased by 53% in comparison with the initial design.

It is worth noting that in such optimization process, the crack pattern can involve multiple cracks, whose trajectories and number fully depends on the geometry of the inclusion phases. Then, it is very difficult to guess a priori the optimal geometry of inclusions to increase the fracture resistance. Finally, the main advantages of the phase field method in topological optimization process are summarized as follows: (a) it is easy to couple the phase field method with a topological optimization algorithm as a fixed mesh can be employed for the fracture simulation; (b) initiation of cracks can be included in the analysis, which would be not possible with techniques like XFEM [114]; (c) including interfacial damage is simple in the present framework, using e.g. extensions of the phase field as proposed in [123]. Using cohesive elements in that case would make the analysis much more complex when defining the sensitivity with respect to the material density in the topological algorithm. Then, the present framework seems to be very promising to design new composite materials with enhanced fracture resistance.

7.3 Topology optimization for maximizing the fracture resistance of periodic composites

This section extends the topology optimization framework of optimal fracture resistance to periodic composites, considering the heterogeneities and their interfaces in the material. The phase field method presented in section 7.2.1 is adopted for modeling fracture propagation in two-phase composites. The composite is assumed to be composed of the substructure or repesentative volume element (RVE) periodically. Therefore, the optimization is carried out only on the RVE, but takes into account the response of the whole composite specimen to maximize its fracture resistence. Extended BESO method is adopted to redistribute the inclusion phase in the RVE with constant volume fraction. In the following, the topology optimization model for maximizing the fracture resistence of periodic composites is proposed in section 7.3.1. Element sensitivity number acounting for complete fracturing process of the whole periodic structure

is defined. Several numerical examples are presented in section 7.3.2 to show significant improvement of the fracture resistence of the optimized periodic composites compared to initial designs. In addtion, the optimized inclusion phase is applied to larger samples, which contain a larger number of unit cells, to further validate the proposed numerical design framework.

7.3.1 Topology optimization model

In this section, the optimization problem is solved to find the optimal material distribution or topology of the inclusion phase within the RVE so as to maximize the fracture resistence of the resulting periodic composites. It is assumed that the total number of substructures/RVEs in the composite is N_s. The fracture resistence maxmization problem can then be formulated using the design variable ρ_e^k, where k and e denote the substructure number and the element number in each substructure, respectively, as:

$$\text{Find} : \{\boldsymbol{\rho}^{(1)}, \ldots, \boldsymbol{\rho}^{(N_s)}\} \tag{7.118}$$

$$\text{Maximize} : J(\boldsymbol{\rho}, \mathbf{u}, \mathbf{d}, \boldsymbol{\beta}) \tag{7.119}$$

$$\text{subjected to} : \mathcal{R} = 0 \tag{7.120}$$

$$: V(\boldsymbol{\rho}) = N_s \sum \rho_e^{(k)} v_e^{(k)} = V_{\text{req}}, \tag{7.121}$$

$$: \rho_e^{(1)} = \cdots = \rho_e^{(N_s)},\ e = 1, \ldots, N_e, \tag{7.122}$$

$$: \rho_e^{(k)} = 0 \text{ or } 1, e = 1, \ldots, N_{\text{e}},\ k = 1, \ldots, N_s. \tag{7.123}$$

where J is known as the fracture energy which is calculated by using numerical integration (7.104). $\mathcal{R}$ denotes the nodal residual force (7.106). In (7.121), $v_e^{(k)}$ is the volume of the $e-$th element in the $k-$th unit cell, and N_e is the number of elements in each cell. Similar to the optimization model defined in Section 5.1 and 5.2 in Chapter 4, the condition $\rho_e^{(1)} = \cdots = \rho_e^{(N_s)},\ e = 1, \ldots, N_e$ ensures that the pseudo densities (0 or 1) of elements at the corresponding locations in each substructure are the same. Following the Equation (7.103) in Section 7.2.2, we have the same material interpolation model:

$$E_e = \rho_e E_{\text{inc}} + (1 - \rho_e) E_{\text{mat}} \tag{7.124}$$

where ρ_e takes the value of zero and one corresponding to the matrix and inclusion phase, respectively.

Based on the sensitivity analysis as formulated in Section 7.2.2, the derivative of the total mechanical work J with respect to the topology design variable ρ_e can be stated as:

$$\frac{\partial \widehat{J}}{\partial \rho_e} = -\frac{1}{2}\sum_{n=1}^{n_{\text{load}}}\left\{\left(\boldsymbol{\lambda}^{(n)}\right)^T \int_{\Omega_i} \mathbf{B}^T(\boldsymbol{\sigma}^e)^{(n)} d\Omega_e + \left(\boldsymbol{\mu}^{(n)}\right)^T \int_{\Omega_e} \mathbf{B}^T(\boldsymbol{\sigma}^e)^{(n-1)} d\Omega_i\right\}. \quad (7.125)$$

However, since the considered composites are periodic in this scheme, the optimization process is carried out only within the substructure/RVE. Therefore, the element sensitivity numbers at the same location in each substructure need to be consistent to enforce the periodic array of the substructures. They are then defined as the summation of the sensitivity of corresponding elements in all substructures, i.e. the sensitivity number α_e is formulated as:

$$\alpha_e = \sum_{k=1}^{N_s} \frac{\partial \widehat{J}}{\partial \rho_e^{(k)}} \quad (7.126)$$

As a result, the above sensitivity information takes into account the fracture response of the whole periodic composite so as to maximize its fracture resistance.

Following Section 7.2.2, the sensitivity numbers associated with the relative ranking of the element sensitivities are treated with the damping as (7.56). In order to avoid checkerboard patterns, the above formulated sensitivity numbers are then smoothed by means of a filtering scheme as (7.57). Due to the discrete nature of design variable of the adopted method and to avoid oscillations in evolutionary history of the design objective value, the current sensitivity number is further averaged with its historical information as (7.59).

It is recalled that the material volume fraction of reinforced inclusion phases is kept constant during the optimization process. However, the geometry of inclusions is optimized in substructure/RVE so as to maximize the fracture resistance of the resulting periodic composite sample. Extended BESO method formulated in Section 7.2.2 is adopted to solve the optimization problem (7.118)-(7.123) by using the above modified sensitivity numbers, which account for the whole fracturing process, involving crack nucleation, propagation and interaction until complete failure of the considered periodic composite.

7.3.2 Numerical examples

In this section, several numerical examples are presented to demonstrate the proposed topology optimization framework for maximizing the fracture resistence of periodic composites. In all tests, regular meshes using quadrilateral bilinear elements are adopted, and plane strain assumption is adopted. The same finite element discretization is employed for both displacement and crack phase fields. The regularization parameter ℓ

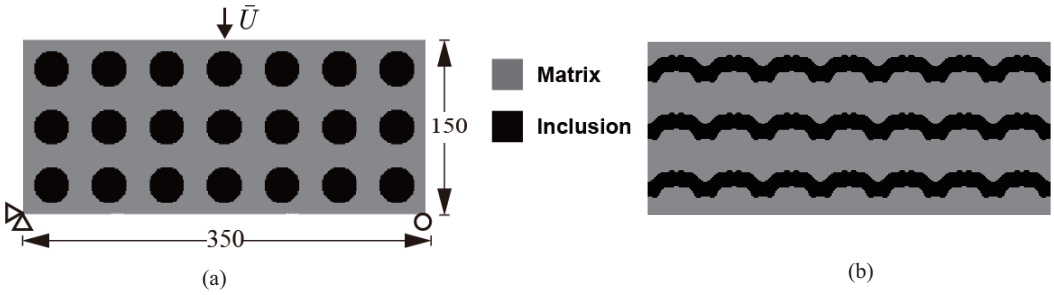

FIGURE 7.37: A periodic composite without initial crack subjected to three-point bending: (a) geometry of the initial design; (b) final design.

describing the width of smeared crack and interface is chosen as twice the finite element size $\ell = 2\ell_e$. In addition, material properties of both matrix and inclusion phases are the same as shown in 7.2.3, and so are the toughness and the interface fracture strength.

7.3.2.1 Design of a periodic composite under three-point bending

The problem geometry of the first example is depicted in Fig. 7.37 (a), where the composite is composed of $N_s = 7 \times 3$ unit cells periodically repeated along $x-$ and $y-$ directions, respectively. In the initial guess design of the RVE as shown in Fig. 7.37 (a), inclusion phase covers the centered circle domain with diameter corresponding to the volume fraction of 30%. The dimensions of the whole composite structure are 350×150 mm, and the domain is uniformly discretized into 350×150 square shaped bilinear elements. The boundary conditions are as follows: the left bottom corner node is fixed, while at the right bottom corner node the y-displacement is fixed and the x-displacement is free. On the upper end, the load consists in a prescribed displacement $\bar{U}$ at the center point. The displacement is prescribed along the y-direction while the displacement along x is free. The computation is performed with monotonic displacement increments of $\bar{U} = 0.01$ mm until the reaction force is below a prescribed criterion value indicating that the structure is completely broken.

During the optimization process, the material volume fraction of the inclusion phase is maintained constant in all next examples. Based on their sensitivity numbers, the inclusion phase will be redistributed within the periodic cell by the extended BESO method so as to improve the fracture resistance of the whole periodic composite. Fig.7.37 (b) shows the final design of inclusion topology and the resulting composite structure. It is observed that the material on the bottom side of the reinforcement inclusion phase moves left and right, and the final design inclusion phases are interconnected in horizontal cells to form a "wave" structure.

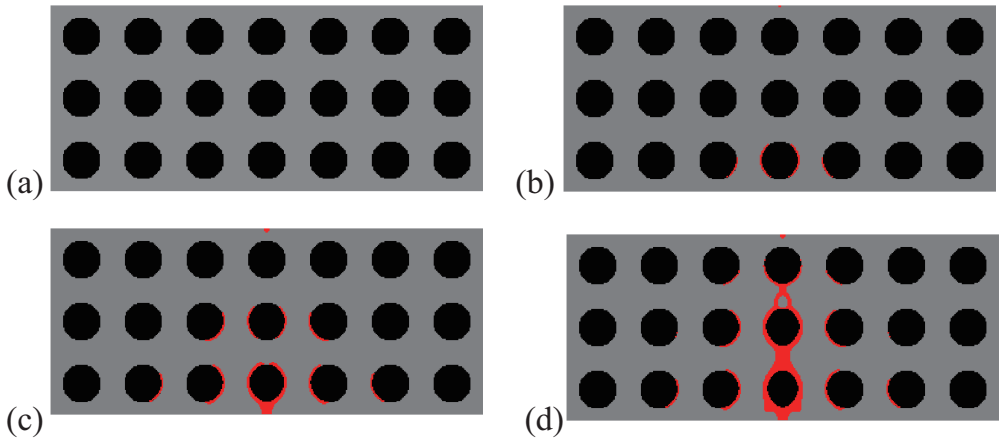

FIGURE 7.38: Crack propagation in the initial periodic composite without initial cracks subjected to three-point bending: (a) $\bar{U} = 0$ mm; (b) $\bar{U} = 0.11$ mm; (c) $\bar{U} = 0.17$ mm; (d) $\bar{U} = 0.20$ mm; (e) $\bar{U} = 0.24$ mm; (f) $\bar{U} = 0.28$ mm.

Detailed propagation of the phase field crack of the initial and finally designed periodic composite subjected to three-point bending with monotonic displacement increments is shown in Fig. 7.38 and Fig. 7.39, respectively. We can see that the trajectories, numbers as well as propagation paths of the phase field cracks are totally different since the geometry of the inclusion phases is changed. However, both crack patterns are symmetric since we use the symmetric boundary conditions, and initial cracks are both generated at the interface between different phases. Subsequently, one bulk crack initiates and propagates along the force direction for the initial design, until the periodic structure is broken. For the optimal design, more interface cracks initiate and propagate along the phase interfaces, resulting in an increase of interface damage of the composite. Finally, bulk cracks propagate vertically as loading continues, until the periodic structure is fully broken. The final crack patterns, the total required fracture energies for complete failure, and the load-displacement curves for the initial and optimal designs are given in Fig. 7.40. In this example, the periodic composite with optimal design is 124% more resistant to fracture than the initial composite structure.

In the following, we use the optimized geometry of the inclusion phase for a larger periodic sample which contains a much larger number of unit cells. The geometries of the initial and optimal design periodic composites are depicted in Fig. 7.41 (a) and (b), respectively. The dimensions of the two composites structures are 700×300 mm and are both uniformly discretized into 700×300 square shape bilinear elements. The boundary conditions are the same as in Fig. 7.37. However, the composites are herein composed of $N_s = 14 \times 6$ unit cells periodically, along $x-$ and $y-$ directions, respectively. The computation is performed with monotonic displacement increments of $\bar{U} = 0.01$ mm until the reaction force is below a prescribed criterion value.

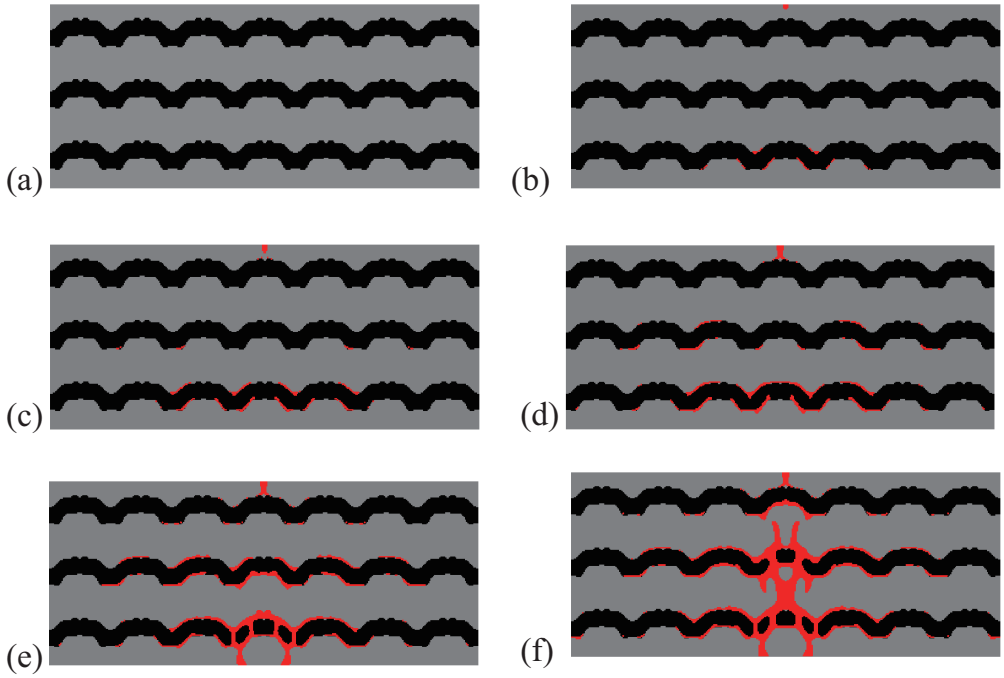

FIGURE 7.39: Crack propagation of the final design periodic composite without initial cracks subjected to three-point bending: (a) $\bar{U} = 0$ mm; (b) $\bar{U} = 0.17$ mm; (c) $\bar{U} = 0.23$ mm; (d) $\bar{U} = 0.28$ mm; (e) $\bar{U} = 0.32$ mm; (f) $\bar{U} = 0.37$ mm.

(a) Initial design, J = 19.7 mJ

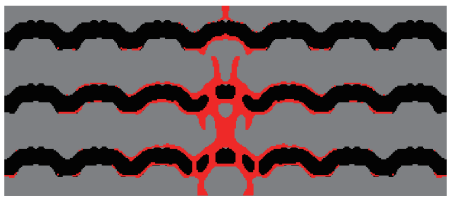

(a) Final design, J = 44.2 mJ

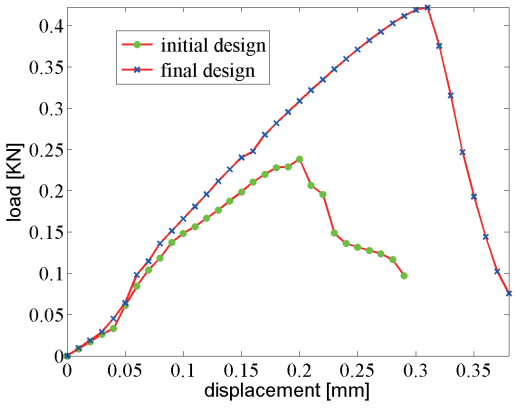

(c)

FIGURE 7.40: Fracture resistance comparison of two periodic composites without initial cracks subjected to three-point bending.

In this case, the detailed propagation of the phase field crack in the initial and optimal periodic composites is shown in Fig. 7.42 and Fig. 7.43, respectively. Again, crack pattern involves multiple cracks, and its trajectory and number fully depend on the geometry of the inclusion phases. The composite structure with optimized inclusion

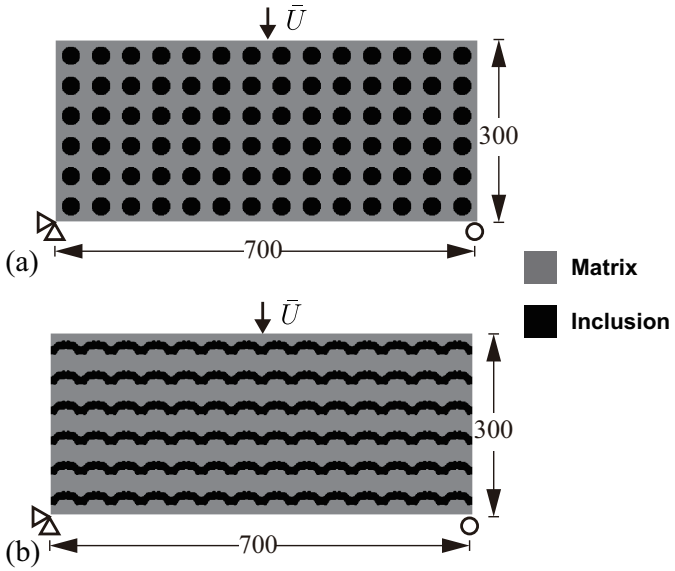

FIGURE 7.41: A larger periodic composite without initial crack subjected to three-point bending: (a) geometry of the initial design; (b) final design.

geometry is more damaged requiring larger mechanical energy for complete failure. The comparisons of final crack paths, the total required fracture energies for complete failure and load-displacement curves between initial and optimal designs are provided in Fig. 7.44. For the larger sample, the resistance to fracture of final periodic composite has been increased by 82.5% in comparison with the initial design.

7.3.2.2 Design of a periodic composite under non-symmetric three-point bending

This example aims to design a periodic composite subjected to non-symmetric three-point bending without initial cracks. Comparing with the boundary condition shown in Fig.7.37, the load in this case consists in a prescribed displacement at the center point of the right half-beam on the top edge, as shown in Fig. 7.45 (a). The vertical displacement is prescribed by an increasing uniform value of $\bar{U} = 0.01$ mm during the simulation, until the considered periodic composite is fully broken. The initial guess design of the inclusion geometry is the same as in the last example, which means that the inclusion phase occupies a volume fraction of 30% of the sample. The considered composite is composed of $N_s = 9 \times 3$ unit cells repeated periodically along each space directions. The dimension of the composite is 450×150 mm, and the domain is uniformly discretized into 450×150 square shape bilinear elements. The redistribution of the inclusion phase is carried out in a single unit cell based on the sensitivity information which accounts for the fracture resistence response of the whole periodic structrue.

The optimized geometry of the inclusion phase as well as the resulting periodic composites are depicted in Fig. 7.45 (b). Detailed propagation of the phase field cracks

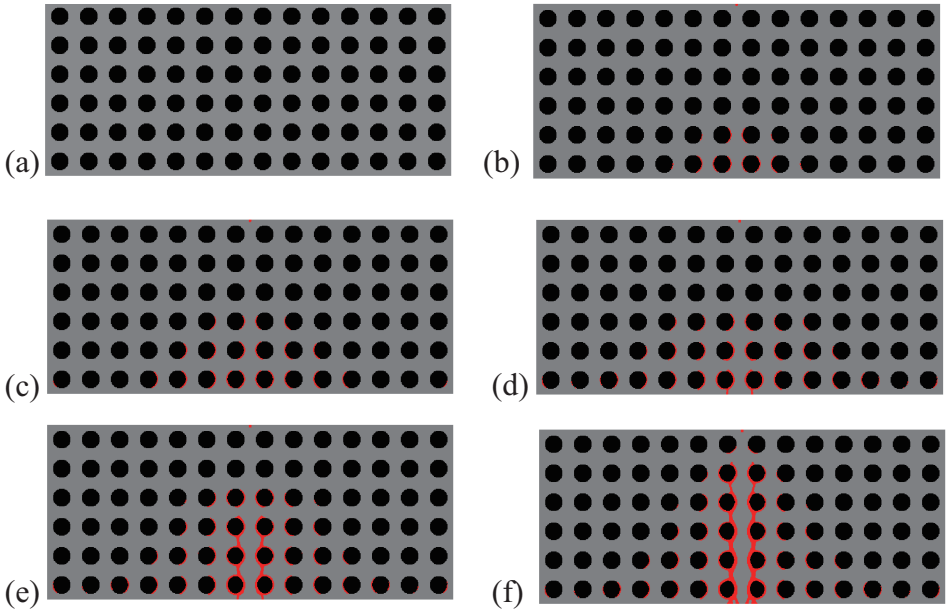

FIGURE 7.42: Crack propagation in the initial periodic composite without initial cracks subjected to three-point bending: (a) $\bar{U} = 0$ mm; (b) $\bar{U} = 0.25$ mm; (c) $\bar{U} = 0.35$ mm; (d) $\bar{U} = 0.41$ mm; (e) $\bar{U} = 0.44$ mm; (f) $\bar{U} = 0.59$ mm.

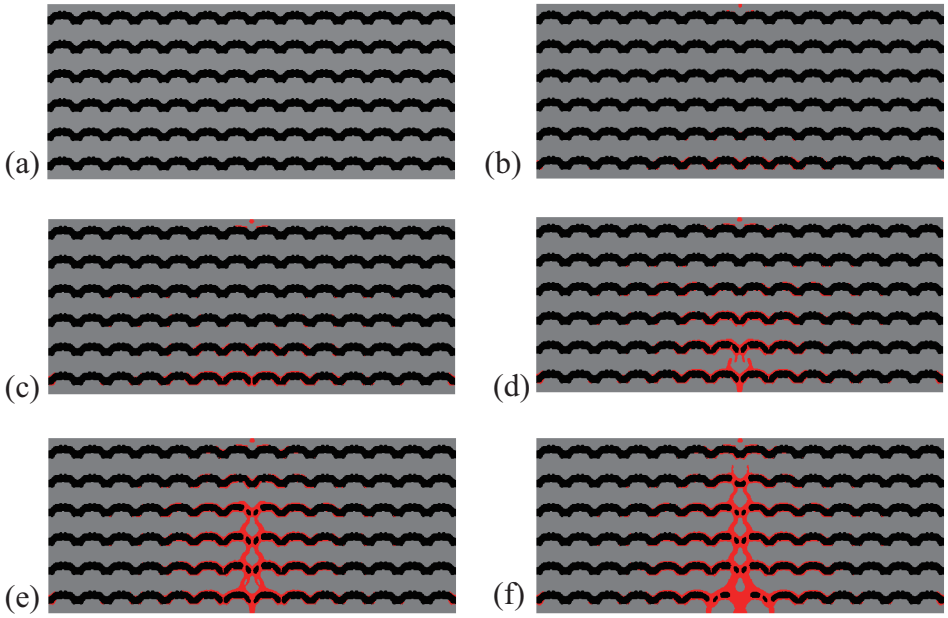

FIGURE 7.43: Crack propagation in the optimized design periodic composite without initial cracks subjected to three-point bending: (a) $\bar{U} = 0$ mm; (b) $\bar{U} = 0.39$ mm; (c) $\bar{U} = 0.52$ mm; (d) $\bar{U} = 0.57$ mm; (e) $\bar{U} = 0.61$ mm; (f) $\bar{U} = 0.72$ mm.

of the initial and finally designed composite structures subjected to incremental traction load are given in Fig. 7.46 and Fig. 7.47, respectively. It is observed that the cracks

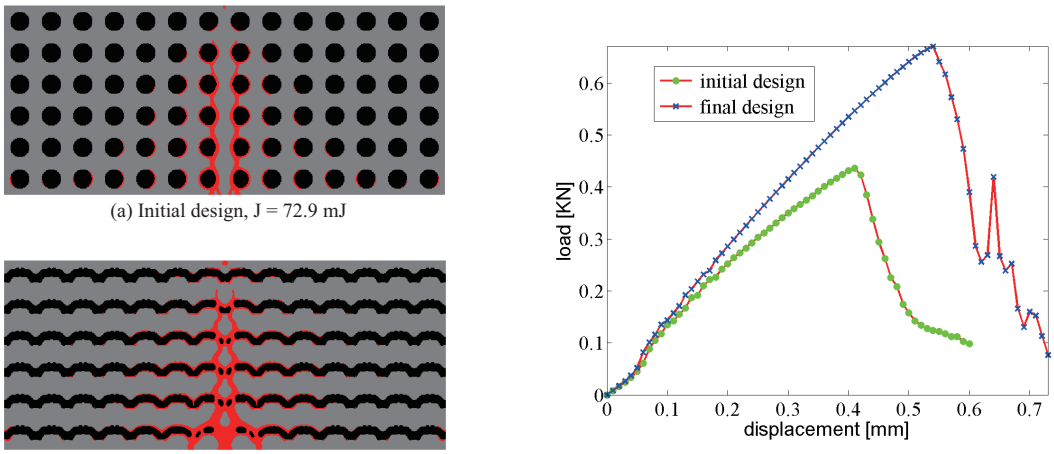

(a) Initial design, J = 72.9 mJ

(a) Final design, J = 129.4 mJ

(c)

FIGURE 7.44: Fracture resistance comparison of two periodic composites with larger number of cells subjected to three-point bending.

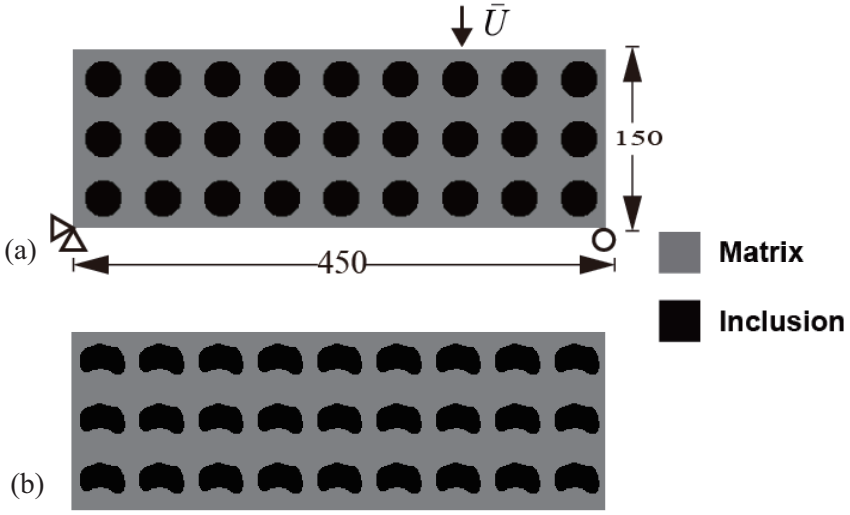

FIGURE 7.45: A periodic composite without initial crack subjected to non-symmetric three-point bending: (a) geometry of the initial design; (b) final design.

are both firstly generated around the material interface below the applied force. Then only one bulk crack along the force direction is generated for the initial guess design, while more complex cracks nucleate for the new design. Finally, cracks propagate vertically until the structure is fully broken in both cases. We can see that the new design periodic composite is more damaged, resulting in larger required fracture energy. The final crack patterns, the total required fracture energies for complete failure, and the load-displacement curves for the initial and final designs are given in Fig. 7.48. In this example, the periodic composite with optimal inclusion geometry is 100.6% more resistant to fracture than the initial composite.

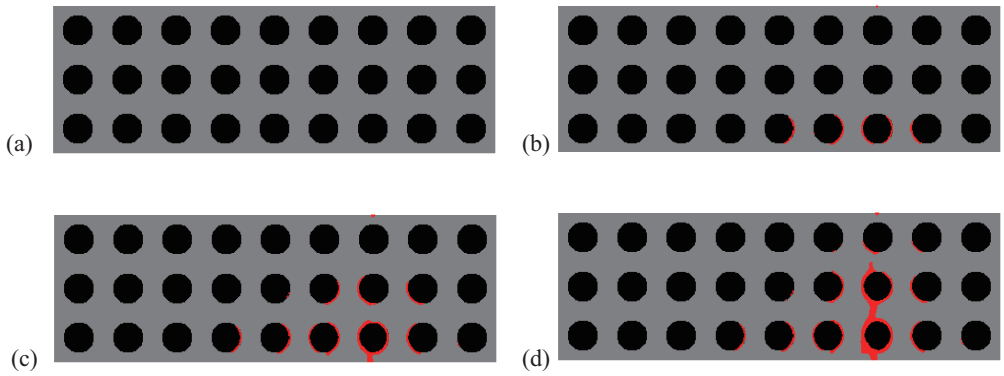

FIGURE 7.46: Crack propagation in the initial periodic composite without initial cracks subjected to non-symmetric three-point bending: (a) $\bar{U} = 0$ mm; (b) $\bar{U} = 0.17$ mm; (c) $\bar{U} = 0.24$ mm; (d) $\bar{U} = 0.30$ mm.

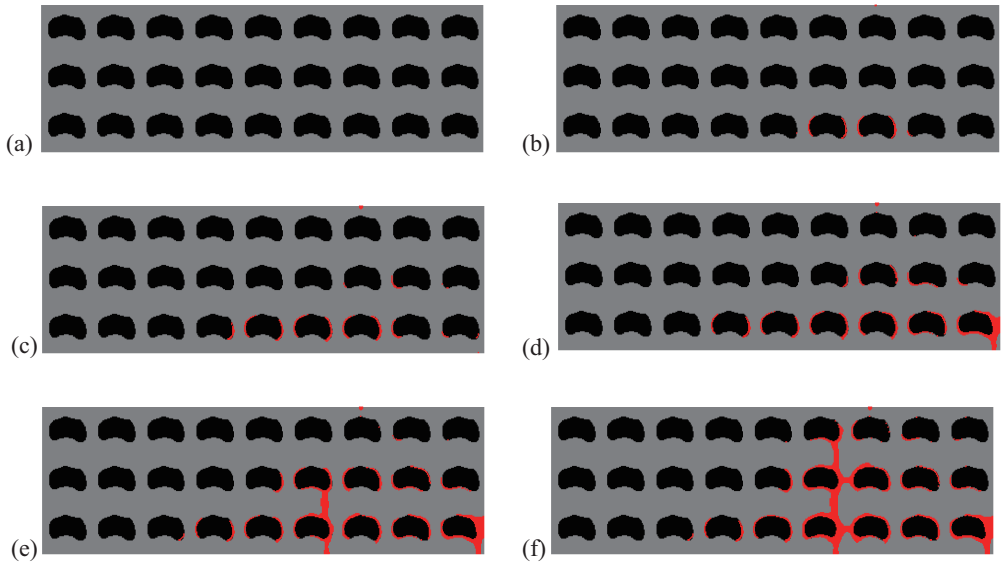

FIGURE 7.47: Crack propagation in the optimized design periodic composite without initial cracks subjected to non-symmetric three-point bending: (a) $\bar{U} = 0$ mm; (b) $\bar{U} = 0.17$ mm; (c) $\bar{U} = 0.24$ mm; (d) $\bar{U} = 0.33$ mm; (e) $\bar{U} = 0.39$ mm; (f) $\bar{U} = 0.44$ mm.

Finally, we apply the optimized geometry of the inclusion phase obtained in the first example for a larger periodic sample but subjected to non-symmetric three-point bending. The dimensions as well as the boundary conditions of the initial and optimal periodic composites are depicted in Fig. 7.49 (a) and (b), respectively. The structures are both uniformly discretized into 900×300 square bilinear elements. The force is applied to the top edge at a distance of 250 mm from the apex of the upper right corner. The vertical displacement is also prescribed as an increasing uniform value of $\bar{U} = 0.01$ mm during the simulation unitl the reaction force goes below a prescribed value indicating that the periodic composite is fully broken. The complete fracture patterns and design

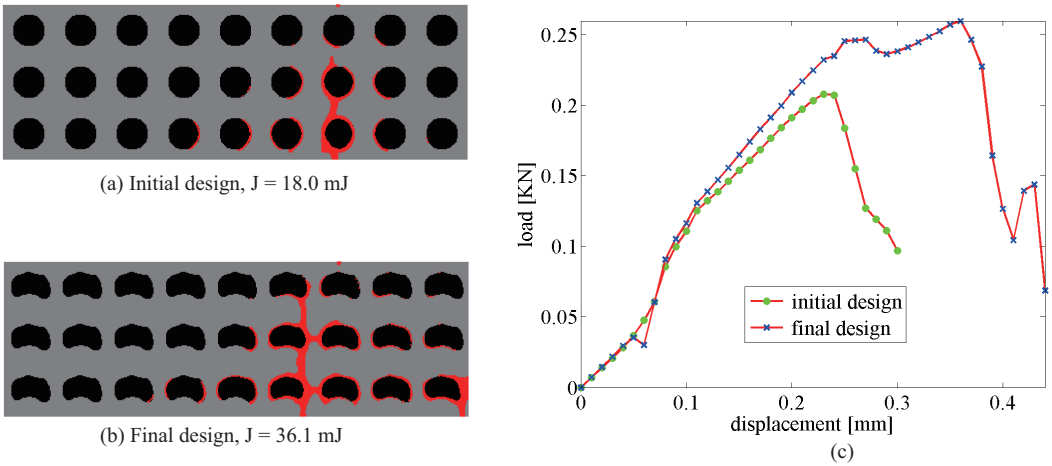

FIGURE 7.48: Fracture resistance comparison of two periodic composites without initial cracks subjected to non-symmetric three-point bending.

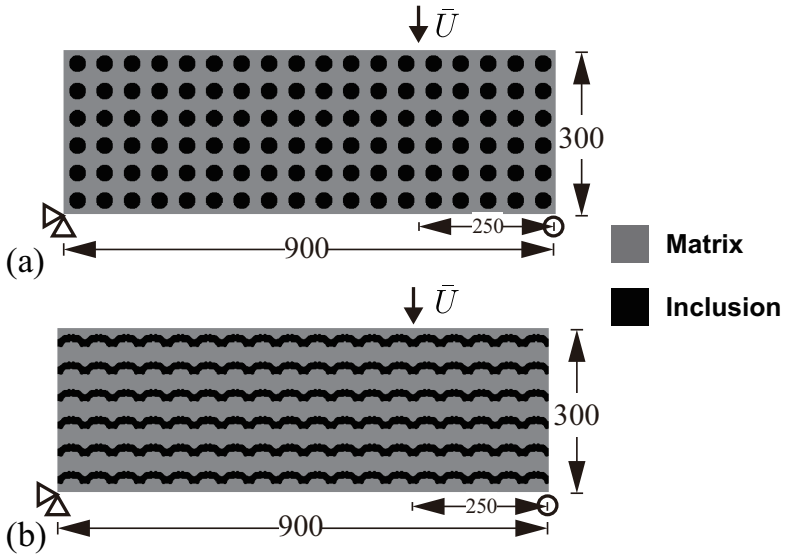

FIGURE 7.49: A larger periodic composite without initial crack subjected to non-symmetric three-point bending: (a) geometry of the initial design; (b) final design.

objective values are shown in Fig. 7.50 (a) for the initial design and in Fig. 7.50 (b) for the optimal design. Both responses are compared in Fig. 7.50 (c). Here, the fracture resistance of the optimized design periodic composite has been increased by 135.4% as compared to the initial design.

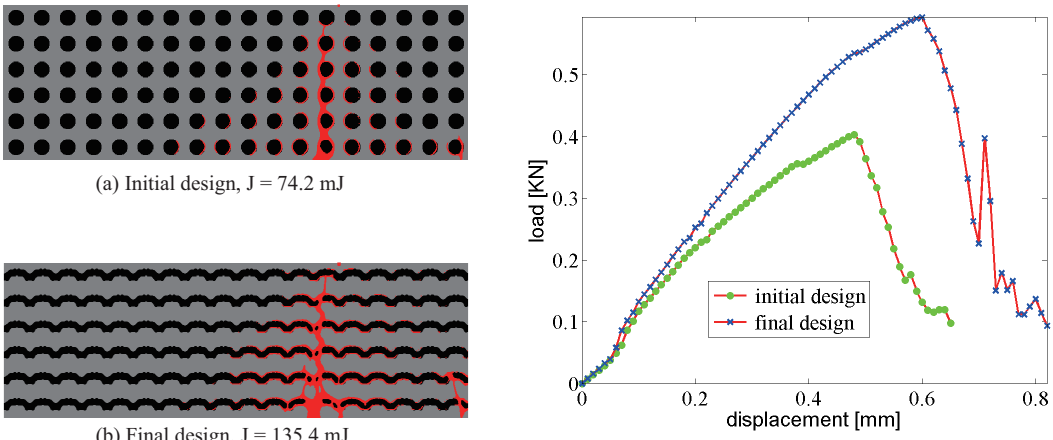

(a) Initial design, J = 74.2 mJ

(b) Final design, J = 135.4 mJ

(c)

FIGURE 7.50: Fracture resistance comparison of two periodic composites with larger number of cells, subjected to non-symmetric three-point bending.

7.4 Concluding remarks

In this section, we have firstly proposed a numerical design framework for fracture resistance of composites, by an optimal design of the spatial distribution of inclusion phase with a given target volume fraction. The phase field method model fracturing with a regularized description of discontinuity has been adopted for the complete fracturing process. One particular merit of the adopted phase field method is the regularized description of discontinuous fields, which avoids the burden of remeshing during the crack propagation which is fully adapted to topology optimization. The optimal design of the spatial distribution of inclusion phase is realized by means of topology optimization using an extended bi-directional evolutionary structural optimization method. Both 2D and 3D benchmark tests have demonstrated that significant improvement of the fracture resistance of composites has been achieved for designs accounting for full failure when compared to conventional linear designs. Compared to previous studies in the literature on the subject, this work provides a much more efficient alternative for the design of high fracture resistant composites. There exist twofold merits of the developed design framework: on the one hand, the adoption of topology optimization provides an uttermost design freedom, yielding higher fracture resistant designs; on the other hand, limited number of iterations is required for the design as a result of gradient information, which is of essential importance dealing with computationally demanding fracturing simulation.

Then, we have developed the topology optimization framework to improve fracture resistance of composites through a redistribution of constant inclusion phases, considering interactions between bulk brittle fracture and interfacial damage. The sole

and unique phase field is employed to describe both bulk brittle fracture and interface cracking, and thus allows interaction between the two types of cracks. Before performing the topology optimization, a computationally efficient adjoint sensitivity formulation is derived to account for the whole fracturing process, involving cracks nucleation, propagation and interaction, either from the interfaces and then through the solid phases, or the composite. Based on the determined sensitivity numbers, the constant amount of reinforced inclusion materials is redistributed by using the extended bi-directional evolutionary structural optimization method. Several benchmark tests have been presented to demonstrate the potential of the proposed design framework. It has been shown that significant improvement of the fracture resistance of the considered composite structures can be achieved for final designs accounting for full failure when compared to the initial guess.

Finally, we have extended the topology optimization framework for maximizing the fracture resistance to periodic two-phase composites. Optimization design domain is defined in a single cell since the considered composite structure is periodic. Element sensitivity number in the cell is then defined as the summation of the sensitivity of corresponding elements in all cells, so as to account for the fracture response of the whole periodic composite during the fracturing process. As a result, the topology optimization is allowed to be carried out in one single cell and the fracture resistence of the whole composite structure is improved. Several numerical examples have demonstrated that the fracture resistance of the considered periodic composite can be improved significantly for final designs accounting for full failure when compared to the initial guess designs. In addition, the optimized geometry of the inclusion phase can be effectively applied to periodic samples which containt a larger number of unit cells. As a conclusion, the presented topological optimization framework has big potential to design new periodic composites with enhanced fracture resistance.

To our best knowledge, the topology optimization for fracture resistance taking into account interactions between interfacial damage and bulk brittle fracture for complete fracturing process has been done for the first time in this work. The presented method then provides a very promising design tool to improve the fracture resistance of heterogeneous materials where both interfacial damage and matrix crack propagation occur, and could constitute a basis for improving other physical properties involving interfacial damages.

Chapter 8

Conclusion and perspectives

In this thesis, we have introduced contributions to the modeling of heterogeneous materials by topology optimization, with special emphasis on: (a) materials with extreme properties; (b) topology optimization in a multiscale context, including non-separated scales and (c) topology optimization of heterogeneous materials to maximize their resistance to fracture.

In the first part, we develop primarily in Chapter 2 a new evolutionary topology optimization method for continuum structures. The newly proposed method determines implicitly the structural topology by a level-set function constructed by nodal sensitivity numbers, resulting in smoothed boundary representation and high robustness. In Chapter 3, we firstly introduce the hybrid cellular automata technique to the design of material periodic microstructures with extreme elastic properties or negative Poisson's ratio. By this method, no sensitivity information is required to find the optimal material geometries, and a local rule is adopted to update design variables iteratively until meeting the prescribed optimality conditions. In the second part, we extend the material design to simultaneous multi-phase materials and structure design in Chapter 4, introducing the underlying three or more phases material microstructures for both the solid and compliant composite phases of the macroscale structures. In Chapter 5, multiscale topology optimization in the context of non-separated scales is studied comprehensively. First, we use a coarse mesh corresponding to a homogenized medium based on the classical numerical homogenization, allowing reducing the micro fields to perform the topology optimization. Size effect of the periodic unit cell is investigated to show that the present framework leads to an optimized structure with higher compliance when the scales cannot clearly be separated. To this end, we develop a new multiscale topology optimization procedure, by using a nonlocal filter-based homogenization scheme to take into account all structural details and the strain gradient effects. We have shown that taking into account strain gradient effects can lead to a significant increase in the stiffness of the lattice associated with the optimized topology. Finally, we extend the multiscale topology optimization framework to the design of the geometry of mesoscopic structures with fixed microscopic unit cells. As expected, periodic

unit cells have major influence on the optimal solutions of the mesoscopic structures. To sum up, topological optimization and numerical homogenization scheme without scale separation are combined in this Chapter, allowing the optimization problem to be performed on a coarse mesh, instead of using the fully detailed description of the structure for computational saving.

In the third part, we propose to investigate the use of topology optimization for maximizing the fracture resistance of heterogeneous structures and materials. In view of future extensions and applications to civil engineering materials, we have proposed a first attempt for the extension of the phase field fracture method to viscoelastic materials in Chapter 6. Both 2D and 3D heterogeneous materials subjected to loading with various durations have been analyzed with regard to different crack patterns. In Chapter 7, we study the topology optimization of heterogeneous materials to maximize their resistance against fracture. The objective here is to maximize the required mechanical work until complete failure of heterogeneous materials, involving cracks nucleation, propagation and interaction. To our best knowledge, this part constitutes the first contribution to propose a numerical design framework for fracture resistance of quasi-brittle composites, by an optimal design of the spatial distribution of inclusion phase with a given target volume fraction. The phase field method to fracturing with a regularized description of discontinuity has been adopted for the modeling of complete fracturing process. Secondly, we extend the design framework for taking into account crack nucleation both in the matrix and in the interfaces. The material volume fraction of reinforced inclusion phases is kept constant during the optimization process. Lastly, we extend the topology optimization framework taking into account interfacial damage to periodic composite. Numerical results show that it is easy to couple the phase field method with a topological optimization algorithm as a fixed mesh can be employed for the fracture simulation. In addition, including interfacial damage is simple in the present framework by the extensions of the phase field modeling. A series of numerical examples demonstrate that the fracture resistance of the (periodic) composite can be significantly increased by the proposed topology optimization process, comparing with the initial designs. Therefore, the present topological optimization framework seems to be very promising to design new composite materials with enhanced fracture resistance.

Generally speaking, design of multiscale structures without scale saparation and fracture resistance optimization are both new fields that remain relatively unexplored so far, until recently. Combining (new) topology optimization techniques and additive manufacturing processes, many potential developments can be carried out for engineering problems. In the following we provide a few perspectives to the present thesis work.

(1) From the Chapter 2, the cellular automata method does not require sensitivity analysis in the optimization process, resulting in a great convenience for structural topology optimization, no matter in mono or multiscale design framework. Further research based on the cellular automata method could be conducted to study the simultaneous heterogeneous materials and structures design in the context of non-separated scales as in Chapter 5. This advantage could be further exploited in non-linear multiscale topology optimization, such as the crashworthiness design of automotive graded structures.

(2) In the context of non-separated scales, improvements of connectivity between optimized periodic cells (see e.g. Fig. 5.17) can be investigated. In addition, the material microstructures have been assumed to be periodic in this work, even though this is not mandatory. Optimization design of non-periodic materials to fully release the design freedom within multiscale framework and achieve higher performance structures could constitute an interesting future study. Furthermore, the development and verification of advanced lattice structure by additive manufacturing processes, while considering large deformation problems and multi-functional and multi-physics behavior would have also great research prospects.

(3) Finally, we have initiated through Chapter 7 a wide field of study concerning topology optimization for maximizing the fracture resistance. The preliminary results presented in this thesis could be further investigated along the following lines: (a) reducing the associated computational costs; (b) experimental validations of the predicted fracture resistance (using e.g. 3D printing, 3D micro tomography and in-situ testing); (c) extension of such studies to other mechanical behaviors (fracture in elastoplastic and viscoelastic materials) and (d) developing multiscale analysis in this context to apply this methodology at the scale of a structure. Recent works [121] could provide promising basis for such explorations.

Appendix A

The ETO Matlab code

This appendix contains a Matlab code for optimal design of continuum structures based on the evolutionary topology optimization (ETO) method proposed in Chapter 2. The code comes primarily from [44], which is developed on top of the 88-line code [12] with the implementation of the ETO method. The design domain is assumed rectangular and discretized into square plane stress elements. The main program is called form the Matlab prompt by the commands

eto(*nelx, nely, volfrac, er, rmin, ctp*)

where *nelx* and *nely* denote the total number of elements in the horizontal and vertical directions respectively, *volfrac* is the prescribed volume fraction, *er* is the evolutionary rate, *rmin* is the filter radius, and *ctp* specifies the case type of benchmark design. The *ctp* takes values 1, 2, and 3 denoting three benchmark design cases of stiffness maximization design subject to volume fraction constraint: half-MBB beam design, clamped cantilever design, and roller-supported halfwheel design.

```
function eto(nelx,nely,volfrac,er,rmin,ctp)
%% INITIALIZATION
vol = 1; change = 1; ij = 0; xmin = 1e-6;
vx = ones(nely,nelx);
%% MATERIAL PROPERTIES
E0 = 1; Emin = E0*xmin; nu = 0.3; pen = 3.0;
%% PREPARE FINITE ELEMENT ANALYSIS
A11 = [12 3 -6 -3; 3 12 3 0; -6 3 12 -3; -3 0 -3 12];
A12 = [-6 -3 0 3; -3 -6 -3 -6; 0 -3 -6 3; 3 -6 3 -6];
B11 = [-4 3 -2 9; 3 -4 -9 4; -2 -9 -4 -3; 9 4 -3 -4];
B12 = [ 2 -3 4 -9; -3 2 9 -2; 4 9 2 3; -9 -2 3 2];
KE = 1/(1-nu^2)/24*([A11 A12;A12' A11]+nu*[B11 B12;B12' B11
    ]);
nodenrs = reshape(1:(1+nelx)*(1+nely),1+nely,1+nelx);
edofVec = reshape(2*nodenrs(1:end-1,1:end-1)+1,nelx*nely,1)
    ;
```

```
15  edofMat = repmat(edofVec,1,8)+repmat([0 1 2*nely+[2 3 0 1]
       -2 -1],nelx*nely,1);
16  iK = reshape(kron(edofMat,ones(8,1))',64*nelx*nely,1);
17  jK = reshape(kron(edofMat,ones(1,8))',64*nelx*nely,1);
18  %% ELEMENTAL NODES AND COORDINATES
19  nodelast = reshape(nodenrs(1:end-1,1:end-1),nelx*nely,1);
20  elenod = repmat(nodelast,1,4) + repmat([1 nely + [2 1] 0 ],
       nelx*nely,1);
21  [nodex,nodey] = meshgrid(0:1:nelx,nely:-1:0);
22  %% DEFINE LOADS AND SUPPORTS
23 switch(ctp)
24  case 1 % HALF-MBB BEAM
25  F = sparse(2,1,-1,2*(nely+1)*(nelx+1),1);
26  fixeddofs = union(1:2:2*(nely+1), 2*(nely+1)*(nelx+1));
27  case 2 % CANTILEVER
28  F = sparse(2*(nely+1)*(nelx+1)-nely,1,-1,2*(nely+1)*(nelx
       +1),1);
29  fixeddofs = (1:2*(nely+1));
30  case 3 % HALF-WHEEL
31  F = sparse(2*(nely+1)*(nelx/2+1),1,-1,2*(nely+1)*(nelx+1)
       ,1);
32  fixeddofs = union(2*nely+1:2*(nely+1), 2*(nely+1)*(nelx+1))
       ;
33  end
34  U = zeros(2*(nely+1)*(nelx+1),1);
35  alldofs = (1:2*(nely+1)*(nelx+1));
36  freedofs = setdiff(alldofs,fixeddofs);
37 %% PREPARE FILTER
38  iH = ones((nelx+1)*(nely+1)*(2*(ceil(rmin)+1))^2,1);
39  jH = ones(size(iH)); sH = zeros(size(iH)); k =0;
40  [elex,eley] = meshgrid(1.5:nelx+0.5,1.5:nely+0.5);
41  for i1 = 1:nelx+1
42    for j1 = 1:nely+1
43       e1 = (i1-1)*(nely+1)+j1;
44         for i2 = max(i1-ceil(rmin),1):min(i1+ceil(rmin)-1,
              nelx)
45            for j2 = max(j1-ceil(rmin),1):min(j1+ceil(rmin)-1,
                 nely)
46               e2 = (i2-1)*nely+j2; k = k+1; iH(k) = e1;
```

```
47              jH(k) = e2;
48              sH(k) = max(0,rmin-sqrt((i1-elex(j2,i2))^2+(j1-
                    eley(j2,i2))^2));
49          end
50        end
51    end
52  end
53  H = sparse(iH,jH,sH); Hs = sum(H,2);
54  %% START ITERATION
55 while change > 0.0001
56  ij = ij + 1; vol = max(vol*(1-er), volfrac);
57  if ij > 1; olddcnd = dcnd; end
58  %% FE-ANALYSIS
59  sK = reshape(KE(:)*(vx(:)'*E0+(1-vx(:))'*Emin),64*nelx*nely
       ,1);
60  K = sparse(iK,jK,sK); K = (K+K')/2;
61  U(freedofs) = K(freedofs,freedofs)\F(freedofs);
62  %% OBJECTIVE FUNCTION AND SENSITIVITY ANALYSIS
63  ce = reshape(sum((U(edofMat)*KE).*U(edofMat),2),nely,nelx);
64  c(ij) = sum(sum((vx.*E0+(1-vx).*Emin).*ce));
65  dc = ((1-vx)*xmin.^(pen-1)+vx)*E0.*ce;
66  %% FILTERING/MODIFICATION OF NODAL SENSITIVITIES
67  dcnd = reshape((H*dc(:)./Hs),nely+1,nelx+1);
68  if ij > 1; dcnd = (dcnd+olddcnd)/2.; end
69  %% OPTIMALITY CRITERIA UPDATE OF DESIGN VARIABLES
70  l1 = min(dcnd(:)); l2 = max(dcnd(:));
71  while (l2-l1)/abs(l1+l2) > 1.0e-9
72  ls = (l1+l2)/2.0;
73  dcth = dcnd(:)-ls;
74    for i = 1:nely*nelx
75       if min(dcth(elenod(i,:))) > 0
76          vx(i) = 1;
77       elseif max(dcth(elenod(i,:))) < 0
78          vx(i) = 0;
79       else
80          ngrid = 40;
81         [s,t] = meshgrid(-1+1/ngrid:2/ngrid:1-1/ngrid,-1+1/
              ngrid:2/ngrid:1-1/ngrid);
```

```
82          ps = (1 - s(:)).*(1 - t(:))/4 * dcth(elenod(i,1)) +
                 (1 + s(:)).*(1 - t(:))/4 * dcth(elenod(i,2))...
83             + (1 + s(:)).*(1 + t(:))/4 * dcth(elenod(i,3)) +
                    (1-s(:)).*(1 + t(:))/4 * dcth(elenod(i,4));
84          vx(i) = length(find( ps >= 0 ))/length(s(:));
85       end
86    end
87  if mean(vx(:)) - vol > 0;
88  l1 = ls;
89  else
90  l2 = ls;
91  end
92  end
93  %% PLOT RESULTS
94  if ij > 10; change = abs(sum(c(ij-9:ij-5))-sum(c(ij-4:ij)))
       /sum(c(ij-4:ij)); end
95  fprintf('It.:%3i Obj.:%8.4f Vol.:%4.3f ch.:%4.5f\n',(ij),c(
       ij),mean(vx(:)),change);
96  contourf( nodex,nodey, (dcnd-ls), [0 0] ); axis equal; axis
        tight; axis off; pause(1e-6);
97  end
98 end
```

Bibliography

[1] MM Abdalla and Z Gürdal. "Structural design using cellular automata for eigenvalue problems". In: *Structural and Multidisciplinary Optimization* 26.3-4 (2004), pp. 200–208.

[2] J Alexandersen and BS Lazarov. "Topology optimisation of manufacturable microstructural details without length scale separation using a spectral coarse basis preconditioner". In: *Computer Methods in Applied Mechanics and Engineering* 290 (2015), pp. 156–182.

[3] G Allaire. *Shape optimization by the homogenization method*. Vol. 146. Springer Science & Business Media, 2012.

[4] G Allaire and F Jouve. "Minimum stress optimal design with the level set method". In: *Engineering analysis with boundary elements* 32.11 (2008), pp. 909–918.

[5] G Allaire, F Jouve, and AM Toader. "Structural optimization using sensitivity analysis and a level-set method". In: *Journal of computational physics* 194.1 (2004), pp. 363–393.

[6] L Ambrosio and VM Tortorelli. "Approximation of functional depending on jumps by elliptic functional via Γ-convergence". In: *Communications on Pure and Applied Mathematics* 43.8 (1990), pp. 999–1036.

[7] O Amir. "A topology optimization procedure for reinforced concrete structures". In: *Computers and Structures* 114 (2013), pp. 46–58.

[8] O Amir and O Sigmund. "Reinforcement layout design for concrete structures based on continuum damage and truss topology optimization". In: *Structural and Multidisciplinary Optimization* 47.2 (2012), pp. 157–174.

[9] S Amstutz et al. "Topological derivative for multi-scale linear elasticity models applied to the synthesis of microstructures". In: *International Journal for Numerical Methods in Engineering* 84.6 (2010), pp. 733–756.

[10] E Andreassen and CS Andreasen. "How to determine composite material properties using numerical homogenization". In: *Computational Materials Science* 83 (2014), pp. 488–495.

[11] E Andreassen and JS Jensen. "Topology optimization of periodic microstructures for enhanced dynamic properties of viscoelastic composite materials". In: *Structural and Multidisciplinary Optimization* 49.5 (2014), pp. 695–705.

[12] E Andreassen et al. "Efficient topology optimization in MATLAB using 88 lines of code". In: *Structural and Multidisciplinary Optimization* 43.1 (2011), pp. 1–16.

[13] R Behrou, M Lawry, and K Maute. "Level set topology optimization of structural problems with interface cohesion". In: *International Journal for Numerical Methods in Engineering* 112.8 (2017), pp. 990–1016.

[14] MP Bendsøe. "Optimal shape design as a material distribution problem". In: *Structural optimization* 1.4 (1989), pp. 193–202.

[15] MP Bendsøe and N Kikuchi. "Generating optimal topologies in structural design using a homogenization method". In: *Computer methods in applied mechanics and engineering* 71.2 (1988), pp. 197–224.

[16] MP Bendsøe and O Sigmund. "Material interpolation schemes in topology optimization". In: *Archive of applied mechanics* 69.9-10 (1999), pp. 635–654.

[17] MP Bendsøe and O Sigmund. *Topology optimization: theory, methods, and applications*. Springer, 2004.

[18] PE Bernard, N Moes, and N Chevaugeon. "Damage growth modeling using the thick level set (TLS) approach: Efficient discretization for quasi-static loadings". In: *Computer Methods in Applied Mechanics and Engineering* 233 (2012), pp. 11–27.

[19] JP Blasques. "Multi-material topology optimization of laminated composite beams with eigenfrequency constraints". In: *Composite Structures* 111 (2014), pp. 45–55.

[20] B Bochenek and K Tajs-Zielińska. "Minimal compliance topologies for maximal buckling load of columns". In: *Structural and Multidisciplinary Optimization* 51.5 (2015), pp. 1149–1157.

[21] B Bochenek and K Tajs-Zielinska. "Topology optimization with efficient rules of cellular automata". In: *Engineering Computations* 30.8 (2013), pp. 1086–1106.

[22] M Bogomolny and O Amir. "Conceptual design of reinforced concrete structures using topology optimization with elastoplastic material modeling". In: *International Journal for Numerical Methods in Engineering* 90.13 (2012), pp. 1578–1597.

[23] B Bourdin. "Filters in topology optimization". In: *International Journal for Numerical Methods in Engineering* 50.9 (2001), pp. 2143–2158.

[24] B Bourdin and A Chambolle. "Design-dependent loads in topology optimization". In: *ESAIM: Control, Optimisation and Calculus of Variations* 9 (2003), pp. 19–48.

[25] B Bourdin, GA Francfort, and JJ Marigo. "Numerical experiments in revisited brittle fracture". In: *Journal of the Mechanics and Physics of Solids* 48.4 (2000), pp. 797–826.

[26] B Bourdin, GA Francfort, and JJ Marigo. "The variational approach to fracture". In: *Journal of elasticity* 91.1-3 (2008), pp. 5–148.

[27] M Bruggi and P Duysinx. "Topology optimization for minimum weight with compliance and stress constraints". In: *Structural and Multidisciplinary Optimization* 46.3 (2012), pp. 369–384.

[28] TE Bruns and DA Tortorelli. "Topology optimization of non-linear elastic structures and compliant mechanisms". In: *Computer methods in applied mechanics and engineering* 190.26-27 (2001), pp. 3443–3459.

[29] T Buhl, CBW Pedersen, and O Sigmund. "Stiffness design of geometrically nonlinear structures using topology optimization". In: *Structural and Multidisciplinary Optimization* 19.2 (2000), pp. 93–104.

[30] JE Cadman et al. "On design of multi-functional microstructural materials". In: *Journal of Materials Science* 48.1 (2013), pp. 51–66.

[31] S Cai and W Zhang. "Stress constrained topology optimization with free-form design domains". In: *Computer Methods in Applied Mechanics and Engineering* 289 (2015), pp. 267–290.

[32] S Cai et al. "Stress constrained shape and topology optimization with fixed mesh: A B-spline finite cell method combined with level set function". In: *Computer Methods in Applied Mechanics and Engineering* 278 (2014), pp. 361–387.

[33] F Cazes and N Moes. "Damage growth modeling using the thick level set (TLS) approach: Efficient discretization for quasi-static loadings". In: *International Journal for Numerical Methods in Engineering* 103.2 (2015), pp. 114–143.

[34] VJ Challis, AP Roberts, and A Wilkins. "Fracture resistance via topology optimisation". In: *Structural and Multidisciplinary Optimization* 36.3 (2008), pp. 263–271.

[35] W Chen and S Liu. "Topology optimization of microstructures of viscoelastic damping materials for a prescribed shear modulus". In: *Structural and Multidisciplinary Optimization* 50.2 (2014), pp. 287–296.

[36] S Cho and HS Jung. "Design sensitivity analysis and topology optimization of displacement-loaded non-linear structures". In: *Computer Methods in Applied Mechanics and Engineering* 192.22-23 (2003), pp. 2539–2553.

[37] DN Chu et al. "Evolutionary structural optimization for problems with stiffness constraints". In: *Finite Elements in Analysis and Design* 21.4 (1996), pp. 239–251.

[38] A Clausen et al. "Topology optimized architectures with programmable Poisson's ratio over large deformations". In: *Advanced Materials* 27.37 (2015), pp. 5523–5527.

[39] PG Coelho, JM Guedes, and HC Rodrigues. "Multiscale topology optimization of bi-material laminated composite structures". In: *Composite Structures* 132 (2015), pp. 495–505.

[40] PG Coelho et al. "A hierarchical model for concurrent material and topology optimisation of three-dimensional structures". In: *Structural and Multidisciplinary Optimization* 35.2 (2008), pp. 107–115.

[41] D Da et al. "Concurrent topological design of composite structures and the underlying multi-phase materials". In: *Computers & Structures* 179 (2017), pp. 1–14.

[42] D Da et al. "Design of material microstructures for maximum effective elastic modulus and macrostructures". In: *Engineering Computations* 35.2 (2018), pp. 622–640.

[43] D Da et al. "Design of materials using hybrid cellular automata". In: *Structural and Multidisciplinary Optimization* 56.1 (2017), pp. 131–137.

[44] D Da et al. "Evolutionary topology optimization of continuum structures with smooth boundary representation". In: *Structural and Multidisciplinary Optimization* 57.6 (2018), pp. 2143–2159.

[45] D Da et al. "Size effect analysis in topology optimization for periodic structures using the classical homogenization". In: *Submitted for publication* (2018).

[46] D Da et al. "Topology optimization of particle-matrix composites for optimal fracture resistance taking into account interfacial damage". In: *International Journal for Numerical Methods in Engineering* (2018), pp. 1–23.

[47] D Da et al. "Topology optimization of periodic lattice structures taking into account strain gradient". In: *Computers & Structures* 10.1016/j.compstruc.2018.09.003 (2018).

[48] D Da et al. "Topology optimization of structures with fixed periodic microstructures". In: *Submitted for publication* (2018).

[49] JD Deaton and RV Grandhi. "A survey of structural and multidisciplinary continuum topology optimization: post 2000". In: *Structural and Multidisciplinary Optimization* 49.1 (2014), pp. 1–38.

[50] J Deng, J Yan, and G Cheng. "Multi-objective concurrent topology optimization of thermoelastic structures composed of homogeneous porous material". In: *Structural and Multidisciplinary Optimization* 47.4 (2013), pp. 583–597.

[51] NP van Dijk et al. "Level-set methods for structural topology optimization: a review". In: *Structural and Multidisciplinary Optimization* 48.3 (2013), pp. 437–472.

[52] P Duysinx and MP Bendsøe. "Topology optimization of continuum structures with local stress constraints". In: *International Journal for Numerical Methods in Engineering* 43.8 (1998), pp. 1453–1478.

[53] AC Eringen and DGB Edelen. "On nonlocal elasticity". In: *International Journal of Engineering Science* 10.3 (1972), pp. 233–248.

[54] GA Francfort and JJ Marigo. "Revisiting brittle fracture as an energy minimization problem". In: *Journal of the Mechanics and Physics of Solids* 46.8 (1998), pp. 1319–1342.

[55] F Fritzen et al. "Topology optimization of multiscale elastoviscoplastic structures". In: *International Journal for Numerical Methods in Engineering* 106.6 (2016), pp. 430–453.

[56] MJ Garcia, OE Ruiz, and GP Steven. "Engineering design using evolutionary structural optimisation based on iso-stress-driven smooth geometry removal". In: *NAFEMS world congress*. 2001, pp. 24–28.

[57] MJ Garcia-Ruiz and GP Steven. "Fixed grid finite elements in elasticity problems". In: *Engineering Computations* 16.2 (1999), pp. 145–164.

[58] MGD Geers, VG Kouznetsova, and WAM Brekelmans. "Multi-scale computational homogenization: Trends and challenges". In: *Journal of computational and applied mathematics* 234.7 (2010), pp. 2175–2182.

[59] LV Gibiansky and O Sigmund. "Multiphase composites with extremal bulk modulus". In: *Journal of the Mechanics and Physics of Solids* 48.3 (2000), pp. 461–498.

[60] RF Gibson. "A review of recent research on mechanics of multifunctional composite materials and structures". In: *Composite structures* 92.12 (2010), pp. 2793–2810.

[61] Grace X Gu et al. "Optimization of Composite Fracture Properties: Method, Validation, and Applications". In: *Journal of Applied Mechanics* 83.7 (2016), p. 071006.

[62] JK Guest and JH Prévost. "Design of maximum permeability material structures". In: *Computer Methods in Applied Mechanics and Engineering* 196.4-6 (2007), pp. 1006–1017.

[63] JK Guest and JH Prévost. "Optimizing multifunctional materials: design of microstructures for maximized stiffness and fluid permeability". In: *International Journal of Solids and Structures* 43.22-23 (2006), pp. 7028–7047.

[64] JK Guest, JH Prévost, and T Belytschko. "Achieving minimum length scale in topology optimization using nodal design variables and projection functions". In: *International journal for numerical methods in engineering* 61.2 (2004), pp. 238–254.

[65] X Guo, W Zhang, and W Zhong. "Doing topology optimization explicitly and geometrically—a new moving morphable components based framework". In: *Journal of Applied Mechanics* 81.8 (2014), p. 081009.

[66] X Guo, W Zhang, and W Zhong. "Stress-related topology optimization of continuum structures involving multi-phase materials". In: *Computer Methods in Applied Mechanics and Engineering* 268 (2014), pp. 632–655.

[67] X Guo et al. "Explicit structural topology optimization based on moving morphable components (MMC) with curved skeletons". In: *Computer methods in applied mechanics and engineering* 310 (2016), pp. 711–748.

[68] X Guo et al. "Multi-scale robust design and optimization considering load uncertainties". In: *Computer Methods in Applied Mechanics and Engineering* 283 (2015), pp. 994–1009.

[69] X Guo et al. "Stress-related topology optimization via level set approach". In: *Computer Methods in Applied Mechanics and Engineering* 200.47-48 (2011), pp. 3439–3452.

[70] Z Hashin. "Analysis of composite materials—a survey". In: *Journal of Applied Mechanics* 50.3 (1983), pp. 481–505.

[71] Z Hashin and S Shtrikman. "A variational approach to the theory of the elastic behaviour of multiphase materials". In: *Journal of the Mechanics and Physics of Solids* 11.2 (1963), pp. 127–140.

[72] B Hassani and E Hinton. "A review of homogenization and topology opimization II—analytical and numerical solution of homogenization equations". In: *Computers & structures* 69.6 (1998), pp. 719–738.

[73] B Hassani and E Hinton. "A review of homogenization and topology optimization I—homogenization theory for media with periodic structure". In: *Computers & Structures* 69.6 (1998), pp. 707–717.

[74] X Huang, A Radman, and YM Xie. "Topological design of microstructures of cellular materials for maximum bulk or shear modulus". In: *Computational Materials Science* 50.6 (2011), pp. 1861–1870.

[75] X Huang and YM Xie. "Bi-directional evolutionary topology optimization of continuum structures with one or multiple materials". In: *Computational Mechanics* 43.3 (2009), p. 393.

[76] X Huang and YM Xie. "Convergent and mesh-independent solutions for the bi-directional evolutionary structural optimization method". In: *Finite Elements in Analysis and Design* 43.14 (2007), pp. 1039–1049.

[77] X Huang and YM Xie. *Evolutionary topology Optimization of Continuum Structures: Methods and Applications*. Chichester: John Wiley & Sons, 2010.

[78] X Huang and YM Xie. "Topology optimization of nonlinear structures under displacement loading". In: *Engineering Structures* 30.7 (2008), pp. 2057–2068.

[79] X Huang et al. "Topology optimization for microstructures of viscoelastic composite materials". In: *Computer Methods in Applied Mechanics and Engineering* 283 (2015), pp. 503–516.

[80] X Huang et al. "Topology optimization of microstructures of cellular materials and composites for macrostructures". In: *Computational Materials Science* 67 (2013), pp. 397–407.

[81] N Inoue, N Shimotai, and T Uesugi. "Cellular automaton generating topological structures". In: *Second European Conference on Smart Structures and Materials*. Vol. 2361. International Society for Optics and Photonics. 1994, pp. 47–51.

[82] K A James and H Waisman. "Failure mitigation in optimal topology design using a coupled nonlinear continuum damage model". In: *Computer Methods in Applied Mechanics and Engineering* 268 (2014), pp. 614–631.

[83] M Jansen et al. "Topology optimization of fail-safe structures using a simplified local damage model". In: *Structural and Multidisciplinary Optimization* 49.4 (2013), pp. 657–666.

[84] H Jia et al. "Evolutionary level set method for structural topology optimization". In: *Computers & Structures* 89.5-6 (2011), pp. 445–454.

[85] Z Kang, P Liu, and M Li. "Topology optimization considering fracture mechanics behaviors at specified locations". In: *Structural and Multidisciplinary Optimization* (2016), pp. 1–18.

[86] J Kato et al. "Analytical sensitivity in topology optimization for elastoplastic composites". In: *Structural and Multidisciplinary Optimization* 52.3 (2015), pp. 507–526.

[87] E Kita and T Toyoda. "Structural design using cellular automata". In: *Structural and Multidisciplinary Optimization* 19.1 (2000), pp. 64–73.

[88] V Komkov, KK Choi, and EJ Haug. *Design sensitivity analysis of structural systems*. Vol. 177. Academic press, 1986.

[89] V Kouznetsova, MGD Geers, and WAM Brekelmans. "Multi-scale constitutive modelling of heterogeneous materials with a gradient-enhanced computational homogenization scheme". In: *International Journal for Numerical Methods in Engineering* 54.8 (2002), pp. 1235–1260.

[90] N de Kruijf et al. "Topological design of structures and composite materials with multiobjectives". In: *International Journal of Solids and Structures* 44.22-23 (2007), pp. 7092–7109.

[91] C Kuhn and R Müller. "A continuum phase field model for fracture". In: *Engineering Fracture Mechanics* 77.18 (2010), pp. 3625–3634.

[92] C Kuhn, A Schlüter, and R Müller. "On degradation functions in phase field fracture models". In: *Computational Materials Science* 108 (2015), pp. 374–384.

[93] BT Kulakowski, JF Gardner, and JL Shearer. *Dynamic modeling and control of engineering systems*. Cambridge University Press, 2007.

[94] P Ladevèze, O Loiseau, and D Dureisseix. "A micro–macro and parallel computational strategy for highly heterogeneous structures". In: *International Journal for Numerical Methods in Engineering* 52.1-2 (2001), pp. 121–138.

[95] J Lamon, N Carrere, and E Martin. "The influence of the interphase and associated interfaces on the deflection of matrix cracks in ceramic matrix composites". In: *Composites A* 31 (2000), pp. 1179–1190.

[96] M Lawry and K Maute. "Level set topology optimization of problems with soliding contact interfaces". In: *Structural and Multidisciplinary Optimization* 52 (2015), pp. 1107–1119.

[97] S Lee and BM Kwak. "Smooth boundary topology optimization for eigenvalue performance and its application to the design of a flexural stage". In: *Engineering Optimization* 40.3 (2008), pp. 271–285.

[98] K Liu and A Tovar. "An efficient 3D topology optimization code written in Matlab". In: *Structural and Multidisciplinary Optimization* 50.6 (2014), pp. 1175–1196.

[99] P Liu, Y Luo, and Z Kang. "Multi-material topology optimization considering interface behavior via XFEM and level set method". In: *Computer Methods in Applied Mechanics and Engineering* 308 (2016), pp. 113–133.

[100] J Luo et al. "A semi-implicit level set method for structural shape and topology optimization". In: *Journal of Computational Physics* 227.11 (2008), pp. 5561–5581.

[101] Y Luo, MY Wang, and Z Kang. "An enhanced aggregation method for topology optimization with local stress constraints". In: *Computer Methods in Applied Mechanics and Engineering* 254 (2013), pp. 31–41.

[102] Z Luo and L Tong. "A level set method for shape and topology optimization of large-displacement compliant mechanisms". In: *International journal for numerical methods in engineering* 76.6 (2008), pp. 862–892.

[103] Z Luo et al. "Design of piezoelectric actuators using a multiphase level set method of piecewise constants". In: *Journal of Computational Physics* 228.7 (2009), pp. 2643–2659.

[104] J Lv, HW Zhang, and BS Chen. "Shape and topology optimization for closed liquid cell materials using extended multiscale finite element method". In: *Structural and Multidisciplinary Optimization* 49.3 (2014), pp. 367–385.

[105] J Martínez-Frutos and D Herrero-Pérez. "Evolutionary topology optimization of continuum structures under uncertainty using sensitivity analysis and smooth boundary representation". In: *Computers & Structures* 205 (2018), pp. 15–27.

[106] K Maute, S Schwarz, and E Ramm. "Adaptive topology optimization of elastoplastic structures". In: *Structural Optimization* 15.2 (1998), pp. 81–91.

[107] J Michel, H Moulinec, and P Suquet. "Effective properties of composite materials with periodic microstructure: A computational approach". In: *Computer Methods in Applied Mechanics and Engineering* 172.1-4 (1999), pp. 109–143.

[108] C Miehe, M Hofacker, and F Welschinger. "A phase field model for rate-independent crack propagation: Robust algorithmic implementation based on operator splits". In: *Computer Methods in Applied Mechanics and Engineering* 199.45-48 (2010), pp. 2765–2778.

[109] C Miehe and S Mauthe. "Phase field modeling of fracture in multi-physics problems. Part III. Crack driving forces in hydro-poro-elasticity and hydraulic fracturing of fluid-saturated porous media". In: *Computer Methods in Applied Mechanics and Engineering* 304 (2016), pp. 619–655.

[110] C Miehe, LM Schanzel, and H Ulmer. "Phase field modeling of fracture in multi-physics problems. Part I. Balance of crack surface and failure criteria for brittle crack propagation in thermo-elastic solids". In: *Computer Methods in Applied Mechanics and Engineering* 294 (2015), pp. 449–485.

[111] C Miehe, F Welschinger, and M Hofacker. "Thermodynamically consistent phase-field models of fracture: Variational principles and multi-field FE implementations". In: *International Journal for Numerical Methods in Engineering* 83 (2010), pp. 1273–1311.

[112] C Miehe et al. "Phase field modeling of fracture in multi-physics problems. Part II. Coupled brittle-to-ductile failure criteria and crack propagation in thermo-elastic-plastic solids". In: *Computer Methods in Applied Mechanics and Engineering* 294 (2015), pp. 486–522.

[113] HP Mlejnek. "Some aspects of the genesis of structures". In: *Structural optimization* 5.1-2 (1992), pp. 64–69.

[114] N Moes, J Dolbow, and T Belytschko. "A finite element method for crack growth without remeshing". In: *International Journal for Numerical Methods in Engineering* 46 (1999), pp. 131–150.

[115] MI Mohammed, PS Badwal, and I Gibson. "Design and Fabrication Considerations for Three Dimensional Scaffold Structures". In: *The International Conference on Design and Technology*. Vol. 2017. 2017.

[116] D Mumford and J Shah. "Optimal approximations by piecewise smooth functions and associated variational problems". In: *Communications on Pure and Applied Mathematics* 42.5 (1989), pp. 577–685.

[117] A Myśliński. "Level set method for optimization of contact problems". In: *Engineering Analysis with Boundary Elements* 32.11 (2008), pp. 986–994.

[118] SS Nanthakumar et al. "Topology optimization of flexoelectric structures". In: *Journal of the Mechanics and Physics of Solids* 105 (2017), pp. 217–234.

[119] SS Nanthakumar et al. "Topology optimization of piezoelectric nanostructures". In: *Journal of the Mechanics and Physics of Solids* 94 (2016), pp. 316–335.

[120] F Narducci and ST Pinho. "Exploiting nacre-inspired crack deflection mechanisms in CFRP via micro-structural design". In: *Composites Science and Technology* 153 (2017), pp. 178–189.

[121] Nhu Nguyen et al. "Identification of fracture models based on phase field for crack propagation in heterogeneous lattices in a context of non-separated scales". In: *Computational Mechanics* (2018), pp. 1–22.

[122] TT Nguyen. "Modeling of complex microcracking in cement based materials by combining numerical simulations based on a phase-field method and experimental 3D imaging". PhD thesis. Université Paris-Est, 2015.

[123] TT Nguyen et al. "A phase-field method for computational modeling of interfacial damage interacting with crack propagation in realistic microstructures obtained by microtomography". In: *Computer Methods in Applied Mechanics and Engineering* 312 (2016), pp. 567–595.

[124] TT Nguyen et al. "A phase field method to simulate crack nucleation and propagation in strongly heterogeneous materials from direct imaging of their microstructure". In: *Engineering Fracture Mechanics* 139 (2015), pp. 18–39.

[125] TT Nguyen et al. "Initiation and propagation of complex 3D networks of cracks in heterogeneous quasi-brittle materials: Direct comparison between in situ testing-microCT experiments and phase field simulations". In: *Journal of the Mechanics and Physics of Solids* 99 (2016), pp. 320–350.

[126] Y Noguchi et al. "Optimum design of an acoustic metamaterial with negative bulk modulus in an acoustic-elastic coupled system using a level set–based topology optimization method". In: *International Journal for Numerical Methods in Engineering* 113.8 (2018), pp. 1300–1339.

[127] Ml Osanov and JK Guest. "Topology optimization for architected materials design". In: *Annual Review of Materials Research* 46 (2016), pp. 211–233.

[128] K-S Park and S-K Youn. "Topology optimization of shell structures using adaptive inner-front (AIF) level set method". In: *Structural and Multidisciplinary Optimization* 36.1 (2008), pp. 43–58.

[129] NL Pedersen. "Maximization of eigenvalues using topology optimization". In: *Structural and multidisciplinary optimization* 20.1 (2000), pp. 2–11.

[130] R Peering et al. "Some observations on localization in non-local and gradient damage models". In: *European Journal of Mechanics A/Solids* 15.6 (1996), pp. 937–953.

[131] RHJ d Peerlings et al. "Some observations on localisation in non-local and gradient damage models". In: *EUROPEAN JOURNAL OF MECHANICS SERIES A SOLIDS* 15 (1996), pp. 937–954.

[132] CL Penninger et al. "Convergence analysis of hybrid cellular automata for topology optimization". In: *Structural and Multidisciplinary Optimization* 40.1-6 (2010), pp. 271–282.

[133] Z Quan et al. "Microstructural design and additive manufacturing and characterization of 3D orthogonal short carbon fiber/acrylonitrile-butadiene-styrene preform and composite". In: *Composites Science and Technology* 126 (2016), pp. 139–148.

[134] A Radman, X Huang, and YM Xie. "Topological design of microstructures of multi-phase materials for maximum stiffness or thermal conductivity". In: *Computational Materials Science* 91 (2014), pp. 266–273.

[135] H Rodrigues, JM Guedes, and MP Bendsoe. "Hierarchical optimization of material and structure". In: *Structural and Multidisciplinary Optimization* 24.1 (2002), pp. 1–10.

[136] Bingbing San and Haim Waisman. "Optimization of Carbon Black Polymer Composite Microstructure for Rupture Resistance". In: *Journal of Applied Mechanics* 84.2 (2016), p. 021005.

[137] S Schwarz, K Maute, and E Ramm. "Topology and shape optimization for elastoplastic structural response". In: *Computer Methods in Applied Mechanics and Engineering* 190.15-17 (2001), pp. 2135–2155.

[138] JA Sethian and A Wiegmann. "Structural boundary design via level set and immersed interface methods". In: *Journal of computational physics* 163.2 (2000), pp. 489–528.

[139] S Setoodeh, MM Abdalla, and Z Gürdal. "Combined topology and fiber path design of composite layers using cellular automata". In: *Structural and Multidisciplinary Optimization* 30.6 (2005), pp. 413–421.

[140] S Setoodeh, Z Gürdal, and LT Watson. "Design of variable-stiffness composite layers using cellular automata". In: *Computer Methods in Applied Mechanics and Engineering* 195.9-12 (2006), pp. 836–851.

[141] O Sigmund. "A 99 line topology optimization code written in Matlab". In: *Structural and multidisciplinary optimization* 21.2 (2001), pp. 120–127.

[142] O Sigmund. "A new class of extremal composites". In: *Journal of the Mechanics and Physics of Solids* 48.2 (2000), pp. 397–428.

[143] O Sigmund. "Design of multiphysics actuators using topology optimization–Part II: Two-material structures". In: *Computer methods in applied mechanics and engineering* 190.49-50 (2001), pp. 6605–6627.

[144] O Sigmund. "Materials with prescribed constitutive parameters: an inverse homogenization problem". In: *International Journal of Solids and Structures* 31.17 (1994), pp. 2313–2329.

[145] O Sigmund. "Morphology-based black and white filters for topology optimization". In: *Structural and Multidisciplinary Optimization* 33.4-5 (2007), pp. 401–424.

[146] O Sigmund and K Maute. "Topology optimization approaches". In: *Structural and Multidisciplinary Optimization* 48.6 (2013), pp. 1031–1055.

[147] O Sigmund and J Petersson. "Numerical instabilities in topology optimization: a survey on procedures dealing with checkerboards, mesh-dependencies and local minima". In: *Structural optimization* 16.1 (1998), pp. 68–75.

[148] O Sigmund and S Torquato. "Design of materials with extreme thermal expansion using a three-phase topology optimization method". In: *Journal of the Mechanics and Physics of Solids* 45.6 (1997), pp. 1037–1067.

[149] N Sukumar, N Moes, and B Moran. "Extended finite element method for three-dimensional crack modelling". In: *International Journal for Numerical Methods in Engineering* 48 (2000), pp. 1549–1570.

[150] Z Sun et al. "Topological optimization of biomimetic sandwich structures with hybrid core and CFRP face sheets". In: *Composites Science and Technology* 142 (2017), pp. 79–90.

[151] P Tanskanen. "The evolutionary structural optimization method: theoretical aspects". In: *Computer methods in applied mechanics and engineering* 191.47-48 (2002), pp. 5485–5498.

[152] A Tognevi, M Guerich, and J Yvonnet. "A multi-scale modeling method for heterogeneous structures without scale separation using a filter-based homogenization scheme". In: *International Journal for Numerical Methods in Engineering* 108.1 (2016), pp. 3–25.

[153] S Torquato et al. "Effective mechanical and transport properties of cellular solids". In: *International Journal of Mechanical Sciences* 40.1 (1998), pp. 71–82.

[154] A Tovar et al. "Bone structure adaptation as a cellular automaton optimization process". In: *45th AIAA/ASME/ASCE/AHS/ASC Structures, Structural Dynamics & Materials Conference*. 2004, p. 1914.

[155] A Tovar et al. "Hybrid cellular automata: a biologically-inspired structural optimization technique". In: *10th AIAA/ISSMO Multidisciplinary Analysis and Optimization Conference*. 2004, p. 4558.

[156] A Tovar et al. "Optimality conditions of the hybrid cellular automata for structural optimization". In: *AIAA journal* 45.3 (2007), pp. 673–683.

[157] A Tovar et al. "Topology optimization using a hybrid cellular automaton method with local control rules". In: *Journal of Mechanical Design* 128.6 (2006), pp. 1205–1216.

[158] V Tvergaard. "Model studies of fibre breakage and debonding in a metal reinforced by short fibres". In: *Journal of the Mechanics and Physics of Solids* 41 (1993), pp. 1309–1326.

[159] CV Verhoosel and R de Borst. "A phase-field model for cohesive fracture". In: *International Journal for Numerical Methods in Engineering* 96.1 (2013), pp. 43–62.

[160] N Vermaak et al. "Material interface effects on the topology optimizationof multi-phase structures using a level set method". In: *Structural and Multidisciplinary Optimization* 50.4 (2014), pp. 623–644.

[161] WM Vicente et al. "Topology optimization of frequency responses of fluid–structure interaction systems". In: *Finite Elements in Analysis and Design* 98 (2015), pp. 1–13.

[162] F Wang, O Sigmund, and JS Jensen. "Design of materials with prescribed nonlinear properties". In: *Journal of the Mechanics and Physics of Solids* 69 (2014), pp. 156–174.

[163] MY Wang and X Wang. ""Color" level sets: a multi-phase method for structural topology optimization with multiple materials". In: *Computer Methods in Applied Mechanics and Engineering* 193.6-8 (2004), pp. 469–496.

[164] MY Wang, X Wang, and D Guo. "A level set method for structural topology optimization". In: *Computer methods in applied mechanics and engineering* 192.1-2 (2003), pp. 227–246.

[165] SY Wang et al. "An extended level set method for shape and topology optimization". In: *Journal of Computational Physics* 221.1 (2007), pp. 395–421.

[166] YQ Wang et al. "Topological shape optimization of microstructural metamaterials using a level set method". In: *Computational Materials Science* 87 (2014), pp. 178–186.

[167] P Wei and MY Wang. "Piecewise constant level set method for structural topology optimization". In: *International Journal for Numerical Methods in Engineering* 78.4 (2009), pp. 379–402.

[168] L Xia and P Breitkopf. "A reduced multiscale model for nonlinear structural topology optimization". In: *Computer Methods in Applied Mechanics and Engineering* 280 (2014), pp. 117–134.

[169] L Xia and P Breitkopf. "Concurrent topology optimization design of material and structure within FE2 nonlinear multiscale analysis framework". In: *Computer Methods in Applied Mechanics and Engineering* 278 (2014), pp. 524–542.

[170] L Xia and P Breitkopf. "Design of materials using topology optimization and energy-based homogenization approach in Matlab". In: *Structural and multidisciplinary optimization* 52.6 (2015), pp. 1229–1241.

[171] L Xia and P Breitkopf. "Multiscale structural topology optimization with an approximate constitutive model for local material microstructure". In: *Computer Methods in Applied Mechanics and Engineering* 286 (2015), pp. 147–167.

[172] L Xia and P Breitkopf. "Recent advances on topology optimization of multiscale nonlinear structures". In: *Archives of Computational Methods in Engineering* 24.2 (2017), pp. 227–249.

[173] L Xia, D Da, and J Yvonnet. "Topology optimization for maximizing the fracture resistance of quasi-brittle composites". In: *Computer Methods in Applied Mechanics and Engineering* 332 (2018), pp. 234–254.

[174] L Xia, F Fritzen, and P Breitkopf. "Evolutionary topology optimization of elastoplastic structures". In: *Structural and Multidisciplinary Optimization* 55.2 (2017), pp. 569–581.

[175] L Xia et al. "Bi-directional evolutionary structural optimization on advanced structures and materials: a comprehensive review". In: *Archives of Computational Methods in Engineering* 25.2 (2018), pp. 437–478.

[176] Q Xia, T Shi, and L Xia. "Topology optimization for heat conduction by combining level set method and BESO method". In: *International Journal of Heat and Mass Transfer* 127 (2018), pp. 200–209.

[177] Q Xia et al. "A level set solution to the stress-based structural shape and topology optimization". In: *Computers and Structures* 90-91 (2012), pp. 55–64.

[178] Z Xia, Y Zhang, and F Ellyin. "A unified periodical boundary conditions for representative volume elements of composites and applications". In: *International Journal of Solids and Structures* 40.8 (2003), pp. 1907–1921.

[179] YM Xie and GP Steven. "A simple evolutionary procedure for structural optimization". In: *Computers & structures* 49.5 (1993), pp. 885–896.

[180] YM Xie and GP Steven. "Basic evolutionary structural optimization". In: *Evolutionary Structural Optimization*. Springer, 1997, pp. 12–29.

[181] YM Xie et al. "Convergence of topological patterns of optimal periodic structures under multiple scales". In: *Structural and Multidisciplinary Optimization* 46 (2012), pp. 41–50.

[182] B Xu, J Jiang, and Yi Min Xie. "Concurrent design of composite macrostructure and multi-phase material microstructure for minimum dynamic compliance". In: *Composite Structures* 128 (2015), pp. 221–233.

[183] Y-M Yi, S-H Park, and S-K Youn. "Design of microstructures of viscoelastic composites for optimal damping characteristics". In: *International Journal of Solids and Structures* 37.35 (2000), pp. 4791–4810.

[184] J Yvonnet. *Computational homogenization with finite elements, In preparation*. Springer, 2018.

[185] J Yvonnet and G Bonnet. "A consistent nonlocal scheme based on filters for the homogenization of heterogeneous linear materials with non-separated scales". In: *International Journal of Solids and Structures* 51.1 (2014), pp. 196–209.

[186] J Yvonnet and G Bonnet. "Nonlocal/coarse-graining homogenization of linear elastic media with non-separated scales using least-square polynomial filters". In: *International Journal for Multiscale Computational Engineering* 12.5 (2014), pp. 375–395.

[187] W Zhang and S Sun. "Scale-related topology optimization of cellular materials and structures". In: *International Journal for numerical methods in Engineering* 68.9 (2006), pp. 993–1011.

[188] W Zhang et al. "A new three-dimensional topology optimization method based on moving morphable components (MMCs)". In: *Computational Mechanics* 59.4 (2017), pp. 647–665.

[189] W Zhang et al. "A new topology optimization approach based on Moving Morphable Components (MMC) and the ersatz material model". In: *Structural and Multidisciplinary Optimization* 53.6 (2016), pp. 1243–1260.

[190] W Zhang et al. "Using strain energy-based prediction of effective elastic properties in topology optimization of material microstructures". In: *Acta Mechanica Sinica* 23.1 (2007), pp. 77–89.

[191] M Zhou and GIN Rozvany. "The COC algorithm, Part II: topological, geometrical and generalized shape optimization". In: *Computer Methods in Applied Mechanics and Engineering* 89.1-3 (1991), pp. 309–336.

[192] ZH Zuo et al. "Comparing optimal material microstructures with optimal periodic structures". In: *Computational Materials Science* 69 (2013), pp. 137–147.

[193] ZH Zuo et al. "Multi-scale design of composite materials and structures for maximum natural frequencies". In: *Materials & Design* 51 (2013), pp. 1023–1034.